UNIVERSITY OF SOUTHAMPTON

Pipe detection and remote condition monitoring using an in-pipe excitation technique

by

Mohammad reza Salimi

Thesis for the degree of Doctor of Philosophy

FACULTY OF ENGINEERING AND THE ENVIRONMENT
Institute of Sound and Vibration Research

August 2020

UNIVERSITY OF SOUTHAMPTON

ABSTRACT

FACULTY OF ENGINEERING AND THE ENVIRONMENT
Institute of Sound and Vibration Research

Doctor of Philosophy

Pipe detection and remote condition monitoring using an in-pipe excitation technique

by Mohammad reza Salimi

Finding the location of underground utilities, essentially plastic water pipes, can be difficult and disruptive, which is due to the lack of efficient techniques that can be used to map these buried network services. Vibro-acoustic techniques to determine the location of buried water pipes have been studied within the Institute of Sound and Vibration Research within (ISVR) in the past 10 years. One technique involves excitation of the water pipe where it is accessible, normally from hydrant, followed by measuring the ground surface vibration, at the vicinity of suspecting pipe location. From an earlier feasibility study it was indicated that the emitted ground borne waves from the waves that propagate along the pipe and its contained fluid can help manifest the pipe location.

Because the attenuation of the waves is generally large for the plastic water pipe, the pipe ground borne waves cannot be sensed at large distances away from the exciter's location, of order of a few tenths of a metre, or at high frequencies, above 100 Hz. This thesis aims at using an in-pipe excitation source, which can be deployed at any desired location along the pipe length, to overcome the attenuation problem.

Although in-pipe sources can transfer energy to the pipe contained fluid and might allow tracking of the pipe at larger ranges, current acoustic exciters are not always appropriate, being cumbersome and too large to fit into a typical buried water pipe. In this thesis, two pneumatic devices were designed with the aim of generating high amplitude signals at low frequencies and with the ability of accessing pipes with a wide range of diameters, down to 1 cm. The devices are experimentally characterised by a series of laboratory tests in a water-filled plastic pipe section. A comparison of the acoustic pressure wave transmitted to a fluid filled pipe between a standard electro-acoustic device, an electromagnetic shaker, and the pneumatic ones is made.

From the previous work on characterization of wave propagation along plastic water filled pipes, it is known that at below 100 Hz, among all kinds of waves, the axisymmetric fluid borne wave can predominately drive the ground borne wave. Owing to

the good coupling of the axisymmetric fluid and the shell borne wave they should be considered altogether. The wave speed and attenuation of both waves were measured experimentally, and the results were checked for consistency with the theory. An analytical simulation was developed to explain the reason of high wave attenuation variances obtained from the experimental measurement. Due to the dependency of the axisymmetric fluid and structural borne waves' amplitude to the elastic properties of the pipe a simple experimental method was proposed to distinguish between the pipe wall displacement that arises from the two axisymmetric waves. Such a technique might help assess the condition of pipes through indicating the reduction in their elastic properties due to ageing.

From the earlier work on detecting buried water pipes, it was indicated that in addition to the axisymmetric fluid borne wave, the exciter applied to the pipe directly/indirectly drives the ground borne waves with substantial amplitudes. To have a better understanding about the overall response of the ground surface, a simple analytical model was developed, taking into account a ground borne wave emitted from the pipe and the source respectively. Like numerous other digital image processing, in the vibro-acoustic technique, an arctangent operator is used to extract the phase or time delay information, as the assumed ground borne waves are emitted and travel to the measurement point. By virtue of the fact that the arctangent operator produces phase images wrapped between $-\pi$ to π, an unwrapping operator is required to remove the phase discontinuities embedded within the image. Therefore, a novel phase unwrapping algorithm is developed with a low-cost computational requirement. Furthermore, different state-of-the-art two-dimensional unwrapping algorithms are reviewed and compared for their ability to remove the phase discontinuities, produced by the model. In addition, a drawback of applying one-dimensional unwrapping to the two-dimensional wrapped phase image, used in the previous study, is discussed.

To benchmark the effectiveness of the developed pneumatic devices, different exciters such as standard mechanical and electroacoustical exciter are utilised to map a buried pipe. Applying mechanical excitation to the pipe is associated to the earlier feasibility study which repeated for the sake of benchmarking the in-pipe exciters' results against it. Of the exciters, one of the designed pneumatic sources successfully mapped the total length (18 m) of the pipe. Because the aim of this thesis is deploying an in-pipe source to overcome the attenuation problem, the utilised acoustical exciters: the underwater speaker and the designed pneumatic sources are deployed at two more locations along the pipe. The results from each exciter are analysed in detail and compared to each other.

Contents

Declaration of Authorship

I, Mohammad reza Salimi, declare that this thesis titled, *Pipe detection and remote condition monitoring using an in-pipe excitation technique* and the work presented in the thesis are both my own, and have been generated by me as the result of my own original research. I confirm that:

- this work was done wholly or mainly while in candidature for a research degree at this University;
- where any part of this thesis has previously been submitted for a degree or any other qualification at this University or any other institution, this has been clearly stated;
- where I have consulted the published work of others, this is always clearly attributed;
- where I have quoted from the work of others, the source is always given. With the exception of such quotations, this thesis is entirely my own work;
- I have acknowledged all main sources of help.
- where the thesis is based on work done by myself jointly with others, I have made clear exactly what was done by others and what I have contributed myself;
- parts of this work have been published as:

– M.Salimi, J. M. Muggleton and E. Rustighi, "Design and laboratory testing of pneumatic devices for the acoustic excitation of water filled plastic pipes," *in XIIIth International Conference on Recent Advances in Structural Dynamics (RASD2019)*, INSA Lyon, France 15 - 17 April 2019.

– M.Salimi, J. M. Muggleton and E. Rustighi, "On the distinction of axisymmetric waves within a fluid-filled pipe using wavenumber measurement," *in 4th International Congress on Sound and Vibration (ICSV24)*, London, UK, July.

– M.Salimi, J. M. Muggleton and E. Rustighi, "Pipe assessment and remote condition using an in-pipe excitation technique," *in 6th International Conference on Acoustics and Vibration*, Tehran, Iran, December.

– M.Salimi, J. M. Muggleton and E. Rustighi, "Analytical simulation of low frequency wave radiation from a buried water pipe," *in The International Conference on Applied Engineering*, Newcastle, United Kingdom, 20-21 October.

Signed: _____

Date: _____

Acknowledgements

I have always been highly independent and believe in myself to achieve the best in every stage of my academic and personal life. Writing this thesis has been another marathon exercise.

I would like to express my sincere gratitude to my supervisors Dr Jen Muggleton and Dr Emiliano Rustighi for their guidance and supervision throughout this project. Their motivation, guidance and support have helped me in all of the time of research and writing of this thesis.

I wish to show my gratitude to Professor Victor Humphery and Professor Phil Joseph for their useful comments, questions and suggestions at each review meeting.

My sincere thanks goes to Dr Saeed Fadaee and Dr Siyavash Mir Ahmadi for their encouraging and friendly advice during my research.

I wish to express my deepest gratitude to Professor Alireza Arabshahi for his continuous guidance and encouragement to take on challenges in my research with great approach.

Sincere thanks to all of those working at the ISVR electrical and mechanical workshops for their help and support to set up my rigs needed for this research.

I would like to pay my special regards to my students at Olympic Wrestling Society. As a coach, your passion to learn new techniques were always admirable and inspiring.

Finally I wish to acknowledge the support of my family. They encouraged me to keep going and without their support, this work would not have been possible.

Nomenclature

Abbreviation	Full-form
B&K	Brüel and Kjær
CSD	Cross Spectral Density
DAC	Digital-to-Analogue Conversion
DCT	Discrete Cosine Transform
FFT	Fast Fourier Transform
FRF	Frequency Response Function
GND	Ground
GPR	Ground Penetration Radar
IFFT	Inverse Fourier Transform
ISVR	Institute of Sound and Vibration Research
MDPE	Medium-density polyethylene
P	Compressional
PE	Polyethylene
PVC	Polyvinyl chloride
PSD	Power Spectral Density
RBI	Risk Based Inspection
SH	Shear horizontal
SNR	Signal to Noise Ratio
SV	Shear vertical

Symbol	Description
Latin letters	
a, b, c ..., q	Pixels parameters in a wrapped image
a, a_i, a_e, a_o	Mean, internal,external shell and orifice radius
A_e, A_t	Cross sectional area of the nozzle outlet and nozzle throat
b_c	Critical pressure ratio
B, B_f, B_m, B_p	General bulk modulus, bulk modulus of fluid, the surrounding medium and the pipe wall
c, c_d, c_r, c_R	General wave speed, compressional, shear, and Rayleigh wave speed
c_s, c_m	Axisymmetric and the surrounding medium wave speed of shell
$DI_{\text{SV, point}}, DI_{\text{p, point}}, DI_{\text{pipe}}$	The reduction term to the amplitude of the ground surface from shear vertical, compressional and wave re-radiation from pipe vibration in the vertical plane, emitted via a buried point source and a pipe wall.
$E[\,]$	The expectation
E, E_p, E_m	General Young's modulus, Young's modulus of pipe and surrounding medium
f_{ring}	Ring frequency $f_{ring} = \frac{c_L}{2\pi r}$
f_1, f_2	Start and end frequencies when using frequency unwrapping
$f_{n+\frac{1}{2}}, f_{n-\frac{1}{2}}$	The two half power frequencies near to the natural frequency of the system
f_s	Sampling frequency
FL_{i}, FL_e	Internal and external fluid loadings
G, G_m	General shear modules, shear modules of surrounding medium
$H(f)$	Transfer function of a linear system

H_{an}	Enthalpy difference
h, h_b	Thickness of pipe walls, depth of buried pipes and point sources
i	$\sqrt{-1}$
$J_n(), J_n^{'}()$	Bessel function of order n and its differentiation
k, k_1, k_2	General wane number, wavenumber of the $s = 1, 2$ wave
k_b	General wane number for body waves in the surrounding soil
k_d, k_r, k_s	Primary and secondary wavenumber in mediums, wavenumber of the axisymmetric waves
$k_{r1}^r, k_{d1}^r, k_{r2}^r, k_{d2}^r$	Radial component of the wavenumber associated to the re-radiated shear and compressional waves, from the axisymmetric fluid and structural borne wave, into the medium
k_m, k_{m1}, k_{m2}	Surrounding medium wavenumber and the radial component of the wavenumber, associated to the axisymmetric fluid and structural borne, in the surrounding medium
k_f, k_L	The free field fluid wavenumber and the compressional wavenumber in a plate
$k_{fs}^r, k_{ds}^r, k_{rs}^r$	Radial wavenumber in the pipe and the surrounding medium from axisymmetric waves
k_{rs}	Shear conical wavenumber
k_{unwrap}	Unwrapped wavenumber
k_m	Bulk modulus of the surrounding medium
L	Length of pipe
m	Mass
M_e	Mach number

$M_{\text{rad1,2}}, R_{\text{rad1,2}}$	Mass and resistance component of the radiation impedance for the axisymmetric fluid and structural borne wave.
n, s	Circumferential modal number and axial wave association
n_r	The number of circumferential mode below the ring frequency $n_r = \left(\frac{h}{\sqrt{12}a}\right)^{1/2}$
n_d	The number of averaging
N	The number of the half wavelengths that fit between adjacent measurement points
p_{air}	Air pressure
p_f, p_m	Induced pressure in pipe and the surrounding medium from the axisymmetric fluid and shell borne wave
p_v	Vapour pressure
P_∞, P_{Pn}, p_e	Ambient pressure, compressed air pressure and pressure inside the exhaust
P_{fs}, P_{ds}, P_{rs}	Pressure amplitude of the $s = 1, 2$ wave within the contained fluid and the surrounding medium
P	Pressure associated to the one dimensional pressure wave within the fluid.
q_{out}	Mass of compressed air flow
Q_0, Q_1, Q_2	Amplitude of the each circumferential $n = 0, 1, 2$ modes
$Q(A, B, C, D)$	Transfer function between measured acceleration of the pipe wall at point A,B,C,D, around pipe circumference with respect to the input energy to the pipe
QM	Quality factor
$r_{\text{pipe,soil}}$	The radial component of conical wave radiation from the pipe wall to the measured point at the surface

r	The radial distance from source to the measurement point
R, Rs	Residue
$D_{\text{pipe}}, r_{\text{point}}$	The distance of the wave radiation from the pipe wall and the point source to the surface respectively.
t	Time variable
$\ddot{u}_f, \dot{u}_f$	Axial fluid displacement and velocity
u, w, v	Displacement components
U_s, V_s, W_s	Amplitude of the axial, circumferential and radial displacement of the $s = 1, 2$ waves
U_m, V_m, W_m	Displacement amplitude of surrounding medium in radial, axial and circumferential direction
V	Applied voltage to a driver
V_1, V_2	Amplitude of wave radiation from point source and pipe
$V_{\text{point}}, V_{\text{pipe}}$	Vibration of the ground surface resulted from radiation of the wave from the point source and the pipe wall
V_{ref}	The reference point which corresponds to the amplitude of the vibration measured at the origin
$V_{ps}^r, V_{fs}^r, V_{ms}^r$	Radial vibration of the pipe wall, contained fluid and the surrounding medium form the s = 1,2 waves
$\mathbf{W}$	Wrapping operator
W_M	Weighting matrix
$x_{\text{pipe}}, D_{\text{pipe}}$	Distance of the wave travelling within the pipe, distance of the wave that travels from the pipe wall till reaches ground surface
x, θ, r	Axial, circumferential and radial directions
x, y, z	Cartesian coordinates system

x_1, x_2	First and second distance from a reference point
$X(f), Y(f), N(f)$	Linear spectrum of x(t) , y(t) and noise n(t) from environment

Greek letters

$\alpha_{\text{point}}, \beta_{\text{point}}$	Angle of wave emission from the point source to the first and second excitation point respectively
β	Fluid loading term $\beta = \frac{2B_f a}{E_p h}\left(1 - v_p^2\right)$
γ	Coherence
Δ	Volume stress
Δx	Distance between the sensors on the pipe wall
Δ_d	Distance between any two point discontinuities
Δ_G	Distance between geophone at the surface
Δ_ϕ	Distance between geophone at the surface
$\varepsilon_1, \varepsilon_2$	Energy per unit length associated to the s = 1,2 waves
$\varepsilon_x, \varepsilon_\theta$	Axial and circumferential strain
ε	Error
η_p, η_m	Damping coefficient of pipe and surrounding medium
$\theta_{\text{point}}, \alpha$	Angle of wave radiation from the point source and the pipe wall to the surface
λ_b	Wavelength of body waves in the surrounding soil
λ_m, μ_m	First and second Lame constant
$\lambda_1, \lambda_{min}, \lambda_{max}$	Wavelength of the $s = 1$ wave, minimum and maximum wavelength
μ	The fluid – shell mass ratio $\mu = \frac{a\rho_f}{h\rho_s}$
ϕ	Wrapped phase value

φ_0	Initial phase
ϕ, ψ	Scalar potential related to the primary wave and vector potential related to the secondary wave
ψ_s	The shell thickness parameter $\psi_s^2 = \dfrac{h^2}{12a^2}$
ρ_f, ρ_p, ρ_m	Density of the fluid, pipe and the surrounding medium
v_p, v_m	Poisson's ratio of pipe wall and surrounding medium
ω	Angular frequency
Ω, Ω_r	The angular and the ring frequency, $\Omega_r = 2\pi f_{\text{ring}}$
Υ	One dimensional unwrapper
σ_x, σ_θ	Stress in the axial and circumferential direction
ψ	Unwrapped phase value
Ω	Normalised Frequency to ring frequency $\Omega = \dfrac{\omega}{\omega_r}$
$\varrho_{i,j}^x, \varrho_{i,j}^y$	Weighting matrix in the x and the y direction
$\aleph(N)$	An integer number used to wrapped the phase data to $(-\pi, \pi)$

Mathematical

$H_d(i,j), D_1(i,j)$ and $V_d(i,j), D_2(i,j)$	The second difference in the horizontal and the vertical direction of the matrix
Im[ ]	Imaginary part of [ ]
Re[ ]	Real part of [ ]
Ro	Rounding operator
$S_{xy}(f)$	Cross-spectral density between $X(f)$ and $Y(f)$
∇^2	The Laplacian operator
∇	Dell, spatial partial derivative operator

$Var[\,]$	Variance of [ ]
$\mathbf{W}$	Wrapping operator
(*)	Complex conjugation

Chapter 1

Introduction and literature review

Effective inspection and condition monitoring of buried water pipes are required to ensure their safe and productive operation. As such, it helps to mitigate the risk of disastrous failure resulting from their deterioration. In most cases, assessing the condition of such pipes, followed by repairing or rehabilitating, requires a knowledge of their route [1].

Traditional techniques to locate buried pipes can be problematic, as it is often necessary to occupy public road space for excavation purposes, at multiple locations [2]. They are likely to hinder pedestrians, produce noise and waste. Additionally, machinery consumes funds and energy, as do the transportation of material to dump sites and to recycling plants [3]. Besides, excavating holes to access buried water pipes adversely affects the sustainability of roads and the embedded service utilities. Having the underground water pipes beneath urban lands, adopting such detection procedures might cause disruptions to traffic at congested area.

Costs directly related to locating buried utility services amount to 1.5 billion pounds per year, in the UK, with 150 million pounds of that attributed to damage to third-party property. The inclusion of social costs directly related to street works brings costs up to 7.0 billion pounds annually [3].

Owing to the continuous development of cities, it is not surprising that buried water distribution systems comprise different materials and technologies. Sustainability, adaptability, lower price, simple to handle and install of plastic pipes have made them to become popular in marketplace and rapidly replacing other types of pipe [4].

Potential techniques that might be adopted to pinpoint the location of plastic water pipes, can be divided into two main categories: Electromagnetic and Vibro-acoustic based techniques. In 2014 a Gyroscopic based system was developed in Belgium by the Reduct NV company and is widely used for remotely detecting buried pipelines, both metallic and non-metallic [5]. Therefore its principles are explained in this chapter. Further detection techniques exist that can be used for tracing buried plastic water pipes. The applications and limitations of these are well documented in [6, 7] and are beyond the scope of this project.

1.1 Electromagnetic based techniques

Of the electromagnetic based techniques, Ground Penetration Radar (GPR) approaches are normally used by pipe locator companies for the detection of underground plastic water pipes. The use of the GPR approach dates back to 1956, when Hulsenbeck, a German scientist, first patented and used pulse electromagnetic wave techniques to illuminate the characteristics of a buried structure [8]. Following this initial development, several other researchers have continued to detect subsurface objects ever since.

The operation of GPR and effective detection ranges are explained in detail by Daniels [9]. To put it briefly, in GPR, high frequency electromagnetic pulses, continuous waves (CW) or step-frequency (SF) signals are transmitted into the ground via a transmitting antenna. Electromagnetic pulses approximately ranging from 1 MHz to 10 GHz lasting from about 1 ns to 30 ns are normally adopted in a GPR survey. The transmitted wave expand similar to spherical wave fronts into the medium. Upon its strike to a boundary between two materials with different dielectric constants, some of the signal reflects from the boundary and detected at the surface via a receiving antenna [10]. Providing that the velocity of the signal in the material is a known parameter, the travelling time indicates the distance of travelling [10]. The velocity of the discharged signal in the subsurface can be estimated the dielectric constant and the relative magnetic permittivity of materials.

In some GPR surveys, for a number of pulses, the transmitter is kept at a constant position and the receiving antenna is moved at equally spaced intervals over the surface, leading to record different time delay. Time traces of the recorded signal and/or the depth of the object along a transect profile can be displayed vertically with the horizontal axis display the receiver position. The recorded data from a subsurface target in an ideal case looks like a hyperbola that is illustrated in Fig. 1.1. The top of the hyperbola, where the receiving antenna and the object are aligned, indicates the centre of the buried object.

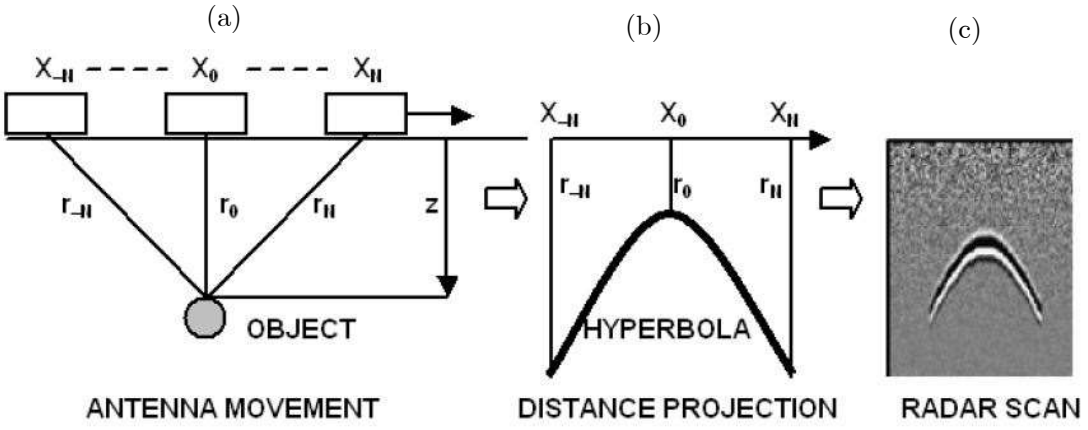

FIGURE 1.1: Detection of a buried object using GPR [11]. (a) Recording the object reflection, buried to a depth of Z, from X_{-N} to X_N.(b) Estimating the travelling distance r_{-N} to r_N. (c) The final image that appears on the radar screen.

In some applications, recording the variation to the transmission of the signal through the medium is more favourable for probing. Both concepts are illustrated in Fig. 1.2.

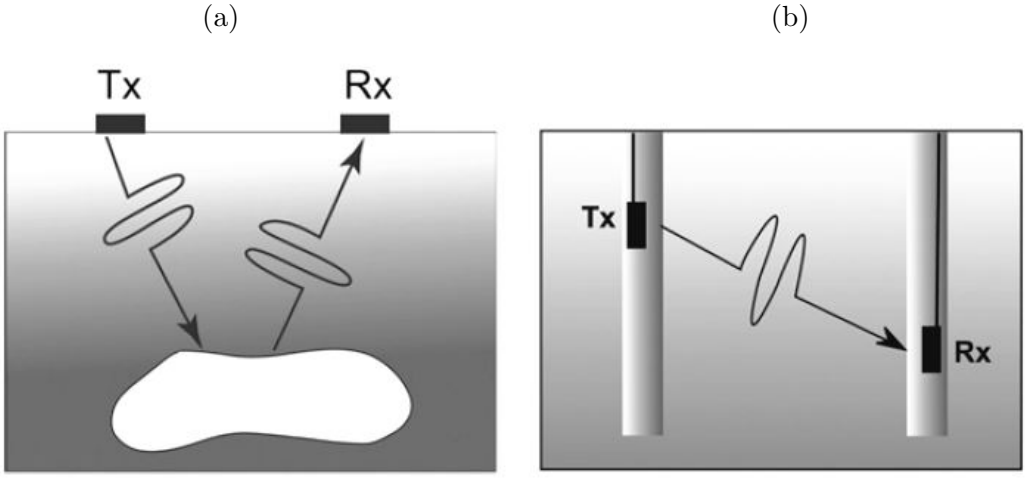

FIGURE 1.2: GPR survey using transmitter Tx and receiver Rx [10].(a) Recording the scattering from the buried object.(b) Recording the transmitted signal through the material.

Several studies were carried out by Ayala-Cabrera *et al.* [12–16] to locate and characterised buried water supply systems using GPR surveys. In reference [16], for instance, the performance of GPR technique on locating pipes made of Polyvinyl chloride (PVC), polyethylene (PE), asbestos cement and cast iron with 0.1 metre in diameter was tested through an experimental measurement. The experimental study consisted of burying the pipes in dry soil to a depth of approximately 1 metre and repeat the test for each sample. They managed to track and localize asbestos cement and cast iron pipes; however, the low amplitude reflected signal from the PVC and the PE did not clearly reveal the contrast of the boundary between the soil and the pipe walls. Similar results were obtained by Ni et al. [17] and it was deduced that plastic materials are transparent to the EM waves. The primary goal of Ni et al. [17], however, was to introduce using discrete wavelet transform as to discriminate the reflection from multiple aligned pipes, buried to the different depth. Ayala-Cabrera *et al.* [12], carried out further post-processing to improve and manifest the scattering from plastic pipes. Beside, some successful detection of a buried plastic pipe at the depth of 10 cm and 1 metre was reported in reference [18].

In the real world situation, however, poor detection rate from GPR approaches, on mapping plastic water pipes was reported. Therefore, an electromagnetic traceable marker is normally integrated with the pipe [19]. Currently there are many electromagnetic traceable markers available in the market place. For the sake of brevity, only one of which; pipe detector tape, is explained in this section.

The pipe detector tape, containing aluminium foil at one side, is normally buried above the pipe axis. Due to the high reflectivity of the material, employing the GPR technique can manifest the pipe route, but not its depth. The tape can act as an dig-in warning to the utility owner prior to damaging the pipe [19]. The excavation for installing new buried assets, however, normally causes the tape to be damaged or removed in part.

With the pipe detector tape, the detection still suffers from some fundamental drawbacks associated to the GPR technique. For instance, the resolution in GPR image is approximately a quarter of the wavelength of the transmitted signal. Increasing the frequency whilst increasing the resolution, reduces the penetration depth [10]. The limitation on penetration depth also originates from inefficient coupling of the emitted signal into the medium, the type and heterogeneous electrical and magnetic properties of the medium

[9, 20, 21]. For example, if the surrounding medium is conductive, contains clay, salts present in water in the material, saturated or even moist soil, the penetration depth of a GPR survey can be restricted to the order of few tenths of a centimetre. This is due to the high attenuation of the transmitted and reflected electromagnetic waves [22]. Moreover, tracking and locating an object beneath the ground surface with a high permeability value results in lower values of the signal amplitude and penetration depth [10].

In summary, despite the electromagnetic traceable marker integration to locate buried objects, the operation of GPR is yet severely affected by the depth and the soil properties where the pipe is buried.

1.2 Vibro-acoustic methods

Several vibro-acoustic techniques were previously studied at the University of Southampton. For the sake of brevity the technique that will be used and developed in this thesis to manifest the pipe location is explained in this section. The technique was patented in 1992 by Huebler and Campbell [23] and further developed by Burns *et al.* [24].

In 2011, Muggleton *et al.* [25] further studied the technique and mentioned that in the presence of a leak, high amount of energy at relatively low frequencies propagates along the pipe and re-radiate to its surrounding medium. The generated noise from pipe and leak are sometimes loud enough to be sensed even via a listening stick above ground. The listening stick contains a ground microphone, amplification and filtering system combined with an electronic listening headphone or amplitude meter [26]. The technique works by steadily move away the listening stick at the vicinity of the suspected noise source above the surface. The location of noise sources, whether the pipe or leak, are assumed respectively to be beneath the path or place where the measured signal reaches to its local maxima [26].

Strong attenuation of the pipe wave due to the material damping of the plastic pipe and spreading of the acoustic wave from the pipe wall to the surrounding medium, above 100 Hz, suggests focusing on the low frequency content for identifying the pipe location. At such a identified frequency range, it is well known the axisymmetric fluid borne wave causes predominantly re-radiation to the surrounding medium. In view of

low energy generation from most leaks, the ground borne wave is normally driven with inconsiderable amplitude. By applying any intentional excitations that can excite the favourable wave type with a high amplitude, over the desired frequency range of interest, a significant re-radiation from the pipe to its surrounding medium can be attained to illustrate its path. Therefore, several vibrating devices have been developed and exploited in industry on this matter and thereby the radiated ground-borne wave from the pipe can be better realised at the surface. Burns *et al.* [24] showed that an analysis of phase measurements obtained from an array of sensors, perpendicular to the pipe axis can illustrate the depth and the path of the pipe. Nevertheless, in industry, the magnitude of the surface vibration is utilised to manifest the pipe location [26]. The novelty of the proposed technique by Muggleton *et al.* [25] lies on plotting the spatial phase data between the measured surface vibration, using an array of sensors, and the input signal from the excitation source. Muggleton *et al.*[25] also mentioned that alongside that of the ground-borne wave from the pipe, the excitation source applied to the pipe tends to generate directly/ indirectly, high amplitude spherical ground borne waves in the medium.

It has been stated that the magnitude of the surface vibration velocity on its own is vulnerable to the ambient noise and for low coherence the standard deviation of the cross spectrum density between the input signal to the driver and the recorded vibration at the surface is approximately 5 times the true value. On the contrary for the same CSD by averaging over 10 records the point at which the phase estimate becomes unreliable is at coherence of 10^{-4}, which is a low value. Beside being dependent to the signal strength, the peak in the magnitude plot changes with respect to the sensor to the ground coupling. Provided that the excitation is reproducible, however, the use of magnitude data might allow recognition of any discontinuities along the pipe and might yield some information about the sudden changes to the elastic properties of the ground surface [25]. Discontinuities in the pipe cause wave reflection and mode conversion of pipe waves and high amounts of energy might radiate into the soil.

The efficiency of the vibro-acoustic search is highly dependent on the excitation source [27], the relative amplitude of the pipe and direct/ indirect source wave, pipe depth and its coupling to the surrounding medium, material properties of the pipe and the surrounding medium as well as the sensor type used to record the ground surface vibration. Although it is reported that the method can successfully detect both iron and

plastic water pipes, the attenuation of the desired wave might not allow the mapping of the pipe that is far way from the excitation source. At relatively low frequency ranges <100 Hz, such attenuations might not be considerable. The maximum length at which a single excitation can be utilised for mapping the buried pipes has not been identified yet. The furthest detection length is 18 m, which was reported in [25] .

1.3 Gyroscope based system

Among gyroscope (or inertial navigation) based systems, an in-pipe device which is initially developed by a Belgium company [5], Pipetrack Ltd, is widely used for mapping buried pipes in three dimensions. Therefore, its working principle, applications and drawbacks are detailed in this section.

The devices are made of a sensor unit and two centralising wheel sets. The sensor unit accommodates 18 sensors comprising the accelerometers, gyroscopes, thermometers and magnetometers inside a long hollow circular bar. The bar length is approximately 0.5 metre and is equipped with the centralizing wheel sets at each side of its end [5]. With a spring and barrel nut attached to the end of the centralizing wheel, the distance between the wheels can be adjusted. The barrel nut also allows a hook rope attach to the device and pulls the probe device along the pipe.

In this technique, before implementing the survey, a hook rope or wire is normally passed along the pipe. By connecting the hook to the device and pulling it from other side of the pipe, the device travels inside the pipe until reaches to the pipe end. As the device travels inside the pipe it automatically collects multiple positional recordings (up to a million individual points per second) along its path. After completing the measurement the raw data are uploaded to a software to compute the angular changes compared to the previous reading. The exact course of the pipe is outlined in accordance to the known entry and exit coordinates of the pipe. The total length of the pipe is estimated from the travelling time and the odometer system, designed at the back wheel set [5].

Unlike the electromagnetic based technique, in this technique the data is not affected by the electromagnetic field that is induced by a nearby power cable. It is claimed that the device performance are not dependant on the burial depth and the surrounding medium material properties to where the pipe is buried. The device can outline the

pipe configuration ranging from 50 mm to 2.5 m in diameter with an error of 0.25 in the horizontal plane and 0.1 in the vertical plane after a single survey. Multiple surveys deliver even more accurate results [5].

The main limitation imposed on this technique is the device size for mapping typical buried water pipes. For a pipe with a diameter of 30 cm unless the bend radius is more than 90 cm the device can enter to it. In practice the elbow bring the pipe to the surface looks like a 'L' or an inverse 'T' shape. As such, the bending radius is approximately equal to the radius of the pipe and therefore the tracker cannot be used [28]. In addition, normally a dewatering is required to deploy the device. Although the radial distance between the centralizing wheels can be adjusted, the device might stop at the position where sediments are accumulated inside the water pipe.

1.4 Changes in the UK water supply regulations

The history of pipelines safety regulation for the UK and Wales can be divided to before 1996 and after 1996 [29]. The regulation up to 1996 was complex and open to interpretation. After revising the regulation and making several improvements, it was allowed to conduct Risk Based Inspection (RBI) on buried water pipes [29]. The RBI inspection is defined as the optimal way of examination [30]. Therefore, the operators, integrity managers and the survey / inspection contractors are allowed to develop the most optimal approach and technique for inspecting the condition of buried water pipes [29]. In essence, inside access to the buried pipes for determining the pipes location and assessing their condition is allowed to the water pipe locator companies. It should be noted that, any implemented test and measurement should comply with the requirements of water supply regulation 1999 [31]. For successful detection of buried pipes their vibration behaviour should be clarified *a priori*. These are explained in the forthcoming section.

1.5 Wave characteristics in fluid filled pipes

The vibration behaviour of thin cylinders surrounded by air and subjected to structural excitations was first studied by Donnell [32] and Flügge [33]. An extensive literature,

regarding the vibration behaviour of cylindrical shells, has been established by Leissa [34]. A shortcoming of [34] is the exclusion of cylindrical shell vibration, when excited by acoustical excitation. Later James [35] described the dynamic behaviour of cylindrical shells subjected to an internal and external excitation. Fuller [36] also investigated the wave propagation characteristics and energy distribution, within empty and fluid filled thin walled cylindrical shells. It was shown that there are groups of waves propagating in the pipe that are either mainly coupled to the fluid or the pipe wall, which may be real, imaginary or complex. These wave types can be described by their circumferential modal number n which defines the radial component of the number of half of the wavelengths that can fit around the periphery of the pipe wall.

For pipe detection to be effective, it is of prime importance to identify the circumferential mode which contains the highest contribution to the radiation of energy to its surrounding medium at the desired frequency range. The radiation of sound under each circumferential mode of a cylinder has been studied by other researchers, for example in references [37, 38], and the results indicate that the sound radiation from the breathing mode can be assumed as a line monopole; the bending mode as a line dipole, the ovalling mode as a line quadrupole, and so forth [38]. In other words, the radiation efficiency of the cylinder decreases by approaching to the higher order modes. As illustrated in Fig. 1.3, below the frequency in which $ka \ll 1$ – where k and a are the wave number of the flexural wave in an empty pipe and the mean radius of the pipe respectively – most of the radiation is a result of pipe wall displacement under breathing mode.

There are a number of waves that propagate for each circumferential mode, given by s, which have their own features. Fuller [36, 39, 40] established a theoretical model to illustrate the energy distribution between different wave types, when a semi-infinite cylinder is subjected to a radial and internal pressure excitation. Their results indicated that, at well below the ring frequency, four types of wave carry the majority of the total energy within water filled thin walled cylinders [41]. Out of four types of wave, three are axisymmetric with $n = 0$, which is also known as a breathing mode. Of these three, only two waves with $s = 1, 2$ carry high amounts of energy compared to the other waves. The wave termed $n = 0, s = 1$ is an axisymmetric fluid borne wave with both axial and radial motion, which are determined by the cylinder wall compliance. The axisymmetric wave termed $n = 0, s = 2$ is predominantly a shell compressional wave with small radial motion [39]. Coupling of the fluid to the pipe wall can be achieved, as dictated by

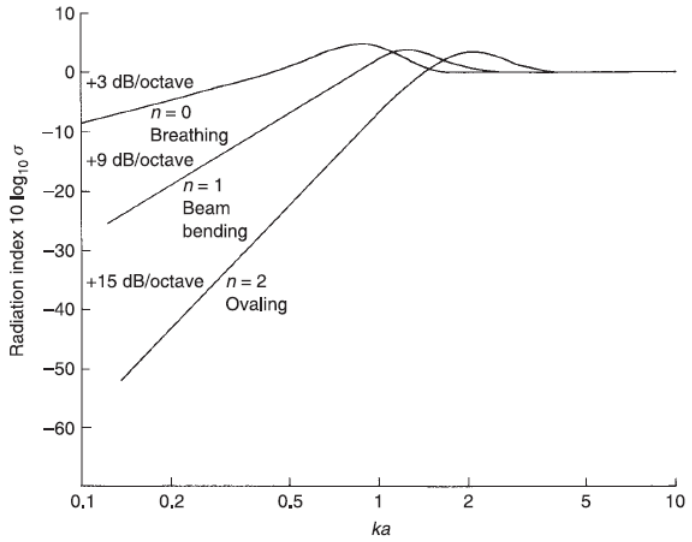

FIGURE 1.3: Radiation efficiency for the first three modes of an uniformly vibrated cylinder. Increasing to the radiation efficiency with respect to the wavenumber of the bending wave multiplied to the cylinder radius, depicted per octave [38].

the Poisson's ratio and the Young's modulus of the pipe wall as well as bulk modulus of the fluid [42]. The axisymmetric wave termed $n = 0, s = 0$ is a torsional wave which twists the pipe cross section and is uncoupled to the fluid. Hence, the energy associated with this wave type is exclusively within the shell [39] and thereby its effects are not considered in this study. The energy distribution amongst these axisymmetric waves is highly dependent on the way at which the pipes are subjected to the excitation [36, 39, 40, 43].

For the $n = 1$ mode, a flexural wave propagates within the pipe. Characteristics of this wave are minor distortion of the cross section of the pipe and added mass loading due to the contained fluid [39]. In this mode, the pipe moves laterally, similar to a Timoshenko beam at low frequency. As a consequence, a small portion of energy is carried by the fluid [39]. On the whole, the waver number of the acoustic waves encompass both the wave speed and attenuation. Fig. 1.4 illustrates the oscillation of the pipe wall for $n = 0$ and $n = 1$. Waves with a circumferential mode where $n > 2$ have a cut off frequency and only propagate above this frequency. A theoretical investigation presented in reference [44] expressed the wavenumber associated with the $n > 2$ waves and some of the results are confirmed from experimental measurements in reference [45].

In water-filled cylinders, the interior fluid has the highest contribution on the radial displacement of the pipe wall under $n = 0$ mode. This is the characteristic which makes

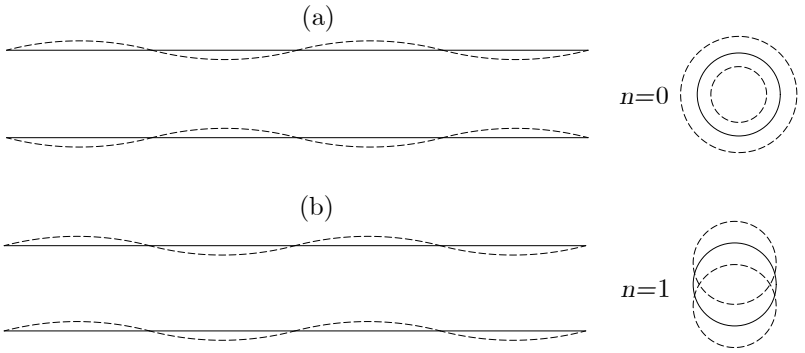

FIGURE 1.4: Oscillation of the pipe wall under $n = 0$ (a) and (b) $n = 1$ mode.

the axisymmetric fluid borne wave of practical interest for detecting buried water pipes through the vibro-acoustic technique. Therefore, the forthcoming section reviews the potential of current acoustic sources that can be deployed into a typical buried pipe and drive the axisymmetric fluid borne wave in the frequency range of interest.

1.6 Sources of excitation

Locating the water pipes by means of internal acoustical exciters is a new area of research and yet no acoustic source has been manufactured for this matter. However, there are a number of sources that can be adopted to directly drive the contained fluid and based on their operation mechanisms, they can be divided into four main source types: (1) Electroacoustic transduction based, (2) Detonative, (3) Electric sparks and (4) Marine seismic sources.

1.6.1 Electroacoustic transduction based source

Electroacoustic sources can be divided into six categories, namely: piezoelectric, electrostrictive, magnetostrictive, electrostatic, variable reluctance, and moving coil transducers. The advantages and drawbacks of each transducer as an underwater source are explained in detail in [46]. Two types of electrostatic sources are normally used for underwater excitation: (i) Piezoelectric transducers (ii) Moving coil transducers.

- Piezo electric transducers

An example of piezo electric transducers is a hydrophone. When a hydrophone is subjected to a relatively high voltage from a specified amplifier, it will transmit power to the fluid. Due to the low damping of the hydrophone, the piezo electric material will transmit relatively high amounts of energy to the fluid at its natural frequency. The source strength of the hydrophone, however is much lower compared to that observed in other sources, e.g. underwater loudspeaker, which is due to its power handling limitation [46].

- Moving coil transducer

An example of a moving coil transducer is an underwater loudspeaker, as it is capable of driving the fluid in the broadband excitation with moderate power [46]. The underwater speakers are designed to excite at high frequencies (above 500 Hz) .

The use of electro acoustic devices for pipe detection, using the vibro-acoustic technique, due to their repeatability and their provided reference signal is satisfying. However, their moderate power delivery ability has led to some motivation to look into other sources of excitation [46].

1.6.2 Detonative source

Detonative sources that are capable of driving the water pipe contained fluid can be divided into two categories; high explosive and propellant explosive [47].

- High explosive

The high explosive sources include fulminates, nitro-glycerine and azides based explosive. The peak pressure resulting from detonation is of the order of 10^9 Pa. During the Second World War, underwater high explosions were an important area of research, as an understanding of the damage caused to ships and submarines by underwater explosions was crucial in the design of both better ships and submarines as well as better explosives [47].

Using high explosive sources in the water filled pipe are dangerous in use and might cause unwanted heat transfer to the fluid and require a licence prior to use in Britain [47].

- Propellant explosive

Propellants explode during a relatively slow burning process, compared to high explosives and drive the fluid with a velocity of few meters per second . They are usually used in the form of blank cartridges, which are used with pistols. The burning process is completed within 0.1-10 ms. The form of resulting pressure waves from this method is dependent upon their size and direction of explosion [47].

1.6.3 Electric sparks source

The idea of using sparks which generate pressure waves in the fluid was first developed by Bjorno [48]. The pressure wave field generated by electric spark is similar to the one generated from high explosives sources.

A high voltage is generated between a pair of electrodes in the water within a microsecond period. Streamers of the electric current are emitted from the electrodes and a weak current will flow. Depending upon the voltage gradient, breakdown of the water between the electrodes will occur and a considerable rise in the current takes place resulting in pressure waves. The time duration of the pulse is about 2 ms. The generated pressure in the fluid is of the order of $10^4 - 10^5$ Pa and a sufficient voltage across the electrode for the discharge to happen lays in the order of $2 - 10$ kV/mm.

There are two main problems associated with underwater sparks as a source of excitation: (1) they are naturally dangerous, as high voltages and electrical charges are necessary to generate discharge; (2) the discharge will emit powerful radio-frequency interference which has the potential to damage test equipment[49].

1.6.4 Marine seismic source

- Air guns

Seismic air guns are widely used in search of oil and gas reserves below the ocean floor. The pressure waves resulting from such sources have much in common with those arising from high explosive sources, for instance dynamites. In fact, air guns were developed to be used, for seismic survey into the oceans, instead of high explosive sources [50].

Normally arrays of air guns with different pressure, volume, port size and firing times are used, to generate broad band high amplitude signal into the water, as do high explosive sources. The generated bubble via an air gun or air guns, which are normally towed behind a ship interacts with each other [51].

The mechanism of air guns in geophysical exploration is relatively simple. Airguns store compressed air in a chamber and release it through a port when a fire command is received [51]. To prevent water penetration to the chamber, the ports are shut while the pressure inside the chamber is higher than the ambient pressure. These devices can be tuned to generate the desired pressure pulse for the geophysics exploration. Initially airguns were operating at 207 bar, leading to produce broad band signals into the ocean. Because of severe damage to the marine life from such a high pressure operating air gun, some researchers suggested to reduce the operational level to 138 bar [52]. Although visual and acoustical monitoring are used to detect marine species, particularly marine mammals that might be present during the seismic survey, the survey process normally begins with a low compressed air releasing as a notification followed by gradually increasing the pressure to the full operational level. In marine seismic survey, the airgun operates by releasing of the compressed air to generate loud blasting into the ocean bottom normally repeated every 10 seconds 24 hours a day for days to weeks or months in end.

High frequency pressure waves >100 Hz emitted from airguns are not useful for geophysical exploration and believed to have high impact on marine fauna. Increasing the air gun volume chamber and decreasing the pressure, whilst maintain the required low-frequency region for geophysical exploration, eliminates the mid and high frequency content that are produced by typical air gun [52]. High volume air discharge to water create bigger bubble. The peak of an airgun signature appears before the whole compressed air discharges to the fluid. This is because the bubble expansion and reaching to its highest volume. The air gun signature is normally explained by dynamics of oscillating bubble and studied by numerous researchers.

A bubble is a globule, like masses of a substance, usually gas, surrounded by a liquid, and is capable of resonating or “ringing” at a frequency, which depends on its size [53]. The bigger the bubble the lower will be the frequency at which rings. The natural frequency of a bubble depends upon the mass density of the liquid, the ambient and compressed

air pressure, the shear viscosity of the liquid, the surface tension of the bubble and its polytrophic index. Depending upon the gas behaviour inside the bubble: adiabatically, isothermally or in between, the polytrophic index changes between unity and the ratio of the specific heats of the gas. A large bubble oscillates in an adiabatic process whereas a small one oscillates in an isothermal process. Because the bubble can be considered as an oscillator system, it can be treated as a resonating system, where the stiffness and the inertia are provided by its inside gas and the surrounding liquid respectively. The damping can be provided by the radiation, viscous and thermal losses. For the purpose air gun modelling, the damping effect due to the flow of compressed air through the air gun ports should be taken into the account.

Fig. 1.5 illustrates the shape variation of the bubble at the different stage of oscillation, when a compressed air was emitted from an air gun [54].

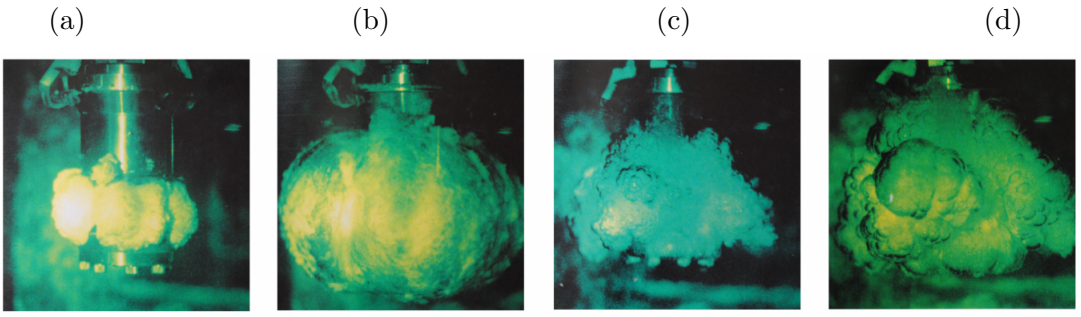

FIGURE 1.5: Pictures of the bubble emitted from an air gun at different stage. (a) Just after firing (b) reaching to its maximum expansion (c) collapsing after the expansion (d) second expansion from the smaller bubble Langhammer [54].

An example of the pressure signature from an air gun taken 1.5 meter from an air gun is illustrated Fig. 1.6 and the main three components which illustrates its pressure signature is shown.

The first peak at 0.01 ms is related to the direct arrival of the pressure when the air gun fires. The second negative peak at 0.02 seconds is associated with the reflected pressure at the water surface known as a ghost and has an opposite polarity compared to the first arrival wave. The other peaks are related to the expansion and collapsing of the other bubbles, which again generates direct arrival of the waves to the hydrophone and the reflected wave from the water surface.

Although airguns are able to generate high amplitude low frequency signals into the fluid, for the purpose of pipe detection, the bubbles generated into the fluid by airguns could

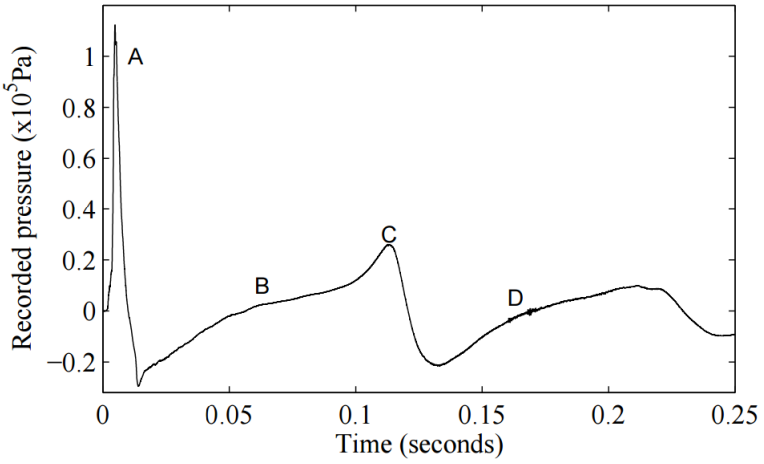

FIGURE 1.6: The pressure perturbation recorded at 1.5 meters from a seismic air gun. The presented results are relative to hydrostatic pressure (approximately 1.7 bar). The points marked 'A' to 'D' correspond approximately to the images in Fig. 1.5 [54].

reduce the wave re-radiation from the buried water pipe and hinder the pipe tracing.

- Water guns

The water gun is a marine seismic source and is well known in the petroleum industry. They are capable of producing a broadband signal in the fluid. The most commonly used water guns are developed in France and operate similarly to the way as air guns do [55]. The water gun comprises of two channels, one filled with high pressure air and the other one is filled with water. When the gun is fired the higher pressure air propels the piston into the water chamber causing the discharge of water from the water chamber ports [56]. The implosion of inertial cavity generated behind a jet of high pressure flow expelled from the water chamber ports drives the surrounding water. In essence, the cavity is formed when the piston suddenly decelerates. Due to the hydrostatic pressure the steam bubble collapses, generating an impulse shock wave into the surrounding water. After firing, the hydrostatic pressure push the firing piston to its initial position and the device is ready for the next firing.

The differences between air and water guns were examined in detail by Hutchinson [55]. Their results indicate that at low frequencies < 200 Hz, the amplitude of the pressure signal from the air gun is much higher than that of water gun [55].

The main disadvantage of using water guns, to internally drives the pipe contained fluid, is the phenomenon of the inertial cavitation collapsing near to a fixed surface.

Such an undesirable characteristic can damage the pipe wall when it occur repeatedly. In nature, the mantis shrimp exploit such a phenomena to smash snail shells to pieces. Other applications of inertial as well as non inertial cavitations are well explained in [53, 57] and are beyond the scope of this study.

1.7 Recording the ground surface vibration

An important requirement of the vibro-acoustic technique for searching the pipes is proposing a sensor which can be well-coupled and be sensitive to the ground surface vibration at the frequency range of interest.

Experimental work has been undertaken by several researchers, for instance [58, 59], to find a suitable way of coupling the accelerometer to the ground surface. These surveys were carried out to assess building stability to the vibration caused by earthquake or blasting, etc. Earthquakes can cause the most destruction to the building and constitute seismic waves with a frequency range of less than 20 Hz. Despite the recommendation on the usefulness of the accelerometers for measurement of low frequency excitation, a theoretical study by Gao *et al.* [60] suggests otherwise.

Gao *et al.* [60] work concerned finding a suitable sensor to measure a wide frequency bandwidth of leak noise in the frequency domain. It was shown that the frequency bandwidth of the Frequency Response Function (FRF) between the induced pressure near to the excitation source and the recorded fluid pressure, pipe wall vibration velocity and the acceleration is different from one to another case. These changes does not have any contradiction to the frequency response of sensors.

As seen in Fig. 1.7 the FRF of a pressure based sensor has the lowest bandwidth and highest sensitivity to the low frequency signals compared with the other two. Such behaviour is associated to the integration of angular frequency when estimating the FRF for the velocity and the acceleration based sensor. Likewise it could be advantageous to record the ground surface vibration by an array of displacement based sensors rather than velocity and acceleration based sensors.

Furthermore, an experimental study also has been undertaken by Muggleton *et al.* [61] to identify a suitable sensor to record vibration of the ground surface for detection of

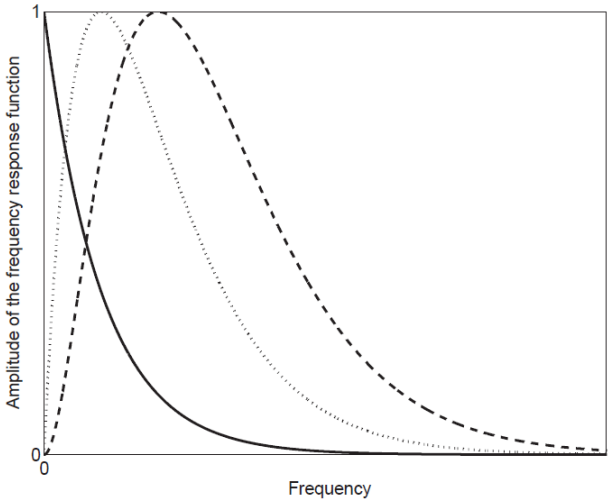

FIGURE 1.7: Illustration of the amplitude of the FRF between Pressure (——), velocity (·····) and acceleration (- - -) and a reference signal, normalised to the corresponding maximum amplitudes.

buried pipes. Their experiment included attaching a shaker to the buried pipe from an access point, followed by recording the ground surface vibration above the pipe axis using geophones and a laser. Their results show that laser performed better on some surface texture than the other, however, poorer quality data was obtained from the laser compared to the geophone. A number of recommendations were listed to boost the reliability of the measured laser data such as: averaging of signal both in space and frequency, using different heights when recording surface displacement, removing dust or gravel from surface and using different input signals. As the geophone measures the surface vibration velocity in m/s, the higher the surface vibration velocity from the desired vibration source, the more the recorded data is away from the noise floor. From the experimental results it was found that the ground surface velocity is a key factor for determining the quality of the data compared to the surface texture [61].

In view of promising results from vibro-acoustic technique at frequencies below 100 Hz, finding a displacement based sensor for recording the surface vibration is favourable for detecting the pipes. Owing to the good coupling of the geophone to the different surface texture, compared to the laser, it was decided to record the surface vibration with them.

1.8 Aim and Objectives

The purpose of this thesis is to enhance the application of vibro-acoustic approach, explained in Section 1.2, by using an internal excitation. The research objectives are therefore to:

- Develop a simple analytical model, taking into account the different wave-types which are likely to determine the ground surface vibration, to capture the dominant physical process of the vibro-acoustic technique.
- Investigate into the use of advanced unwrapping methods to remove discontinuities embedded within the images generated by the vibro-acoustic technique.
- Apply the previously used excitation method, a mechanical vibration, to a buried water pipe to determine its location. The obtained data will be used for benchmarking the experimental results of in-pipe excitations.
- Critically assess and examine acoustic sources, or instead develop or re-engineer one, which are reproducible, controllable, can fit into a typical water filled pipe and drive the axisymmetric fluid borne wave with a high amplitude over the frequency range of interest, 10 Hz - 100 Hz.
- Utilise the examined or the developed acoustic source/s to map a buried pipe followed by comparing the obtained data obtained from the utilised exciters. A comparison between the results obtained from acoustical and mechanical vibration of the pipe, will also be made.
- Deploy the acoustic source/s at multiple locations within the buried pipe and repeat the vibro-acoustic measurement with a view to provide a better insight into the use of such an excitation technique and assess the performance of the exciter/s at different points.

1.9 Contributions of the thesis

In the accomplishment of the research objectives, the following contributions have been made:

1. The wave speed and attenuation of the axisymmetric structural borne wave has been measured through an experimental measurement. Furthermore, a simple analytical simulation has been developed to explain a potential reason for the high variance of the imaginary component of the measured axisymmetric fluid and structural borne wave.

2. Decomposition of the axisymmetric fluid and the structural borne wave components of the radial displacement of the pipe wall through an experimental measurement.

3. A novel pneumatic source has been developed and another one has been re-engineered to drive the axisymmtric fluid borne wave with high amplitude, at the frequency of interest. A series of laboratory measurements have been performed to validate their applicability. Furthermore, a simple analytical simulation that contributes to the explanation of each parameter on the generated pressure wave from the pneumatic devices has been developed.

4. An analytical model has been developed to enhance physical insight into the use of the vibro-acoustic technique. Furthermore, a simple unwrapping algorithm has been developed to retrieve the contiguous form of phase images.

5. The ability of state-of-the-art two dimensional phase unwrapping algorithms to unwrap the phase data from the analytical simulation has been assessed. Of the utilised unwrapping algorithm, including the one that developed in this study, one algorithm has been proposed to post process the experimental data.

6. Implementing experimental studies, using the developed pneumatic devices and a standard electroacoustic source for the pipe detection. Further experimental studies have been carried out at multiple locations along the pipe.

1.10 Synopsis of the Thesis

This dissertation is organised in seven chapters; Chapter 2 reviews some basic theory of axisymmetric fluid and shell borne wave propagation in a cylindrical shell. It also provides the theoretical expressions for the axisymmetric fluid and structural borne wave contribution to the pipe wall displacement when the pipe subjected to an acoustical or

mechanical excitation. Furthermore, the fundamental of the body wave propagation into an infinite and half space elastic medium are described.

Chapter 3 starts by measuring the wave speed of axisymmetric fluid and structural borne wave through measuring their wave number by an experimental measurement. It introduces a new experimental method to decompose the two aforementioned waves, from the collected experimental data.

Chapter 4 introduces two novel pneumatic sources to drive the axisymmetric fluid borne wave at the frequency range of interest. The developed devices are benchmarked against a standard electro-acoustic and an electromagnetic shaker.

Chapter 5 presents the analytical simulation of wave propagation in the surrounding medium due to radiation of wave from a point and pipe source. A novel spatial phase unwrapping algorithm is explained in this chapter and a review of advanced two-dimensional phase unwrapping algorithm is presented.

Chapter 6 details the application of an in-pipe excitation, by deploying an underwater loudspeaker within the pipe and measuring the ground vibration via an array of geophones in a grid. It is shown that there is a close agreement between the results obtained from experimental study and the analytical simulation. Further survey is carried out to determine the value of the wave speed in the pipe and the surrounding medium.

Chapter 7 draws conclusions and outlines the future works.

Chapter 2

Theory of the ground surface vibration generated by acoustic wave propagation along a pipe

In this chapter, the vibrational behaviour of cylindrical shells is studied. This is followed by a description of the analytical expressions for the wavenumber of the axisymmetric fluid and the structural borne wave. From estimating the wavenumber of each wave, both the wave speed and attenuation can be realised. The values of such wavenumbers are sometimes highly contingent on the properties of the inside and outside fluid.

Fundamental equations of motion of infinite and semi-infinite elastic media are presented in Section 2.5, which are related to the two wave types that can propagate within an infinite elastic medium: compressional and shear waves. Information about mode conversion when the body waves meet boundaries is also established in Section 2.6.

2.1 Wave propagation in a cylindrical shell

This section provides a brief review of the free vibration of a fluid filled pipe. There are many mathematical representations describing the free vibration of thick and thin cylindrical shells. For the purposes of this study, the vibration behaviour of thin cylinders is of interest only. Consider a cylindrical shell with constant thickness h and mean

radius a. Shell coordinate are taken axially in $x-$direction, radially in $r-$direction and angularly in $\phi-$direction, shown in Fig. 2.1. The equation of the motion of a shell can

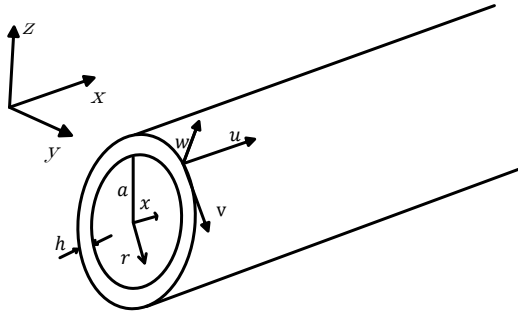

FIGURE 2.1: Coordinate system for a thin walled cylindrical shell. u, v and w describe the shell displacement in the axial, radial and tangential direction.

be written in a compact way as:

$$[\mathbf{L}]\{\mathbf{u}_i\} = 0, \tag{2.1}$$

where the displacement vector $\{\mathbf{u}_i\}$ is given by:

$$\{\mathbf{u}_i\} = \begin{bmatrix} u \\ v \\ w \end{bmatrix}. \tag{2.2}$$

Here $[\mathbf{L}]$ is a differential operator matrix which is treated as the sum of two operators, given by:

$$[\mathbf{L}] = [\mathbf{L}_{\mathrm{DM}}] + \psi^2_{\mathrm{Shell}}[\mathbf{L}_{\mathrm{MOD}}], \tag{2.3}$$

where $[\mathbf{L}_{\mathrm{DM}}]$ is a 'modifying' operator which is different for each shell theory. The ψ_{Shell} term is the shell thickness parameter and is defined by: $\psi^2_{\mathrm{Shell}} = \dfrac{h^2}{12a^2}$. ψ^2_{Shell} is very small for thin shells where $h \ll a$. $[\mathbf{L}_{MOD}]$ is the differential operator related to the Donnell-Mushtari theory. The vibrational behaviour of the fluid filled pipe can be established in terms of the displacement in the axial, radial and circumferential direction, by substituting the following wave expressions into Eq. (2.1):

$$
\begin{aligned}
u &= \sum_{n=0}^{+\infty}\sum_{s=0}^{+\infty} U_{nx}\cos(n\phi)\,\mathrm{e}^{\mathrm{i}(\omega t - k_{ns}x + \pi/2)},\\
v &= \sum_{n=0}^{+\infty}\sum_{s=0}^{+\infty} V_{nx}\cos(n\phi)\,\mathrm{e}^{\mathrm{i}(\omega t - k_{ns}x)},\\
w &= \sum_{n=0}^{+\infty}\sum_{s=0}^{+\infty} W_{nx}\cos(n\phi)\,\mathrm{e}^{\mathrm{i}(\omega t - k_{ns}x)},
\end{aligned}
\tag{2.4}
$$

where k_{ns} is the axial wavenumber of the particular mode n and associated axial wave s. The U_{nx}, V_{nx} and W_{nx} terms are the modal wave amplitudes in x, r and ϕ respectively. The n and s parameters are the circumferential mode number and its branch number respectively, discussed in detail in Section 1.5. Free wave solutions can be found by equating the determinant of the amplitude coefficients given by matrix $[\mathbf{L}_{DM}]$ in Equation (2.3) to zero, e.g. $\det[\mathbf{L}_{\mathrm{DM}}] = 0$. This leads to a set of non-trivial characteristic equations, which can be solved for either empty or fluid filled pipes and can be divided into the different categories in terms of the circumferential modal number.

2.2 Effect of the internal and the external fluid loading

Depending on the value of the excitation frequency, higher circumferential modes appear within pipes. For buried water pipes, however, the external loading from the soil becomes important for the higher modes, where $n > 1$, compared to the $n = 0$ mode. Hence, a noticeable reduction to their amplitude is expected. The fluid loading of the contained fluid and external medium is given by [39]

$$
FL_i = \frac{\rho_f}{\rho_p}\frac{a}{h}\frac{\Omega^2}{k_{ns}^r}\frac{J_n(k_{ns}^r)}{J_n'(k_{ns}^r)}, FL_e = -\frac{\rho_m}{\rho_p}\frac{a}{h}\frac{\Omega^2}{k_{ns}^r}\frac{H_n(k_{ns}^r)}{H_n'(k_{ns}^r)},
\tag{2.5}
$$

where ρ_f, ρ_p and ρ_m are the density of the contained fluid, pipe wall and the external medium respectively. The J_n and H_n terms are the Bessel and the Hankel function of order n respectively and the prime illustrates their differentiation. k_{ns}^r is the radial wavenumber associated to each circumferential mode of the pipe. $\Omega = k_L a$, where $k_L = \omega\sqrt{\dfrac{\rho_p\left(1-v_p^2\right)}{E_p}}$ is the compressional wavenumber of the plate, a and h are the mean radius and the thickness of the pipe wall respectively. The effect of loading of the surrounding medium for the axisymmetric fluid waves, termed $n = 0, s = 1$, is studied

in reference [62]. The results show that for a water filled buried water pipe, the external loading, when the pipe surrounded by soil or submerged to water, is smaller compared to internal fluid loading. Therefore, the speed and attenuation of the axisymmetric fluid wave due to the loading from surrounding medium, slightly alters compared with the in-vacuo situation.

2.3 Wavenumber of the axisymmetric fluid and shell borne waves

Due to promising results from the vibroacoustic technique at low frequencies ($< 100\,\mathrm{Hz}$), it was decided to mainly focus on the vibration behaviour of the thin cylinder in the low frequency range. Well below the ring frequency, most of the energy in the fluid filled pipe is carried by the waves termed $n = 0$, $s = 1$ and $s = 2$, with minor contribution from the torsional waves and the bending waves [39]. Therefore, the presented wavenumbers in this thesis are based on simplified forms of Kennard's shell equations. These equations are valid only well below the ring frequency and exclude the contribution of the bending wave and the rotational inertia.

2.3.1 Axisymmetric fluid borne wave

By assuming zero density for the surrounding medium and neglecting the radiation into the surrounding medium, the wavenumber of the axisymmetric fluid borne wave at well below the ring frequency is given by [63]:

$$k_1^2 = k_f^2 \left(1 + \frac{2B_f/a}{E_p h/a^2 - \omega^2 \rho_p h}\right), \tag{2.6}$$

where B_f and ω are the fluid bulk modulus and angular frequency respectively; E_p, ρ_p, h and $r$are the Young's modulus, density, thickness and the mean radius of the pipe wall respectively. At low frequencies, the term $\omega^2 \rho_p h$ which is related to the pipe wall inertial term, can be discarded. Therefore, the fluid wavenumber equals its free field wavenumber multiplied by a ratio, named the degree of coupling, containing the bulk modules of fluid and elastic and geometrical properties of the pipe wall [42]. For a pipe

with structural damping, the imaginary component of the Young's modulus, $E(1+\mathrm{i}\eta_p)$ reduces the amplitude of waves inside the pipe. The term is known as a material loss factor of the pipe shell. As illustrated by Eq. (2.6) for the steel pipes the wavenumber of the axisymmetric fluid borne wave is close to its free field wavenumber, since the elastic modulus of the pipe wall is much higher than the fluid bulk modulus. The wavenumber of the axisymmetric fluid borne wave for a pipe surrounded by an infinite elastic medium, is transformed by neglecting the shear coupling between the pipe wall and the surrounding medium to [64]:

$$k_1^2 = k_f^2\left(1+\frac{2B_f/a}{E_p h/a^2-\omega^2(\rho_p h+M_{\mathrm{rad1}})+\mathrm{i}(\omega R_{\mathrm{rad1}}+\eta_p E_p h/a^2)}\right). \tag{2.7}$$

Here M_{zrad1} and R_{rad1} are the mass and resistance component of the $s=1$ wave radiation impedance and are given by [64]:

$$z_{\mathrm{rad1}} = R_{\mathrm{rad1}}+\mathrm{i}\omega M_{\mathrm{rad1}} = \sum_{m=1}^{+\infty}\frac{-\mathrm{i}\rho_m c_m k_m}{k_{m1}^r}\frac{H_0(k_{m1}^r a)}{H_0'(k_{m1}^r a)}, \tag{2.8}$$

where ρ_m, k_m and c_m are density, wavenumber and wave speed of the surrounded medium, the summation presented for different waves in the surrounding medium. H_0 is the Hankel function of the second kind and zeroth order which represents the outgoing wave from cylindrical shells. k_{m1} is the radial component of the wavenumber in the surrounding medium, given by [64]:

$$(k_{m1}^r)^2 = k_m^2 - k_1^2. \tag{2.9}$$

By considering the effect of shear coupling between the pipe and the surrounding medium the $s=1$ wavenumber modifies to [65]:

$$\begin{aligned} k_1^2 = k_f^2(1+\frac{2B_f/a}{E_p h/a^2-\omega^2\rho_p h+\mathrm{i}\omega\frac{\lambda_m}{\lambda_m+2\mu_m}\left[1-2\frac{k_1^2}{k_r^2}\right]z_{\mathrm{rad1}}\ldots} \\ \frac{}{-2\frac{\mu_m}{a}\left[1-2\frac{k_1^2}{k_r^2}\right]k_{d1}^r a\frac{H_0''(k_{d1}^r a)}{H_0'(k_{d1}^r a)}-4\frac{\mu_m}{a}\frac{k_1^2}{k_r^2}k_{r1}^r a\frac{H_1'(k_{r1}^r a)}{H_1(k_{r1}^r a)}}), \end{aligned} \tag{2.10}$$

where $H_0(\,)$ and $H_1(\,)$ are the Hankel functions of second kind, zero and first order respectively. These functions describe the outgoing waves. The k_{d1}^r and k_{r1}^r terms can be obtained from Eq. (2.9), and λ_m and μ_m are the Lamé constants which are explained in Section 2.5.

Because in vibro-acoustic technique frequencies below 100 Hz are of interest, taking any of the three axisymmetric fluid borne equations, Eqs. (2.6) (2.7) (2.10), will produce almost identical results. At higher frequencies, the frequency range which is not useful in vibro-acoustic water pipe detection, the output from each equation significantly differ from each other. Therefore, depending on the type of the surrounding medium and the frequency range of interest, an appropriate equation can be selected.

2.3.2 Axisymmetric shell borne wave

The wavenumber associated to the axisymmetric shell borne wave for a thin cylinder in vacuo, by assuming zero density of the surrounding medium and the radiation impedance, is expressed by [63]

$$k_2^2 = k_L^2 \left(1 + \frac{v_p^2}{1 - v_p^2} \frac{E_p h/a^2}{E_p h/a^2 + (2B_f/a)\omega^2 \rho_p h} \right), \tag{2.11}$$

where k_L and v_p are the compressional wavenumber in a plate and its Poisson's ratio respectively. The remaining parameters have been previously explained, when used in Eq. (2.6). The assumption made to obtain Eq. (2.11) is that the wavenumber of the wave termed $n = 0, s = 2$ is much smaller compared to the free-field wavenumber of its contained fluid, so $k_2^2 \ll k_f^2$. It is shown in [63, 64]: that this approximation does not induce significant error. The wavenumber of the axisymmetric shell borne wave for a pipe surrounded by a fluid, by neglecting the shear coupling between the pipe wall and the surrounding medium, is given by [64]:

$$k_2^2 = k_L^2 \left(1 + \frac{v_p^2}{1 - v_p^2} \frac{E_p h/a^2 (1 + \mathrm{i}\eta_p)}{(E_p h/a^2) - (2B_f/a) - \omega^2(\rho_p h + M_{\mathrm{rad2}}) + \mathrm{i}(\omega R_{\mathrm{rad2}} + \eta_p E_p h/a^2)} \right). \tag{2.12}$$

Here M_{rad2} and R_{rad2} are the mass and resistance component of the radiation impedance for the $n = 0, s = 2$ wave and are given by [64]:

$$z_{\text{rad2}} = R_{\text{rad2}} + \mathrm{i}\omega M_{\text{rad2}} = \sum_{m=1}^{+\infty} \frac{-\mathrm{i}\rho_m c_m k_m}{k^r_{m2}} \frac{H_0(k^r_{ns}a)}{H_0'(k^r_{m2}a)}, \tag{2.13}$$

where k^r_{m2} is the radial component of the wavenumber in the surrounding medium, given by:

$$(k^r_{m2})^2 = k^2_m - k^2_{m2}. \tag{2.14}$$

Inclusion of shear coupling between the pipe and the surrounding medium changes Eq. (2.12) to [65]:

$$k_2^2 = k_L^2\Big(1 + \frac{v_p^2}{1-v_p^2} \frac{E_p h/a^2}{E_p h/a^2 - \omega^2\rho_p h + 2B_f/a + \mathrm{i}\omega \dfrac{\lambda_m}{\lambda_m + 2\mu_m}\left[1 - 2\dfrac{k_2^2}{k_r^2}\right] z_{\text{rad2}} \ldots}$$
$$\frac{}{-2\dfrac{\mu_m}{a}\left[1 - 2\dfrac{k_2^2}{k_r^2}\right] k^r_{d2}a \dfrac{H_0''(k^r_{d2}a)}{H_0'(k^r_{d2}a)} - 4\dfrac{\mu_m}{a}\dfrac{k_2^2}{k_r^2} k^r_{r2}a \dfrac{H_1'(k^r_{r2}a)}{H_1(k^r_{r2}a)}}\Big). \tag{2.15}$$

The k^r_{d1} and k^r_{r1} terms can be obtained from Eq. (2.14),

Similar to the comments made on the axisymmetric fluid borne wavenumber, at the frequency range of interest, approximately below 100 Hz, changes to the wave speed and attenuation of the axisymmetric shell borne wave are insignificant. For high frequencies, approximately above 100 Hz, the output from each equation, Eqs. (2.11),(2.12), (2.15), is different.

2.4 Dynamic behaviour of a fluid filled pipe

The dynamic behaviour of a fluid filled pipe has been previously investigated in references [34, 63, 66]. In this study, the models developed by Pinnington and Briscoe [63] are used for further analysis. In their model, Kennard's shell equations are utilised; the contribution from the bending wave and the rotational inertia and shear transfer of the pipe are disregarded and are only valid at well below the ring frequency. For the fluid

filled pipe illustrated in the axial and radial vibration of the pipe wall which arises from combination of the waves termed $n = 0, s = 1, 2$ can be expressed by:

$$u = \sum_{s=1}^{2} U_s e^{\mathrm{i}(\omega t - k_s x)}, w = \sum_{s=1}^{2} W_s e^{\mathrm{i}(\omega t - k_s x)}, \tag{2.16}$$

where U_s and W_s are the amplitude of the pipe wall displacement, arise from the wave termed $n = 0, s = 1, 2$ in the axial and radial direction respectively. The definition of n and s are given in Section 1.5. The k_s term is the wav number associated to the axisymmetric waves, expressed in Eqs. (2.6) and (2.11) respectively, ω and x are the angular frequency and the pipe axis respectively. The pressure within the fluid, $p(x, r, t)$,is given by:

$$p(x, r, t) = \sum_{s=1}^{2} P_s J_0 \left(k_s^r r\right) e^{\mathrm{i}(\omega t - k_s x)}. \tag{2.17}$$

Here P_s , J_0 and r are the amplitude of the fluid pressure arises from the wave termed $n = 0, s = 1, 2$, Bessel function of order zero and the radial distance in cylindrical coordinate system respectively. The k_s^r term is the radial wavenumber expressed via fluid wavenumber and the axisymmetric wavenumbers by: $(k_s^r)^2 = (k_f)^2 - (k_s)^2$. The relationship between fluid pressure and radial motion of the pipe wall associated with the waves termed $n = 0, s = 1, 2$ can be represented as:

$$\frac{W_1}{W_2} = -\frac{P_1}{P_2}\left[\frac{\beta}{1 - v_p^2 - \Omega^2}\right], \tag{2.18}$$

where v_p is the Poisson's ratio of the pipe wall, Ω is a normalized ring frequency; $\Omega = k_L a$, where a is the pipe mean radius. The β term is called fluid loading which is given by:

$$\beta = \frac{2B_f a}{Eh}(1 - v_p^2), \tag{2.19}$$

where B_f, E_p and h are the fluid bulk modulus; pipe wall Young's modulus and its thickness respectively. The axial and radial motion of the pipe wall arising from the axisymmetric fluid and the shell borne wave are related together by:

$$\frac{U_1}{U_2} = \frac{W_1}{W_2}\frac{k_2}{k_1}\frac{v_p^2}{(1+\beta-\omega^2)}. \tag{2.20}$$

2.4.1 Axial excitation of the pipe wall

The pressure associated with each wave, within a semi-infinite pipe can be expressed as:

$$P(x) = P_1 e^{\mathrm{i}(k_1 x)} + P_2 e^{\mathrm{i}(k_2 x)}. \tag{2.21}$$

As illustrated in Fig. 2.2 applying axial excitation to the pipe wall gives zero pressure within the fluid at $x = 0$, which can be written as:

$$P(0) = P_1 + P_2 = 0. \tag{2.22}$$

Applying this boundary condition to Eq. (2.22) results in $P_1 = -P_2$ at $x = 0$ and therefore by substituting in Eq. (2.18) gives:

$$\frac{W_1}{W_2} = \left[\frac{\beta}{1 - v_p^2 - \omega^2}\right] \tag{2.23}$$

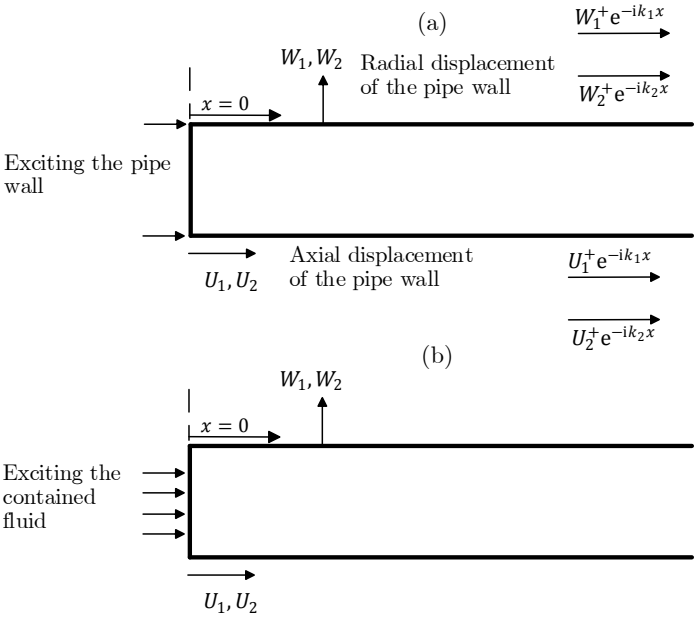

FIGURE 2.2: Semi-infinite fluid filled pipe subjected to (a) structural and (b) fluid excitation.

Substituting Eq. (2.23) into Eq. (2.20) gives the relative amplitudes of the each wave, in axial direction, as:

$$\frac{U_1}{U_2} = \left(\frac{v^2}{1+\beta-\Omega^2}\right)\left(\frac{\beta}{1-v_p^2-\Omega^2}\right)\frac{k_2}{k_1}. \tag{2.24}$$

2.4.2 Fluid excitation

The axial stress within the pipe wall at any position along the pipe is given by:

$$\sigma(x) = -\mathrm{i}\rho_m\omega^2\left[\frac{U_1\mathrm{e}^{-\mathrm{i}k_1x}}{k_1} + \frac{U_2\mathrm{e}^{-\mathrm{i}k_2x}}{k_2}\right]. \tag{2.25}$$

By assuming the free edge in Fig. 2.2 and applying pressure to the fluid gives zero axial stress in the shell wall at $x = 0$, where the fluid was excited. Therefore, by setting $\sigma(0) = 0$ in Eq. (2.25), gives:

$$\frac{U_1}{U_2} = -\frac{k_1}{k_2}. \tag{2.26}$$

The relative wave amplitudes in the radial direction is established via substituting Eq. (2.26) into Eq. (2.20), as:

$$\frac{W_1}{W_2} = \left(\frac{k_2}{k_1}\right)^2\frac{1+\beta-\Omega^2}{v_p^2}. \tag{2.27}$$

2.4.3 Energy ratio

The energy associated with each wave per unit length of the pipe is provided by:

$$e_1 \cong P_1^2\frac{\pi a^2}{\rho_f c_1^2}, e_2 \cong U_2^2\omega^2 2\pi a h\rho_p, \tag{2.28}$$

where P_1^2 and U_2^2 are the spatial average mean-squares of the pressure and axial displacement respectively. ρ_f,and ρ_p are the densities of the contained fluid and the pipe wall respectively. a and h are the mean radius and thickness of the pipe wall respectively. c_1

is the velocity of the wave termed $n = 0, s = 1$ wave. At low frequencies when $\Omega \ll 1$ and by assuming $v_p^2 < \beta$, the relative energy associated to each wave can be expressed by:

$$\frac{e_1}{e_2} \cong \left(\frac{W_1}{W_2}\right)^2 \frac{v_p^2(1-v_p^2)^2}{\beta(1+\beta)^2}. \tag{2.29}$$

2.5 Wave propagation in a surrounding medium

There are two types of wave that can propagate through in an infinite elastic medium, compressional waves and shear waves. Compressional waves are also referred to as primary waves, longitudinal waves, dilatational waves or P-waves. Shear waves are also referred to as secondary waves, transverse waves or S-waves. In this study, primary waves are referred to as compression waves, and secondary waves are referred to as shear waves.

For an infinite elastic isotropic medium, the Navier equations can be expressed by [67–70]:

$$(\lambda_m + \mu_m)\frac{\partial \Delta}{\partial x} + \mu \partial \nabla^2 u = \rho_m \frac{\partial^2 u}{\partial t^2}, \tag{2.30}$$

where ρ_m is the density of the medium, λ_m and μ_m are the Lamé constant and the shear modulus of the surrounding medium respectively. The λ_m and μ_m parameters are frequency dependent and related to elastic properties of the medium by:

$$\lambda_m = \frac{E_m v_m(1+\mathrm{i}\eta_m\omega)}{(1+v_m)(1-2v_m)} \text{ and } \mu_m = \frac{E_m(1+\mathrm{i}\eta_m\omega)}{2(1+v_m)}. \tag{2.31}$$

The $\Delta = \nabla.\mathbf{u}$ term is the divergence of the vector $\mathbf{u}(x, y, z, t)$, which shows the volume strain, given by [67–70]:

$$\Delta = \frac{\partial u_x}{\partial x} + \frac{\partial u_y}{\partial y} + \frac{\partial u_z}{\partial z}, \tag{2.32}$$

where ω and η_m are the angular frequency and the surrounding medium loss factor respectively. E_m and v_m are the elastic modulus and the Poisson's ratio of the medium respectively, which are given by [67]:

$$E_m = \frac{\mu_m(3\lambda_m + 2\mu_m)}{(\lambda_m + \mu_m)}, v_m = \frac{\lambda_m}{2(\lambda_m + \mu_m)}. \tag{2.33}$$

In compressional waves, particle motion is initiated by alternating dilation and compression, and the direction of the propagation is parallel to the particle motion. Once the wave has passed, the material returns to its original position. These waves are analogous to sound waves in air. By differentiating Eq. (2.30) with respect to x, y, z, gives [67–70] :

$$(\lambda_m + \mu_m)\nabla^2\Delta = \rho_m \frac{\partial^2 \Delta}{\partial t^2}, \tag{2.34}$$

where ∇^2 named Laplacian operator which denotes the gradient of the del operator. Applying vector operation of divergence to Eq. (2.34), gives the wave equation as [67–70]:

$$\nabla^2\phi = \frac{1}{c_d^2}\frac{\partial^2 \phi}{\partial t^2}, \tag{2.35}$$

where ϕ is the compressional scalar potential, c_d is the velocity of compressional waves and can be expressed by [67–70]:

$$c_d = \sqrt{\frac{\lambda_m + 2\mu_m}{\rho_m}} = \sqrt{\frac{K_m + (4/3)\mu_m}{\rho_m}}, \tag{2.36}$$

where K_m is the bulk modulus of the medium. As an alternative to Eq. (2.36), velocity of the compressional wave in infinite homogeneous isotropic medium can be represented as a function of E_m, v_m and ρ_m, [67–70]:

$$c_d = \sqrt{\frac{E_m(1 - v_m)}{\rho_m(1 - 2v_m)(1 + v_m)}}. \tag{2.37}$$

In shear waves, particle motion is perpendicular to the direction of the wave. The shear wave particle motion may have components in the vertical plane called a SV-wave, and also parallel to the horizontal plane called a SH-wave. Distinguishing these polarized waves are not achievable, due to symmetry of the medium, unless they arrived at the

surface. Performing Curl operation to Eq. (2.30), because the curl of the scalar is zero, the wave equation of shear waves becomes [67–70]:

$$\nabla^2\psi = \frac{1}{c_r^2}\frac{\partial^2\psi}{\partial t^2}, \tag{2.38}$$

where ψ is the distortional vector potential, c_r is the velocity of shear waves which can be expressed as [67–70]:

$$c_r = \sqrt{\frac{\mu_m}{\rho_m}}. \tag{2.39}$$

The shear wave propagates with a slower speed compared to the compressional wave, and has the same speed in the one-dimensional and three-dimensional elastic medium. The ratio of these two wavespeed in terms of the Lamé constants and medium's Poisson's ratio can be expressed as [67–70]:

$$\frac{c_d}{c_r} = \left(\frac{\lambda_m + 2\mu_m}{\mu_m}\right)^{1/2} = \left(\frac{2 - 2v_m}{1 - 2v_m}\right)^{1/2}. \tag{2.40}$$

Furthermore, for the isotropic elastic medium, the value of the Poisson's ratio can be formulated in accordance with the velocity of the shear and the compressional wave as:

$$v_m = \frac{c_d^2 - 2c_r^2}{2\left(c_d^2 - c_r^2\right)}. \tag{2.41}$$

Propagation of the compressional wave within saturated soil composes of two wave components; fluid and frame waves that can propagates through water and solid structure respectively [71].

2.6 Wave propagation in a layered medium

In general, soil profile comprises of different layers with different values of stiffness. These layers may lay in the horizontal or vertical direction. As a result, the propagation of waves into the soil become dispersive. Usually for the homogeneous isotropic soil, the wave speed increases proportionally to the depth. The soil's mechanical properties can

be found in many handbooks i.e. [70]; usually soil characteristics such as shear strength and stiffness are a function of the void ratio and the degree of saturation. The incidence of the bulk waves at the boundary of each layers causes reflection and refraction of these waves. Incidence of the primary wave at the boundary between two layers generates a reflection and refraction of the P and SV wave [68]. Similar to the P wave, incidence of SV wave at the boundary generates a reflection and refraction of the SV and P wave. Incidence of the SH wave, however, at the boundary only gives the reflection and refraction of the SH waves without any conversion that implies uncoupling of this wave to the compressional wave. The angle of reflection and refraction can be simply determined using Snell's law. The refraction of the waves takes place unless the angle of incidence is larger than the critical angle, more details are explained in reference [68].

2.7 Summary

This chapter has provided the fundamental description of the vibrational behaviour of fluid filled pipes followed by an explanation of the effects of the interior and exterior fluid. Theoretical expressions of the $n = 0, s = 1, 2$ waves' wavenumbers along the pipe are presented, based on Kennard's equation, in which excludes the effects of rotational inertia, transvers shear and the bending about pipe shell wall. In the interest of mapping buried water pipes using the vibro-acoustic technique, it is important to propose a source of excitation which can deliver high amounts of energy to the axisymmetric fluid borne wave, in the low frequency range (frequencies lower than 100 Hz). Therefore, a theoretical explanation of the vibro-acoustic power transmission to fluid filled pipes has been provided for later study of the power transmission to the axisymmetric fluid borne wave via different excitation sources. The fundamental theory of propagation of body waves within an infinite elastic medium, is discussed. These waves are likely to be the dominant wave types that cause ground surface vibration in the vibro-acoustic technique.

Chapter 3

Wave speed measurement and decomposition of axisymmetric fluid and structural borne wave

At low frequencies, where the result from vibro-acoustic technique is reported as being the most promising, the pipe wave re-radiation to the surrounding medium is due to the axisymmetric fluid borne wave. Initially an experimental technique was proposed and used by Prek [72] to experimentally validate the theoretical model for the wave speed and attenuation of the axisymmetric fluid borne wave. Later Muggleton *et al.* [73] modified the post processing of the technique and carried out a similar measurement as performed by Prek [72].

Although measured wave speeds were consistent with the theory, a considerable data variance in the imaginary component of the wave number, compared to the theory, is observed. Furthermore, in view of good coupling between the axisymmetric fluid and structural borne wave, they must be considered together.

In this chapter the value of the wave speed and the attenuation of the axisymmetric fluid and structural borne waves are established through estimation of their wave number, by an experimental method. In addition, a simple analytical simulation is developed to explain a potential reason for the existing high variance in the imaginary component of the measured data.

In light of substantial differences in the speed of the waves termed $n = 0, s = 1, 2$, a simple experimental method was proposed to distinguish between the pipe wall displacement that arises from the two axisymmetric waves. Owing to the dependency of the ratio from the two waves to the elastic properties of the pipe, utilising such a method may help to assess the condition of pipes through indicating the reduction in their elastic properties due to ageing.

3.1 Parameter ratios between the axisymmetric fluid and shell dominated waves

In this section the wavenumber measurement technique developed by Prek [72], is revised to evaluate the wave speed and attenuation of the wave termed $n = 0, s = 1, 2$. The technique can only probe the wave number of a particular wave type. Several wave types, however, under each circumferential mode $n = 0, 1, 2, ...$ propagate along the pipe. Hence, prior to the measurement a wave decomposition should be carried out at the pipe wall cross section. Of the circumferential modes, only the axisymmetric vibration of the pipe wall, called breathing mode, is under focus in this study. Therefore the more sensors are used to measure in phase expansions and contractions of the pipe wall the better the decomposition will be achieved. The minimum sensor number to measure the axisymmetric vibration of the pipe wall is one.

For each circumferential mode, however, several wave types propagate. The relative amplitude of each wave type depend upon the pipe configuration and material properties, type of contained fluid and surrounding medium as well as the excitation method.

The material properties of the used MDPE pipe and the contained fluid are tabulated in Table 3.1. The pipe material properties were measured as described in Appendix A, through an experimental measurement in a laboratory and for brevity the final results are demonstrated in here. The theoretical model which shows the the relative amplitude of the axisymmetric fluid and structural borne waves subjected to the contained fluid and structural excitation is presented in Section 2.4. The theoretical ratios illustrated in Eqs. (2.23), (2.24), (2.26) and (2.27) are calculated in accordance with the data provided in Table 3.1 and are listed in Table 3.2.

TABLE 3.1: Material properties of MDPE pipe, contained fluid and its surrounding medium.

Parameter	Description of parameter	MDPE	Water	air
a	Mean radius (m)	8.45×10^{-2}	-	-
h	Wall thickness (m)	11×10^{-3}	-	-
E	Young's modulus (Gpa)	1.65	-	-
v	Poisson's ratio	0.4	-	-
B	Bulk modulus (Gpa)	-	2.18×10^{9}	1.42×10^{5}
ρ	Density(m^3)	880	1000	1.29

The data in Table 3.2 illustrates that when the pipe is subjected to the fluid excitation, the axisymmetric fluid borne wave becomes predominant in both axial and circumferential direction. Moreover, when the water filled pipe is subjected to an axial structural excitation, the axisymmetric axial and radial pipe excitation is mainly due to the axisymmetric shell and fluid borne waves respectively. In this case, the axisymmetric fluid borne wave carries a small amount of energy. Therefore it is possible to measure the wavenumber of both axisymmetric waves when the pipe is subjected to an axial shell vibration.

TABLE 3.2: Theoretical ratios of variables related to the axisymmetric fluid and shell borne wave within the MDPE pipe loaded via different excitation sources at frequency of 10 Hz and 400 Hz.

	Frequency (Hz)	$\frac{W_1}{W_2}$	$\frac{U_1}{U_2}$
Structural excitation of the water filled pipe	10 Hz	15.4	5.5×10^{-5}
	400 Hz	17.9	6.2×10^{-5}
Fluid excitation of the water filled pipe	10 Hz	3015	5.0
	400 Hz	3055	5.1

3.2 Description of selected wave speed measurement technique

Upon identifying the particle motion of desired waves, the pipe wall circumference should be instrumented at three equidistant points, as shown in Fig. 3.1. The direction of

mounted transducers should be aligned to the particle motion of the wave under interrogation.

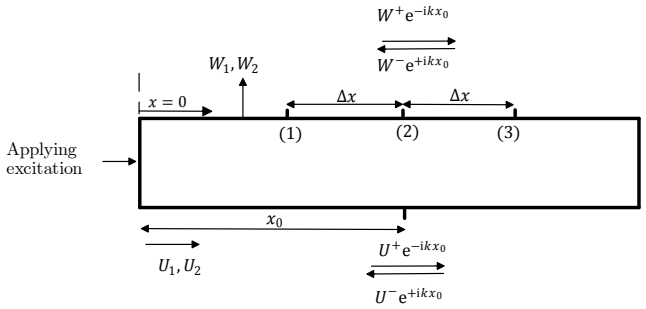

FIGURE 3.1: Diagram showing the arrangement used to apply the structural excitation to the fluid filled pipe, followed by measurement of the pipe displacement at three equidistant positions. W^+, W^- and U^+, U^- are associated with the axisymmetric radial and the axial displacement of the pipe wall. The subscript one and two illustrates the axisymmetric fluid and structural borne wave types respectively and the superscripts – and + illustrate the direction of propagation of the wave.

The frequency response function (FRF) of the measured signals with respect to the excitation signal is represented by: $H_{1,\mathrm{ref}}, H_{2,\mathrm{ref}}, H_{3,\mathrm{ref}}$ at locations 1,2 and 3 respectively, as shown in Fig. 3.1. By assuming $H_{2,\mathrm{ref}} \neq 0$, the wavenumber of a wave type can be identify by [72]:

$$k = \frac{1}{\Delta x} \arccos\left(\frac{H_{1,\mathrm{ref}} + H_{3,\mathrm{ref}}}{2H_{2,\mathrm{ref}}}\right). \tag{3.1}$$

The obtained wavenumber might be complex, which allows extraction of the wave speed and the attenuation. The real and imaginary component of the measured wavenumber presented in Eq. (3.3) are limited between $[0, 2\pi]$. According to the Nyquist criterion when more than half of the wavelength fits between successive measurement points an unwrapping should be applied to remove the ambiguity, which is explained by Muggleton *et al.* [73] as:

$$\begin{aligned} \mathrm{Re}\left\{k_{\mathrm{unwrap}}\right\} &= \frac{1}{\Delta x}((nl+1)\pi - \mathrm{Re}\left\{k\Delta x\right\}),\ nl \text{ odd}, \\ \mathrm{Re}\left\{k_{\mathrm{unwrap}}\right\} &= \frac{1}{\Delta x}(nl\pi + \mathrm{Re}\left\{k\Delta x\right\}),\ nl \text{ even}, \\ \mathrm{Im}\left\{k_{\mathrm{unwrap}}\right\} &= \frac{1}{\Delta x}(-1)^{nl}\mathrm{Im}\left\{k\Delta x\right\}. \end{aligned} \tag{3.2}$$

Here nl is the number of half wavelengths between successive measurement points along the pipe. Finally, the wave speed and attenuation associated to each wave are determined by the real and imaginary component of the unwrapped wavenumber respectively:

$$c\ (\mathrm{m/s}) = \frac{\omega}{\mathrm{Re}(k_{\mathrm{unwrap}})}, \mathrm{attenuation}\ (\mathrm{dB/m}) = \frac{20\,\mathrm{Im}(k_{\mathrm{unwrap}})}{\ln(10)}. \tag{3.3}$$

3.3 Experimental set up and procedure

In this measurement, an MDPE pipe with a length of 2.1 m was hung vertically from a jack and subjected to an axial excitation via a shaker mounted on the plate and placed on top of the pipe. Geometrical and material properties of the pipe are illustrated in Table 3.1. The schematic of source-sensor arrangement, used to estimate wavenumber within the pipe, is presented in Fig. 3.2. The measurement was undertaken 50 cm from each endpoint of the pipe at equidistant locations from the mid-section of the pipe, as illustrated in Fig. 3.2.

The measurement was carried out by four accelerometers and it was decided to mount all accelerometers at each measurement point at the range of $\pi/2$ around the pipe circumference and repeat the measurement for three locations. To measure the wavenumber of axisymmetric fluid and structural borne wave, accelerometers should be mounted to the pipe wall circumference to measure its circumferential acceleration in radial and axial direction respectively.

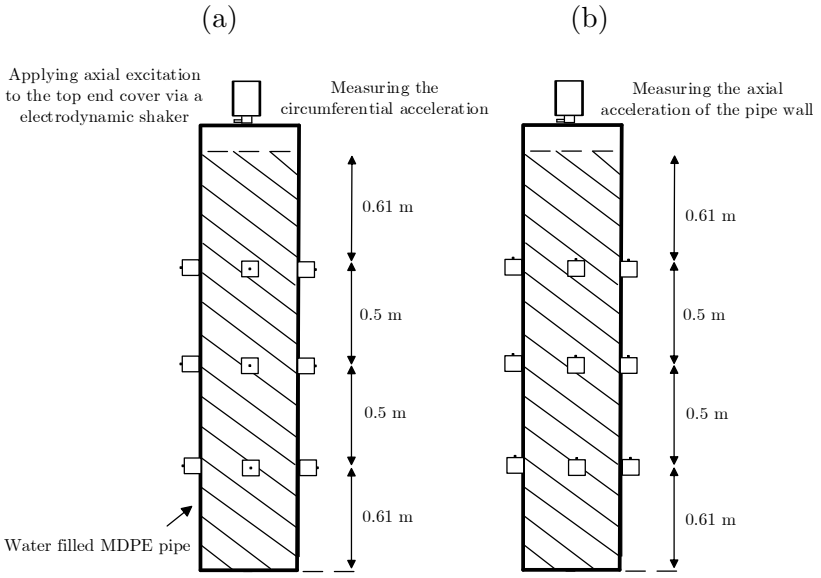

FIGURE 3.2: Experimental arrangement to estimate the axisymmetric fluid and the shell borne wave speeds by measuring the pipe wall vibration in the (a) circumferential and (b) axial direction. The dot on the squares illustrates the direction of measurement.

The time extended signal sent into the shaker was linear chirp ranging from 10 Hz to 1.6 kHz, averaging of the 16 times for each sensor, the transfer function averaging, reduces the effect of noise on the measured data. The data was recorded using a ProSig P8020 with a sampling frequency of 4 kHz and low pass filters of 1.6 kHz was built into the ProSig to avoid aliasing. FRF between the source and the sensors was carried out using 2000-points FFT, rectangular window with 50 % overlap and power spectrum averaging.

3.4 Experimental results

The experimental data corresponding to the real and imaginary component of the axisymmetric fluid and the shell borne wave wavenumber is plotted in Fig. 3.3 and compared to the theoretical wavenumber of these two waves as expressed in Eqs. (2.6) and (2.11) respectively.

The wave speed of these two waves is in line with the theory, although the wave termed $n = 0, s = 1$ deviates from the theory after approximately 600 Hz. The data measured from the radially mounted accelerometers is mainly attributed to the wave termed $n = 0, s = 1$ wave, while the collected data from the axially mounted one is corresponded to the wave termed $n = 0, s = 2$.

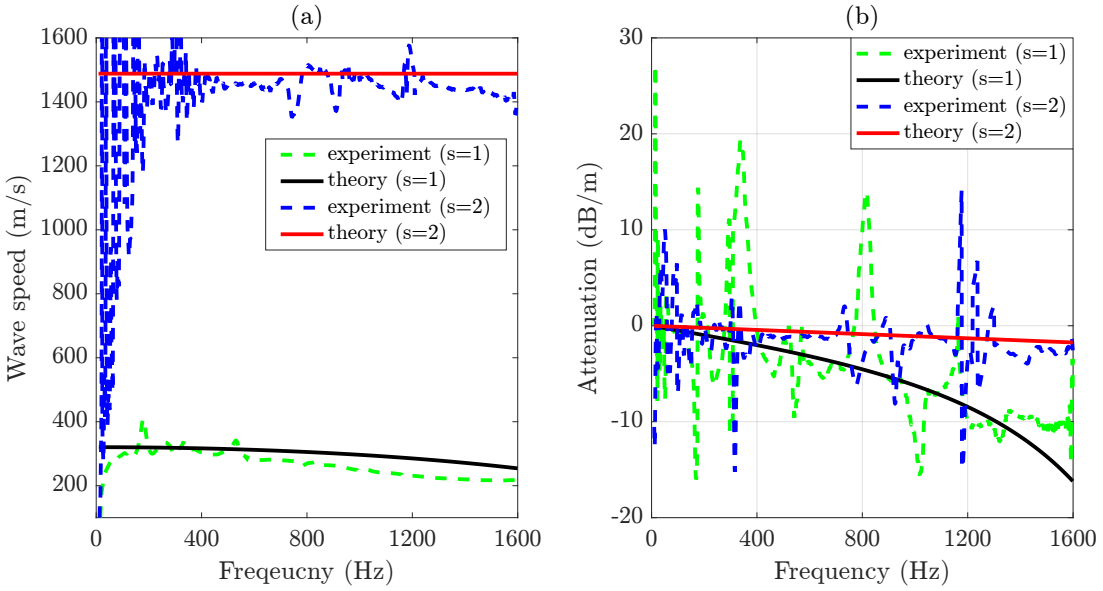

FIGURE 3.3: (a) The wave speed and (b) the attenuation related to the axisymmetric fluid and structural borne wave. Theoretical formulae of these two waves, which are used to extract the wave speeds are expressed in Eqs. (2.6) and (2.11).

The obtained data from the demonstrated result in Fig. 3.3 confirmed that any physical quantities that changes due to the presence of the wave, i.e. axial acceleration or circumferential strain can be adopted for the measurement of the wave speed and its attenuation.

The loss value of these two axisymmetric wavenumbers deviates from theoretical predictions. At low frequency, these errors arise from ambient noise, as the imaginary component of the wave number is small compared to the real part and the effects of ambient noise are significant. At higher frequencies, above 600 Hz for instance, high amount of the fluctuation is observed, however, their overall trend is consistent with the theory. A potential reason for such oscillations is explained in the next section.

Details of the data associated with the axisymmetric fluid and the shell borne wave including the mean value of wave speeds, the deviation from theoretical predictions and the dispersive behaviour are summarised in Table 3.3 and Table 3.4 respectively. Since the axisymmetric fluid borne wave exhibits dispersive behaviour, its data is separated into two frequency regions.

As illustrated in Table 3.3 the axisymmetric fluid borne wave has a lower wave speed compared to its equivalent free field wave, which is 1500 m/s, and exhibits higher dispersive behaviour after 400 Hz. In contrast, it can be seen from Table 3.4 that the

TABLE 3.3: Details of the measured data associated to the real component of the axisymmetric fluid borne wave.

Data related to the axisymmetric fluid borne wave up to 600 Hz			
Mean value of the wave speed	Standard deviation	Mean value of the wave speed deviation from theory	Linear dependency of the wave speed to the frequency
297 m/s	3.6 m/s	5 m/s	$300 - 0.01f$
Data related to the axisymmetric fluid borne wave from 600 Hz-1600 Hz			
Mean value of the wave speed	Standard deviation	Mean value of the wave speed deviation from theory	Linear dependency of the wave speed to the frequency
255 m/s	10.8 m/s	24 m/s	$285 - 0.05f$

TABLE 3.4: Details of the measured data associated to the real component of the axisymmetric shell borne wave between 10 Hz to 1.6 kHz.

Mean value of the wave speed	Standard deviation	Mean value of the wave speed deviation from theory	Linear dependency of the wave speed to the frequency
1445 m/s	1.2 m/s	15 m/s	$1440 + 0.006f$

axisymmetric shell borne wave exhibits less dispersive behaviour and its speed rises approximately by 10 % compared to the calculated compressional wave speed in the empty pipe.

3.5 Effect of location errors and ambient noise on the measured wave speed

The aim of this section is to assess the data obtained in Section 3.4 and particularly explain what would happen if the transducers are not mounted to the pipe wall at equal distances along the pipe length. The relationship between any specific wave types wave number and the measured transfer function at the three equidistant points along the pipe is explained in Eq. (3.1). The calculated wavenumber encompasses both the real and imaginary part, and depending on the wave type under investigation; the measured wave numbers might be (1)- complex and (2)- purely real or (3)- purely imaginary. If the measured wave number encompasses both real k_{RE} and the imaginary components k_{IM}, $k = k_{\mathrm{RE}} + \mathrm{i}k_{\mathrm{IM}}$, then Eq. (3.1) is transformed to:

$$\frac{H_{1,\text{ref}} + H_{3,\text{ref}}}{2\,H_{2,\text{ref}}} = \cos(k_R \Delta x)\,\cosh(k_I \Delta x) + \mathrm{i}\,\sin(k_R \Delta x)\,\sinh(k_I \Delta x). \tag{3.4}$$

Curve fitting of the data using right hand side of Eq. (3.4), reveals both the real and imaginary components of the wave number. The real component of the wavenumber, $\cos(k_r \Delta x)\,\cosh(k_I \Delta x)$, in Eq. (3.4) reveals the wave speed as $c = \omega/(k_R)$. Since the real component of the wave number contains $\cosh(k_I \Delta x)$, a material with structural damping possesses a lower wave speed compared to one without. When the sensors are not placed at equal distances along pipe length, it is possible for errors to occur. Therefore, an analytical simulation has been developed to illustrate the effects of these errors. In this simulation the effect of errors on the wave termed $n = 0, s = 1, 2$ are considered only. The applied excitation and measurement locations are illustrated in Fig. 3.4.

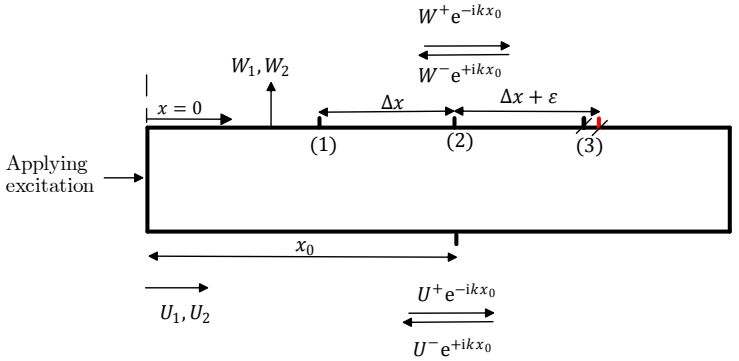

FIGURE 3.4: The simulation configuration for the wavenumber measurement when there is an small error in the location of one transducer with respect to the other two.

The full derivation of pressure wave propagation along a pipe section is given in Appendix B. The recorded circumferential strain of the pipe wall at each position can be explained by:

$$\begin{aligned} W(x_0 - \Delta x) &= W^+ \mathrm{e}^{-\mathrm{i}k(x_0 - \Delta x)} + W^- \mathrm{e}^{\mathrm{i}k(x_0 - \Delta x)} \\ W(x_0) &= W^+ \mathrm{e}^{-\mathrm{i}kx_0} + W^- \mathrm{e}^{\mathrm{i}kx_0} \\ W(x_0 + \Delta x + \varepsilon_0) &= W^+ \mathrm{e}^{-\mathrm{i}k(x_0 + \Delta x + \varepsilon)} + W^- \mathrm{e}^{\mathrm{i}k(x_0 + \Delta x + \varepsilon)} \end{aligned} \tag{3.5}$$

Combining the expressions in Eq. (3.5) gives a function as:

$$\begin{aligned} &\frac{W(x_0 - \Delta x) + W(x_0 + \Delta x + \varepsilon)}{2\,W(x_0)} = \\ &\cos(k_1 \Delta x) + \frac{W^+ \mathrm{e}^{-\mathrm{i}k(\Delta x + \varepsilon)} + W^- \mathrm{e}^{\mathrm{i}k(\Delta x + \varepsilon)}}{W^+ \mathrm{e}^{-\mathrm{i}kx_0} + W^- \mathrm{e}^{\mathrm{i}kx_0}} \end{aligned} \tag{3.6}$$

In the light of provided formula in Eq. (3.6), it can be seen that its outcome is no longer equals to $\cos(k_1 \Delta x)$. Therefore the wavenumber will change due to the latter term on the right hand side of Eq. (3.6) with respect to the distance errors and the reflection coefficient at the pipe endpoint. Effects of added terms are plotted in Fig. 3.5.

Apart from the location errors, the imaginary component of the wavenumbers in Fig. 3.5 seems to be sensitive to the effects of ambient noise. This phenomenon occurs as the imaginary component of the wavenumber is much smaller than its real component and the contribution of noise becomes significant on the obtained data. To make the simulation accurately reflect the experimental situation, it is desirable to consider the effect of noise on the obtained data.

Therefore, a Gaussian distribution with the standard deviation of 5×10^{-4} , or approximately 41 dB signal to noise ratio (SNR) for this example, has been included in the simulation. The exact value of SNR can be estimated by switching off the excitation source and recoding signal from the utilised sensors. Since this simulation lies in the frequency domain, the data has been converted to the time domain via Inverse Fourier Transform (IFFT), followed by the addition of noise to it. The data is then again converted to the frequency domain using Fast Fourier Transform (FFT).

By assuming the obtained results from misplacement sensors is still equal to $\cos(k_1 \Delta x)$ and following the procedure explained in Section 3.2, the obtained data is expected to deviate from its true value. The wave speed of the axisymmetric fluid and shell borne wave is plotted in Fig. 3.5 (a) and (b) respectively.

The deviation of wave speed values associated with each wave type are summarised in Table 3.5. The specified errors, $\varepsilon = 1\,\text{cm}$ and $\varepsilon = 2\,\text{cm}$, cause the averaged experimental wave speed to deviate from the theoretical predictions by 5.7 m/s and 7.6 m/s for the axisymmetric shell borne wave and by 7.8 m/s and 10.1 m/s for the axisymmetric fluid borne wave, respectively, at the frequency range of 10 Hz-1600 Hz.

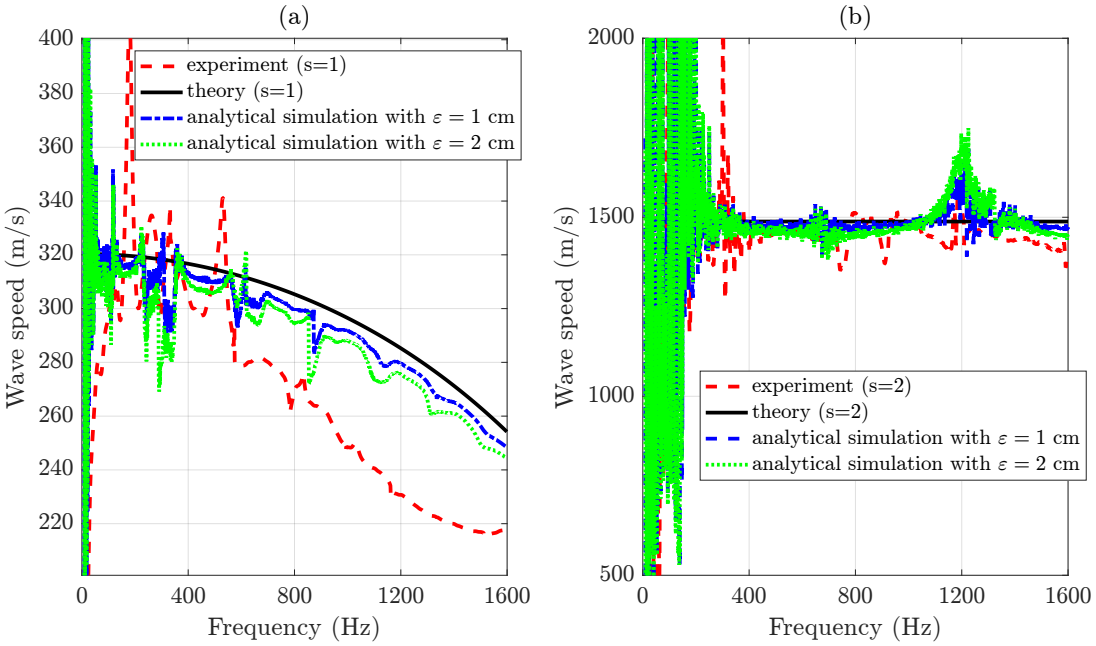

FIGURE 3.5: The wave speed of the axisymmetric fluid (a) and shell (b) borne wave. Data from (——) experimental study, (- - -) theory, (-·-·) analytical simulation with $\varepsilon = 1\,\text{cm}$ and (·····) with $\varepsilon = 2\,\text{cm}$ respectively. Theoretical wavenumber of these two waves expressed in Eqs. (2.6) and (2.11).

TABLE 3.5: Deviation of the wave speeds due to 1 and 2 cm distance errors of the misplaced sensor compared to the ideal one.

	Mean value of the wave speed deviation from theory due to	
	$\varepsilon = 1$ cm errors (m/s)	$\varepsilon = 2$ cm errors (m/s)
Axisymmetric shell borne wave	5.7 m/s	7.6 m/s
Axisymmetric shell borne wave	7.8 m/s	10.1 m/s

The deviation of the wave speed due to other errors related to misplacement of the sensors, has been evaluated for two more different values of the distance error (except the two values which have been illustrated in Table 3.5. The results were then processed by curve fitting of the data and plotted in Fig. 3.6.

Similar to the obtained data from the real component of the wavenumbers, the imaginary component of $\cos(k_1 \Delta x)$, was plotted for different distance errors for the axisymmetric fluid and shell borne waves and is illustrated in Fig. 3.7 (a) and (b) respectively.

As seen in Fig. 3.7(a) the experimental data peaks pattern is irregular while the data from the model shows a regular pattern of peaks, appearing at approximately every 350

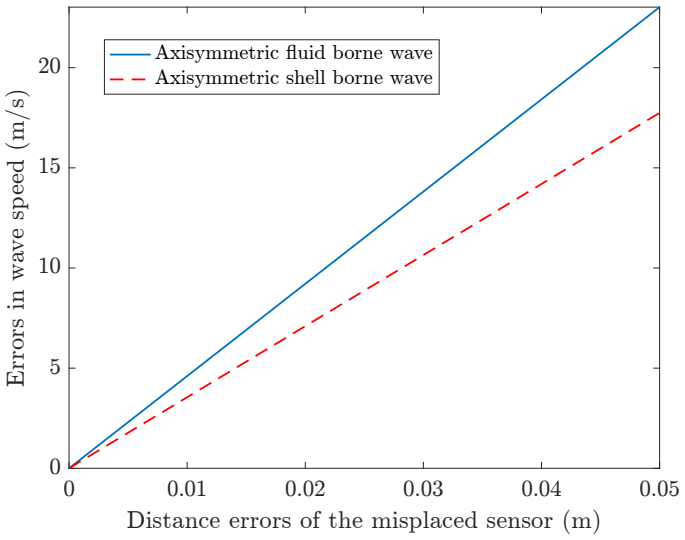

FIGURE 3.6: Mean errors in the wave speed of the axisymmetric fluid and shell borne wave due to the distance errors of a misplaced sensor. The error values are calculated with respect to the theoretical wave speed.

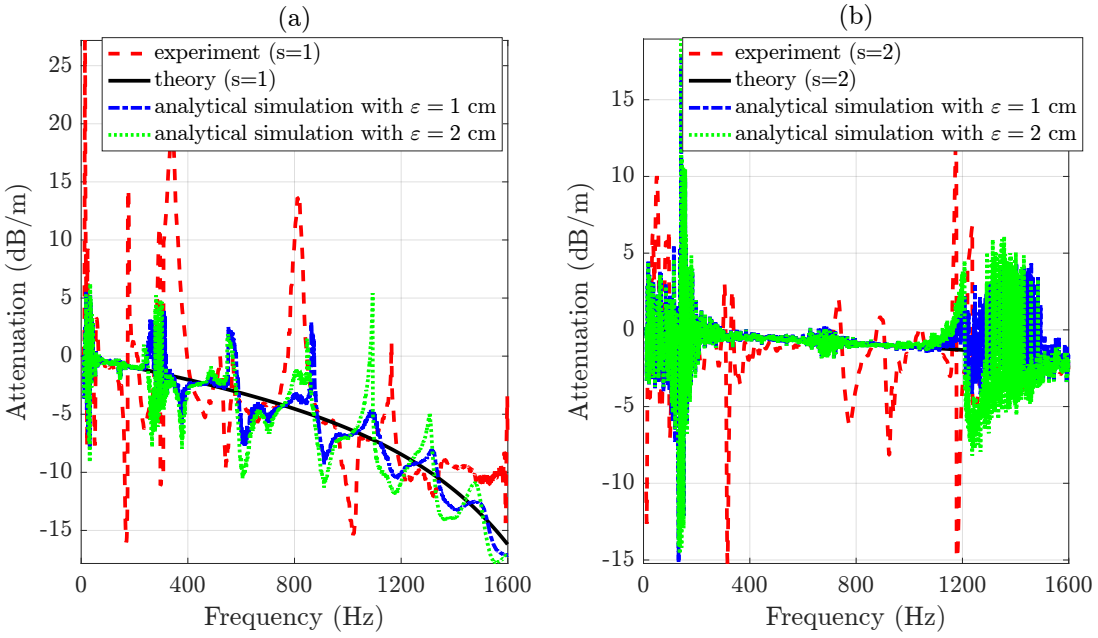

FIGURE 3.7: The attenuation associated to the axisymmetric fluid (a) and shell (b) borne wave. Data from (——) experimental study, (- - -) theory, (-·-·) analytical simulation with $\varepsilon = 1\,\text{cm}$ and (·····) with $\varepsilon = 2\,\text{cm}$ respectively.Theoretical wavenumber of these two waves expressed in Eqs. (2.6) and (2.11).

Hz. Nevertheless, the undertaken analytical simulation shows some small peaks which are approximately observed in the same location as in the experimental study. There are other peaks in the experimental data which do not appear in the developed model. The model for the two axisymmetric waves only demonstrates the noise effect at where the arccos function in Eq. (3.1) reaches to 0 and 2π. These discrepancies might be due

to, for example, cross sensitivity error resulting from propagation of higher order modes along the pipe length. The effect of such error, however, is not considered in this study.

3.6 Decomposition of the axisymmetric fluid and the shell borne wave

Due to the substantial differences between the wave speed of the axisymmetric fluid and structural borne wave, showed in Section 3.3, a simple technique is proposed to distinguish between the two wave contributions to the pipe wall displacement. Decomposition of the two waves will help quantify the characteristics of the radiated wave from the pipe wall into the surrounding medium. The radiation loss from these two waves into the surrounding medium is greatly affected by the density and wave speed of the surrounding medium. As a first try, selecting an ideal situation where both wave types have the same magnitude might help achieve successful wave decomposition (see Table 3.2). However, none of the ratios presented in Table 3.2 are close to unity. Thus, the best option might be focusing on the ratio obtained from the radial or the axial pipe wall displacement, when the pipe was subjected to an axial or an internal excitation, respectively. In this section, the former situation is selected for further investigation.

The measurement in this section was conducted on the pipe rig that used for the wave number measurement. The test specimen was assembled by placing four PCB Brüel and Kjær accelerometers type 4883, radially around the circumference of the pipe. More details about the utilised accelerometers are given in Table A.1. Spatial averaging of the data from a group of accelerometers reduces the effect from higher order modes on the pipe wall displacement.

The time extended signal sent into the shaker was linear chirp ranging from 10 Hz to 1 kHz, averaging of the 16 times for each sensor, the transfer function averaging, reduces the effect of surrounding noise on the measured data. The data was recorded using a ProSig P8020 with a sampling frequency of 2.5 kHz and low pass filters of 1 kHz was built into the ProSig to avoid aliasing. FRF between the source and the sensors was carried out using 1250-points FFT, rectangular window with 50 % overlap and power spectrum averaging.

This measurement was taken at four locations along the pipe length, with interval distances of $\Delta z = 0.3m$ between each adjacent transducer, as illustrated in Fig. 3.8. Several important parameters were incorporated in this technique, namely the wave speeds, spacing between sensors and the location of the sensors. The optimal distance for transducer placement is given by [74] as $0.1\pi < k\Delta x < 0.8\pi$, where k is the wave number and Δx is the distance between adjacent transducers. The measurements were taken at 40 cm distance from each end of the pipe. The effects from evanescent waves might become significant for either short pipes or at lower frequency. In this experiment, the cylinder was subjected to a structural excitation and the pipe wall acceleration is recorded at the four positions, as shown in Fig. 3.8.

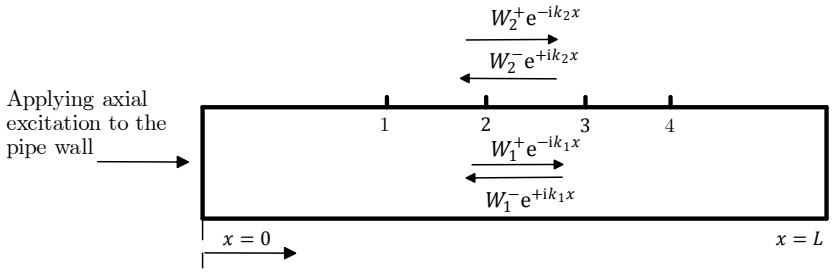

FIGURE 3.8: Diagram showing the arrangement used to decompose the radial motion of the shell comprising of the $n = 0, s = 1, 2$ waves when the excitation was applied to the pipe wall via an electrodynamic shaker.

The recorded radial acceleration of the pipe wall composes of four independent elements, namely: two axisymmetric waves in the radial direction, travelling up and down along the pipe. The general form for decomposition of the amplitude of each axisymmetric wave acting in the radial displacement of the pipe wall can be achieved by (i) Substitution of the transfer functions $Q(x_1)...Q(x_n)$, which are obtained via measurement of the radial acceleration of the pipe wall, at locations $x_1...x_n$, with respect to the applied voltage to the speaker followed by dividing them by ω^2, in the matrix in Eq. (3.7). (ii) Substitution of the wave numbers of the two axisymmetric waves, k_1 and k_2 from the analytical simulation given in Eq. (2.6) and (2.11), into Eq. (3.7). Therefore the only unknown terms are W_1 and W_2 which represent the amplitudes of the axisymmetric waves with respect to the applied voltage and the superscripts $+$ and $-$ represent the waves travelling in the positive and negative direction with x_0 the distance from the excitation point:

$$\frac{\mathbf{1}}{-\boldsymbol{\omega}^{\mathbf{2}}}\mathbf{Q} = \boldsymbol{\Lambda}\mathbf{W}, \tag{3.7}$$

where

$$\mathbf{Q}^T = [Q(x_1)Q(x_2)...Q(x_n)], \mathbf{W}^T = [W_1^+ W_1^- W_2^+ W_2^-]$$

$$\mathbf{\Lambda} = \begin{bmatrix} \mathrm{e}^{-\mathrm{i}k_1 x_1} & \mathrm{e}^{\mathrm{i}k_1 x_1} & \mathrm{e}^{-\mathrm{i}k_2 x_1} & \mathrm{e}^{\mathrm{i}k_2 x_1} \\ \vdots & \vdots & \vdots & \vdots \\ \mathrm{e}^{-\mathrm{i}k_1 x_n} & \mathrm{e}^{\mathrm{i}k_1 x_n} & \mathrm{e}^{-\mathrm{i}k_2 x_n} & \mathrm{e}^{\mathrm{i}k_2 x_n} \end{bmatrix}.$$

By performing matrix inversion into Eq. (3.7), the amplitude of each axisymmetric wave can be expressed by:

$$\mathbf{W} = \frac{1}{-\omega^2}\mathbf{\Lambda}^{-1}\mathbf{Q}. \tag{3.8}$$

In the case of an overdetermined matrix the wave amplitude can be found in a least square manner through using the Moore-Penrose inverse [75] gives:

$$\mathbf{W} = \frac{1}{-\omega^2}(\mathbf{\Lambda}^H\mathbf{\Lambda})^{-1}\mathbf{\Lambda}^H\mathbf{Q}, \tag{3.9}$$

where $(...)^H$ illustrates the Hermitian transform of the matrix inside the bracket. The ratio of the W_1^+/W_2^+ and W_1^-/W_2^- obtained from Eq. (3.9) is plotted in Fig. 3.9 using the blue and red dotted lines respectively. Discrepancy between the data from experimental study and analytical simulation is observed at frequencies above 150 Hz. The observed peaks at 93 Hz, 295 Hz are related to the cut off frequencies of the $n = 2, 3$ mode. The cut-off frequencies of the higher order modes, for the empty and the water filled MDPE pipe when it is surrounded by air, are provided in Eq. (3.13). At higher frequencies of excitation, starting at 93 Hz where $n \geq 2$, the higher order modes propagate effectively along the pipe and slight perturbations from higher order modes within the pipe resulted in divergence of the experimental data from the theoretical predictions.

There will be inevitably errors in both transformation matrix $\mathbf{\Lambda}$ and the vector of experimental matrix $\mathbf{Q}$. These errors results from natural frequency of higher circumferential modes or errors in experimental measurement i.e. misplaced sensor in the experimental measurement, as well as inappropriate knowledge of structural properties. Effects of foregoing items on the decomposed data are investigated in the following subsections.

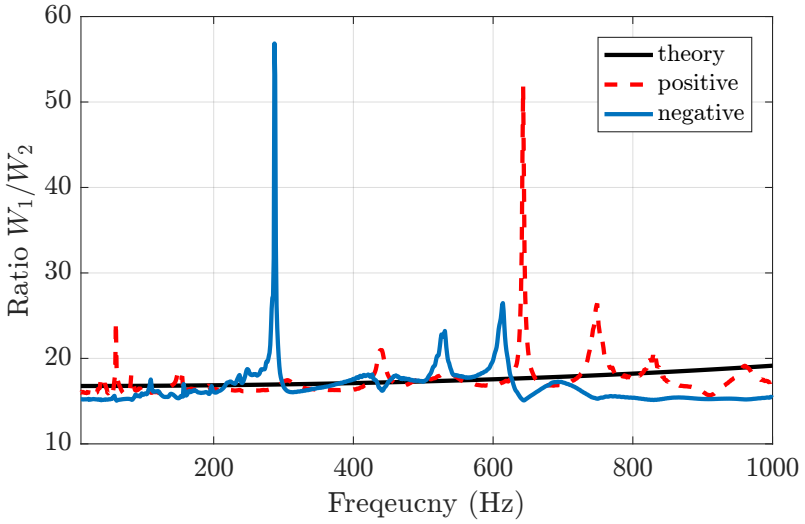

FIGURE 3.9: The ratio between s=1,2 waves contributions to the radial displacement of the pipe wall, for fluid excitation at frequency 10 Hz to 1000 Hz.

3.6.1 Effect of sensor misplacement and wavenumber errors on the wave decomposition

Another reason of oscillations after the wave decomposition, could be due to the effect of sensor mislocation spacing along the pipe. An overview of the mislocation errors is illustrate in Fig. 3.10.

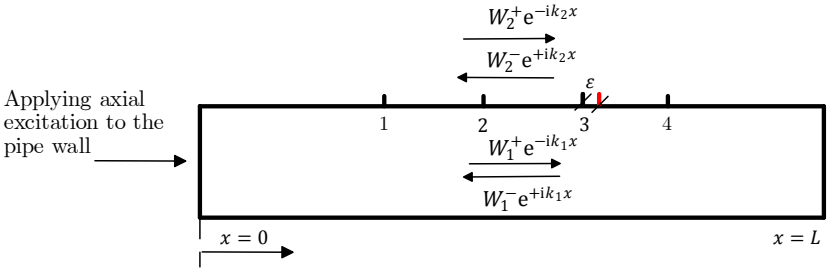

FIGURE 3.10: A diagram of the analytical simulation for decomposing the radial vibration of the pipe wall from the positive and negative the $n = 0, s = 1, 2$ waves propagation within the pipe. The mislocation error is illustrated by ε.

The general solution for radial vibration of the pipe wall arising from propagation of the axisymmetric wave can be expressed by: $Q(x) = W_1^+ e^{-ik_1x} + W_1^- e^{ik_1x} + W_2^+ e^{-ik_2x} + W_2^- e^{ik_2x}$. Substituting $W_1^- = R_1 W_1^+$ and $W_2^- = R_2 W_2^+$ in the foregoing expression

gives:

$$Q(x) = W_1^+ \mathrm{e}^{-\mathrm{i}k_1 x} + W_1^- \mathrm{e}^{\mathrm{i}k_1 x} + W_2^+ \mathrm{e}^{-\mathrm{i}k_2 x} + W_2^- \mathrm{e}^{\mathrm{i}k_2 x} = W_1^+ \left[\mathrm{e}^{-\mathrm{i}k_1 x} + |R_1|\mathrm{e}^{-\mathrm{i}\,(k_1 x + \phi_{R_1})}\right] + W_2^+ \left[\mathrm{e}^{-\mathrm{i}k_2 x} + |R_2|\mathrm{e}^{-\mathrm{i}\,(k_2 x + \phi_{R_2})}\right]. \tag{3.10}$$

In Eq. (3.10), effects of near field waves and radiation of the waves into the surrounding medium are discarded. Substitution of the wave amplitudes of the two waves in accordance with theory is presented Eq. (3.11).

$$|W_1^+| = 17 = |W_2^+|, R_1 = R_2 = -1, \phi_{W_1^+} = \phi_{W_2^+} = 0, \phi_{R_1} = \phi_{R_2} = \pi/2. \tag{3.11}$$

Substituting the above data into Eq. (3.10) gives the complex numbers for each individual point along the pipe. In the given matrices (see Eq.(3.8)) all values are substituted except the amplitudes of the axisymmetric waves. Since in the experimental studies the only unknown parameter is their amplitude. By considering misplacement error, which occurs at the location $x3$, matrix $\mathbf{\Lambda}$ in Eq. (3.7) becomes:

$$\mathbf{\Lambda} = \begin{bmatrix} \mathrm{e}^{-\mathrm{i}k_1 x_1} & \mathrm{e}^{\mathrm{i}k_1 x_1} & \mathrm{e}^{-\mathrm{i}k_2 x_1} & \mathrm{e}^{\mathrm{i}k_2 x_1} \\ \mathrm{e}^{-\mathrm{i}k_1 x_2} & \mathrm{e}^{\mathrm{i}k_1 x_2} & \mathrm{e}^{-\mathrm{i}k_2 x_2} & \mathrm{e}^{\mathrm{i}k_2 x_2} \\ \mathrm{e}^{-\mathrm{i}k_1 (x_3+\varepsilon)} & \mathrm{e}^{\mathrm{i}k_1 (x_3+\varepsilon)} & \mathrm{e}^{-\mathrm{i}k_2 (x_3+\varepsilon)} & \mathrm{e}^{\mathrm{i}k_2 (x_3+\varepsilon)} \\ \mathrm{e}^{-\mathrm{i}k_1 x_4} & \mathrm{e}^{\mathrm{i}k_1 x_4} & \mathrm{e}^{-\mathrm{i}k_2 x_4} & \mathrm{e}^{\mathrm{i}k_2 x_4} \end{bmatrix}. \tag{3.12}$$

As can be seen in Fig. 3.11, a slight mislocation of the sensor along the pipe will causes a rippling into the ratio of the decomposed wave type. Dividing the magnitude of the positive and the negative going wave along the pipe is illustrated in Fig. 3.11.

High value of the deviation below 200 Hz can be explain through matrix conditioning. The conditioning of a matrix lies at the heart of the wave decomposition and its evaluation considered in this section. It is normally used to estimate the sensitivity of the decomposed wave to any source of errors; such as noise and misplaced sensor location. The sensitivity of the decomposed wave amplitude to such errors can be estimated via the conditioning of the problem.

As illustrated in Fig. 3.12, at frequencies below 200 Hz the matrix $\mathbf{\Lambda}$ is close to singularity. Therefore the results illustrated in Fig. 3.9 and Fig. 3.11 are reliable above 200Hz.

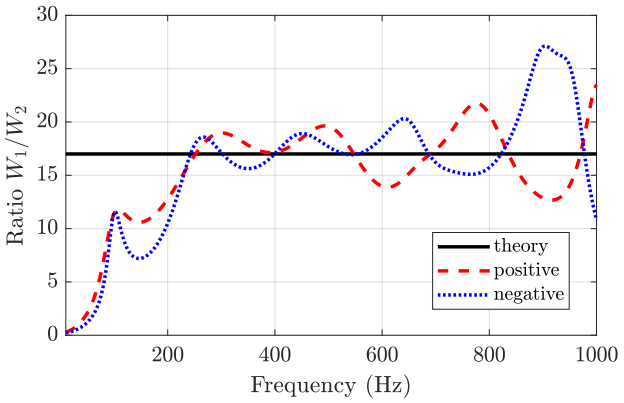

FIGURE 3.11: The ratio between $s = 1, 2$ waves amplitude that contributes to the radial displacement of the pipe wall from theoretical measurement, for an axial structural excitation at frequency 10 Hz to 1000 Hz. The illustrated results associate to the mislocation error of $\varepsilon = 1$ cm, shown in Fig. 3.10

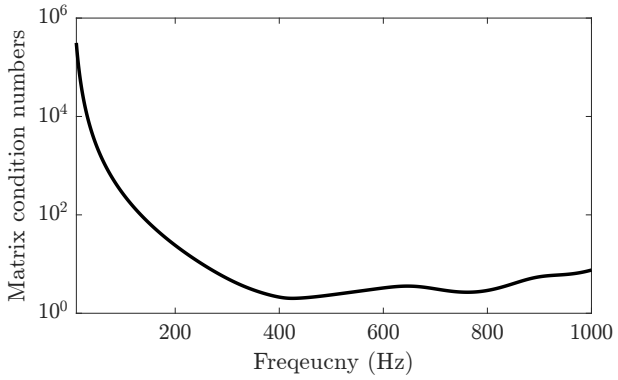

FIGURE 3.12: Estimates of $\mathbf{\Lambda}$ matrix condition expressed in Eq. (3.7).

Minimising the value of the condition number reduces the errors on the amplitude of the decomposed wave. To reduce conditioning number, hybrid measurement systems are nominated by several authors. In practical measurement, however, one must calibrate the sensors and be assured that all the different nominated transducers work in phase.

3.6.2 Cut-off frequency of higher circumferential modes of a thin walled shell

As illustrated in Fig. 3.9, the measured data was slightly deviated from the theory. Therefore, an investigation was carried out to find the cut-off frequency of the higher order modes within the plastic pipe when it is empty and when it is filled with water, which is given by [76]:

$$f_c = f_{\text{ring}} \sqrt{\frac{\psi^2 n^2 (n^2-1)^2}{n^2 + 2\mu n + 1}}, \tag{3.13}$$

where $\mu = \frac{a\rho_f}{h\rho_s}$is the fluid–shell mass ratio, $f_{\text{ring}} = \frac{c_L}{2\pi a}$ is the pipe ring frequency, and $\psi^2 = \frac{h^2}{12a^2}$ is the shell thickness parameter. A similar formula is established by Moser [77] (Eq. (4) of the mentioned paper). Substituting the parameter, using Table 3.1, the cut-off frequency of the higher modes for the empty and the water filled pipe is given in Table 3.6.

TABLE 3.6: Cut-off frequency of the MDPE pipe when it is empty and when filled with the water.

Mode number	$n = 2$	$n = 3$	$n = 4$	$n = 5$
cut-off frequency of the empty pipe in Hz	259	732	1408	2279
cut-off frequency of the fluid filled pipe in Hz	93	297	632	1177

Below the cut-off frequency of each mode, there would be evanescence or quasi-propagation of these waves within the pipe. Plane waves, torsional waves, and bending waves propagate along the pipe without a cut off frequency. The energy associated with the torsional and bending waves is restricted exclusively to the pipe wall with marginal amounts of coupling to the fluid. Note that the cut-off frequency increases as the pipe wall thickness increases and decreases as the mass of the contained fluid and the pipe's radius increases. Furthermore, there are other methods of finding the cut-off frequency of the higher order modes within steel or plastic pipes, detailed in reference [78].

3.7 Summary

Tracking a typical buried water pipe by the vibro-acoustic methods requires an in-depth understanding of the axisymmetric fluid borne wave. Due to the good coupling of the axisymmetric fluid and the structural borne wave, the effects of these two waves should always be taken into account simultaneously.

The wave speed and attenuation of the two waves are measured in this section through measuring their wave number by an experimental technique developed by Prek [72] and

Muggleton *et al.* [73]. The results from the experimental study were compared against the theory. Although the obtained speed from each wave was close to the theory, the high variation in the imaginary component of the wave number was noticeable.

Although several researchers have carried out experimental measurement and identified the speed and attenuation of axisymmetric fluid wave, the reason for high variation at the imaginary component was open to question. The analytical simulation displayed in this chapter provides a potential reason of high variation.

An experimental technique was developed to pinpoint the amplitude of the each axisymmetric wave using a proper array of accelerometers. The results from experimental studies are compared with theoretical predictions and a good agreement has been obtained. Establishing this discrimination provides a better understanding about the changes to the material properties of the pipe wall due to ageing.

Chapter 4

Design and laboratory testing of pneumatic devices for an acoustic excitation of water filled pipes

The current vibro-acoustic technique for tracing underground plastic pipes involves the excitation of the pipe wall or the contained fluid at a fixed location. In this technique, the ability of excitation sources to deliver energy at low frequencies, ranging from 10 Hz to approximately 100 Hz, to the axisymmetric fluid borne wave affects the distance at which buried water pipes can be located. Below 10 Hz the environmental noise is dominant and beyond 100 Hz attenuation due to material damping of the pipe wall, as well as the re-radiation of the acoustic wave from the pipe wall to the surrounding medium is too strong.

Although in-pipe sources can be moved and generate the required acoustic signal along the pipe, current acoustic exciters are not always appropriate, being cumbersome and often too large to fit into a typical buried water pipe with a diameter of 18 cm.

In light of above, in this chapter, two pneumatic devices are considered; a balloon gun and water gun were developed and re-engineered respectively. The aim of such designs is both generating high amplitude signals at low frequencies and accessing pipes with a wide range of diameters, down to 1 cm. The devices are characterised by a series of laboratory tests and benchmarked against a standard electro-acoustic and an electromagnetic shaker

which are typically used to apply mechanical and acoustical excitation to the fluid filled pipe.

4.1 Description of the experimental rig and power transmission measurement

In this section the experimental rig and the procedure of ranking each excitation source ability on driving the axisymmetric fluid borne wave are explained. All the measurements were conducted on the pipe rig used in Chapter 3 as shown in 4.1. The 2.1 metre pipe was filled up to two metres with water and was hung vertically from a jack. The geometrical and material properties of the pipe are illustrated in Table 3.1.

Recording either the fluid pressure at a unique position or the source power transmitted into the axisymmetric fluid borne wave can lead to characterize the potential each source. The former technique was used and to measure the pressure transmitted to the axisymmetric fluid borne wave the acoustic pressure was measured at 1.3 m distance from the water surface using a hydrophone. The latter technique, whilst it was well developed in this study, it has been included in Appendix D. This is because the technique requires a successful wave decomposition a priori, which is not always an easy task to achieve.

It is desirable, when measuring the pressure transmission to the contained fluid, to be able to measure or predict input powers to excitation sources or structures. This allows making a comparison between the different sources of excitation, in terms of the power transmitted and input powers. The time averaged electrical power input to a system can be calculated by multiplying the instantaneous voltage by the current and integrating over a specific time period as shown below:

$$< \widehat{W}_{EL} >= -\frac{1}{T} \int V(t) \times I(t) dt, \tag{4.1}$$

where $V(t)$ and $I(t)$ are the input voltage and current which are supplied to the excitation source and can be evaluated by placing a resistor between the utilised circuit. Use of the power spectral density allows to model the signal in the frequency domain. For instance,

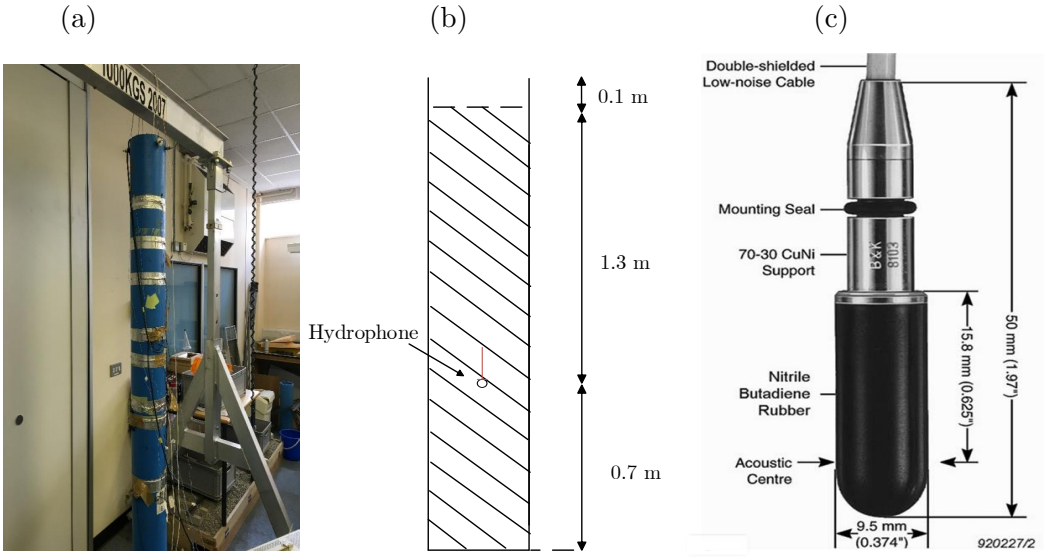

FIGURE 4.1: The pipe rig and the sensor position for measuring pressure transmission to the contained fluid. (a) The pipe is hung vertically from a jack. (b) Position of hydrophone and the level at which the pipe is filled with the water. (c) A picture of the Brüel and Kjær 8103 used to measure the fluid pressure.

if the driving voltage is random with spectral density G_{VV} and this voltage produces a current of G_{II} , then the input electrical power given by Eq. (4.1) becomes:

$$< \widehat{W}_{EL}/\text{Hz} >= Re\{G_{VI}(\omega)\}, \tag{4.2}$$

where G_{VI} is the one sided cross spectral density between the voltage and current. Results for the pressure transmitted to the fluid borne wave from the utilised electroacoustic devices were normalised with respect to the input electrical power of the exciter, with the aim of estimating the efficiency of each excitation source or configuration.

It can be seen from Eq. (4.2), that estimation of the electrical power can be achieved by recording the current and the applied voltage to an exciter. In view of changes to the driver impedance with frequency, a resistor box was placed between the amplifier and the exciter and the supplied current has been estimated by recording the voltage across the resistor box, V_2 as illustrated in Fig. 4.2. The input voltage to the driver,V_3, was recorded directly.

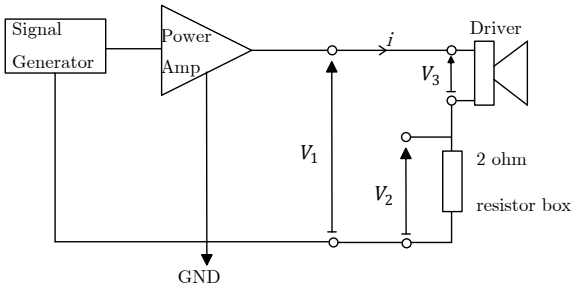

FIGURE 4.2: Circuit diagram for measuring electrical power.

4.2 Measurement with shaker excitation

In this section, three different configurations were tested using an electromagnetic shaker. In the first configuration, illustrated in Fig. 4.3 (a), the pipe shell was subjected to an axial structural excitation by mounting the shaker to an end plate, made of high density foam, followed by glueing the end plate to the top end of the pipe. In the second configuration, shown in Fig. 4.3 (b), structural excitation was applied radially at the top end of the pipe. This type of excitation can resemble the situation where a buried pipe is subjected to an axial structural excitation from a hydrant. In this case, normally the pipe has a 'L' or an inverse 'T' shape configuration. Applying axial excitations to the hydrant can be deemed as a radial excitation for the horizontal buried pipe. Finally, in the third configuration, the fluid was excited by attaching a light and rigid piston, obtained from composite honeycomb sandwich panel, to the shaker. To ensure that the water column was excited, the bottom part of honeycomb piston was submerged 1 cm in the water.

For each test, the shaker was driven with 16 linear chirps ranging from 10 Hz to 1000 Hz, each lasting 2 seconds. Signals were measured with a sampling frequency of 2.5 kHz and a low pass filter was set into the Prosig 8000 Data Acquisition System to avoid aliasing. Although the frequency range of interest for detection is between 10 Hz and 100 Hz, a larger frequency range was acquired for the sake of comparison of the different devices.

As shown in Fig. 4.4 , for the same electrical input, axial shell excitation delivers the least amount of pressure to the fluid borne wave. This is due to the small radial component of the axisymmetric shell borne wave to amplify the axisymmetric fluid borne wave. Using this type of source configuration transfers most of the energy to the pipe wall but it could be suitable for driving a fluid borne wave where there is a discontinuity such as

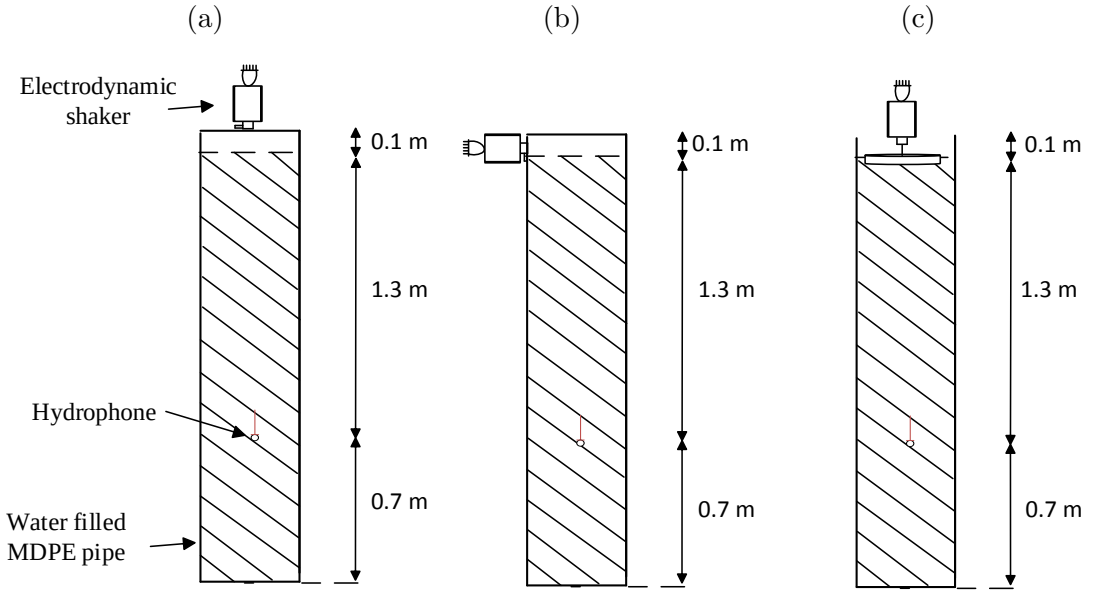

FIGURE 4.3: Pipe excitation arrangement using electromagnetic shaker. To increase energy transmission from the shaker to the pipe, the base of the shaker was clamped to a rigid support. (a) Axial excitation to the shell. (b) Radial excitation to the shell. (c) Direct fluid excitation.

a bend along the pipes. Direct fluid excitation is the most effective way to amplify the axisymmetric fluid borne wave as it directly drives the fluid and less energy flux into the shell. Radial excitation of the pipe wall will encourage flexural waves to effectively be propagated around the pipe circumference. Although flexural waves are not coupled to the fluid borne wave, the high radial displacement of the pipe wall at one side drove the fluid to higher amplitudes when compared to that of axial excitation.

4.3 Excitation with the underwater speaker

Measurements of the axisymmetric fluid borne wave pressure transmission were made by using a moving coil underwater loudspeaker 1932 type, manufactured by AQ sound, with a diameter of 110 mm. A cabinet was built, as is illustrated in Fig. 4.5, and sealed in the back to minimize rearward energy escape.

For comparison, the same location where the pipe was subjected to the shell excitation was selected to apply acoustic excitation. The underwater loudspeaker needs to be submerged to transfer energy to the fluid, so there is a small difference between the location where the shell excitation was applied in Section 4.2 and where excitation is applied here. Although the power transmission to the fluid borne wave is independent

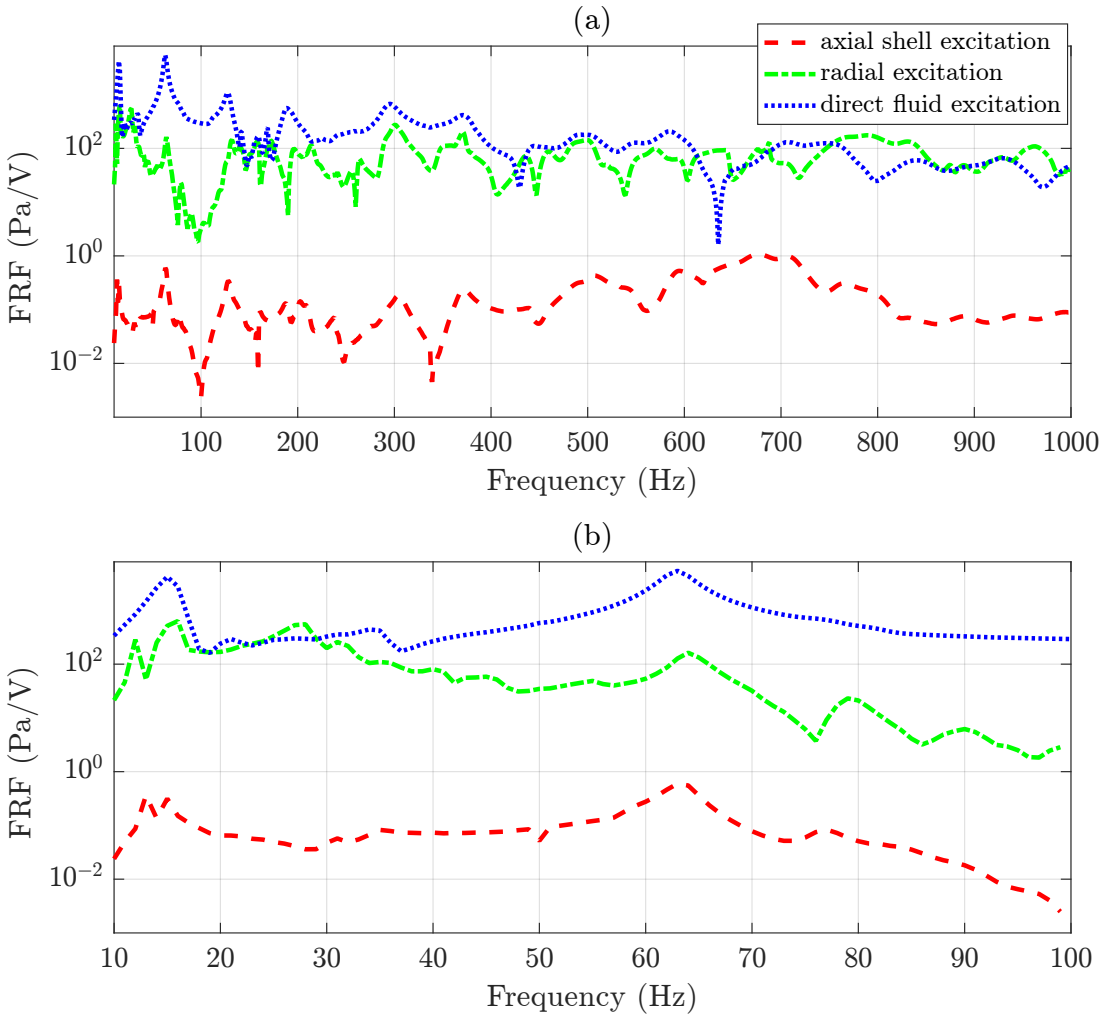

FIGURE 4.4: (a) FRF between the recorded pressure from hydrophone and the input voltage to the shaker, V_3, when the pipe subjected to axial shell excitation (- - -), radial shell excitation (-·-·), and the direct fluid excitation (·····). (b) Data at the desired frequency range 10 Hz - 100 Hz.

to the location of excitation, the pressure value changes with distance. The test rig for this measurement, the loudspeaker and its cabinet is illustrated in Fig. 4.6.

For each test, the loudspeaker was driven with a swept sine from 10 Hz to 1 kHz. The sampling frequency of the recorded signal here was 2.5 kHz, and a filter was built into the Prosig filtering above 1 kHz to prevent aliasing. Fig. 4.7 illustrates that the speaker with the cabinet slightly decreases pressure transmission over the frequency range of 10 Hz - 100 Hz, compared to without the cabinet.

In this measurement configuration, as shown in Fig. 4.6, the back of the speaker was near to the water surface. Therefore, a strong reflection at the boundary between the water and the air, due to the impedance mismatch of the two media, was expected.

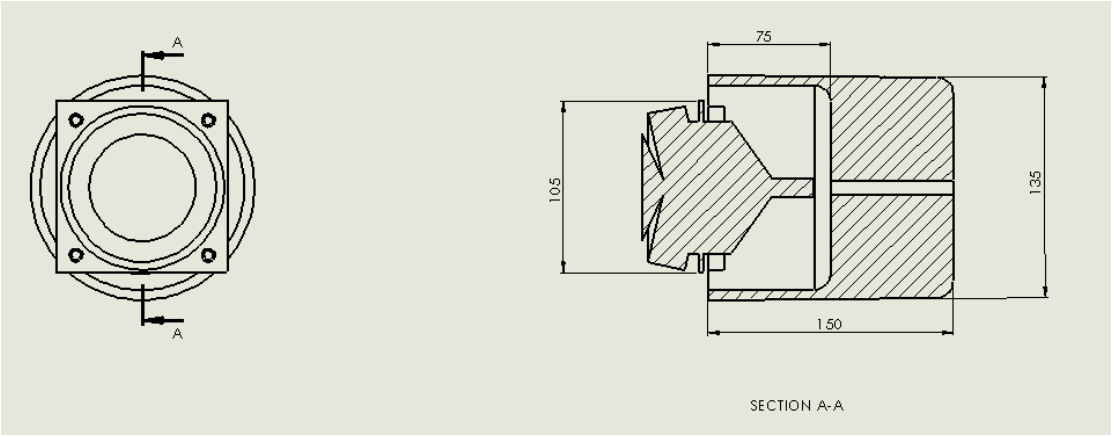

FIGURE 4.5: The dimension of the loudspeaker cabinet in millimetres.

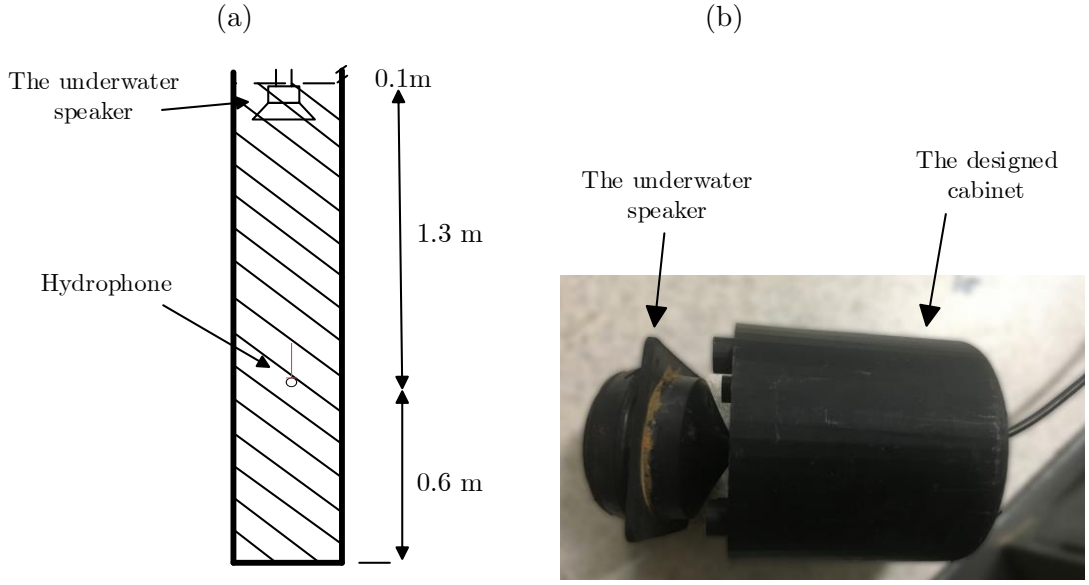

FIGURE 4.6: (a) The pipe configuration and location of source and sensors (b) The loudspeaker and its cabinet.

Since the speaker operates a dipole source, the reflected perturbation from the back of the speaker, becomes in phase with the signals emitted from its front. Hence, the reflected signals increase the transmitted pressure to the water column.

With the cabinet, the perturbation from the back of the speaker are passed, reflected and absorbed by the cabinet. The signal absorption and possibly lower reflected from the cabinet compared to the water surface leads to have a lower signal amplitude in PSD compared to the speaker without cabinet.

Effects of the cabinet to increase the radiation efficiency might become more obvious when the speaker is located at the middle of a long water filled pipe.

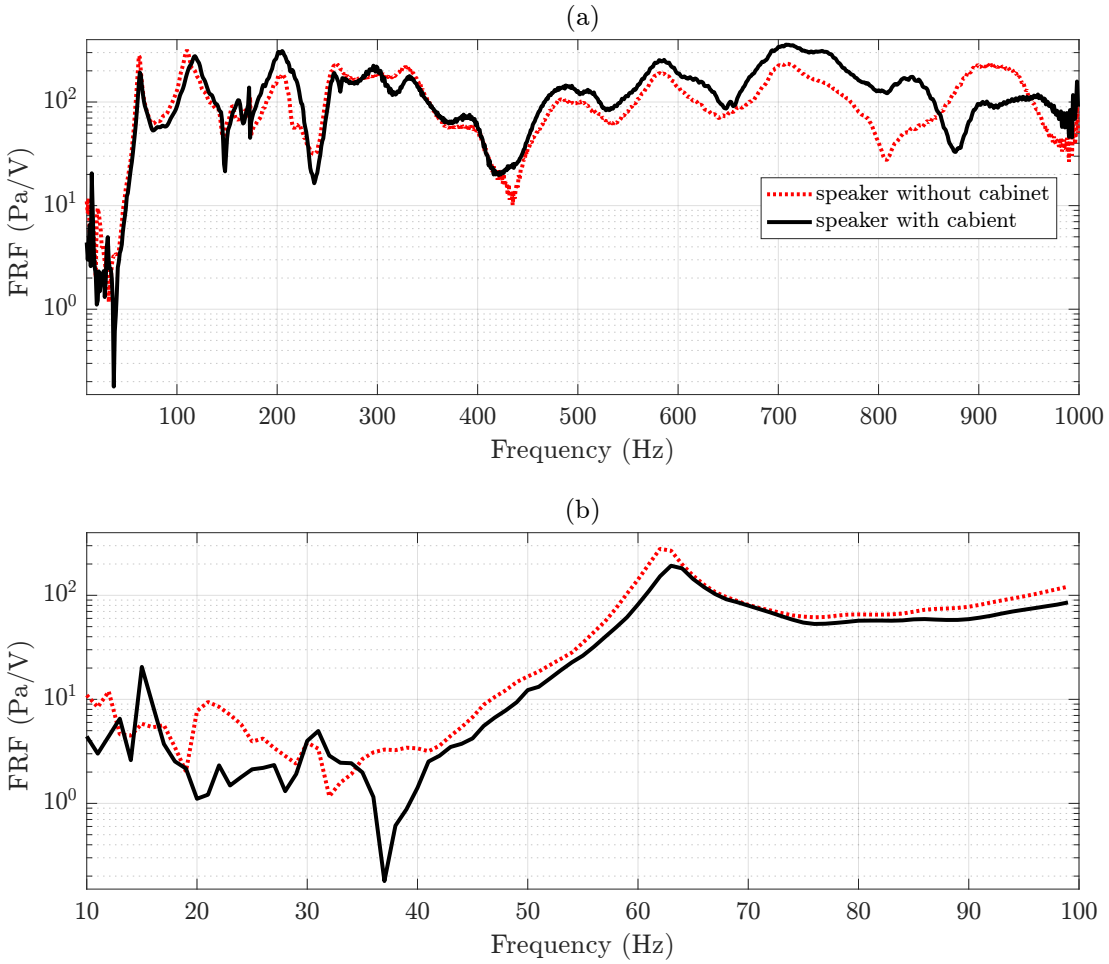

FIGURE 4.7: (a) FRF between the recorded pressure from hydrophone and the input voltage to the speaker, V_3. (b) The data at the desired frequency range 10 Hz - 100. The underwater speaker with (- - -) and without (——) the cabinet.

4.4 Discussion

Fig. 4.8 illustrates the results from all tests analysing the pressure wave transmission to the fluid borne wave using different sources and configurations. The fluid borne wave is derived with higher amplitudes when it was directly excited. Low amplitude pressure wave transmission to the fluid borne wave from the utilised electro acoustical sources below $<$ 100 Hz is due to their power handling limitation. Using a device with a higher power ramp does not guarantee a high amount of energy transmission to the fluid borne wave at low frequencies. Therefore, the following sections discuss alternative sources of excitation to generate high amplitude signal at the frequency bands of 10 - 100 Hz.

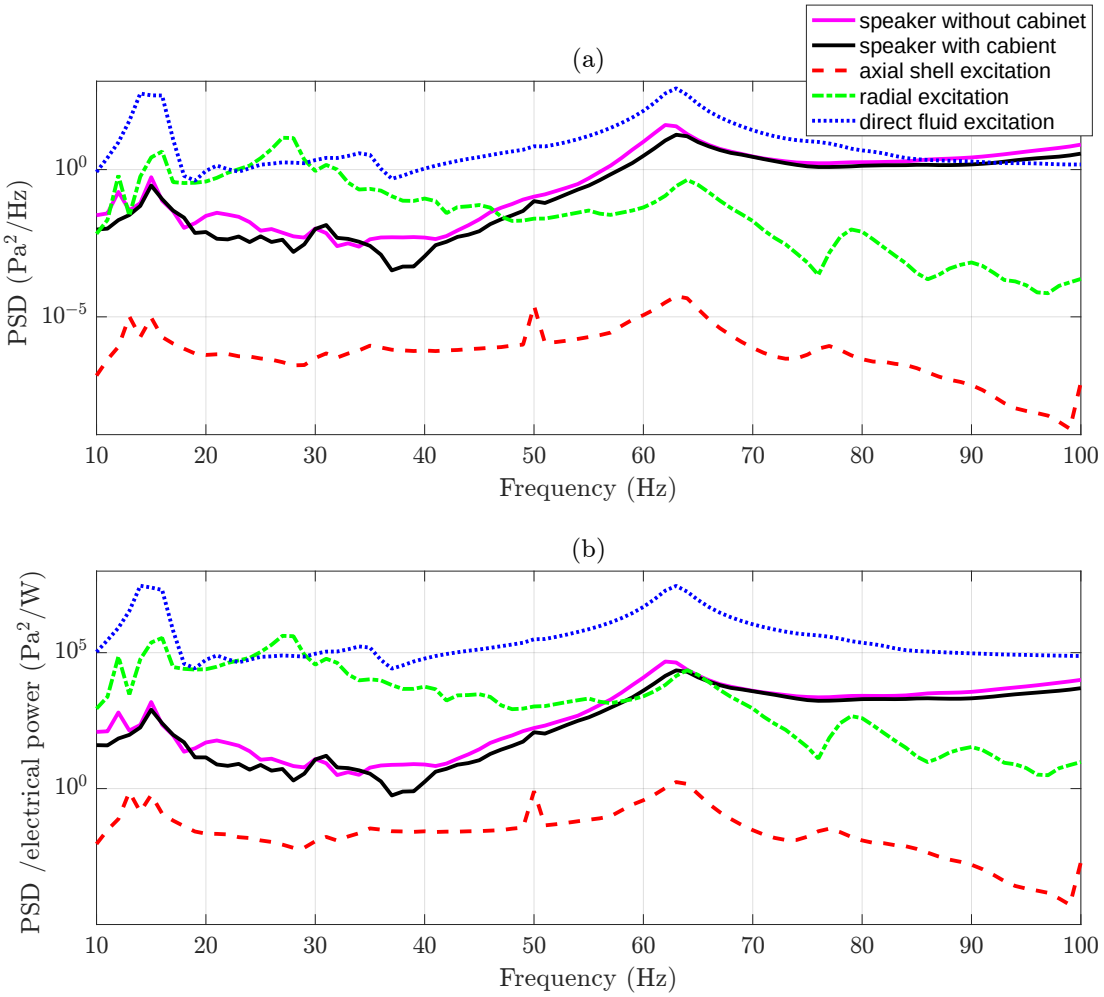

FIGURE 4.8: (a) PSDs of the recorded pressure from the hydrophone, obtained from different excitations and configuration. (b) Ratio between the PSDs and the input electrical power.

4.5 Design of the pneumatic devices

The design structure of the balloon gun and of the pipe water gun is explained in this section. Creating such devices mainly requires a mechanism able to release compressed air in a time and pressure controllable way. How the compressed air is then drained of the device from an outlet is also of prime importance.

4.5.1 Working principle

A pressure regulator was attached to an air compressor device to control the pressure of the released compressed air. To control the release time of the compressed air from the pressure regulator a three port solenoid valve was connected to the pressure regulator

and controlled with an Arduino. The Arduino acted as a time controller and specifies the time at which the valve opens and closes. Despite this, it was found that the opening time of the valve could vary up to 0.5 ms due to the mechanical variation in the opening and closing mechanisms of the valve. In view of such variances, a reference signal can be established by wrapping a polyvinylidene fluoride (PVDF) film, discussed in detail in Section 4.5.2, around the hosepipe near to the output port of the solenoid valve. A schematic of each pneumatic device is illustrated in Fig. 4.9. The utilised valve is normally closed (see Fig. 4.9 (a)) and it operates within the required pressure range. A reinforced pressure hosepipe was connected to the output port of the solenoid valve to transfer compressed air from the valve to the inside of the reinforced pipe. In the case of a pipe water gun the end of the hosepipe ends possesses a metal orifice with a calibrated hole, as shown in Fig. 4.10. In the case of a balloon gun a rubber balloon is wrapped around the orifice. A party balloon, made of rubber with a nominal diameter of 30 cm was used. When the balloon is not inflated its thickness is about 0.5 mm. In light of much higher balloon capacity compared to the volume of the transferred compressed air, it is very unlikely to have a burst. In the case of the balloon gun, when the valve is opened the compressed air goes into the balloon and expands it. When the valve is closed the third port of the valve acts as an output port and it drains the trapped air in the balloon. In the case of the pipe water gun the hosepipe is submerged and the water fills it. When the valve is opened the compressed air pushes the penetrated water out of the orifice and generate the required pulsation into the water filled pipe. Since most of the buried water pipes are buried at a depth of 1 to 1.25 m, this type of excitation source has a potential to be used and create the required pressure wave into the fluid.

The opening time of the valve can vary by 0.05 ms due to the mechanical variation in the opening and closing mechanisms of the valve. Because of this difference, a reference signal was established by wrapping a PVDF sensor with eleven turns around the hosepipe connected to the output port of the solenoid valve. Providing such a reference signal, discussed in the next section, can be suitable when the device is utilised for the detection of buried water pipes. Hence, the next section discusses on the calibration of a PVDF sensor.

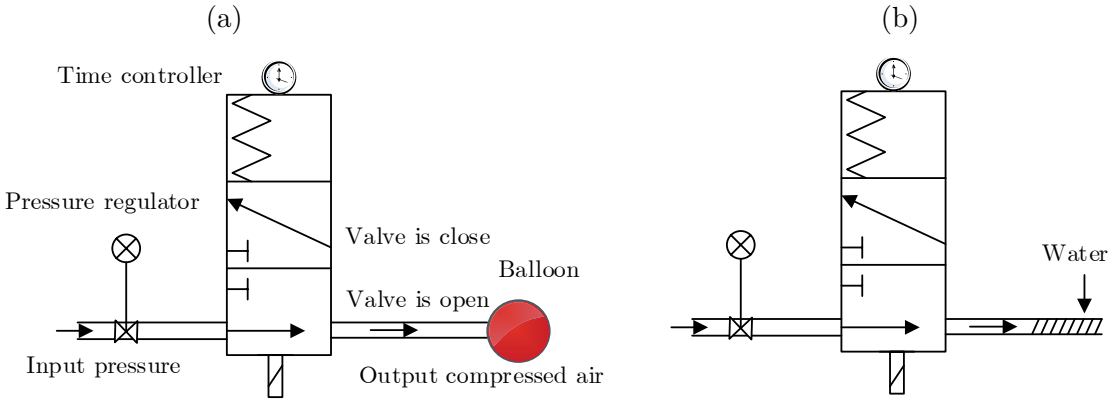

FIGURE 4.9: The diagrams of the developed pneumatic devices: balloon gun (a) and pipe water gun (b) configurations.

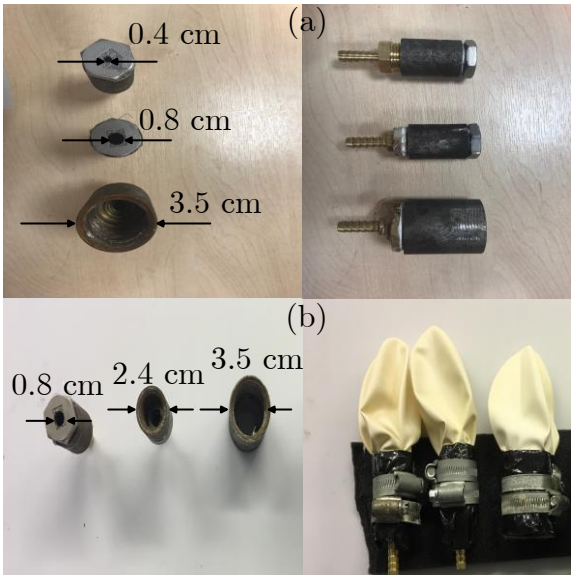

FIGURE 4.10: A picture of the end connections attached to the reinforce exhaust outlet. (a) The three different tips used for the water gun, showing the difference between their orifice diameters. (b) The three tips used for the balloon gun.

4.5.2 Sensitivity of the reference PVDF sensor on a flexible hose pipe

Analysis of PVDF sensors when bounded to a plate and shell are fully explained in references [41] and [79] respectively. The elongation of these sensors, when they are wrapped an integer number of times around the pipe circumference, is given by [63]:

$$\text{extn} = 2\pi N \frac{a_{\max}}{a} W, \tag{4.3}$$

where N, a and $a_{\max}$ are the number of loops of the PVDF wires around pipe circumference, the mean value and the outer pipe wall radius respectively. The W term is the axisymmetric displacement of the pipe wall. The results from [41] and [79] show that these sensors are sensitive in all directions of applied stress; however, they possess greater sensitivity along their length. Thus, the output charge from the PVDF wire is mainly dependent on their longitudinal extension and is given by [63]:

$$q_p = \text{extn}.S_m, \tag{4.4}$$

where S_m is the charge sensitivity of PVDF wires in pC/m, evaluated in this survey. As an alternative, it is possible to find the charge sensitivity in pC/Pa rather than pC/m. The relationship between the acoustic pressure due to the axisymmetric fluid borne wave P_1 and axisymmetric displacement of the pipe wall in the radial direction W_1 is given by [63]

$$W_1 = \frac{P_1 a^2}{hE}\left[\frac{1}{1-\Omega^2/(1-v_p^2)}\right]. \tag{4.5}$$

All the parameters have been previously explained, when used in Eq. (2.18). Substituting Eq. (4.5) into Eq. (4.3) and rearrange it, gives the charge sensitivity, S_p, with sensitivity in pC/Pa as:

$$S_p = \frac{2\pi N a_{\max} a}{Eh}\left[\frac{1}{1-\Omega^2/(1-v_p^2)}\right]. \tag{4.6}$$

As seen from Eq. (4.5) the pressure sensitivity of PVDF wires vary depending upon the length of wires, geometrical and material properties of pipe.

In this measurement it is assumed that the output pressure from the hydrophone sensor exhibits the correct value of the axisymmetric acoustic pressure, and works in accordance with the charge sensitivity given in its calibration sheet. Therefore, to calibrate the PVDF sensors, via the hydrophones data, these two sensors are positioned at the same location along the pipe as depicted in Fig. 4.11 and excitation has been induced in the fluid via an underwater speaker.

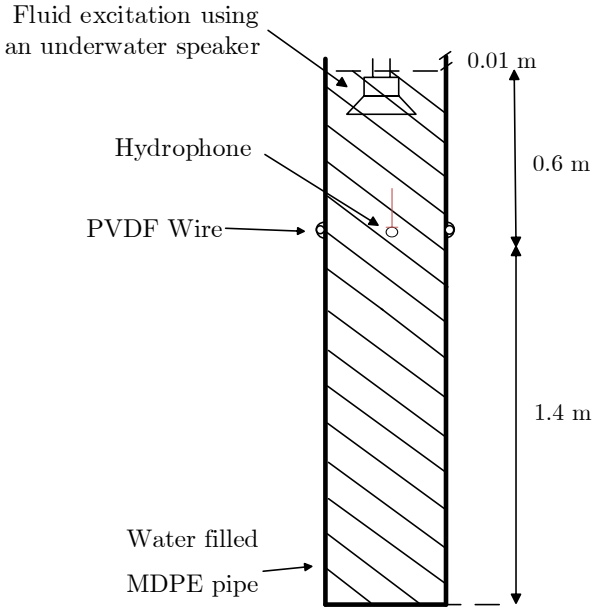

FIGURE 4.11: Experiment configuration used for the calibration of the PVDF sensor using the measured acoustic pressure via hydrophone.

The excitation signal was a sweep sine with a frequency range between 10 Hz and 1kHz and recorded with a sampling frequency of 2.5 kHz. A low pass filter was built into the acquisition system, filtering signals above 1kHz so as to avoid aliasing.

The initial charge sensitivity of the PVDF was set up for 1 pC/m. By dividing the pressure measured via the hydrophone and the pressure measured via the PVDF wires, Eq. (4.8), and the data given in Table 3.1, the sensitivity of the transducer can be estimated, as illustrated in Fig. 4.12 (a). The obtained sensitivity is in agreement with the specification supplied by the manufacture.

Wrapping the PVDF sensors around the circumference of flexible pipes, however, adds stiffness to the pipe wall and Eq. (4.5) will no longer reveal the true value of the contained fluid pressure. For the flexible pipe, the relationship between the pressure and the radial displacement of the pipe shown in Eq. (4.5) is converted to [80]:

$$W_1 = P_1 \left(\frac{a^2}{h_p E_p} + \frac{a^2}{h_w E_w} \right) \left[\frac{1}{1 - \Omega^2/(1 - v^2)} \right]. \tag{4.7}$$

Assuming that the wire thickness is small compared to the pipe radius, substituting Eq. (4.7) into Eq. (4.3) and rearranging provides that the modified pressure sensitivity, S_{mode}, is given by [80]:

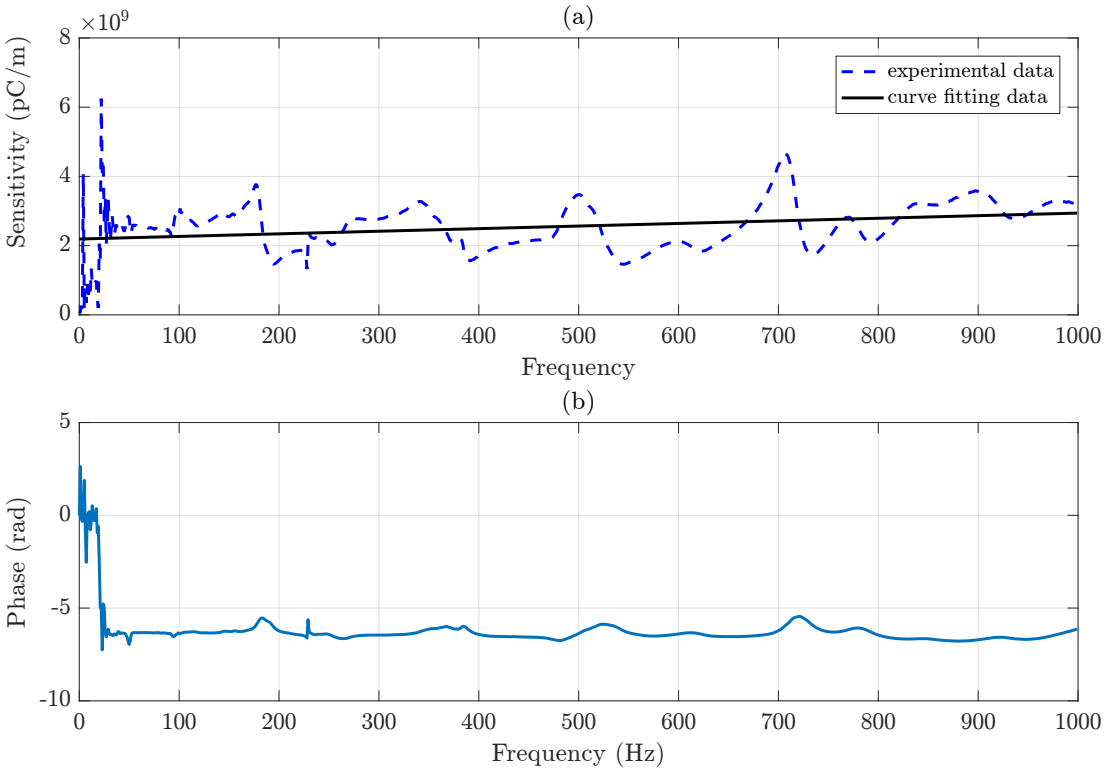

FIGURE 4.12: Comparison of the FRF of the pressure measured via PVDF wires and hydrophone with respect to the voltage sent into the speaker between 10 Hz - 1000 Hz. (a) FRF ratio of the two transducers, exhibits the sensitivity of the PVDF wire in pC/m. (b) Phase lag between the two transducers.

$$S_{\text{mode}} = \frac{S_p}{1 + \dfrac{h_w E_w}{hE}\left(\dfrac{a}{a + \dfrac{h + h_w}{2}}\right)^2}. \tag{4.8}$$

The pressure sensitivity of the reference PVDF sensor, using Eq. (4.8), for eleven turns of the PVDF sensors around the pipe circumference, is evaluated approximately 0.4 pC/Pa. The parameter, which was used to evaluate the pressure sensitivity of the PVDF wires for this measurement is illustrated in Table 4.1.

The standard deviation, presented in Table 4.1 implies slight differences between the measured pressures from the two transducers.

TABLE 4.1: Properties of PVDF wire and the flexible hosepipe used to calculate the pressure sensitivity of the PVDF wire wrapped around the circumference of the flexible hosepipe.

	Mean radius (m)	Wall thickness	Young's modulus (GPa)
Flexible pipe	6.5×10^{-3} (a)	2.5×10^{-3} (h)	0.2 (E)
PVDF charge sensitivity			
2.35×10^{8} pC/extn	7.25×10^{-4} (a_w)	2.5×10^{-3} (h_w)	1.45×10^{-3} (E_w)

4.5.3 Parametric study

In this section experimental studies were undertaken on the rig shown in Fig. 4.1, in order to characterise the performance of the developed devices. The fluid pressure was measured via the hydrophone at 1.3 m from the water surface. For the both devices, an initial measurement was carried out by adjusting the pressure regulator to release a pressure of 3 bar, and the valve was set to open for 20 ms and close for 4.98 seconds. The signals were acquired for a time duration of 80 seconds, using 16 firings from the valve, at a sampling rate of 2.5 kHz. A low pass filter with a cut-off frequency at 1 kHz was used to avoid aliasing. To fill the reinforced exhaust with the water, the last 20 cm of it was placed like a coil and submerged to the water at the top of the pipe. Following this, further experimental work has been performed to investigate the effect of changes on the generated acoustic wave into the water filled pipe to some parameter such as increasing the compressed air pressure and release time as well as the size of outlet orifice. A picture of the orifices attached to the end of reinforce exhaust is illustrated in Fig. 4.10. The PSDs of the transmitted pressure obtained by the balloon gun from changing the aforementioned parameters are plotted in Fig. 4.13. Due to high changes to the value of the PSD at low and high frequencies it is difficult to discuss on the result by looking at Fig. 4.13 (a). Since the low frequency region is of the interest, it was decided to plot the data between 10 -100 Hz in Fig. 4.13 (b). As illustrated from Fig. 4.13 (b), by doubling the pressure of the compressed air, the PSD of the recorded signal increases approximately 6 dB. Increasing the release time or changing the diameter of the orifice seem to have minor effects on the generated signal compared to its initial setup.

A similar procedure was followed for the pipe water gun and the results are plotted in Fig. 4.14. Similar to the obtained data from the balloon, a rapid change to the value of the PSDs from low to high frequencies makes it difficult to discuss on the result by

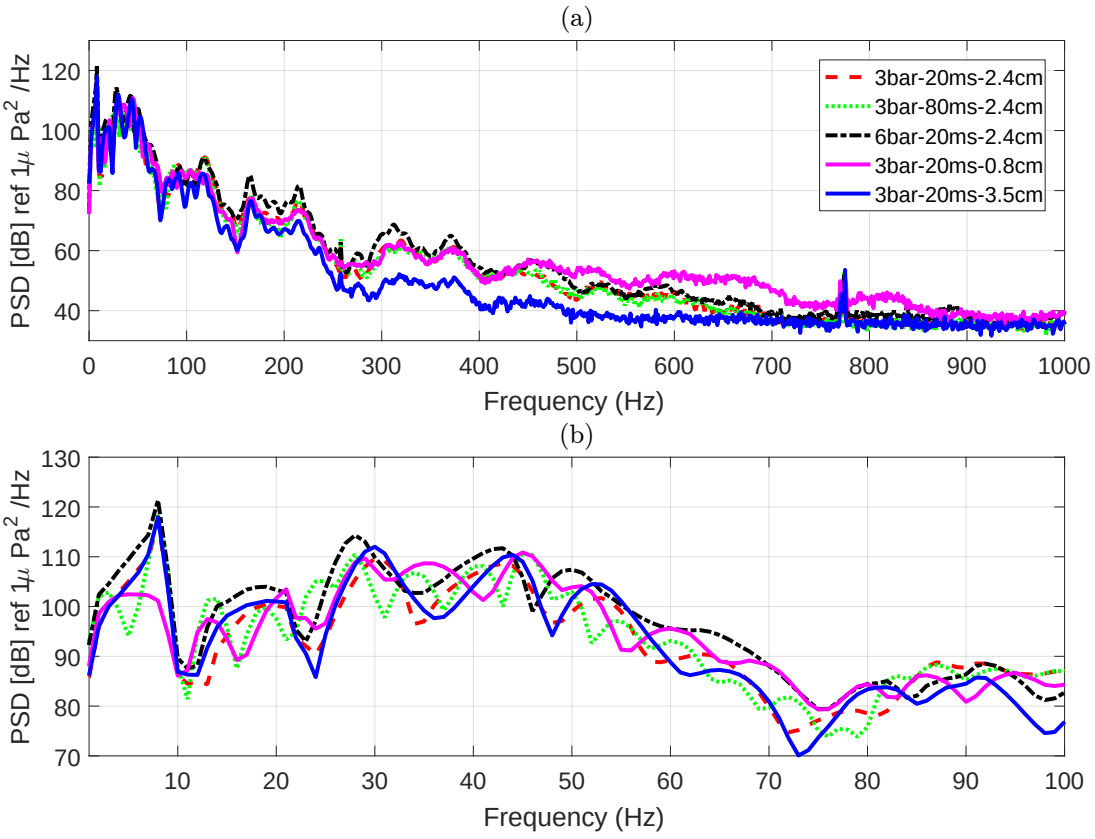

FIGURE 4.13: PSDs of the water pressure generated by the pipe balloon gun. (- - -): Compressed air supplied at 3 bar for 20 ms duration with a 2.4 cm diameter orifice. (·····): Time of the release increased to 80 ms. (-·-·): Pressure increased to 6 Pa. (——): orifice diameter reduced to 0.8 cm and (-.-): increased to 3.5 cm.

looking at Fig. 4.14 (a), therefore, the results are replotted in the frequency range of interest in Fig. 4.14 (b). As shown in Fig. 4.14 (b), a considerable change to the values of the PSDs were observed by increasing the size of the orifice from 0.4 cm to 0.8 cm and 3.5 cm. In this case, the PSD amplitude increased 10 dB at 20 Hz-75 Hz and 6 dB from 75 Hz-100 Hz, when the orifice diameter increased to 3.5 cm. Changes to the time duration seems to have no considerable effect on the obtained data, while doubling the pressure of the compressed air increased the PSD value by 12 dB, from 50 Hz to 100 Hz.

4.5.4 Comparison

In this section a comparison between the obtained data from the two pneumatic devices and the results from the loudspeaker is made. As shakers cannot be inserted into the buried water pipes and generate an in-pipe excitation along the pipe, its data excluded in this section. The PSDs of the measured pressure from the two pneumatic devices

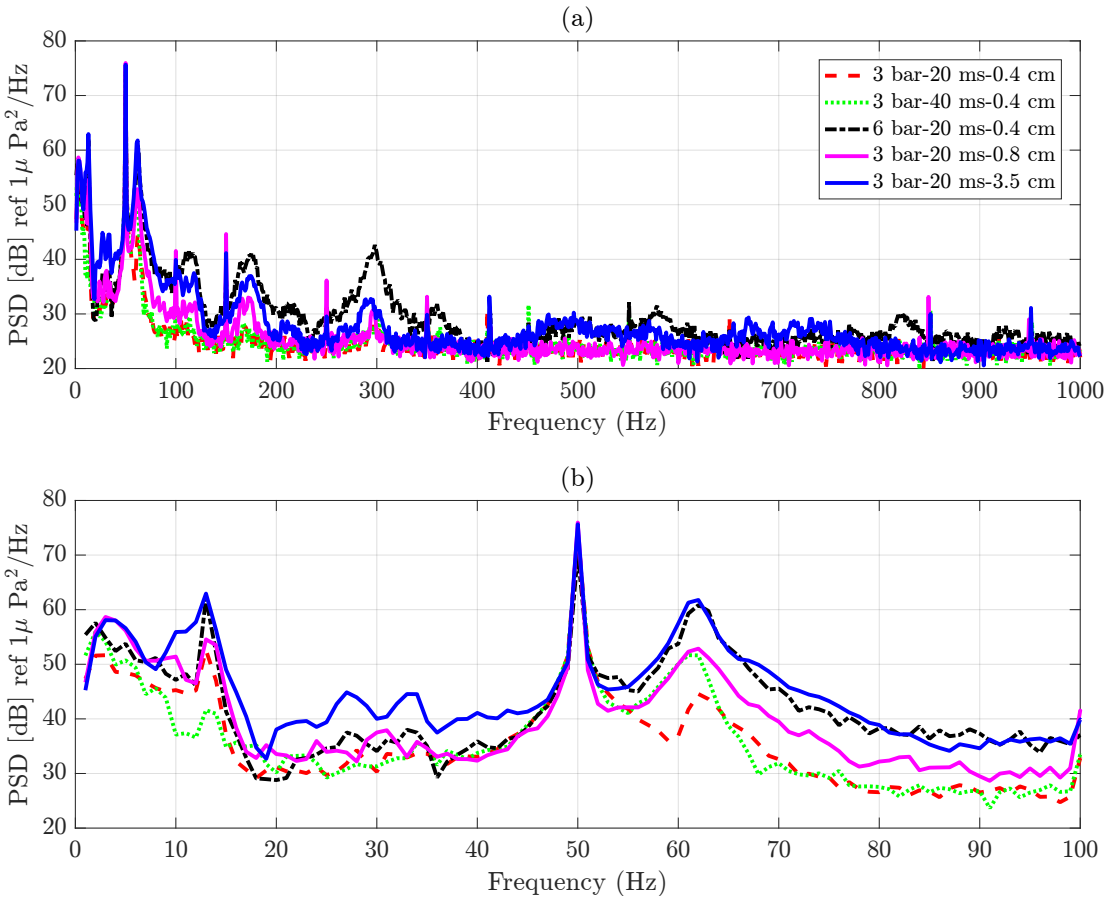

FIGURE 4.14: PSDs of the water pressure generated by the pipe water gun. (- - -): Compressed air supplied at 3 bar for 20 ms duration with a 0.4 cm diameter orifice. (·····): Time of the release increased to 40 ms. (-·-·): Pressure increased to 6 Pa. (——): orifice diameter increased to 0.8 cm and (-.-): 3.5 cm.

with a pressure of 3 Pa, release time of 20 ms and orifice diameter of 0.8 cm, plotted in Figs. 4.13 and 4.14, are compared to the results from the loudspeaker with the cabinet, illustrated in Fig. 4.7, and replotted for convenience in Fig. 4.15. As illustrated in Fig. 4.15, using the balloon gun as the excitation source will drive the fluid more strongly, approximately 20 dB higher in PSD amplitude, compared to the pipe water gun. Since the number of chirp signal used for the loudspeaker was equal to the number of pulsations made from the pneumatic devices, it might be fair to compare their results to one another. Although lower value of the signal was obtained from the loudspeaker at frequencies up to approximately 100 Hz, it can drive the fluid with higher amplitude afterward. One might claim that amplifying the signal through the power amplifier will cause to generate a higher pressure wave from the loudspeaker into the fluid. It should be noted that the maximum power at which the loudspeaker can operate is 20 watt. In the loudspeaker measurement, the maximum current that passed through the resistor

box was 0.4 ohms. Assuming that the resistance of the loudspeaker is constant and is 8 ohms, the loudspeaker can approximately perform 24 dB better at the best. This, however, does not mean that the data at the frequencies below 100 Hz also benefit from such improvement. It is worth to note that the developed device has potential to be used within smaller pipes down to 1 cm and are the most cost-effective devices that can be utilised for the pipe detection.

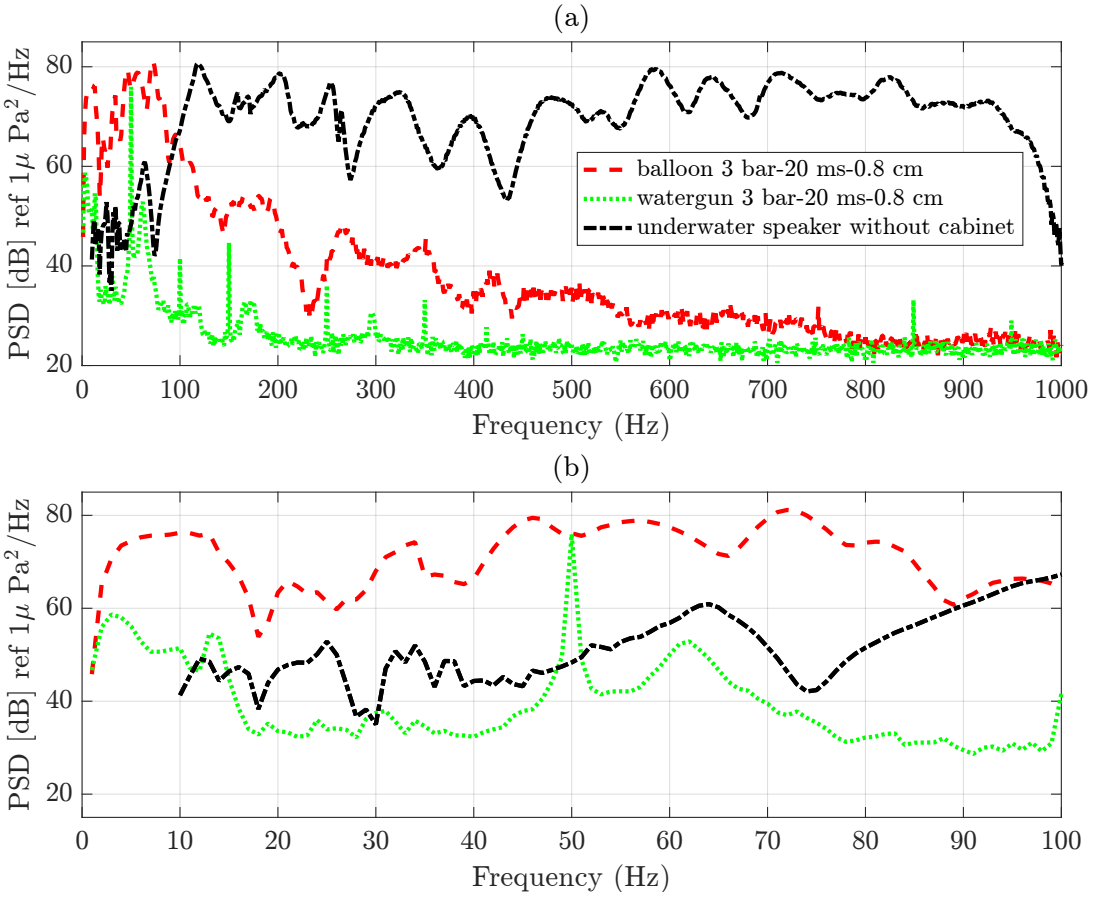

FIGURE 4.15: PSDs of the water pressure in logarithmic scale, generated by the balloon gun (- - -) and by the pipe water gun (·····) with a pressure of 3 Pa, release time of 20 ms and orifice diameter of 0.8 cm; and PSD of the water pressure obtained from the loudspeaker (-·--·).

4.6 Pressure loss along the reinforced exhaust

As the compressed air flows through the reinforced exhaust its pressure drops with respect to the material properties and length of the exhaust. To illustrate the pressure drop of the outgoing gas flow, a test with a 2 m reinforced exhaust was conducted to excite the fluid pipe and repeated when the exhaust length was increased to 15 m. For

the both tests the pressure regulator was adjusted to a release pressure of 3 bar, and the valve was set to open for 20 ms and close for 4.98 seconds.

The water filled pipe configuration and the hydrophone location is the same as the one illustrated in Fig. 4.1. Although the focus of this chapter is centred on the performance of the developed pneumatic sources, here the third port of the solenoid valve, discussed in Fig. 4.9, was closed and the device was acting as a pipe air gun. Because we are interested on the reduction to fluid pressure due to the drop pressure along the exhaust this is a reasonable test to perform.

The PSDs of the output signals of the hydrophone from the two repeated test, using the pipe air gun are illustrated in Fig. 4.16. With using longer exhaust, the peaks and the depths location in the PSD is changed. By calculating the difference between the peaks and the depths which occurred at approximately same frequency it is founded that the PSD amplitude reduced 360 times, meaning that by increasing the exhaust length by one meter the PSD amplitude reduces 48 Pa^2/Hz.

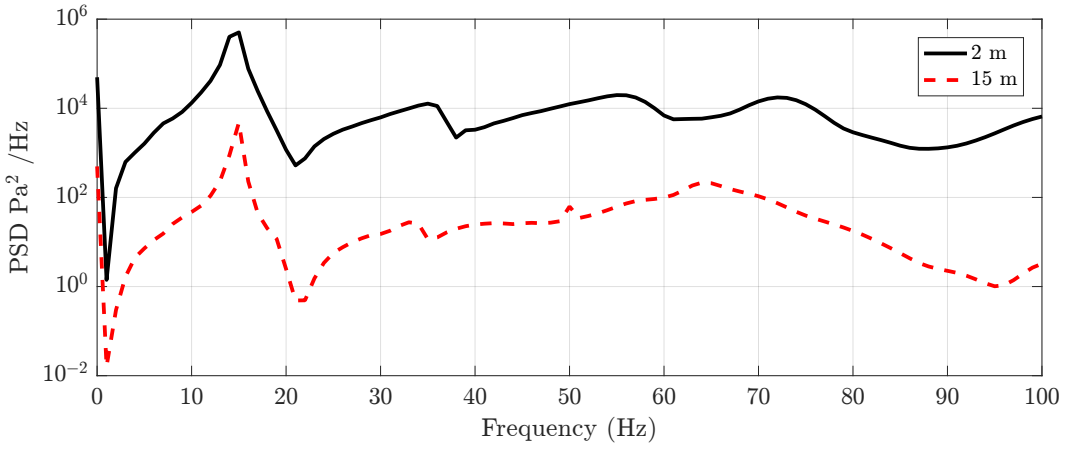

FIGURE 4.16: (a) Recording data from the hydrophone resulted from the air-gun excitation, (——) 2 m and (- - -) 15 m.

4.7 Analytical simulation for the balloon gun and water gun

This section aims to provide a theoretical explanation of the acoustic signature generated by each pneumatic source. The model for each source, illustrated in Fig. 4.17 has three

components: 1- compressed air discharging from the air compressor 2- dynamics and 3- pressure perturbations.

The first component of the model, the rate of gas flow from the air compressor toward the reinforced exhaust, is assumed to be identical for each source. On the contrary, the other two components of the model are relatively different for each source. Hence, different approaches under a number of assumptions are followed to describe them.

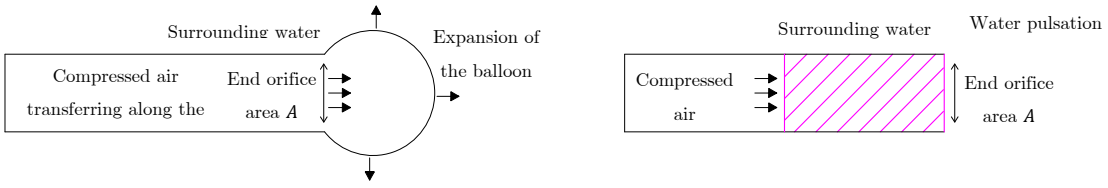

FIGURE 4.17: Schematic of the balloon gun and the water gun. The discharged compressed air is the source of energy which causes an inflation-deflation and a shuttle motion to the balloon and water gun receptively.

Because of buoyancy, the inflated balloon moves toward the water surface. Likewise, an intense discharging of the water from the reinforced exhaust, pushes the end orifice opposite to the direction of discharging. The buoyancy effect might become important in marine exploration, for example, the reduction to the hydrostatic pressure changes the bubble oscillation periods and its emitted pressure wave field. In this simulation, the effect of such a phenomenon on the wave perturbation from each source is discarded and it is assumed that (1) the process of compressed air discharging and draining is very quick and (2) the end connector, illustrated in Fig. 4.10 is weighty enough to resist the movement.

4.7.1 Outgoing compressed air flow

The rate of mass discharging from the air compressor port to the exhaust, $\frac{dq_{\text{out}}}{dt}$, can be expressed by:

$$\frac{dq_{\text{out}}}{dt} = \begin{cases} \sqrt{\frac{\gamma}{R_g}}\left(\frac{\gamma+1}{2}\right)^{(\gamma+1)/2(\gamma-1)} \frac{p_{pn}}{\sqrt{T}} A_t \sqrt{1-\left(\frac{(P_e/p_{pn})-b_c}{1-b_c}\right)^2} & \text{for subsonic flow,} \\ \sqrt{\frac{\gamma}{R_g}}\left(\frac{\gamma+1}{2}\right)^{(\gamma+1)/2(\gamma-1)} \frac{p_{pn}}{\sqrt{T}} A_t & \text{for supersonic flow,} \end{cases} \tag{4.9}$$

where γ, R_g, T and A_t are the ratio of heat capacity, specific gas constant, temperature of the air compressor gas and the cross section area of the nozzle throat respectively. The p_{pn}, p_e and b_c terms are the released compressed air pressure, pressure inside the exhaust and the critical pressure ratio of the gas in the compressor port respectively.

When $\frac{p_e}{p_{pn}} < b_c$ the outgoing gas flow is supersonic and vice versa. For convergence-divergence nozzles, b_c, is given by:

$$b_c = \left(1 + \frac{\gamma - 1}{2} M_e^2\right), \tag{4.10}$$

where M_e is the nozzle Mach number and needs to be calculated from:

$$\frac{A_e}{A_t} = \frac{1}{M_e} \left(\frac{2}{\gamma + 1}\right)^{(\gamma+1)/2(\gamma-1)} \left(1 + \frac{\gamma - 1}{2} M_e^2\right)^{(\gamma+1)/2(\gamma-1)}. \tag{4.11}$$

In the above equation A_e is the cross sectional area of the nozzle outlet. Provided that the flow is subsonic, the p_e parameter in Eq. (4.9) should be estimated by the pressure at the valve outlet, which is linked to the source dynamics.

As illustrated in Eq. (4.9) rate of mass flow from the air compressor to the exhaust is a function of the valve's inlet and outlet port size, its opening time as well as the inlet and the outlet (ambient) pressure. To connect the valve to the pressure regulator and the air compressor device, snap couplings and snap adopters with the port and nozzle dimension of 2.5 cm and 5 mm in diameter respectively, are used. The solenoid valve orifice size was 2.2 mm in diameter as well. Therefore, in this simulation it is assumed that the outlet and the throat port are equivalent to the solenoid valve orifice and the pressure regulator port dimension respectively. The other parameters that are used to estimate the rate of outgoing mass flow, is illustrated in the following table.

TABLE 4.2: Parameters used to calculate the volume of the compressed air flow through the orifice of the valve.

Parameter	value	Parameter	value	Parameter	value
R_g	287.06 J/kgK	γ	1.4	P_{pn}	3 $\times 10^5$ Pa
A_e	3.8 10^{-6} m^2	T	273+ 25 K	t	30 ms
A_t	2 10^{-5} m^2	P_e	101325 Pa		

The value of air transmission to the fluid was estimated by substituting the parameters illustrated in Table 4.2 into Eqs. 4.11, 4.10 and 4.9, and is evaluated to be 9×10^{-4} m^3.

The compressed air is discharged from the chamber in tens of milliseconds followed by draining it in the same amount of time. Thus, a Gaussian pulse can be used to represent the volumetric compressed air flow into and discharge from the end orifice as follows:

$$s(t) = Se^{-\frac{t^2}{\sigma^2}}, \tag{4.12}$$

where S is the source amplitude and σ determines the width. The source amplitude is normalised to make its peak to be equivalent to the total discharge compressed air volume from the valve.

4.7.2 Balloon dynamics

In this section, the balloon dynamic is described by the Gilmore equation that is widely used for modelling the air guns signatures. Gilmore described the bubble dynamics by [81]:

$$R\ddot{R}\left(1-\frac{\dot{R}}{c_1}\right)+\frac{3}{2}\dot{R}^2\left(1-\frac{\dot{R}}{3c_1}\right)=H_{an}\left(1+\frac{\dot{R}}{c_1}\right)+\frac{R\dot{H_{an}}}{c_1}\left(1-\frac{\dot{R}}{c_1}\right), \tag{4.13}$$

where $R, \dot{R} = dR/dt$ and $\ddot{R} = d^2R/dt^2$ are the bubble radius, first and second derivative of the bubble's radius in time respectively. The c_1 term is the fluid wave speed, explained in Eq. (2.6). The H_{an} and $\dot{H_{an}}$ terms are the enthalpy difference and its derivative respectively. The enthalpy difference can be expressed by [81]:

$$H_{an} = n_b\left(\frac{p_\infty + B_b}{(n_b-1)\rho_f}\right)\left[\left(\frac{p+B_b}{(p_\infty+B_b)}\right)^{(n_b-1)/n_b}-1\right], \tag{4.14}$$

where B_b and n_b are constants: n_b= 7 and B_b = 304 MPa for water. The compressed air pressure inside the bubbles p and the ambient pressure p_∞ can be expressed by [81]:

$$p = \frac{mR_GT}{V} + p_v - \frac{2\sigma}{R} - \frac{4\mu\dot{R}}{R}, p_\infty = p_0 + \rho_\infty g h_b. \tag{4.15}$$

Here p_v, σ, μ and h_b are the vapour pressure, surface tension,the water viscosity term and the depth at which the balloon is located.

There are two fundamental differences between the approach followed in this section and the Gilmore equation.

(i) In the seismic air gun modelling, a constant compressed air volume and consequently a constant radius is assumed while in the balloon gun, the balloon undergoes a rapid inflation/deflation. Parametrizing the radius with a Gaussian pulse shape whilst resembles the situation that balloon gun drives its surrounding fluid, it causes singularity to Eq. (4.13) when $R(t) = 0$. Therefore, it was decided to parametrise such a procedure into the pressure emission from the valve. The relation between the air pressure P_{air} and its volume V_{air} is given by:

$$P_{\text{air}} = \frac{n_{\text{air}} R_g T_{\text{air}}}{V_{\text{air}}}, \tag{4.16}$$

where T_{air} and n_{air} are the temperature and the number of moles of compressed air. In the balloon gun, the pressure is constant while its volume change. Nevertheless, in this simulation it is assumed that the volume is constant and the pressure change in accordance with Eq. (4.12). Accordingly, the source amplitude is normalised to make its peak to be equivalent to the maximum pressure of discharging compressed air.

(ii) For modelling the air gun signature, the discharged compressed air is surrounded by water. In this study, similar phenomenon is under investigation, however, the compressed air is surrounded by a flexible membrane. To include this effect, the surface tension term is specified in accordance with the balloon surface tension. The balloon surface tension has not measured by the author. The surface tension of a similar balloon to the one used in this study was measured in reference [82]. The results indicated that the balloon surface tension changes rapidly, from 40 N/m to 50 N/m when its circumference changes from 0 cm (deflated balloon) to 30 cm. For the balloon gun source, the balloon undergoes a rapid inflation/deflation, with the maximum circumference of approximately 6 cm. Therefore, the surface tension is allowed to change rapidly from zero to 42 N/m and from 42 N/m to zero. The time variant of the balloon surface tension is assumed linearly changes with time.

4.7.3 Acoustic wave perturbation from balloon gun

The acoustic wave emission from the balloon gun is expressed via a similar formula that used to describe the air gun signature, expressed by Keller and Kolodner [83]. The difference between the formula presented in this section and the one used to describe the air gun signature is that the pressure perturbation in the water filled pipe contains no geometrical loss. Hence the pressure wave emission to the pipe can be explained by:

$$\Delta p(t,r) = \rho_{Fl}\left[\frac{\ddot{V}_b}{4\pi} - \frac{\dot{V}_b^2}{32\pi^2}\right], \tag{4.17}$$

where $\dot{V} = dV/dt$ and $\ddot{V} = d^2V/dt^2$ are the first and second derivative of the assumed spherical shape with respect to time respectively.

4.7.4 Balloon gun results

In light of pressure drop along the exhaust, discussed in Section 4.6, the pressure value, at the desired point along the pipe is estimated using Eq. B.5. The reflection coefficient of the pipe end is assumed -1. The reflection coefficient is normally a complex number, changes with respect to the material properties of the pipe end and frequency, which could be estimated from the data plotted in Fig. (3.9). The PSD of the pressure at location 1.3 distance from the top end of the pipe is then estimated and plotted in Fig. 4.18 against the experimental measurement when the pressure, opening time and orifice diameter were set to 3 bar-20 ms-0.8 cm respectively.

The high amplitude pressure perturbation in the fluid at frequencies 20- 40 Hz could be due to the interaction of the reflected pressure wave and the balloon oscillation, which is not included in the analytical simulation. The higher amplitude of the analytical simulation compared to the experimental data at frequencies above approximately 250 Hz could be due to the further reduction to the water filled pipe reflection coefficient, compared to the one assumed in the analytical simulation.

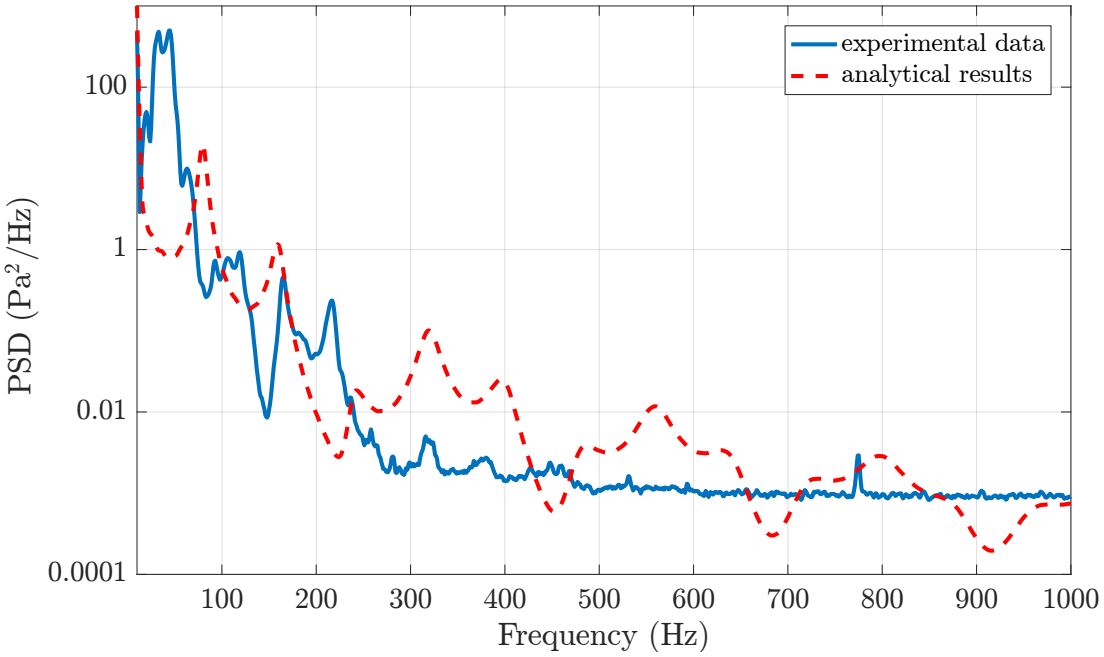

FIGURE 4.18: PSDs of the pressure at a 1.3 m distance from the water surface. (——) results from experimental study where the pressure, opening time and orifice diameter of the balloon gun were 3 bar-20 ms-0.8 cm respectively, (- - -) results from analytical simulation.

4.7.5 Water gun modelling

In this modelling the water gun is assumed operating as a pressure transmitter. When the compressed air drives its inside water ,the generated wave then propagates along the exhaust and re-radiate to the desired pipe. Full derivation of wave propagation along the pipe is provided in Appendix B. It was shown that the pressure wave at any point along the pipe, in the frequency domain, can be expressed by:

$$p(x_e) = p_0 \frac{\left(\mathrm{e}^{-\mathrm{i}k_{e1}x_e} + \hat{r}_e \mathrm{e}^{-\mathrm{i}k_{e1}(2l_e - x_e)}\right)}{1 + \hat{r}_e \mathrm{e}^{-2\mathrm{i}k_{e1}l_e}}, \tag{4.18}$$

where p_0 is the pressure generated from the device, the $\hat{r}_e$ term is the reflection coefficient associated to the end orifice,x_e is the location for estimating the pressure, l_e and k_{e1} are the length and wavenumber of the exhaust contained fluid respectively. From the Euler equation, the particle velocity can be explained through:

$$u(x_e) = \frac{p_0}{\rho c_{e1}} \frac{\left(\mathrm{e}^{-\mathrm{i}k_{e1}x_e} - \hat{r_e} \mathrm{e}^{-\mathrm{i}k_{e1}(2l_e - x_e)}\right)}{1 + \hat{r_e} \mathrm{e}^{-2\mathrm{i}k_{e1}l_e}}. \tag{4.19}$$

In he above equation the ρ_f and c_{e1} terms are the density and wave speed of the exhaust contained fluid respectively.

There are two approaches to identify the reflection coefficient:

(i) Finding the reflection coefficient from the formula given for the change of cross section due to an impedance mismatch. As illustrated in Fig. 4.19, provided that there is no reflection in the second medium, the reflection coefficient can be expressed by:

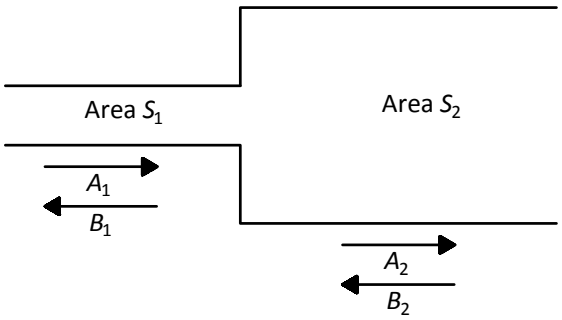

FIGURE 4.19: Positive and negative outgoing wave in a medium with a cross section area of S_1 to the second medium with a cross section area of S_2.

$$\hat{r}_e = \frac{B1}{A_1} = \frac{S1 - S2}{S1 + S2}. \tag{4.20}$$

(ii) In the second method, which is adopted to find the reflection coefficient, it is assumed that the impedance at the end orifice is equivalent to the radiation impedance of a piston vibration. The reason of selecting this method is that it takes into account the effect of loading from the surrounding medium to the excitation source. From Eqs. (4.18) and (4.19) the exhaust output impedance can be explained as:

$$Z(l_e) = \rho c S_a \frac{\mathrm{e}^{-\mathrm{i}k_{e1}l_e} + \hat{r}_e \mathrm{e}^{-2\mathrm{i}k_{e1}l_e}}{\mathrm{e}^{-\mathrm{i}k_{e1}l_e} - \hat{r}_e \mathrm{e}^{-2\mathrm{i}k_{e1}l_e}}, \tag{4.21}$$

where S_a is the cross section area of the end orifice. Kinsler et al.[84] explained the piston radiation impedance function as:

$$Z_{\mathrm{rad}} = R_{\mathrm{rad}} + \mathrm{i}X_{\mathrm{rad}}, \tag{4.22}$$

where R_{rad} and X_{rad} are the radiation resistance and reactants respectively:

$$R_{\text{rad}} = Z_a \left[\frac{(k_1 a_o)^2}{2} - \frac{(k_1 a_o)^4}{2^2 3} + \frac{(k_1 a_o)^6}{2^2 3^2 4} - ... \right], \tag{4.23}$$

and

$$X_{\text{rad}} = \frac{Z_a}{\pi (k_1 a_o)^2} \left[\frac{(2k_1 a_o)^3}{3} - \frac{(2k_1 a_o)^5}{3^2 5} + \frac{(2k_1 a_o)^7}{3^2 5^2 7} - ... \right]. \tag{4.24}$$

In the above equation, $Z_a = \dfrac{\rho_f c_1}{a_o}$, where a_o is the orifice radius. By setting $Z(L) = Z_{\text{rad}}$, the reflection coefficient and hence the pressure and particle velocity at $x = l$ can be estimated from Eqs. (4.18) and (4.19) respectively.

4.7.6 Wave radiation from water gun

The pressure wave emitted from the piston in far field, in the desired pipe where there is a spherical geometrical attenuation, can be explained by Kinsler *et al.* [84]:

$$p(x_p) = \frac{\mathrm{i}\omega \rho_f a_o^2 u(l_e)}{2x_p} \mathrm{e}^{-\mathrm{i}k_1 x_p} \left[\frac{2\mathrm{J}_1(ka_o \sin(\theta))}{ka_o \sin(\theta)} \right], \tag{4.25}$$

where J_1 is a Bessel function of order one, θ and r is the angle and the distance between the source and the sensor respectively. The a_o term is the end orifice radius.

The pressure wave radiation from the pipe water gun into the pipe, which contain no geometrical attenuation at low frequencies, where $ka \ll 1$, can be explained by:

$$p(x_p) = \mathrm{i}\omega \mathrm{e}^{-\mathrm{i}kx_p} \frac{\rho_f}{2} \frac{u(l_e)}{\pi}. \tag{4.26}$$

4.7.7 Water gun results

The pressure radiation from the analytical simulation and the experimental data for when the pressure, opening time and orifice diameter were set to 3 bar-20 ms-0.8 cm respectively, is plotted in Fig. 4.20. The figure shows the PSD of the pressure at 1.3 m distance from the excitation source using the method explained in Appendix B and similar to the balloon gun the pressure drop along the exhaust, discussed in Section 4.6 is taken into the account. The reflection coefficient of the pipe end is assumed -1. Lower

amplitude of the experimental data compared to the theory originates from using the end connection to assemble the end orifice to the reinforced exhaust. Such a part acts as a Helmholtz resonator, which decreases the amplitude of the generated wave to the desired pipe. The effect of end orifice connection has not included in the modelling. Because the environment noise is dominant at frequencies above approximately 300 Hz, a Gaussian noise with a mean and variance deviation of 0.15 and 6×10^{-4} is added to the signal.

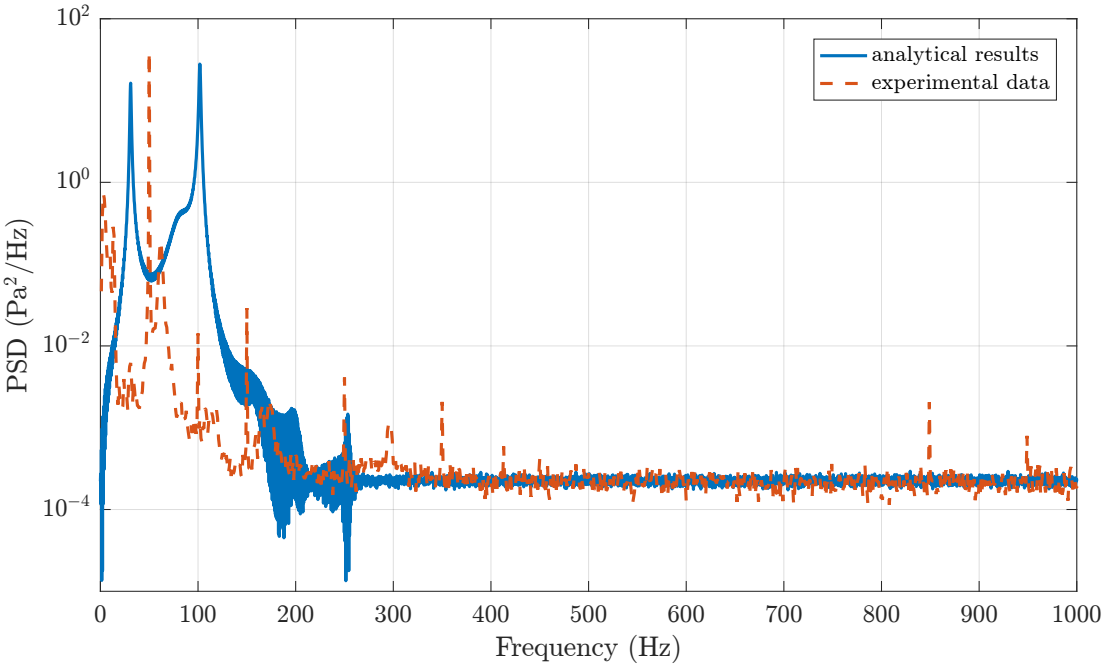

FIGURE 4.20: PSDs of the pressure at a 1.3 m distance from the water surface. (——) results from experimental study where the pressure, opening time and orifice diameter of the pipe water gun were 3 bar-20 ms-0.8 cm respectively, (- - -) results from analytical simulation.

4.8 Summary

This study was carried out with the aim of developing vibro-acoustic techniques to determine the location of buried water pipes using an excitation source inside the pipes that can be moved along the pipe length. Due to promising results from the previous vibro-acoustic technique at low frequencies (<100 Hz), a novel pneumatic device, the balloon gun, has been designed with the aim of generating high amplitude low frequency pressure wave into buried water pipes with wide range of diameter. Another pneumatic device called pipe water gun has been re-engineered for the same purposes. Although the

obtained pressure wave from the pipe water gun is slightly lower in amplitude compared to the balloon gun, it can produce a pressure wave, at the frequency range of interest, into the fluid comparable to current underwater loudspeakers that can fit into a typical buried water pipe. The main disadvantage of using a shaker is its immobility. Current underwater speakers can be an ideal source of excitation to drive the fluid when they are used in water filled pipes with relatively large diameter > 25 cm.

Chapter 5

Analytical simulation of low frequency wave radiation from a buried water pipe

In this chapter an analytical model is developed to help cast some light on the concept of the vibro-acoustic technique and bring out the dominant physical processes. By applying an excitation to a buried water pipe, several waves are, to a certain extent, generated within the pipe and will propagate along its length. Of the propagating waves, the re-radiation from the axisymmetric fluid borne wave effectively gives rise to the surface vibration. Additional to conical wave fronts, spherical wave fronts due to direct wave propagation into the surrounding medium, from the exciter are expected. The pipe configuration used for analytical model, the assumptions, the analytical description of the two wave types radiation and propagation within the assumed medium are explained in Section 5.1.

From the point where the amplitude of the conical wave fronts become dominant, the pipe path can be manifested. In light of highly attenuated conical wave fronts recorded at the surface, it was proposed by Muggleton *et al.* [25] to exploit the phase lag or the time delay of the recorded surface vibration rather than the magnitude. As an arctangent operator is used to extract phase data, the resultant values are limited to $(-\pi, \pi)$, which is called wrapped phase. A wrapped phase image shows several phase jumps which complicate the process of the pipe detection. To reconstruct contiguous

signature of the spherical wave fronts and particularly conical wave fronts, a robust two-dimensional phase unwrapping algorithm is required. For understanding the general concept of phase unwrapping, a review of one-dimensional unwrapping is presented in Section 5.2. With a two-dimensional image, made of several erratic regions, applying one-dimensional phase unwrapping to the row and the column of the image leads to the propagation of errors along the image [85].

A new unwrapping algorithm with the aim of reducing the computational effort is proposed in Section 5.3, implemented upon the wrapped analytical data and its performance examined.

To isolate the erratic regions and untangle the unwrapping problem, hundreds of two-dimensional algorithms have been designed and developed during the last three decades [86]. Such developed algorithms can be divided into two categories: local and global unwrapping algorithm. A robust algorithm from each category is described in Sections 5.4.1 and 5.4.2 respectively. In section 5.4.3 each described two-dimensional unwrapping algorithm is applied to the wrapped data, to facilitate greater insight into the use of vibro-acoustic technique for pipe detection. Having observed spatial aliasing due to low wave speed of spherical wave fronts, a simple method was proposed in the aforementioned section to increase the resolution of the image. A further investigation on the unwrapped data was carried out in Section 5.6 to find out the region where each wave type is dominant as well as estimating the wave speed in each region.

5.1 Analytical explanation of the vibroacousitic technique

In this section, a theoretical explanation of the vibro-acoustic technique, experimentally applied in Chapter 6, is given. In the theoretical modelling the following assumptions are made:

- Surrounding medium is isotropic and homogeneous, therefore the effect of the body waves reflection, refraction and mode conversion due to soil heterogeneity are discarded. In a real medium, composed of different layers, additional waves might be generated such as Lamb wave and Stoneley wave at the interface of two different layers. Furthermore other wave types such as Biot waves exist due

to the soil porosity. Here the aim, however, is to use a simple model which can encapsulate much of the essential physical process within the surrounding medium.

- The pipe is buried in a semi-infinite medium and only two types of wave will be formed within the surrounding medium; spherical and conical wave fronts. Although superposition of body waves at the surface of the half space generates surface waves, they undergo faster attenuation than the body wave. Hence their effects are not considered in this modelling. The effect of the body wave reflection at the surface as well as re-excitation of the pipe by the reflected wave is neglected. Furthermore, the effect of shear coupling at the pipe-soil interference is discarded and a lubricant connection between the two medium is considered.

Expected wave radiation from the buried pipe configuration used for experimental investigation in Chapter 6, when it was subjected to a structural and an acoustical excitation is illustrated in Fig. 5.1 and Fig. 5.2 respectively. A solid and a dashed line show generation of spherical and conical wave fronts into the external medium respectively. Conical wave fronts are resulted from the axisymmetric fluid borne wave propagation along the pipe. The spherical wave fronts, are due to direct wave radiation from the exciter and/or wave radiation from the discontinuities along the pipe into the surrounding medium. For the test rig shown in Fig. 5.1, a high amplitude spherical wave spreading from the right angled bend is expected. This type of test rig can be deemed as a soil excitation via a large vertical buried stinger. The axisymmetric fluid borne wave is mainly excited at the right angled bend, where a coupling (mode conversion) between fluid and the structural borne waves takes place.

When the pipe is subjected to an in-pipe excitation, the radiation of the spherical wave fronts into the external medium might be due to the high amount of pipe wall expansion and contraction at the source location as well as the direct wave radiation from the exciter into the surrounding medium. In this case, generation of the conical wave fronts into the surrounding medium is resulted from direct fluid excitation leading to propagation of the axisymmetric fluid borne wave into the pipe. Generation of the spherical wave in the surrounding medium is assumed due to both direct wave propagation from the exciter and wave radiation from the discontinuities into the surrounding medium.

As seen in Figs. 5.1 and 5.2, spherical waves radiate at the discontinuities along the pipe. The places far away from the exciter location, however, do not possess high value

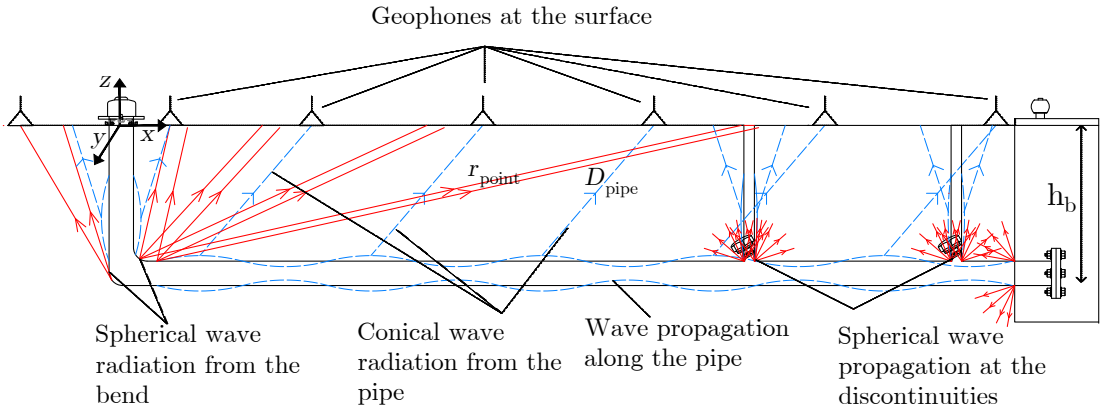

FIGURE 5.1: A schematic of the wave propagation into the pipe and the surrounding medium when it is subjected to a structural excitation, in XZ plane. The dashed blue and the solid red lines with the arrow show the radiation from the pipe wall and point source into the external medium respectively.

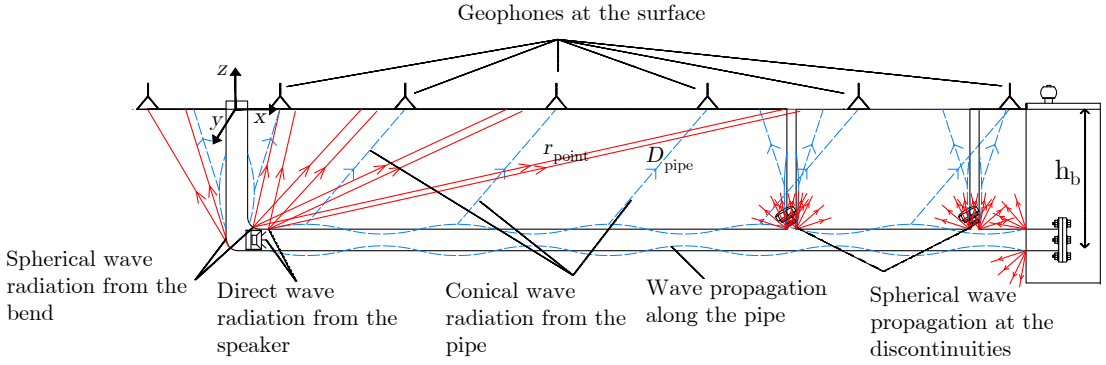

FIGURE 5.2: A schematic of the expected wave propagation into the pipe and the surrounding medium when it is subjected to an internal excitation, in XZ plane. The dashed and the solid lines with the arrow show the radiation from the pipe wall and point source into the external medium respectively.

of the source strength and their effects can be neglected. A comprehensive modelling of the wave radiation from the point sources and the pipe is knotty and beyond the scope of this study.

Although different measurement grid can be utilised in practical measurement, the selected grid of measurement points in here is the one that covers the whole length of the pipe, and is shown in Fig. 5.3. The grid spacing is set at 1 m and 0.75 m in the x and the y axis respectively.

In the next chapter, experimental measurements will be carried out using a number of geophones which can record the surface vibration velocities in three orthogonal direction. Since the pipe axis is unknown and velocity is a vectorial quantity the surface vibration

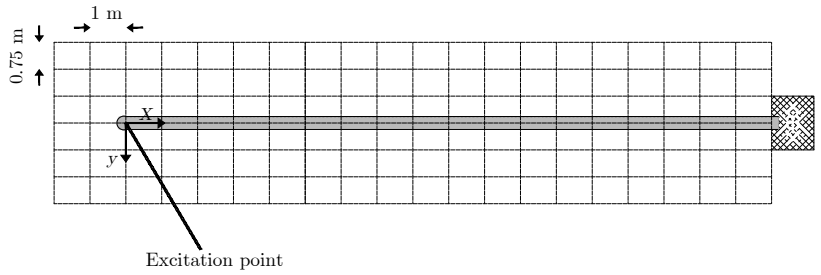

FIGURE 5.3: A plan view of the measurement grid point used to record the surface vibration in the analytical model. The grid spacing is set at 1 m and 0.75 m in the x and the y axis respectively.

in the vertical plane is of interest only. Accordingly, an investigation was carried out to identify the induced vibration in the desired plane.

5.1.1 Wave radiation from a point source

A theoretical explanation of the spherical wave generation, shown in Fig. 5.1 and Fig. 5.2, within the surrounding medium is given in this section. The harmonic vibration velocity of the surface, based on the assumption made in Section 5.1, due to the pulsation of a buried monopole source in the positive r direction can be given by:

$$V_{\text{point}}(r,t) = \frac{V_{1\text{point}}}{r_{\text{point}}} \mathrm{e}^{\mathrm{i}(\omega t - k_r r_{\text{point}})}. \tag{5.1}$$

Here $V_{1\text{point}}$ represent the amplitude of the generated body wave, which might be complex i.e.$V_{1\text{point}} = |V_{1\text{point}}|e^{\mathrm{i}(\phi)}$, $|V_{1\text{point}}|$ is the magnitude and ϕ is the relative phase. The term -$k_r r_{\text{point}}$ represents a phase delay term due to the increasing distance from the point of excitation, in the positive r_{point} direction. Suppressing time dependence for simplicity in Eq. (5.1) allows expressing the phase change per unit of distance. A Schematic of a spherical wave front which spread uniformly into the surrounding medium is given in Fig. 5.4.

In the following simulations it is assumed that only shear and compressional waves spread into the surrounding medium. Although the generated ground vibration from the shear waves consists of two polarized wave with the perpendicular particle motion, due to symmetry of the medium discriminating these polarized waves are not achievable within the surrounding medium. Upon their arrival, however, these two polarized waves

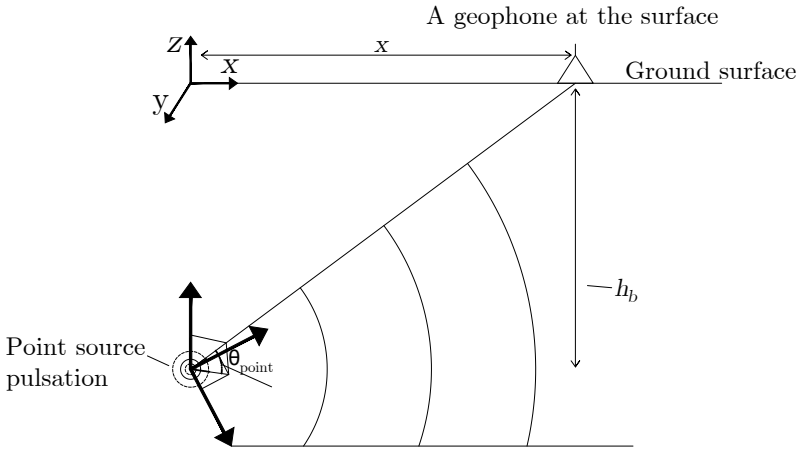

FIGURE 5.4: A spherical spreading of the body wave into surrounding medium. The coordinates of the source are $(0, 0, -h_b)$. The location of displayed geophone is $(x, 0, 0)$.

can be differentiated [87]. The resultant surface vibrational velocity amplitude, when a shear wave impinges to it, in the vertical plane, can be explained by:

$$DI_{SV,\text{point}} = \cos(\theta_{\text{point}}) = \frac{\sqrt{x^2 + y^2}}{\sqrt{h_b^2 + x^2 + y^2}}. \tag{5.2}$$

To find the surface vibrational velocity amplitude, due to the impingement of spherical compressional wave fronts to the surface, in the vertical plane, its amplitude should be multiplied to the following parameter:

$$DI_{P,\text{point}} = \sin(\theta_{\text{point}}) = \frac{\sqrt{h_b^2}}{\sqrt{h_b^2 + x^2 + y^2}}. \tag{5.3}$$

Consequently, the vibration of the ground surface in the vertical plane can be expressed by:

$$V_{\text{point}}(r, t) = DI_{P,\text{point}} \frac{V_P}{r_{\text{point}}} e^{-\mathrm{i}k_P\, r_{\text{point}}} + DI_{r,\text{point}} \frac{V_r}{r_{\text{point}}} e^{-\mathrm{i}k_r r_{\text{point}}}. \tag{5.4}$$

The effect of soil damping is included by using a complex wave number as follows:

$$k = \frac{\omega}{c\left(\sqrt{1 + \mathrm{i}\eta_m}\right)}, \tag{5.5}$$

where η_m is a surrounding medium loss factor.

5.1.2 Wave re-radiation from pipe wall

This section discusses on the theoretical explanation of the conical wave radiation from a fluid filled pipe into the surface. A schematic of axisymmetric waves propagation and conical wave re-radiation to the surrounding medium is shown in Fig. 5.5. Of the axisymmetric waves, the fluid borne has the highest contribution on the radial displacement of the pipe wall. Owing to the higher wave speed of the axisymmetric fluid borne wave the emitted wave fronts from the pipe wall possesses an angle. Accordingly, the travelling distance of conical wave fronts illustrated in Fig. 5.5 (a) is longer compared to the one depicted in Fig. 5.5 (b).

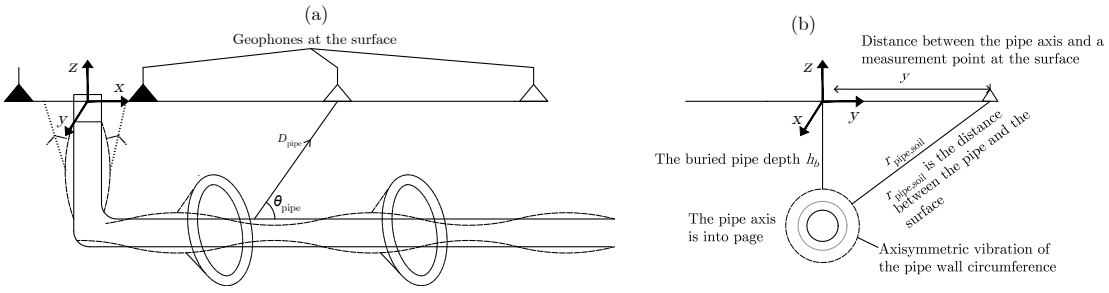

FIGURE 5.5: Conical wave re-radiation from the pipe wall to the surface . (a) side view (b) front view . D_{pipe} is the actual distance of wave travelling from the pipe to the surface and is used for spatial phase estimation while the h_b distance is used for geometrical attenuation.

The radial component of the conical wave radiation from the pipe wall to the surface can be explained by:

$$r_{\text{pipe,point}} = \sqrt{y^2 + h_b^2}, \tag{5.6}$$

where y is the distance of the measurement point with respect to the pipe axis at the surface and h_b the depth of the buried pipe.

A theoretical investigation by Gao *et al.* [88] on the same pipe experimented in Chapter 6, illustrated that the vertical displacement of the surface are controlled by shear conical waves below ($<$ 200 Hz). Since the results from the vibro-acoustic are mainly focused at low frequencies (approximately below 100 Hz), effects of compressional conical waves

were excluded. The angle of shear conical wave fronts emission from the pipe, illustrated in Fig. 5.5 (a), into the external medium can be expressed using Snell's law as:

$$\theta_{\text{pipe}} = \arccos\left(\frac{c_S}{c_r}\right), \tag{5.7}$$

where c_s and c_r are the speed of axisymmetric fluid borne and the shear wave in the surrounding medium respectively. Hence the radiated wave distance from the pipe wall to the surface can be explained by:

$$D_{\text{pipe}} = \frac{r_{\text{pipe,point}}}{\sin(\theta_{\text{pipe}})}. \tag{5.8}$$

In this simulation, it is assumed that the surface vibrational velocity is only due to vertically polarised shear waves. Therefore to simulate their recorded particle vibration velocities by gephones its amplitude should be multiplied by:

$$DI_{r,\text{pipe}} = \cos(\theta_{\text{pipe}})\frac{\sqrt{h_b^2}}{\sqrt{h_b^2 + y^2)}}. \tag{5.9}$$

Consequently the surface vibrational velocity due to shear conical wavefronts impinge to the surface can be expressed by:

$$V_{\text{pipe}}(x, r) = \frac{V_{s-r} DI_{r,pipe} e^{-\mathrm{i}\,(k_s x_{\text{pipe}} + k_r D_{\text{pipe}})}}{\sqrt{r_{\text{pipe,point}}}}, \tag{5.10}$$

where V_{s-r} is the amplitude of the wave radiated from the pipe wall, which might be complex i.e. $V_{s-r} = |V_{s-r}t|e^{\mathrm{i}\phi_{s-r}}, |V_{s-r}|$ is a magnitude and ϕ_{s-r} is a relative phase. k_s is the wave number related to the axisymmetric fluid borne wave within the pipe. The x_{pipe} term is the distance that the wave travels inside the pipe and is given by:

$$x_{\text{pipe}}(x, r) = x - D_{\text{pipe}}\cos(\alpha), \tag{5.11}$$

where x is the distance of the measurement point with respect to the origin where $(x = 0)$. Attenuation of the fluid borne wave amplitude due to the radiation loss is

included by adopting the low frequency radiation impedance formula, given by Junger and Feit [89], into the axisymmetric fluid borne wave number given by [64] :

$$k_1^2 = k_f^2 \left(1 + \frac{2B_f/a}{E_p h/a^2 - \omega^2(\rho_p h) + \mathrm{i}(\omega z_{\mathrm{rad1}})}\right). \tag{5.12}$$

All the parameter are defined when previously used in Eq.(2.7), in Chapter 2. The radiation impedance z_{rad1} which contains resistive and reactive components, can be explained by:

$$z_{\mathrm{rad1}} = \sum_{m=0}^{+\infty} \left(\rho_m a\omega(\pi/2 + \mathrm{i}\ln|k_{m1}^r a)|\right). \tag{5.13}$$

Having the wave number variable to define the radiation impedance value in Eq. (5.13), to estimate the wavenumber of the axisymmetric fluid borne wave; its value should be calculated recursively.

5.1.3 Spherical and conical wave radiation from a buried pipe

The harmonic surface vibration velocity due to simultaneous impinges of the shear conical and spherical waves to it, discussed in Sections 5.1.1 and 5.1.2, can be explained by:

$$V_{\mathrm{total}}(f) = V_{\mathrm{pipe}}(x, r, f) + V_{\mathrm{point}}(r, f). \tag{5.14}$$

Mathematical derivation of V_{pipe} and V_{point} are described in Eqs. (5.4) and (5.10) respectively. Extraction of the phase data from Eq. (5.14) can be achieved by applying arctangent function as follows:

$$\psi(f) = \arctan\left(\frac{\mathrm{Re}(V_{\mathrm{total}}(f))}{\mathrm{Im}(V_{\mathrm{total}}(f))}\right), \tag{5.15}$$

where Re( ) and Im( ) refer to real and imaginary component and arctan is the four quadrant arctangent function. Due to employing of the arctangent operator, the resultant phase data is limited to $(-\pi, \pi)$, called wrapped phase.

Similarly there are several other fields in which the four quadrant arc tangent function is employed and thereby wrapped phase images are generated.

In most of such applications, namely, magnetic resonance imaging (MRI), synthetic aperture radar (SAR), adaptive optics, optical and microwave interferometry and seismic processing, etc, the phase is a physical quantity. For instance, the degree of magnetic field inhomogeneity in the water/fat separation problem in magnetic resonance imaging (MRI), the ground surface height for geophysical study in interferometry, wave-front distortion in adaptive optics, relationship between the object phase and its bispectrum phase in astronomical imaging [90].

5.1.4 Simulation Prameters

The material properties of the parameters used in this simulation are gathered in Table 5.1.

TABLE 5.1: Material properties of MDPE pipe, external and internal medium.

Parameter	Description of parameter	MDPE	Water	soil
a	Mean radius (m)	$8.45 \times 10^{-}2$	-	-
h	Wall thickness (m)	$11 \times 10^{-}3$	-	-
E	Young's modulus (Gpa)	1.65	-	-
v	Poisson's ratio	0.4	-	-
B	Bulk modulus (Gpa)	-	2.18	0.053
G	Shear modulus (Gpa)	-	-	0.02
η	Material loss factor	0.06	-	0.05
ρ	Density(m^3)	880	1000	2000

Along with soil density, substituting the value of bulk modulus and shear modulus, illustrated in Table 5.1, respectively into Eqs. (2.36) and (2.39) reveals the wave speeds of the shear and compressional wave. Following the identification of the wave speed, the wave number of each wave can be found using Eq. (5.5).

On the grounds that the described pipe parameters are identical to the experimented pipe in Chapter 3, the wavenumber and attenuation of the axisymmetric fluid borne wave can be found in the aforementioned section. The wave speed of shear conical wave fronts, emitted from the pipe wall to the medium, is analogous to the spherical shear body waves.

The relative amplitude of spherical and conical wave fronts depends upon type of exciter and the location to where the pipe is subjected to an excitation. Approximate amplitude of each dominant wave type into the surrounding medium might be identified through examining spatial unwrapped phase plot from experimental data which are discussed in Chapter 6 and Section 5.6.

To obtain coincide results with the in-pipe excitation measurements in Chapter 6, particularly in Sections 6.3 and 6.5, it is assumed that the pipe discussed in Section 5.1, undergoes an excitation at the reference location and the shear and compressional spherical wave fronts hold two times higher amplitude compared to the conical ones. It means that:

$$|V_P| = |V_r| = 2|V_{s-r}| = 1 \text{ m/s} \tag{5.16}$$

Furthermore it is assumed that the generated waves are in phase; meaning that $\phi_{V_p} = \phi_{V_r} = \phi_{V_{s-r}} = 0$.

5.1.5 Wrapped phase image

To have a better insight about the spatial wrapped phase image, wrapped values of the simulated model are plotted in Fig. 5.6 at four frequencies. As seen in Fig. 5.6, specifically at 55 Hz after approximately a nine metre distance from the origin, an ordinary conical shape phase jump or fringe appears along the wrapped phase plot and its number increases by increasing frequency. In experimental data, low signal to noise ratio, interference of several wave types and heterogeneity within the surrounding medium might not allow clearly visualising such trends along the wrapped phase images. The illustrated wrapped phase images incorporate a multiple integer of 2π out of phase from the true phase. To retrieve the signature of underlying contiguous wave fronts an unwrapping operator has to be applied. Hence, the next three sections reviews the literature on phase unwrapping principle

5.2 One-dimensional phase unwrapping

Phase refers to the location of a point along a wave in respect of a reference point or the comparative movement between two or more waves. The phase is a characteristic of

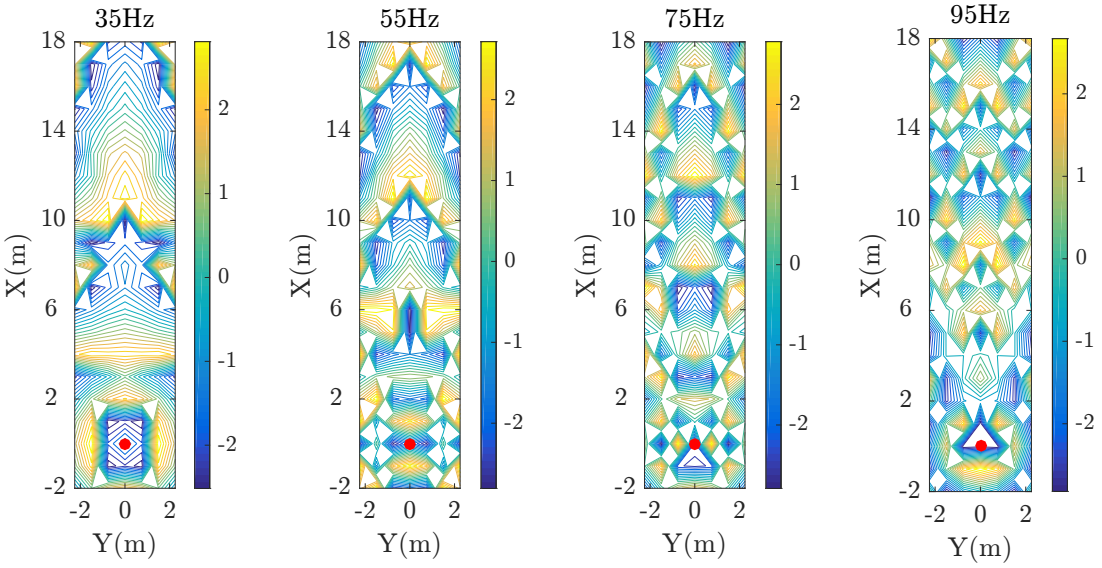

FIGURE 5.6: The wrapped phase data in radians, governed from the simultaneous shear conical and spherical wave fronts propagation into the elastic medium at four frequencies between 35 Hz and 95 Hz, spaced every 20 Hz.

a signal, however, it can be treated as a signal by itself. As an example lets assume the recorded complex signal is a sinusoidal signal of frequency 5π:

$$x(t) = e^{\mathrm{i}5\pi t} \qquad 0 < t < 1, \tag{5.17}$$

and we wish to reconstruct from $x(t)$ the continuous phase $\phi(t) = 5\pi t$ through the arctangent operator, which can be counted as a wrapping operator:

$$\psi(f) = \arctan\left(\frac{\mathrm{Re}(x(t))}{\mathrm{Im}(x(t))}\right). \tag{5.18}$$

True and wrapped phase of Eq. (5.18) are plotted in Fig. 5.7. As seen in Fig. 5.7, although the wrapped phase encoded time delay information, it is a multiple integer of 2π out of phase from the true phase. In other words, with the exception of the phase jump area, the gradient of the wrapped phase and its true value are identical.

In 1983, Itoh [91] mentioned that the one-dimensional phase unwrapping can be achieved by applying summation to the wrapped differences of the wrapped phases:

$$\phi(N) = \phi(1) + \sum_{t=2}^{N} \mathbf{W}\left\{\phi(t) - \phi(t-1)\right\}, \tag{5.19}$$

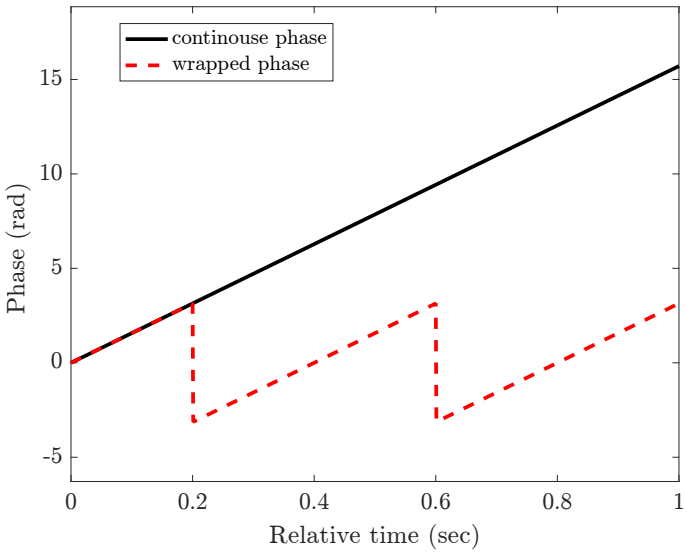

FIGURE 5.7: Plot of the true and the wrapped phase of Eq. (5.18). The true phase is a linear function while the wrapped phase in a saw tooth function. Phase unwrapping usually achieved through adding an appropriated multiple of 2π radians.

where $\mathbf{W}$ is the wrapping operator and wrap the data of the bracket in the interval $(-\pi, \pi)$. $\phi(t)$ is the wrapped phase value at point t. The two main problems which impede to successfully reconstruct the one-dimensional unwrapped phase from its wrapped data are under sampling and noise contamination of phase.

5.2.1 Phase sampling rate

Provided that the phase difference between two successive points exceeds π radians, the phase unwrapper recognise the existence of a wrap at this location. This could be either an actual phase wrap or due to the under sampled data, called fake wrapping. Obviously the output phase from the signal is in the wrapped form and its recognition is difficult. Nevertheless, the problem can be addressed by sampling the signal itself at the Nyquist rate or higher. In other words, by imposing the Nyquist criterion on the recording signal, it can be assured that the phase difference between any two consecutive points is less than π radians.

5.2.2 Effect of noise

Apart from aliasing, noise is another source of errors which might cause calamitous failure in phase unwrapping. To avoid fake wrapping in a phase image, the variance of

the phase should be low enough to avoid catastrophic results. There are two ways to illustrate the effect of noise on the phase unwrapping process, expressing by (1) Noise variance and (2) Signal to noise ratio parameters. The effect of noise variance on the phase unwrapping process can be explained by adding white noise to the same phase data expressed in Eq. (5.17), as follows:

$$\phi(t) = 5\pi t + n(t). \tag{5.20}$$

The true phase is sampled well above the Nyquist limit to avoid phase aliasing. Different noise variances are chosen to illuminate the effect of noise variation on the phase unwrapping process. Then the noise contaminated phase data is wrapped into (-π, π):

$$\psi(t) = \mathbf{W}(5\pi t + n(t)). \tag{5.21}$$

Following this, the noisy wrapped signals are unwrapped with the Itoths method and the results are illustrated in Fig. 5.8.

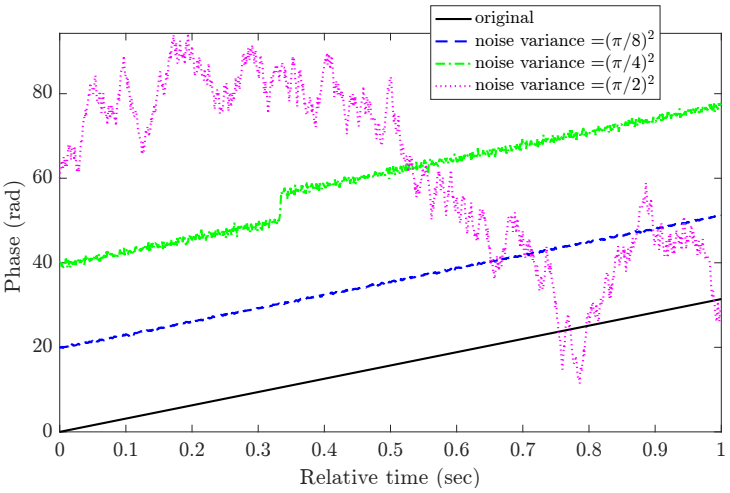

FIGURE 5.8: The effect of noise variance on phase unwrapping. The lower solid line is the true phase signal and the higher curves are the unwrapped results for the data with noise variance of $(\pi/8)^2$, $(\pi/4)^2$ and $(\pi/2)^2$ respectively.

The lines above the original phase represents the unwrapped results with increasing the noise variance. The unwrapping can capture the noisy estimate of true phase until the noise variance reaches to $\pi/8$. The first phase jump is evident for noise variance of $\pi/4$ and catastrophic results occur when noise variance= $\pi/2$.

To reduce the noise variance and improve phase quality, the signal quality itself should be improved. Signal averaging are normally adopted to reduce phase noise variances. For example, in Cross Spectrum Density (CSD) function, the variation of the phase value when n_d number of averaging was performed can be explained by:

$$Var|\phi| \approx \frac{1-\gamma_{xy}^2}{2\gamma_{xy}^2 n_d}, \tag{5.22}$$

where γ_{xy} is the coherence function. For low coherence, Eq. (5.22) becomes $\text{Var}|\phi| \approx \frac{1}{2\gamma_{xy}^2 n_d}$, which should be less than $(\pi/8)^2$ for unwrapping. Hence:

$$\frac{1}{2\gamma_{xy}^2 n_d} < \left(\frac{\pi}{8}\right)^2 \rightarrow \gamma_{xy}^2 > \frac{32}{\pi^2 n_d} \approx \frac{6.4}{n_d}. \tag{5.23}$$

As shown in Eq. (5.23), by increasing the signal averaging, the obtained phase data from even very low coherence data can be unwrapped. Depending upon the variation to the phase value, the unwrapped phase may not represents the original noisy phase.

Signal to noise ratio (SNR) is another parameter that can be used to express the effect of background noise on the unwrapping process. To this end, complex Gaussian noise $n(t)$ is added to the phasor signal used in Eq. (5.17) as follows:

$$x(t) = e^{\mathrm{i}5\pi t} + n(t). \tag{5.24}$$

Here the SNR defined as the peak signal divided by the noise variance. The wrapped phase is extracted as explained in Eq. (5.18) and the phase unwrapping was achieved by the Itoh's method explained in Eq. (5.19). The unwrapped phase results for different SNR values are shown in Fig. 5.9.

As seen in Fig. 5.9, the unwrapping results resemble the true signal until the SNR reduces to 3. The first fake phase jumps appears for SNR=2, and catastrophic results occur when the SNR drops to near unity.

To have a better understanding about the effect of SNR on the unwrapping process, the contaminated signal by a noise cloud is shown in Fig. 5.10. Increasing the variance of the noise to cover the origin, the signal can swing in both magnitude and phase from one instance in time to the next. When the signal phase pass from zero, π radians

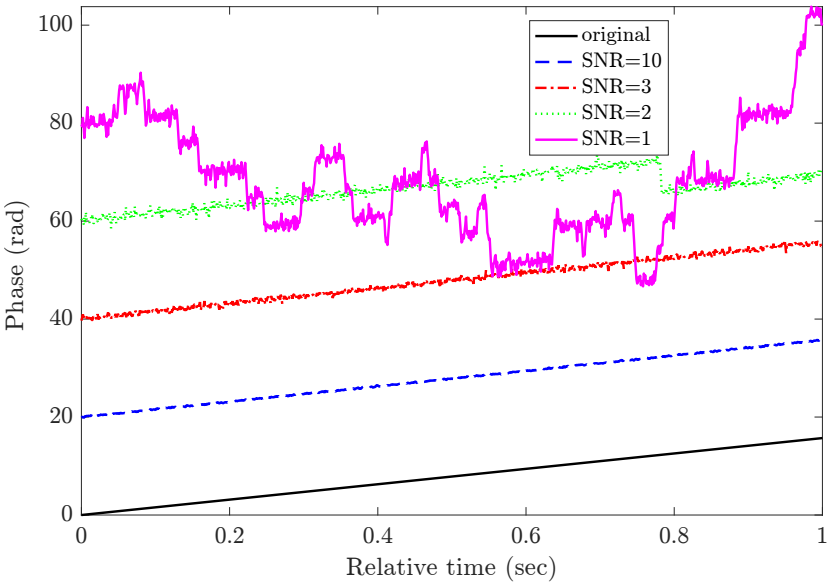

FIGURE 5.9: Effect of noise on phase unwrapping. The lower line is the original phase. The next higher lines are the unwrapped results for SNR =10, 3, 3 and 1 respectively. catastrophic results occur when the SNR drops too low.

phase change happens. Such rapid changes to the phase cannot be distinguished from a genuine phase wrap. Hence, the unwrapping algorithm cannot reconstruct the relative true phase.

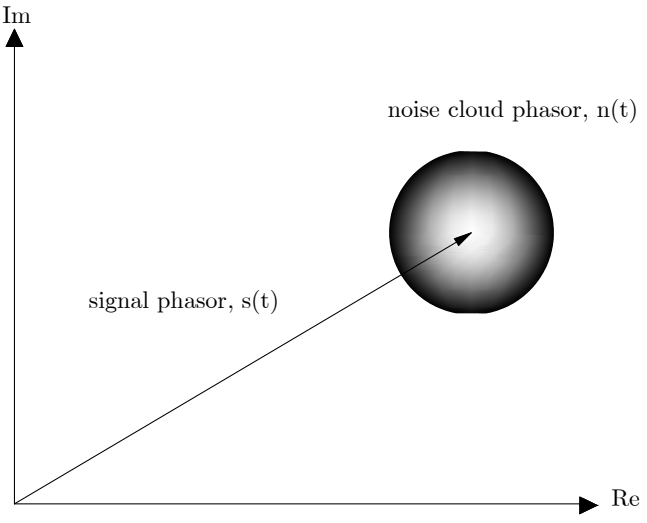

FIGURE 5.10: Effect of noise on phase unwrapping when the complex phasor of interest is perturbed by a noise cloud.

5.2.3 Applying one-dimensional unwrapping to the wrapped phase image

This section is an attempt to expose the issue of applying one dimensional phase unwrapping to the rows and columns of a wrapped phase image. In this method, phase unwrapping achieved through integrating the wrapped phase difference between any two successive points along the rows and columns of a wrapped phase image and can be explained by:

$$\phi(x,y) = \phi(x_0,y_0) + \sum_{x=1}^{M}\sum_{y=1}^{N} \mathbf{W}\left\{\Delta_\phi(x,y)\right\}. \tag{5.25}$$

Here $\phi(x,y)$, $\phi(x_0,y_0)$ are the unwrapped phase at an arbitrary point (x,y) and the initial point (x_0,y_0) respectively. Δ is the phase difference between two successive pixels. As seen in Eq. (5.25), the unwrapped phase at pixel (x_1,y_0) can be estimated from the unwrapped phase at the pixel (x_0,y_0) plus the wrapped phase difference between (x_0,y_0) and (x_1,y_0).

It is possible to either apply the unwrapping to the rows and then to the columns or vice versa. In practice, applying such a plain unwrapping algorithm to a wrapped phase image containing noise contaminated or spatially aliased region, causes the propagation of errors, called residues, over the image [85]. Without phase image unwrapping operation, the errors do not propagate on its own throughout a wrapped phase image. To prevent degrading of unwrapped phase images, first the residues location must be identified and then be somewhat isolated from the rest of pixel during the unwrapping process. A method of detecting residues Rs is integration of the phase difference in a 2×2 closed path as shown in below [85].

$$\begin{aligned} Rs = \mathrm{Ro}\left[\frac{\psi_{i+1,j}-\psi_{i,j}}{2\pi}\right] + \mathrm{Ro}\left[\frac{\psi_{i+1,j+1}-\psi_{i+1,j}}{2\pi}\right] + \\ \mathrm{Ro}\left[\frac{\psi_{i,j+1}-\psi_{i+1,j+1}}{2\pi}\right] + \mathrm{Ro}\left[\frac{\psi_{i,j}-\psi_{i,j+1}}{2\pi}\right], \end{aligned} \tag{5.26}$$

where, Ro is an operator which round the value inside the bracket to the nearest integer. Providing that a residue exists, the value of Rs in Eq. (5.26) is 1 or -1 and $Rs = 0$ indicates that there is no residue. $RS = +1$ indicates the presence of positive residue or positive polarity and when $RS = -1$, a negative residue or polarity exist in the

calculated pixel. A brief explanation on identifying the residue in a two-dimensional matrix is illustrated in Fig. 5.11.

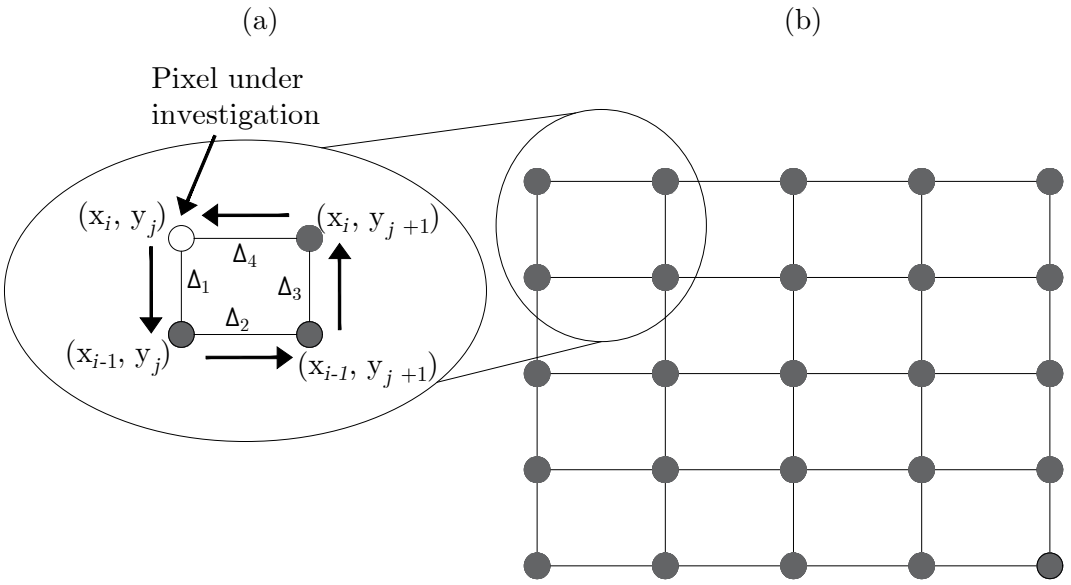

FIGURE 5.11: (a) The pixel under intergeneration (b) in a wrapped phase image.

As an example, the one dimensional unwrapping algorithm is applied to the simulated wrapped phase images, shown in Section 5.1.5, parallel to the y and x axis respectively, and plotted in Fig. 5.12. By applying the one-dimensional unwrapping algorithm, the shapes of the unwrapped images almost change for every frequency. The appeared artefacts at the middle of the contour plots at 35 Hz could be an ideal simulation results to confirm experimental results in [25]. The two parallel lines originated at a 4 m distance from the excitation source, are due to the residues propagation from the aforementioned location. The residues location is illustrated in Fig. 5.13.

The data at 55 Hz reports the supremacy of conical wave fronts on vibrating the surface after a six metre distance from the excitation source. Owing to the equal number of positive and negative residues along the final unwrapping path, x-direction, the propagation has not observed at the region where the conical wave fronts are dominant. At a 2 m distance from the excitation point along the x axis, however, two residues propagate and stop at a 6 m distance from the same source, where they reaches to their opposite polarity, illustrated in Fig. 5.13.

Despite spatial aliasing at the proximity of the excitation source at 55 Hz, the errors has not propagated along the image. Therefore the propagation of errors along the image is mainly affected by the presence of the residue and the method of unwrapping. Spatial

aliasing referred to the situation where the difference in phase between any two pixels is beyond π radians. The frequency at which the two sources; pipe and direct source, violets the Nyquist sampling rate for the spatial unwrapping,is explained in Appendix E.

Similar to 35 Hz, at 75 Hz the wave fronts from the source directly propagated to the medium, appeared around the excitation source and the pipe wave dominates along the pipe axis in a narrowed area. For the same reason explained for 35 Hz and 55 Hz, errors propagate from the residues. At 95 Hz, the spatial aliasing from the point source can be clearly seen at where it is dominant and the wave fronts from the pipe wave are reversed shape hyperbole. A reverse to the conical wave fronts at 95 Hz, is due to the higher changes to the phase data related to the propagation of the residue at a 6 m distance from the excitation source, along the image.

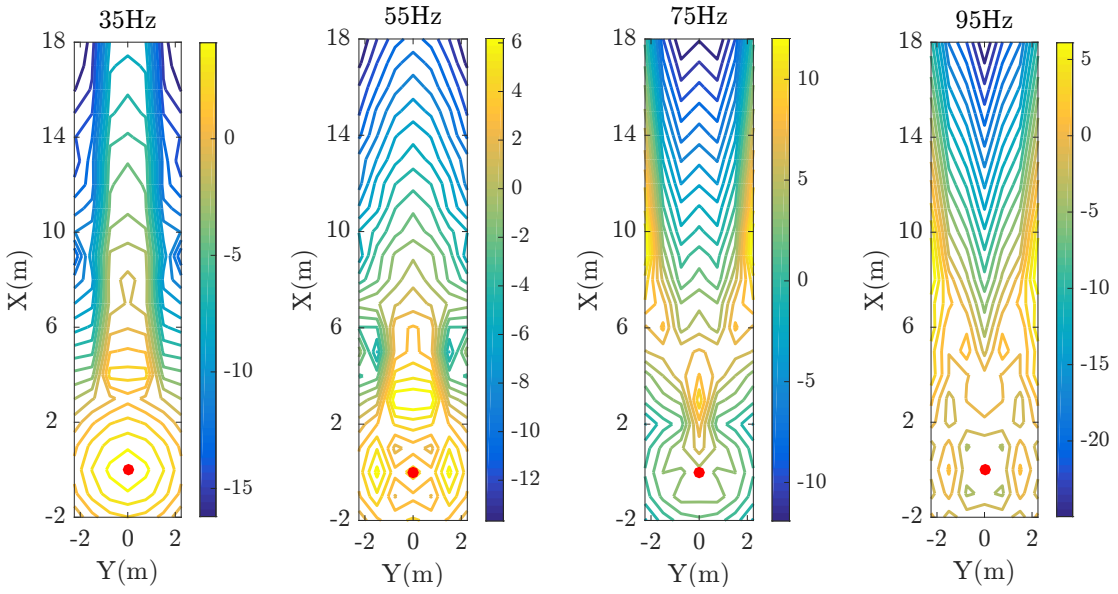

FIGURE 5.12: Applying one-dimensional phase unwrapping algorithm to the wrapped phase governed in radians.The red spot illustrates the origin.

5.3 Radial phase unwrapping

Here a new technique for unwrapping two-dimensional image with the aim of reducing the computational effort to find the pipe axis is proposed. In this technique the data is unwrapped with respect to a reference point; the position where the excitation applied to the pipe. Such a location normally can be found using spatial magnitude plots. Lets

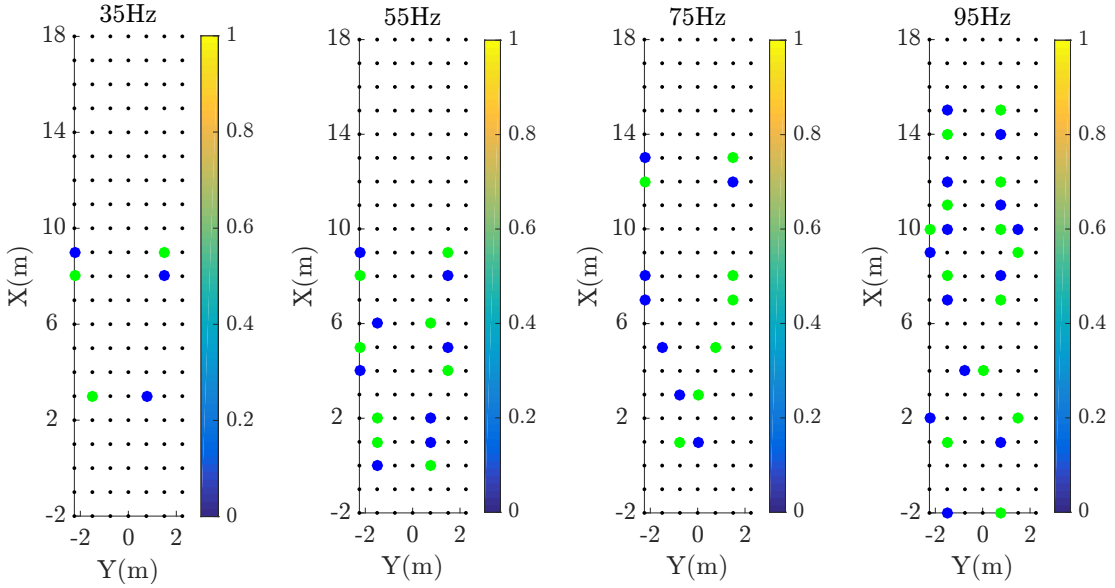

FIGURE 5.13: Residues of wrapped images illustrated in Fig. 5.6. The small black dots, filled blue and green dots illustrate the residue of 0, +1 and -1 respectively.

assume $\mathbf{W}$ is the wrapping operator which wraps the phase $\phi_f(f)$ to the interval $(-\pi, \pi)$. For this case, the frequency wrapped phase value of each point can be explained by:

$$\mathbf{W}[\phi_f(f)] = \psi(f)\phi_f + 2\pi\aleph(N), \tag{5.27}$$

where $\phi(f)$ is the true phase at frequency f. $\aleph(N)$ is an integer number and selected so that:

$$-\pi < \psi(f) < \pi \tag{5.28}$$

An image $M(x, y, f)$ comprises wrapped phase data on the rows x and y and might contain several phase jumps as all the points value are limited into the interval $(-\pi, \pi)$. Provided that the image points are sampled at the Nyquist rate or higher, wrapped phase difference or the wrapped partial derivative of each measurement point can be explained by:

$$\mathbf{W}\{\Delta M(x, y, f)\} = \mathbf{W}\{M(x, y, f) - M(x, y, f-1)\} \tag{5.29}$$

The wrapping operator is implemented to extract the true phase differences, specifically from the areas where a phase jump occurs. Then the algorithm proceeds to transform the phase gradient data at each frequency, from Cartesian to polar coordinates. The reason for this transformation is to help the procedure of the data unwrapping in the

radial direction. Therefore less computational effort is required to identify the path. This approach relies on the assumption that the measured data above the pipe axis has high quality and do not hold any residue. The procedure of data transformation algorithm from Cartesian to polar coordinates can be summarized as follows:

1. Defining the grid of data in the polar coordinate system that cover the data location in the Cartesian coordinate.

2. Transforming the grid point from the polar to the Cartesian coordinate system.

3. Applying a bilinear interpolation to find the new data at the required grid point. The algorithm find the value of the unknown point utilising a weighted sum of the four neighbouring points. A detail explanation of the algorithm is explained in reference [92], and for brevity is not repeated here.

Only when the spatial phase differences between any transformed points in the radial axis exceeds the interval $(-\pi, \pi)$, can a finer polar grid be used to have data at Nyquist rate or higher. Before continuing, it should be noted that the reason for transforming the phase difference rather than the actual wrapped phase is due to the limitation of the wrapped data to the interval $(-\pi, \pi)$. With applying the bilinear interpolation, the estimated pixel value might be undesirably altered by the phase jump areas.

Upon the estimation of the phase gradient in the polar coordinates, the frequency wrapped phase difference of each point, in the polar coordinate, is added to its previous value,

$$M(r, \theta, f) = \sum_{f=1}^{n-1} \mathbf{W}\{M(r, \theta, f-1) + M(r, \theta, f)\}. \tag{5.30}$$

Upon adding the phase gradient of each pixel to its previous value, the constructed phase image will exceed the interval $(-\pi, \pi)$. Therefore a wrapping operator was applied to the data to produce a wrapped image in the frequency range of interest.

Next, one-dimensional phase unwrapping operator is applied along the radius to the wrapped data with respect to the origin. It is important to apply the unwrapping function parallel to the radial axis. A schematic of one-dimensional unwrapping when it is applied to data in Cartesian and a polar coordinate is illustrated by an arrow in Fig. 5.14 (a) and (b) respectively. Then the algorithm proceeds by returning the

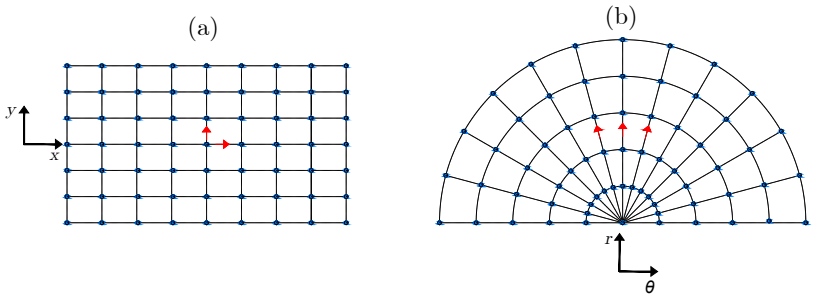

FIGURE 5.14: Data located in (a) a Cartesian and (b) a polar coordinate system. The red arrows show the direction of applying one-dimensional unwrapping algorithm into each coordinate system.

data back into its initial grid in the Cartesian coordinate. Since the Cartesian location of the unwrapped data in the polar coordinate was previously specified, the bilinear interpolation exploited to estimate the data on its initial coordinate with a finer spacing. By applying the bilinear transformation, the requested data might lie beyond the image axes. To recover the missing data, an algorithm based on sparse-representation image decomposition was adopted which is fully explained in detail by Garcia [93].

5.3.1 Results from Radial unwrapping

The developed unwrapping algorithm was applied to the wrapped data, which was discussed in Section 5.1.5 and the results are presented in Fig. 5.15. On the basis of the results showed in Fig. 5.15, it can be concluded that the width of the conical wave's pattern is not confined to its pipe axis at the surface. They also provide confirmatory evidence that after some distance from the excitation point only the pipe wave dominates. In practice, the starting region where the pipe wave dominates depends upon the relative particle velocity from the pipe wall compared to the source wave. For the purposes of removing the effect of under sampling, sometimes called spatial phase aliasing, in where the body waves dominates, the grid data in the polar coordinates selected 0.2 m and $\pi/20$ in the r and the θ axes respectively. With the presence of several disturbances along the image, radial phase unwrapping might cause them to propagate along the image. In an attempt to prevent the propagation of errors along the image and isolate the unreliable areas, hundreds of two-dimensional unwrapping algorithms have been designed in the past three decades [86]. Using such unwrapping algorithms and

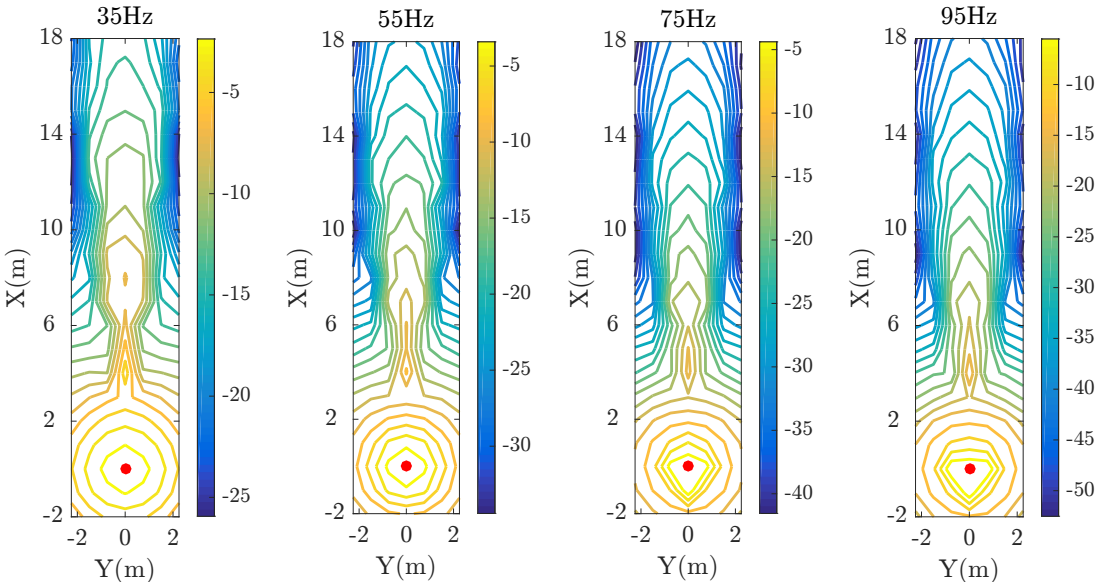

FIGURE 5.15: Illustrative of spatially unwrapped phase, in radians, using radial unwrapping. Transformation from Cartesian to polar coordinates carried out with a thinner grid in the polar coordinate; 0.2 m and $\pi/20$ in the r and the θ axes were selected. The corresponding wrapped data is illustrated in Fig. 5.6.

applying them to the two-dimensional wrapped data might bring to light new information. The principle behind all of such algorithms can be divided into two categories. A robust algorithm from each category is explained in the forthcoming section.

5.4 Two-dimensional phase unwrapping

Two-dimensional phase unwrapping algorithms try to minimize the effect of corrupted pixels on the rest. Several algorithms are proposed on this matter. The differences between the established algorithms are the computational effort and accuracy of results. Most of the developed unwrapping algorithms can be classified into two major categories: local and global phase unwrapping algorithms. A thorough review of these two classes of phase unwrapping algorithm is established by Ghiglia and Pritt [90]. The aim of this section, however, is to explain a robust algorithm from each category followed by applying them to the simulated wrapped phase images explained in Section 5.1.3.

5.4.1 Quality guided path unwrapping algorithm

Of the local unwrapping techniques, quality guided path unwrapping algorithm is selected in this section. In this method the unwrapped phase is accomplished by integrating the wrapped phase difference between two successive points, along a definite path. Quality guided algorithm requires a quality map to lead the algorithm for unwrapping high quality data first and unwrap the rest based on its quality in descending quality order.Therefore a reliable quality map can dramatically enhance the output.

Among the previously developed quality maps, the two-dimensional second difference quality map introduced by [94] has been nominated by several researchers (e.g. Abdul-Rahman [95]), as the most robust quality map. This quality map, however, reveals the badness of the data rather than the goodness. Therefore the reciprocal of the output describes the goodness of pixels. The algorithm defines the goodness of pixel QM by [94]:

$$QM(i,j) = \frac{1}{\sqrt{H_d^2(i,j) + V_d^2(i,j) + D_1(i,j) + D_2(i,j)}}, \tag{5.31}$$

where;

$H_d(i,j) = \Upsilon(\psi(i-1,j) - \psi(i,j)) - \Upsilon(\psi(i,j) - \psi(i+1,j)),$

$V_d(i,j) = \Upsilon(\psi(i,j-1) - \psi(i,j)) - \Upsilon(\psi(i,j) - \psi(i,j+1)),$

$D_1(i,j) = \Upsilon(\psi(i-1,j-1) - \psi(i,j)) - \Upsilon(\psi(i,j) - \psi(i+1,j+1)),$

$D_2(i,j) = \Upsilon(\psi(i-1,j+1) - \psi(i,j)) - \Upsilon(\psi(i,j) - \psi(i+1,j-1)).$

Here $H_d(i,j)$ and D_1 illustrating the second difference in the horizontal and $V_d(i,j)$ and D_2 illustrating the second difference in the vertical direction of the matrix. The $\Upsilon[\,]$ term is a one-dimensional unwrapper.

The quality path unwrapping algorithm starts by adding the reliability value of each pixel to its neighbouring pixels. The accumulated value is written at the edge where the two pixels are connected. The pixel reliabilities and edge values of a part of a wrapped image are illustrated in Fig. 5.16 (a) and (b) respectively.

The unwrapping algorithm starts by unwrapping pixels which share the highest edge value. In Fig. 5.16 (c), the pixels g and f are first unwrapped with respect to one another. Next, the unwrapping applied to the wrapped pixels with the next highest

edge value; a and b which in this case constructs the second group. The unwrapping algorithm follows such a trend and unwraps the pixels with respect to their reliability values in the descending order; performed next between i and j. As seen in Fig. 5.16 (d) and (e), of the wrapped pixels the edge connecting pixels a and e has the forth highest value. Therefore, the unwrapping of pixel e carried out with respect to pixel a and therefore three pixels a, b and e are in the same group.

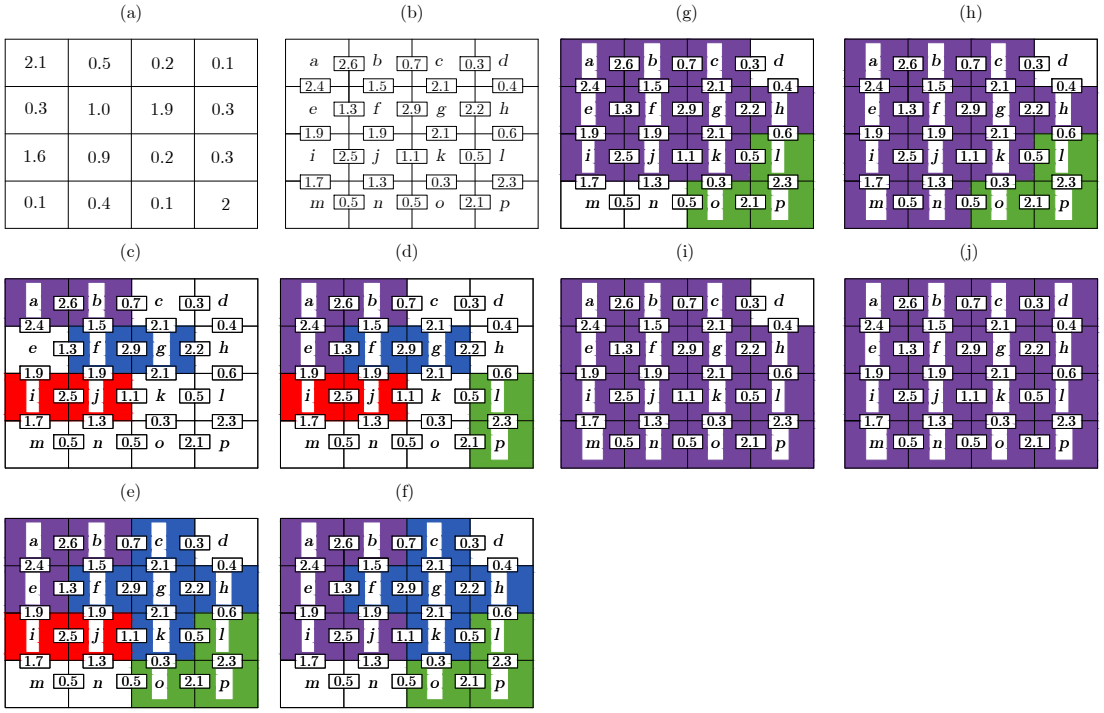

FIGURE 5.16: An example of unwrapping of a part of a wrapped image using quality map. (a) The reliability and (b) edge values of pixels. (c) Unwrapping pixels which have the highest edge value. (d) Unwrapping the wrapped pixels with respect to each other and a group of unwrapped phase. (e) Unwrapping the wrapped pixels, which has the highest edge value, with respect to a unwrapped group. (f,g) Unwrapping two groups of unwrapped phase with respect to each other (h) Unwrapping two pixels with respect to each other followed by re-unwrapping them with respect to the bigger unwrapped group. (i) Unwrapping the smaller unwrapped group with respect to the bigger one. (j) Unwrapping the last pixel with respect to the unwrapped group.

A similar trend is followed for the wrapped pixels which share the highest edge value with any unwrapped pixel group. Provided two groups share a highest edge value, the unwrapping carried out between the two group, as illustrated in in Fig. 5.16 (e) and (f). In this case the smaller group is unwrapped with respect to the other one. In Fig. 5.16 (f) the two groups with a blue and purple colour share the edge value of 1.9 which is the highest value compared to the other wrapped values. In the situation of equal pixel number for each group, the unwrapping between the two groups can be carried out in either way. As seen in 5.16 (g) and (h) the rest of pixels are unwrapped according to

their edge value and connected to the purple group. The disconnected unwrapped group and pixels shown in Fig. 5.16 (h) and (i) are unwrapped with respect to the purple group and the final unwrapped image is achieved as shown Fig. 5.16 (h). As a whole, in this unwrapping algorithm three cases are possible:

1- There is two wrapped pixels. The two pixels should be unwrapped with respect to one another.

2- There are two pixels; one of which is previously unwrapped and belongs to a group and the other one is wrapped. In this situation the wrapped pixel should be unwrapped with respect to the wrapped pixels.

3- There are two group pixels which are previously unwrapped independently, while they share the highest edge value. The pixels belongs to the smaller group need to be unwrapped with respect to the bigger group.

As seen in Fig. 5.16, the unwrapping is carried out along a certain path and the individual pixels are under focus at each step rather than the whole image.

5.4.2 Weighted least squared method

Weighted least squared method is a branch of global phase unwrapping algorithm. Global phase unwrapping methods are the second class of two-dimensional phase unwrapping algorithms. Calling the approaches global unwrapping is due to the minimization of errors over the entire wrapped phase images. These approaches aim to find an unwrapped phase when rewrapped, the error between the gradient of the re-wrapped phase and initial wrapped phase is minimised, as illustrated in bellow:

$$\varepsilon^2 = \| \text{ solution} - \text{problem } \|^2 . \tag{5.32}$$

For an image containing some corrupted regions, large amount of unnecessary computations, however, have to be carried out over the corrupted area. As this technique focuses on minimization of the phase gradient difference, equalizing the contribution from the high quality and residues pixels might generate undesirable results. A weighting function, for instance the one explained in Section 5.4.1 can be used and wight the phase

data prior to unwrapping. Eq. (5.32) with a weighting function can be rewritten as:

$$\varepsilon^2 = \sum_{i=0}^{M-2}\sum_{j=0}^{N-1} U(i.j)\left(\phi_{i+1,j} - \phi_{i,j} - \Delta_{i,j}^{x}\right)^2 + \sum_{i=0}^{M-1}\sum_{j=0}^{N-2} V(i,j)\left(\phi_{i,j+1} - \phi_{i,j} - \Delta_{i,j}^{y}\right)^2, \tag{5.33}$$

where $\Delta_{i,j}^{x}$ and $\Delta_{i,j}^{y}$ are the wrapped value of the wrapped phase difference between two successive pixels along the x and y direction of the image. The $\phi_{i,j}$ term is the unwrapped phase solution which minimises Eq. (5.33). The U(i,j) and V(i,j) terms are the gradient weights given for the x-gradient and y-gradient of a wrapped phase image respectively. These gradient weights can be expressed by:

$$U_{i,j}^{x} = \min(\varrho_{i+1,j}^2 + \varrho_{i,j}^2),\ V_{i,j}^{y} = \min(\varrho_{i,j+1}^2 + \varrho_{i,j}^2), \tag{5.34}$$

where $\varrho_{i,j}$ is the quality of the pixel (i,j), $0 \leqslant \varrho_{i,j}^{x}, \varrho_{i,j}^{y} \leqslant 1$. The quality map can be calculated using, for example, the function discussed in Section 5.4.1. Eq. (5.33) explains the relation between the weighted phase difference at the rows and the columns and their unwrapped phase $\phi_{i,j}$, which can be simplified to:

$$\begin{aligned} U(i,j)\Delta^x\phi(i,j) - U(i-1,j)\Delta^x\phi(i-1,j) + \\ V(i,j)\Delta^y\phi(i,j) - V(i,j-1)\Delta^y\phi(i,j-1) = \rho_{i,j} \end{aligned} \tag{5.35}$$

where

$$\begin{aligned} \rho_{i,j} = (U(i,j)\Delta^x\psi(i,j) - U(i-1,j)\Delta^x\psi(i-1,j)) \\ + (V(i,j)\Delta^y\psi(i,j) - V(i,j-1)\Delta^y\psi(i,j-1)) \end{aligned} \tag{5.36}$$

Eq. (5.33) can be transformed into a matrix vector to form a problem into a linear system as:

$$\mathbf{D}\phi = \rho, \tag{5.37}$$

where ϕ is the columns vector unwrapped phase solution and $\mathbf{D}$ is the discrete weighted Laplacian operator defined in the left hand side of Eq. (5.36).

Solving the weighted least squared method directly through Fast Fourier transform ,FFT, and Discrete Cosine Transform, DCT, can not be achieved [96]. Instead, Gauss-Seidel relaxation method can be used and provide the unwrapped phase iteratively using the

equation:

$$\phi_{i,j} = \frac{U(i,j)\phi_{i+1,j} + U(i-1,j)\phi_{i-1,j} + V(i,j)\phi_{i,j+1} + V(i,j-1)\phi_{i,j-1} - \rho(i,j)}{v_{i,j}}, \tag{5.38}$$

where $v_{i,j}$ is defined by:

$$v_{i,j} = U(i,j) + U(i-1,j) + V(i,j) + V(i,j-1). \tag{5.39}$$

The convergences of this algorithm is slow and normally multigrid methods are used to accelerate it. Furthermore, a number of iterative methods for instance Picard iteration method, the preconditioned conjugate gradient (PCG) and the weighted multigrid algorithms, have been developed to solve the weighed method [96].

5.4.3 Applying the two-dimensional phase unwrapping to the wrapped data

The quality guided path following and the weighted least squared unwrapping are applied to the wrapped data explain is Section 5.1.5, and the results are illustrated in Figs. (5.17) and (5.18) respectively. Although the unwrapping algorithm of these two methods is different from one another, the obtained results are somewhat identical. The produced plots are very similar to the ones obtained from the radial unwrapping algorithm, which were illustrated in Fig. 5.15. Because the unwrapping operations were performed without increasing the wrapped phase image resolution, above approximately 50 Hz, a corrupted area from under sampling can be seen, at where the body waves dominate, in Figs. (5.17) and (5.18). Presence of the corrupted areas suggest that the absolute difference between two successive samples is larger than a value of π. In both figures, the corrupted area from under sampling are well localised and the error does not propagate throughout the unwrapped phase images. At higher frequencies (aproximately $> 160\,\text{Hz}$), which is not presented here, the wrapped phase data from the conical wave fronts violates the spatial Nyquist sampling criterion and whole the image is contaminated with spatial aliasing and the results are no longer presentable.

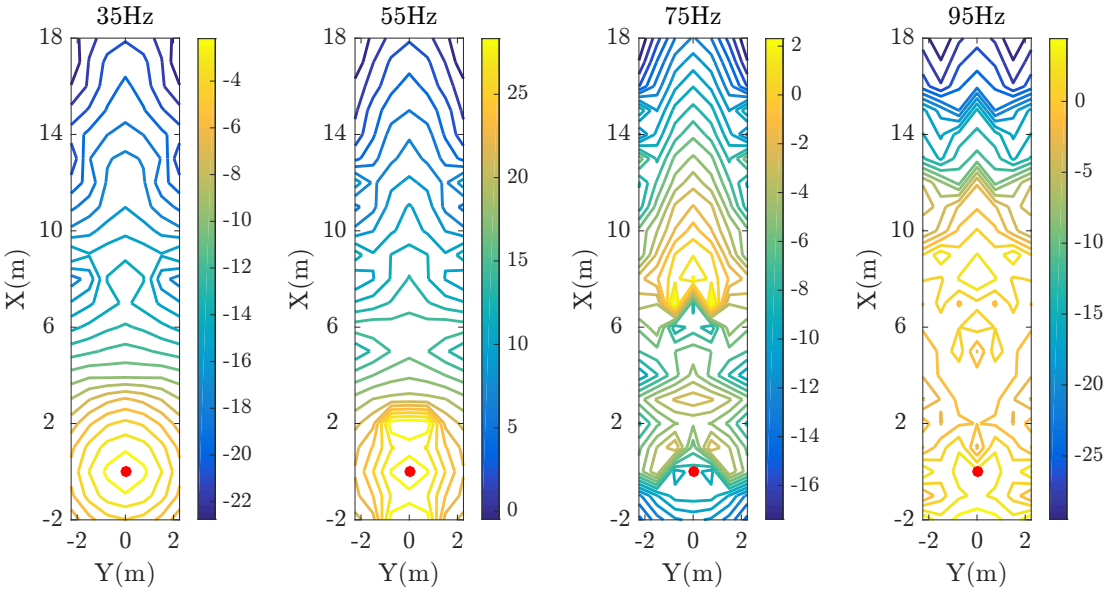

FIGURE 5.17: Illustrative of spatially unwrapped phase, in radians, using quality guided path following approach explained in Section 5.4.1. The unwrapping operation was performed without increasing the wrapped phase image resolution and the corresponding wrapped data is illustrated in Fig. 5.6.

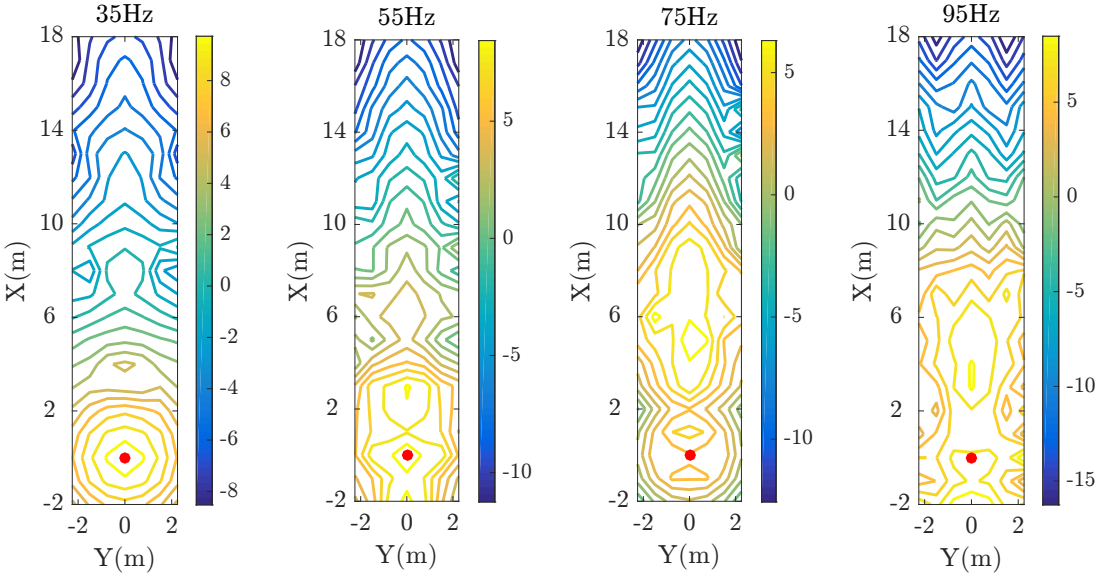

FIGURE 5.18: Illustrative of spatially unwrapped phase, in radians, using weighted least squared approach with the quality factor explained in Eq. (5.31). The unwrapping operation was performed without increasing the wrapped phase image resolution and the corresponding wrapped data is illustrated in Fig. 5.6.

5.4.4 Improving the image resolution

This section aims to propose a simple method to overcome the problem of phase aliasing in the wrapped and unwrapped images. In this method, frequency wrapped phase from each pixel is exploited to resample the wrapped image at the Nyquist rate or higher.

Wrapped phase difference or the partial derivative of each measurement point can be calculated as follows:

$$\mathbf{W}\{\Delta M(x,y,f)\} = \mathbf{W}\{\Delta M(x,y,f) - M(x,y,f-1)\}. \tag{5.40}$$

By assuming that the frequency wrapped phase data is well sampled, the value of the wrapped phase difference in Eq. (5.40) should lie into the interval $(-\pi, \pi)$. Next, a bilinear interpolation should be applied to the wrapped phase differences matrix so as to increase the image points. Therefore, the new matrix contains a higher number of measurement points compared to its initial. Then, the interpolated data at every frequency is added to its previous value followed by re-wrapping the image as follows:

$$\mathbf{W}\{\Delta M(x,y,f)\} = \sum_{f=1}^{n-1} W\{M(x,y,f-1) + M(x,y,f)\}. \tag{5.41}$$

The reconstructed signal now has higher points compared to its initial grid points. After applying the two-dimensional unwrapping operator, the bilinear interpolation is again used to represent the data at its initial grid spacing.

Each of the two-dimensional unwrapping algorithms is applied to the wrapped phase data, based on the description given in Section 5.4.4. The unwrapped phase data from the quality guided path and the weighted least squared method is illustrated in Fig. 5.19 and Fig. 5.20 respectively. As shown in the two following figures, there is no sign of spatial aliasing at the areas where the body waves are dominant. The data from the following figures suggests that tracing the pipe via the vibro-acosutic technique, provided that the Nyquist sampling rate is not violated, should not be limited to a low frequency region. This view is grounded on the assumption that below the ring frequency, most of the energy are carried by the axisymmetric fluid borne wave, causing re-radiation of energy into the external medium.

5.5 Performance of the proposed unwrapping algorithms

This section aims to discuss performances of the unwrapping algorithms applied to the simulated wrapped phase images displayed in Fig. 5.6. The radial unwrapping outcomes

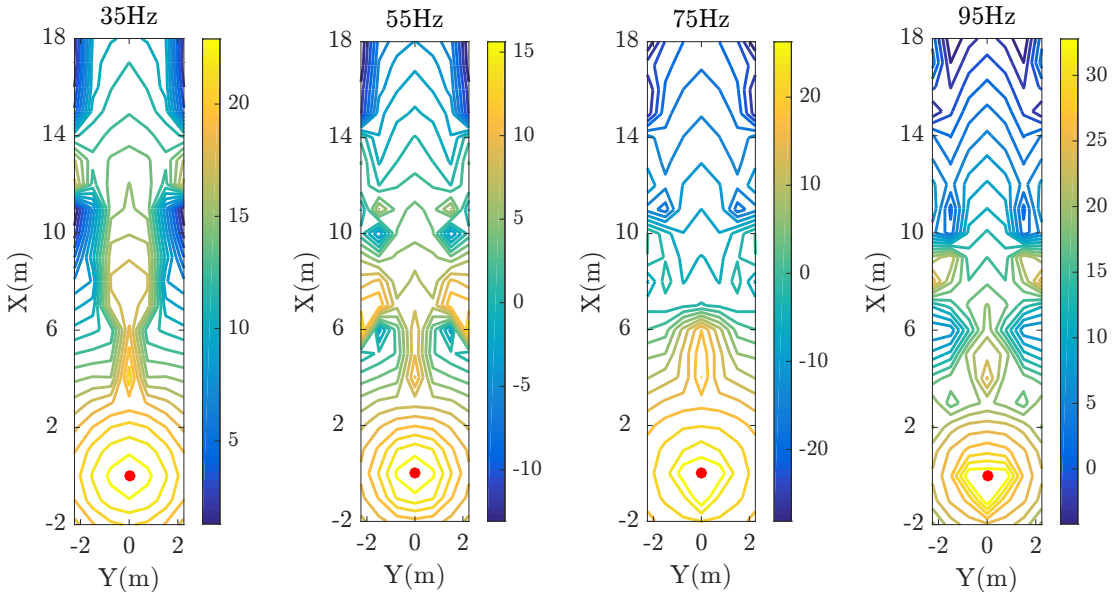

FIGURE 5.19: Illustrative of spatially unwrapped phase, in radians, using quality guided path following approach. The resolution of images is increased artificially.

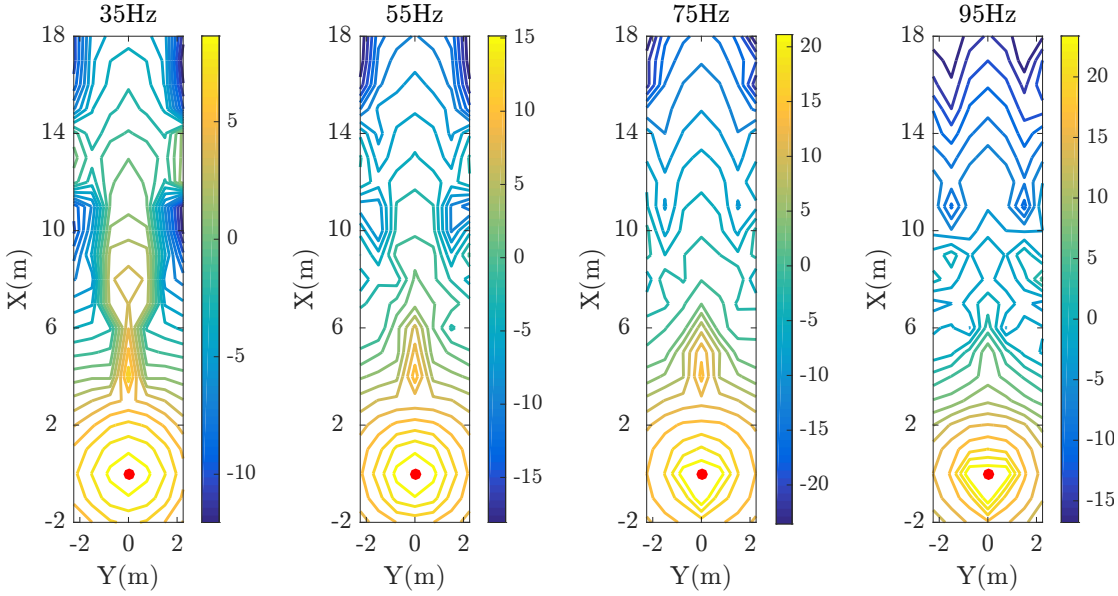

FIGURE 5.20: Illustrative of spatially unwrapped phase, in radians, using weighted least squared approach with the quality factor explained in Eq. (5.31). The resolution of images is increased artificially.

was very similar to that of two-dimensional unwrapping. Given that the method is very simple to be implemented, it does not benefit from any quality map. In this case, it is very likely to have propagation of errors along the image. To advance the technique, a weight function can be incorporated to the algorithm to isolate the residues.

Both adopted two-dimensional unwrapping algorithm are able to successfully unwrapped the images. Owing to have negligible output difference, it is hard to nominate any of

which as a more robust algorithm. Because of less computational requirement of quality guided path following method, it was decided to select it for unwrapping the phase data in the next chapter.

5.6 Discussion on the data analysis

Further investigations on the unwrapped phase data of the model illustrated in Section 5.1.4 allow:

1. to determine the region where the two wave types; spherical and conical waves are dominant.
2. to estimate the wave speed of the pipe and the surrounding medium.

Given that the shape of appeared continuous wave fronts illustrates the approximate dominance region of each wave type, it is worth to indicate from where exactly the magnitude of the the conical wave front become comparable to the body wave fronts. With the experimental output, determining such regions are not feasible. The reason of recalculating the input wave speeds from unwrapped phase data, is to check whether it is feasible to end up with the desired values.

5.6.1 Width of conical wave fronts

In this section, the discussion will point to identifying the region where the shear conical and the spherical wave fronts are dominant. Although the dominant region of each source slightly alters with the excitation frequency, it is worth to estimate it for a single frequency. The selected region, shown in Fig. 5.21, involves six measurement lines crossing the pipe axis starting from one metre distance from the origin.

Quantifying the amplitude of the surface vibrational velocity from each source is achieved by taking the absolute value of each wave equation at the specified location and frequency. As seen in Fig. 5.22, these results provide confirmatory evidence that the region where several wave types contribute with similar amplitudes, are not reliable and can be referred as corrupted areas. In this context, the aforementioned area is the region where the conical wave fronts starts to dominate. Identifying the dominant area of

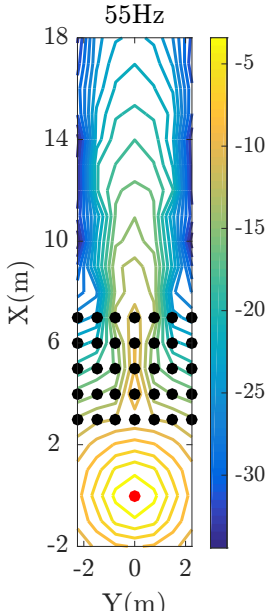

FIGURE 5.21: The selected measurement points, highlighted with red dots are in grid lines perpendicular to the pipe axis, started from 3 m up to 7 m distance from the origin.

each source in practice depend partially on how and where the pipe is subjected to the excitation, on pipe configuration, material properties of the pipe, on the internal and external media and is different from case to case.

If the point source comprises a relatively high amplitude compared to the pipe source, at a distance far away from the excitation source, plane wave fronts should appear on the plot. To have a deeper insight about this phenomenon, lets assume that only a single wave emitted from the point source causes the surface vibration. The radial distance from the point source to the measurement point can be explained by:

$$r^2 = x^2 + y^2 + h^2 = Y^2 \left(1 + {}^{x^2}/_{y^2} + {}^{h^2}/_{y^2}\right). \tag{5.42}$$

Provided that $y \gg x, h$, Taylor expansion of equation(5.42) gives:

$$r = Y \left(1 + {}^{x^2}/_{2y} + {}^{h^2}/_{2y} + ...\right) \longrightarrow r \approx {}^{x^2}/_{2y} + {}^{h}/_{2y}. \tag{5.43}$$

As a result, at a far away distance from the excitation point the appearance of a plane wave from the point source is expected. Owing to a higher amplitude of pipe source, under an in-pipe excitation compared to the structural excitation, after some distance

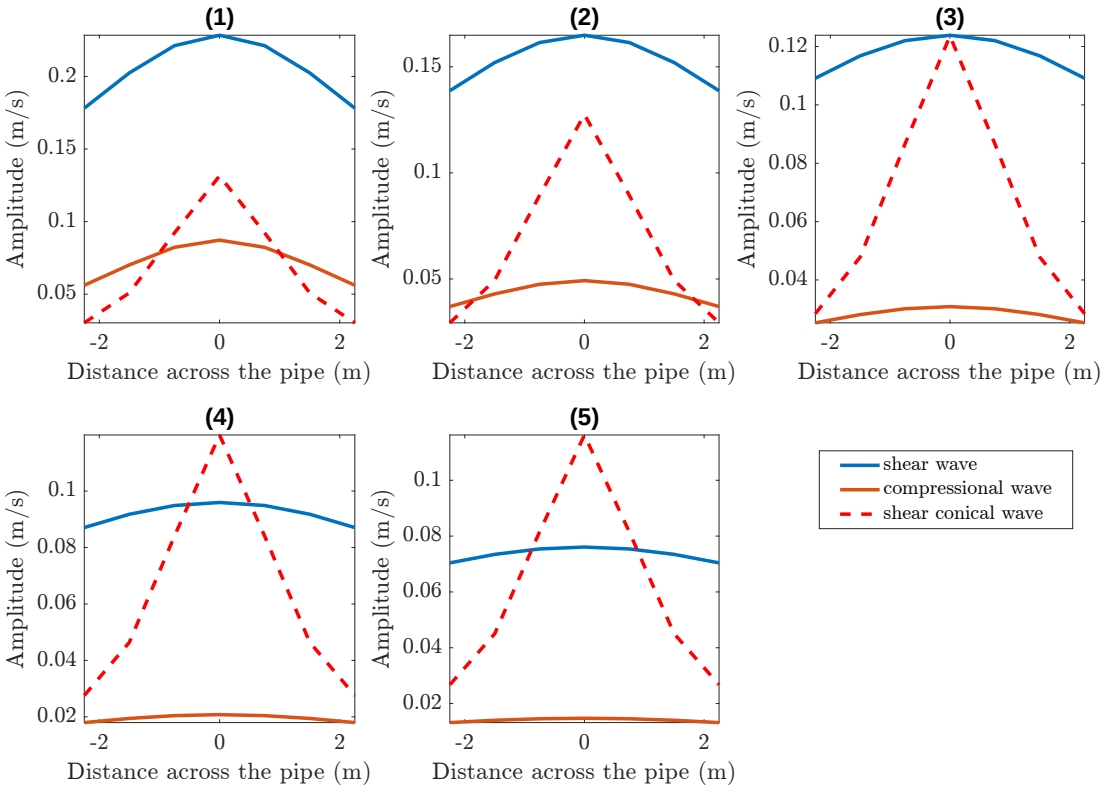

FIGURE 5.22: A comparison between the amplitudes of the body waves and the shear conical waves, for each grind line perpendicular to the pipe axis shown in Fig. 5.21 at 55 Hz, in m/s.

from the excitation source the surface vibration become due to mostly a conical wave front.

5.6.2 Estimation of the pipe source wave speed

On the obtained numerical results, inversion analysis is carried out, to find the value of the pipe source wave speed. To this end, a number of points above the pipe axis illustrated in Fig. 5.23 are selected for further examination.

There are several ways to extract the pipe wave speed. In here, the gradient of the difference between two measurement points along the pipe axis is used. Therefore the wave speed along the pipe, c_1, can be obtained as follows:

$$c_1 = \left(\frac{2\pi}{\frac{d}{df}\left(\mathbf{W}\left(\frac{d\psi(f)}{dx}\right)\right)} \right) \text{m/s}, \tag{5.44}$$

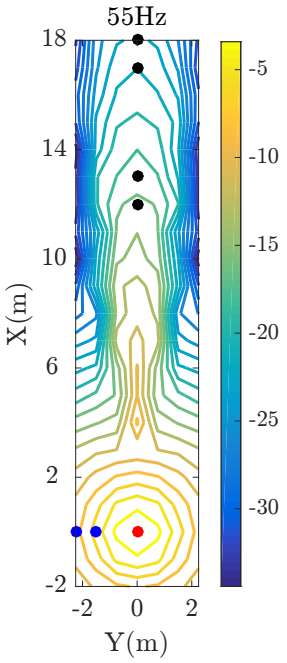

FIGURE 5.23: The selected points for post processing. The black points parallel to the pipe axis are used to estimate the wave speed within the pipe. The blue points perpendicular to the pipe axis are used to estimate the wave speed within the surrounding medium and the red spot illustrates the origin.

where:

$$\mathbf{W}\left(\frac{d\psi(f)}{dx}\right) = \mathbf{W}\left(\psi_{x_2}(f) - \psi_{x_1}(f)\right), \text{and } \left(\frac{d\psi(f)}{dx}\right) = \dot{\psi}(f). \tag{5.45}$$

Here the subscript 1 and 2 refer to the two subsequent measurement points along the pipe axis at the surface. The obtained wave speed from the two sets of points is plotted in Fig. 5.24. The value of the estimated wave speed from the two points at the middle of plots deviates from its nominal value and possesses higher fluctuation compared to the other one.

Deviation of wave speed values associated with each two sets of the points are reported in Table 2. Although the relatively faraway location along the pipe axis encodes more accurate information of the pipe wave speed, attenuation of the pipe wave due to the pipe material damping and the radiation loss might lead to masking of the signal by the environmental noise.

Coupled with the interference of the spherical and the conical wave front, a common source of error in practical measurement is due to the misplaced sensors within the

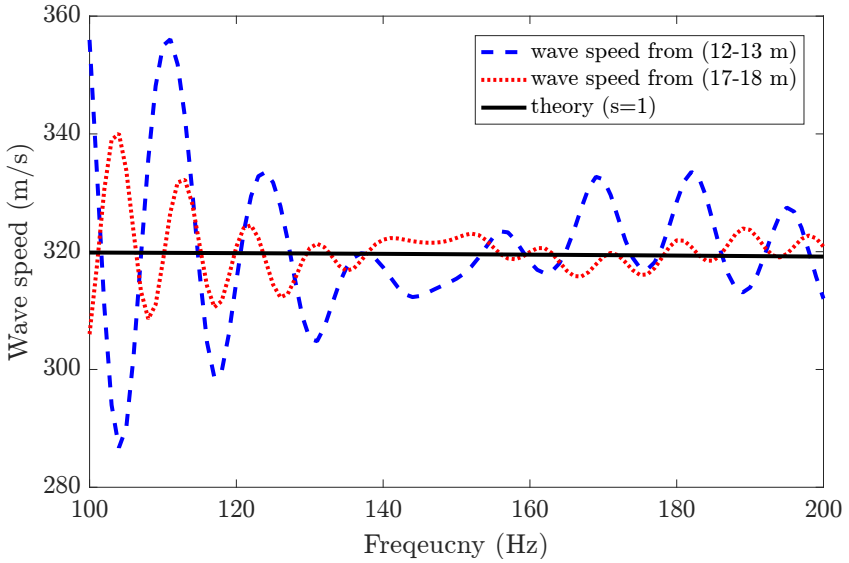

FIGURE 5.24: Illustration of the pipe wave speed estimated from the point located at 12 m and 13 m distance; (- - -), 17 m and 18 m; (·····), distance from the point source at the surface. The input wave speed for the pipe source; (——). Below 100 Hz the data variation is extremely high and further 200 Hz it becomes negligible.

TABLE 5.2: Deviation of the wave speeds due to interference of the conical and spherical wave fronts.

Data related to 100 Hz to 200 Hz bandwidth		
Distance of the point source set from the source at the surface	Standard deviation	Mean value of the wave speed deviation from theory
First two set points located at (12 m-13 m)	10 m/s	35 m/s
First two set points located at (17 m-18 m)	5 m/s	10 m/s

measurement grid. A closer look at Eq. (5.44) indicates that increasing the distance between the two grid points along the pipe axis by ε_P causes underestimation of the pipe wave speed by $\frac{\varepsilon_P}{c_1}$ (m/s). Furthermore, the ground surface normally is not perfectly flat, leading to an increase to the approximation of the estimated value. In this cause, if the next point is not on the same level, the approximation would be $\frac{\varepsilon_G}{c_{s-SV}}$ (m/s), where c_{s-SV} is the speed of shear conical wave fronts emitted from the pipe.

5.6.3 Estimation of the wave speed in the soil

To estimate the speed of dominant wave within the soil, two-measurement points in a line crossing the pipe at the origin should be selected. This automatically excludes the effect of the conical wave fronts, leading to a better estimation. Since the distance from the point source to the measurement points at the surface varies with $r_p = \sqrt{y^2 + h_d^2}$

the speed of the dominant wave can be identified by using the phase data from the two measurement points as follows:

$$c = \frac{2\pi}{\frac{d}{df}\left(\frac{df}{dx}\right)}\left(\sqrt{y^2+h_d^2}-\sqrt{y^2+h_d^2}\right) \tag{5.46}$$

Applying the above equation to the selected points phase data, results in an erroneous wave speed shown in Fig. 5.23. On the basis of the illustrated data it can be concluded that at the presence of the two waves, utilising the above equation would not be effective. Hence, for the wave speed estimation to be effective, a wave decomposition must be performed a priori. In practice, it is likely that the ground surface vibration is due to only one wave type. Removing one of the utilised body wave amplitude leads to obtaining the nominal wave speed but for brevity it is not shown here. In the case where a surface wave dominates, Eq. (5.46) should be equal to zero.

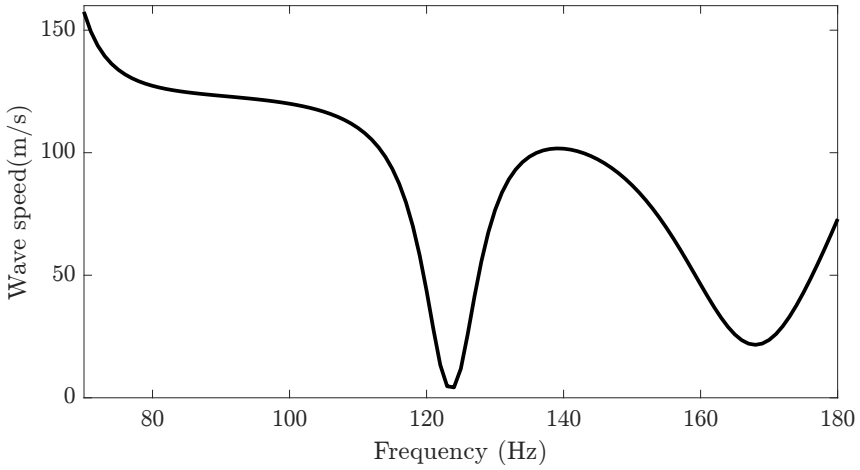

FIGURE 5.25: Estimation of the wave speed within the surrounding medium. Data obtained from the two points in the line that crosses the pipe axis at the origin shown in Fig. 5.23.

5.7 Summary

In this chapter an analytical simulation was developed to provide a new insight into the concept of vibro-acoustic technique.

An important requisite to localise buried pipes through the vibro-acoustic approach is unwrapping the obtained phase data with the assistance of a robust algorithm. A

brief review on the concept of unwrapping processes and the shortcoming of applying one-dimensional unwrapping algorithm to the wrapped image was fully discussed.

A simple unwrapping algorithm, named radial unwrapping, was developed with the aim of reducing the computational effort. Having applied the algorithms to the simulated wrapped images, it was learned that the body waves only dominate near to the source and are local. In addition, interference of the body waves and shear conical wave front does not take place at a lateral distance far form the pipe axis; along the pipe. Provided that the there is no reflection from the pipe end, after a certain distance from the excitation source, the pipe waves dominates over the whole image rather than a narrow area over the pipe axis.Although the radial unwrapping is suitable to reconstruct a continuous shear and conical wave fronts, it is unable to isolate the region where residues exist. Therefore, the technique is not sufficiently robust to be applied on the experimental data. Adding a weighting, however, can solve the problem.

Given that hundreds of unwrapping algorithm were previously developed for different applications, a state-of-the-art algorithm from two major categories of two-dimensional unwrapping are explained in detail and applied to the wrapped simulated phase data. Even though from the unwrapped phase images the region where each wave is dominate, further post processing is carried out to indicate the location where the pipe waves amplitude become comparable to that of source waves.

Coupled with the attenuation, spatial aliasing causes the pipe localisation become limited to a limited frequency band. In this regard, the role of spatial aliasing is more important. In this simulation it is shown that the reconstructed surface vibration form the body started to have aliasing from some region at 50 Hz. Although it was attempted to overcome such an issue through artificially increasing the measurement points, yet it is not clear to whether the method is feasible on the experimental data.

Further attempt to estimate the wave speed and attenuation of the each wave type was carried out. It was shown that it is very unlikely to end up with the same input value. Even though it is assumed only one wave type emitted from the pipe, estimating its input value was severely affected by the point source wave. As at well below the ring frequency, the axisymmetric wave causes most of the radiation to the surrounding medium, it was suggested to work out on the data at higher frequency ranges >100

Hz. Likewise exploring the data at higher frequency ranges >200 Hz might reveals the dominated source wave speed.

Chapter 6

Experimental investigation to trace buried water pipes

The purpose of this chapter is tracing buried water pipes using the designed pneumatic devices in Chapter 4 and validate the simulation in Chapter 5. To benchmark the effectiveness of the designed pneumatic devices, different exciters such as standard mechanical and electro acoustical exciter are employed as well. The obtained results are analysed in detail and compared to each other.

To check the repeatability of measurements, more than one test was made for each measurement. Discussing all the data in detail, however, is not possible due to the large mount of data acquired. Therefore, repeatability of the measurements are briefly discussed for each sources. Furthermore, to facilitate the interpretation of the results, the back ground noise level was recorded and discussions about the signal to noise ratio are provided in in Section 6.7.

Measurements with the speaker were made on the 13th and the 14th April 2018. The temperature on both days during the measurements was approximately 10 °C. There was no raining from one day before starting the measurements and the soil was dry.

The measurement with the pipe water gun was made on 5th May 2018. The day was sunny and the temperature was approximately 22 °C. there was no raining up to three weeks before the measurement and the soil was dry.

The shaker measurement on the water filled and the empty pipe was made on the 11th and the 17th of May 2018 respectively. On both days, the days was sunny and the temperature was approximately 15 °C. During the measurement on 17th of May the soil was dry, but there was a light raining when the last five array of the grid was recorded.

The measurement with the pipe balloon gun was made on the 11th and the 15th of June 2018. The days were sunny and the temperature during the measurements on both days was approximately 20 °C. As measurements were carried out on different days, the soil condition varies from case to case. Nevertheless, for all measurements the soil was relatively dry and there was no raining at the day before conducting the measurement.

6.1 Description of the experimental rig

The rig consists of a 18 metre long, medium density plastic pipe (MDPE) with Young's modulus of 2×10^9 (N/m^2), wall thickness of 11×10^{-3} m and a mean radius of 8.45×10^{-2} m, buried approximately 1 to 1.25 metres deep into the soil [25]. As illustrated in Fig. 6.1, access to the pipe can be gained at two positions; (i) from the pipe start point where the pipe right angled bend brings the pipe to the surface (ii) and from a pit at the pipe end. A schematic of the test rig is shown in Fig. 6.1 and the accesses to the pipe are labelled. As seen in Fig. 6.2 the pipe was previously instrumented with two small pipes to remove trapped bubbles and to monitor the pressure respectively [97]. The main pipe could not be filled up to the rim and the last approximately 50 cm of the vertical pipe was empty. Assuredly, the less the pipe is pressurised the lower radiation from the fluid dominated axisymmetric wave to the surrounding medium is expected when subject to an excitation. Having observed a water accumulation at the manhole, a water leak from the small pipe near to the pipe end was suspected.

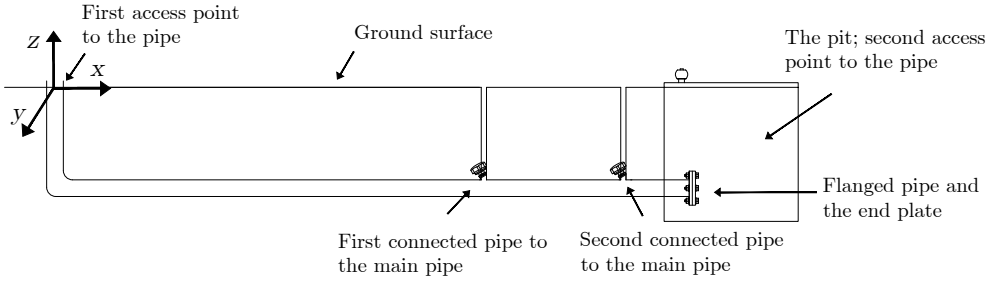

FIGURE 6.1: A schematic of the experimental test rig.

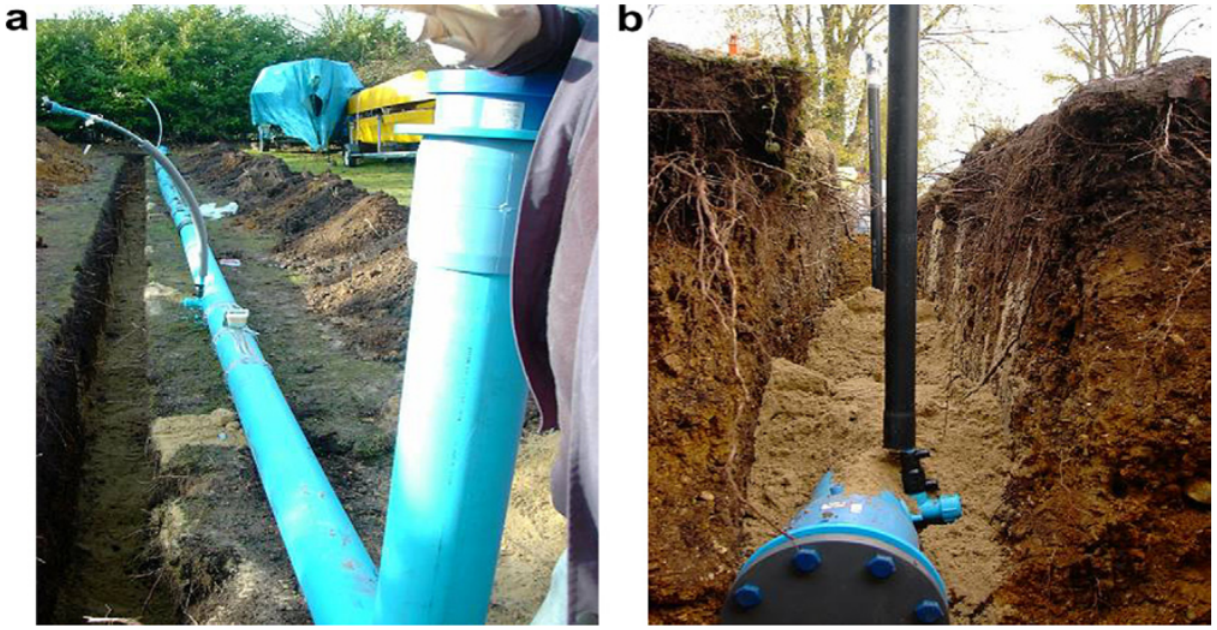

FIGURE 6.2: Placing pipe into the ground: (a) before burying the pipe; (b) burying the pipe to the ground and covering its main axis via sandy soil [97].

It is well-known that the axisymmtric fluid borne wave causes radiation to the surrounding medium. That said, applying any intentional excitation that is able to transfer a high amplitude low frequency signal to this wave, will then lead to the detection of buried pipes through the vibro-acoustic technique. To assess the feasibility of using in-pipe excitations for pipe tracing, the pipe was subjected to internal excitations at three different locations. The selected internal excitation locations were at the right angle bend, and at 6 m and 12 m offset from it. In this measurement, the first and the second access point to the pipe are referred to as starting and ending point respectively.

Recordings of the ground surface vibration, using tri-axial I/O SM-24 geophones, were carried out over a rectangular grid of measurement points, spaced 0.75 metre apart in the y and 1 metre apart in the x direction. The origin for every measurement is assumed the location at which the excitation is applied to the pipe and the pipe runs up the centre-line in all of them.

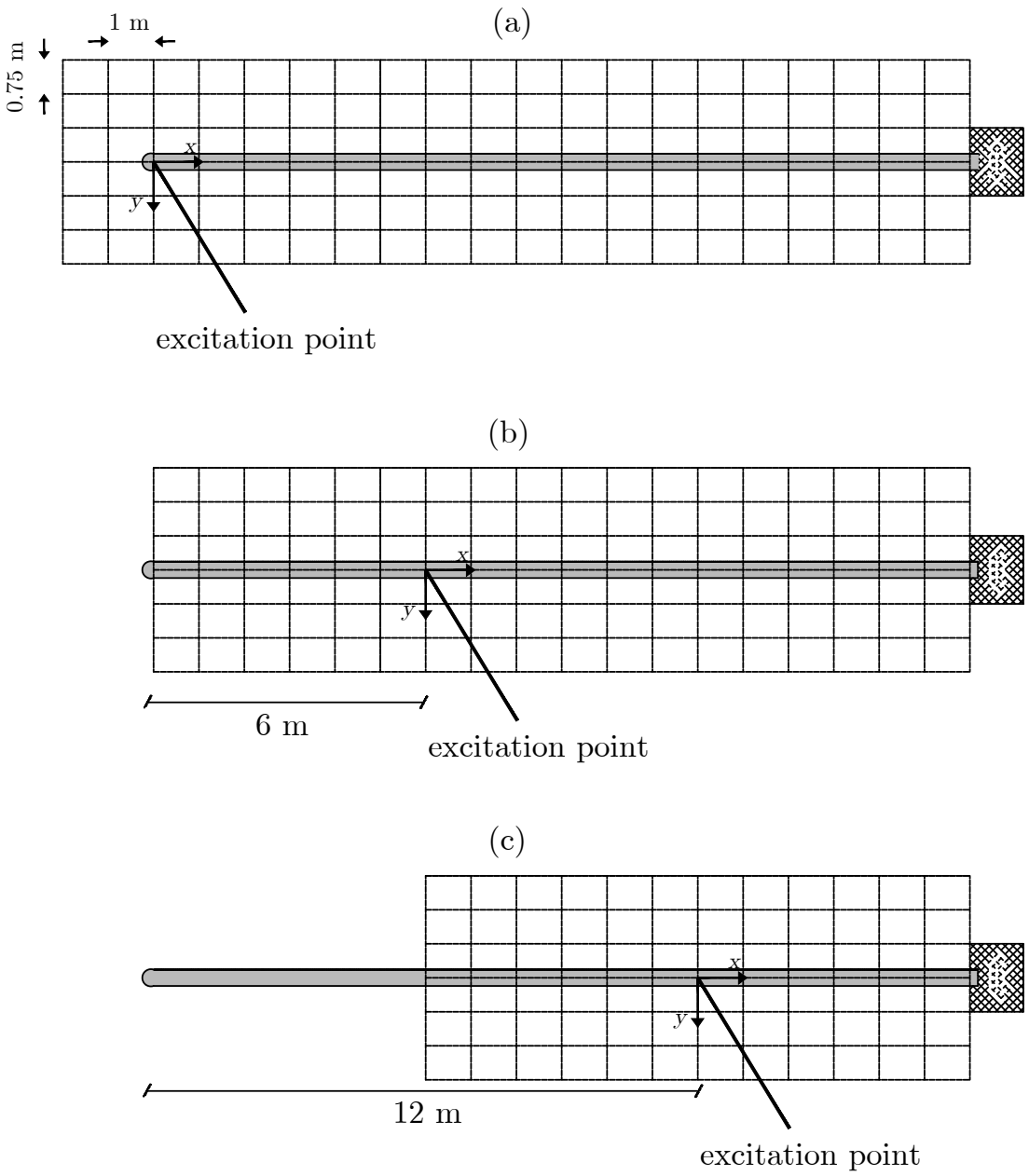

FIGURE 6.3: A plan view of the measurement grid points used to record the surface vibration. (a) First selected location for the exciter and its measurement grid. The selected measurement grid points for the shaker is the same as this one. (b) Second selected location for the exciters and its measurement grid points (c) Third selected location for the exciters and its measurement grid.

The first grid covers the whole length of the pipe plus two metres behind the excitation point, where the right angle bend brings the pipe to the surface . The second and the third grid cover the pipe length from the 6 metres behind their excitation position up to the pipe end; where the manhole allows the access to the pipe, as illustrated in Fig. 6.3. A photograph of the geophone array used to measure the ground surface vibrational velocity is illustrated in Fig. 6.4.

The utilised internal sources are the two pneumatic exciters, which are developed and re-engineered in Chapter 4, as well as the Coomber 1932 underwater loudspeaker that was used in the same chapter. For the sake of comparison, the pipe was subjected also to a similar excitation source that was used in reference [25]. The mechanical excitation was only applied from the start point to the pipe.

FIGURE 6.4: Experimental set up employing an in-pipe excitation technique to locate buried MDPE pipes. (a) Illustration of the third geophone array, the excitation source located on the ground surface and the pipe's main axis at the surface. (b) The position of the sixth geophone array.

6.2 Signal processing

The ground surface vibration velocity was measured with seven tiaxial geophones with the sensitivity of 21 $\left(\frac{\text{m/s}}{\text{V}}\right)$, using the Prosig 8000 DATA Acquisition System which possesses 24 input channels. The measurement system is illustrated in Fig. (6.5).

A noise free reference signal with high level of correlation to the input signal to the system is required to find a reliable phase spectrum. This signal can be acquired by recording the supplied voltage to the acoustic and the mechanical device. For the pneumatic sources, the output signal from the PVDF sensor was routed to the Brüel and Kjær charge amplifier type 2635 and recorded via the Prosig. Furthermore, in all measurements, an extra reference signal was acquired via placing a hydrophone near to the exciters.

The data from the acquisition was stored in a PC for further analysis. If cross spectrum form S_{xy}, between the input source to the system and measured ground surface, might ends up with several unwanted phase jumps. Reducing the number of jumps can be

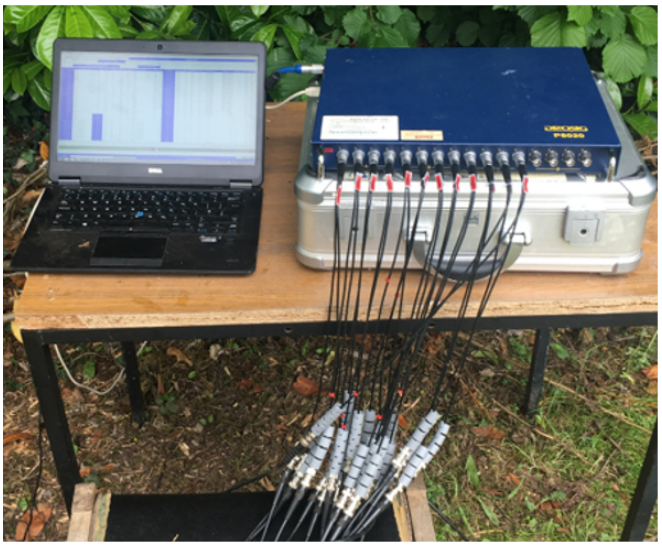

FIGURE 6.5: A picture of the Prosig and the laptop used to digitised and store the data.

achieved by dividing the obtained cross spectral density to the spectrum density of the point, $S_{Vy_{\text{ref}}}(f)$, which is the closest to the excitation source. Hence:

$$S_{Vy_{\text{norm}}}(\omega) = \frac{S_{Vy}}{S_{Vy_{\text{ref}}}}. \tag{6.1}$$

The output of $S_{Vy_{\text{norm}}}$ is a complex number, with the magnitude spectrum of $|S_{xy.ref}|$ with the phase spectrum $\psi = \arctan\left[\text{Im}(S_{Vy_{\text{norm}}})/\text{Re}(S_{Vy_{\text{norm}}})\right]$ where Re and Im refer to the real and the imaginary parts of the recorded signal and arctan is the four quadrant arc tangent operator, hence $-\pi < \psi < \pi$. Therefore the obtained measured phase is wrapped between $-\pi$ and π and a phase unwrapping algorithm is required to reconstruct a continuous phase lag as fully discussed in Chapter 5. Of the explained unwrapping algorithms, the quality guided path following method, which was explained in Section 5.4.1 is utilised in this section.

Assuming buried pipes are a good transmitter of vibrational energy, many pipe locator devices are designed to process magnitude data for addressing the pipe location. Sensing the magnitude of the ground surface vibration in the current technology lead to a poor detection rate specifically in noisy areas. Despite this, the magnitude of the surface vibration velocity suddenly drops after a distance of order 2-3 metres from the excitation point. Provided that the excitation is reproducible, however, the use of magnitude data

$|S_{xy,ref}|$ might allow recognition of any discontinuities along the pipe and provide some information about the sudden changes to the properties of the external medium [25].

6.3 Measurement with the pipe balloon gun

In this section, measurements were carried out to map the buried pipe using the pneumatic device with a balloon. A picture of the designed pneumatic devices is illustrated in Fig. 4.9. The pressure regulator attached to the air compressor valve specifies the pressure of the realising compressed air, transferring to the solenoid valve. An Arduino specifies the time at which the current and voltage are sent to the valve through the power supplies and hence controls the opening and closing of the valve. When the solenoid valve opens, the compressed air is transferred through the reinforced hose pipe and expands the balloon which is surrounded by water. Immediately after closing of the valve output port, the third port opens to drain the trapped air in the balloon. This pulsating expansion and relief drives the fluid with high amplitudes at low frequency. The PVDF sensors wrapped around the reinforced exhaust was provided a reference signal. The hydrophone at 15 cm distance from the balloon was for measuring the fluid excitation and was not related to the operation of the proposed vibro-acoustic technique. The signal from the PVDF sensor and the hydrophone were input into two separate Brüel and Kjær charge amplifiers, of Type 2635.

The utilized signal was composed of 8 pulses of 30 ms, each segment had 5 second duration. The signal was measured with a sample rate of 1 kHz, and with a low pass filter built into the DAC unit eliminating frequencies above 400 Hz to avoid aliasing. Discussion on the reproducibility of the pipe balloon gun is given in Appendix C.

Cross Spectrum Density (CSD) between the recorded pressure from the PVDF wire and the recorded surface vibrations from the geophones were computed by segmenting averaging using a rectangular window of 5000 samples with 50 % overlap.

6.3.1 Measurement data from the first grid

The measurement grid point and the excitation source location, used in this section, is shown in Fig. 6.3 (a). The way at which phase information was extracted from the

experimental data and the unwrapping process are explained in Sections 6.2 and 5.4.1. The contour plots of the unwrapped phase for a number of sample frequencies are given in Fig. 6.6 for a 10 Hz interval, from 37 to 97 Hz.

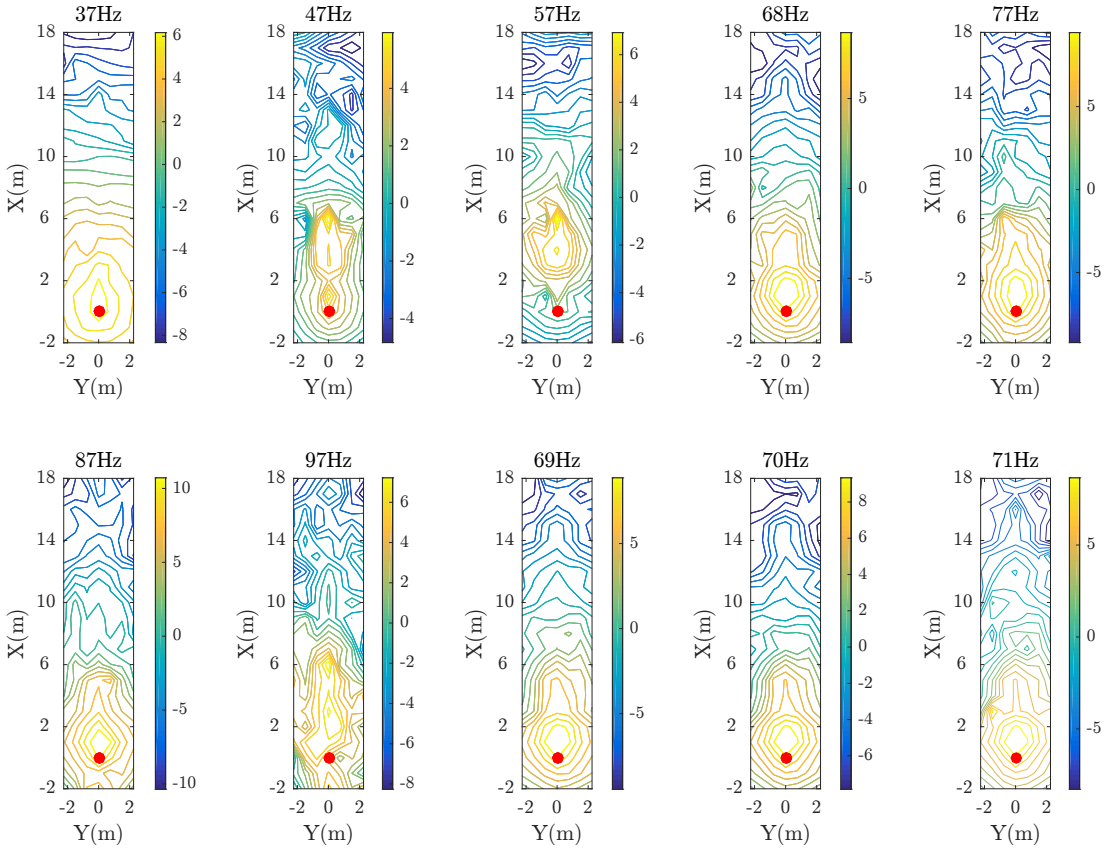

FIGURE 6.6: Contour plots of spatially-unwrapped phase of the normalised CSD between the ground surface vibration and the pressure sensed by the PVDF wire, in radians, using balloon gun. The x- and y-axes correspond to the axes shown in Fig. 6.3 (a).

The obtained data at 37 Hz shows spherical wave fronts near to the source location. The backside spherical wave fronts at the pipe end is due to the energy radiation from the pipe end. Emergence of the surface vibration due to conical wave fronts become more evident at 47 Hz and 57 Hz. The image at 67 Hz is reassuring and most of the conical wave fronts dominate. From the graph at 77 Hz, 87 Hz and 97 Hz, the contribution of the conical wave fronts on the ground surface vibration is obvious up to 12 metre distance. The frequency band at which the pipe location become the most obvious is 67-77 Hz.

6.3.2 Measurement data from the second grid

The measurement grid point and the excitation source location, used in this section, is shown in Fig. 6.3 (b). The way at which phase information was extracted from the experimental data and the unwrapping process are explained in Sections 6.2 and 5.4.1 respectively. The contour plots of the unwrapped phase for a number of sample frequencies are given in Fig. 6.7 for a 10 Hz interval, from 32 to 62 Hz.

Similarly to the results in Section 6.5.2, the obtained data from this section illustrate both the source position and the conical wave fronts signature. The misshape of the wave pattern is due to the reflection from the pipe end can for every contour plot. Lower energy transmission to the frequency above 80 Hz, result in higher noise contribution on the phase data and decreased its reliability.

6.3.3 Measurement data from the third grid

The measurement grid point and the excitation source location, used in this section, is shown in Fig. 6.3 (c). The contour plot of the unwrapped phase for a number of sample frequencies are given in Fig. 6.8 for a 10 Hz interval, from 40 to 55 Hz.

At higher frequencies, phase aliasing occurs and the results are not presentable, meaning that the surface vibration is determined by the direct source waves and conical wave fronts are not dominant. Furthermore, closing to the pipe end, high amount of the wave reflection and radiation in the pipe and into the surrounding medium is expected.

6.4 Measurement with the pipe water gun

By removing the balloon, the device can be used as a pipe water gun. The utilized signal was composed of 8 pulses of 30 ms, each segment had 5 second duration. Reproducibility of the pipe water gun is examined separately in the lab and the results are given in Appendix C.

The signal was measured with a sample rate of 1 kHz, and with a low pass filter built into the DAC unit eliminating frequencies above 400 Hz to avoid aliasing. Cross Spectrum Density (CSD) between the recorded pressure from the PVDF wire and the recorded

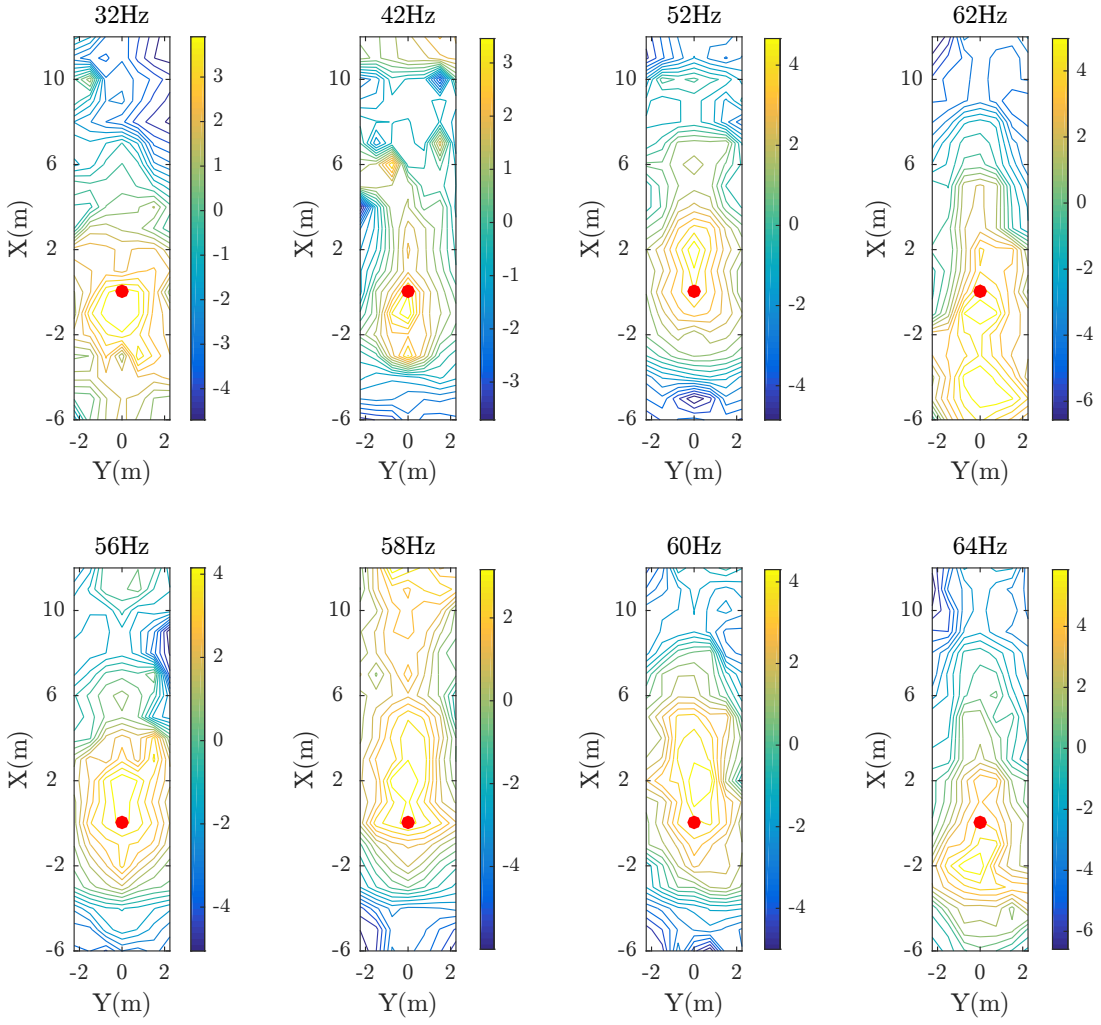

FIGURE 6.7: Contour plots of spatially-unwrapped phase of the normalised CSD between the ground surface vibration and the pressure sensed by the PVDF wire, in radians, using pipe balloon gun. The x and y axes correspond to the axes shown in Fig. 6.3 (b).

surface vibrations from the geophones were computed by segmenting averaging using a rectangular window of 5000 samples with 50 % overlap. The way at which phase information was extracted from the experimental data and the unwrapping process are explained in Sections 6.2 and 5.4.1 respectively. The contour plot of the unwrapped phase for a number of sample frequencies are given in Fig. 6.9 for a 10 Hz interval, from 45 to 75 Hz.

The frequency band at which the pipe location become the most obvious is 50-60 Hz and some of the frequencies are illustrated in Fig. 6.9. The other set of measurement was not producing any presentable results and it is suspected that this is resulted from

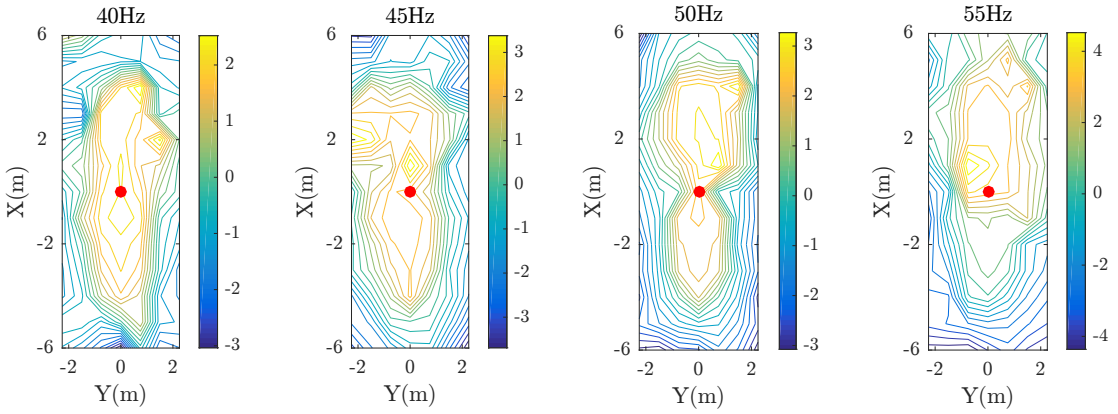

FIGURE 6.8: Contour plots of spatially-unwrapped phase of the normalised CSD between the ground surface vibration and the pressure sensed by the PVDF wire, in radians, using balloon gun. The x and y axes correspond to the axes shown in Fig. 6.3 (c).

an extreme reduction to the level of pipe pressurisation, in other words the water level at which the pipe was filled.

6.5 Mapping the pipe using a standard electroacoustic device

In this section an underwater speaker was adopted to generate a pressure wave into the pipe contained fluid. The speaker initially worked as a dipole source: while the front pushes the fluid out, the back pulls fluid in. It is well-known that dipoles do not radiate low frequency sound as well as monopole do [38]. Therefore the speaker was boxed for turning it into a monopole source. It is assumed that the excitation source is 100 % reproducible. As shown in Fig. 6.10 a hydrophone was placed at the front of speaker to record the pressure of generated disturbance to provide an extra reference signal, which has not been used in data processing.

The utilized time extended signal was composed of 64 linear chirps from 10 Hz to 400 Hz, each lasting two seconds. The signal was measured with a sample rate of 1 kHz, and with a low pass filter built into the DAC unit eliminating frequencies above 400 Hz to avoid aliasing. Cross Spectrum Density (CSD) between the input signal to the speaker and the recorded surface vibration from the sensor was computed by segmenting averaging using a rectangular window of 2000 samples with 50 % overlap.

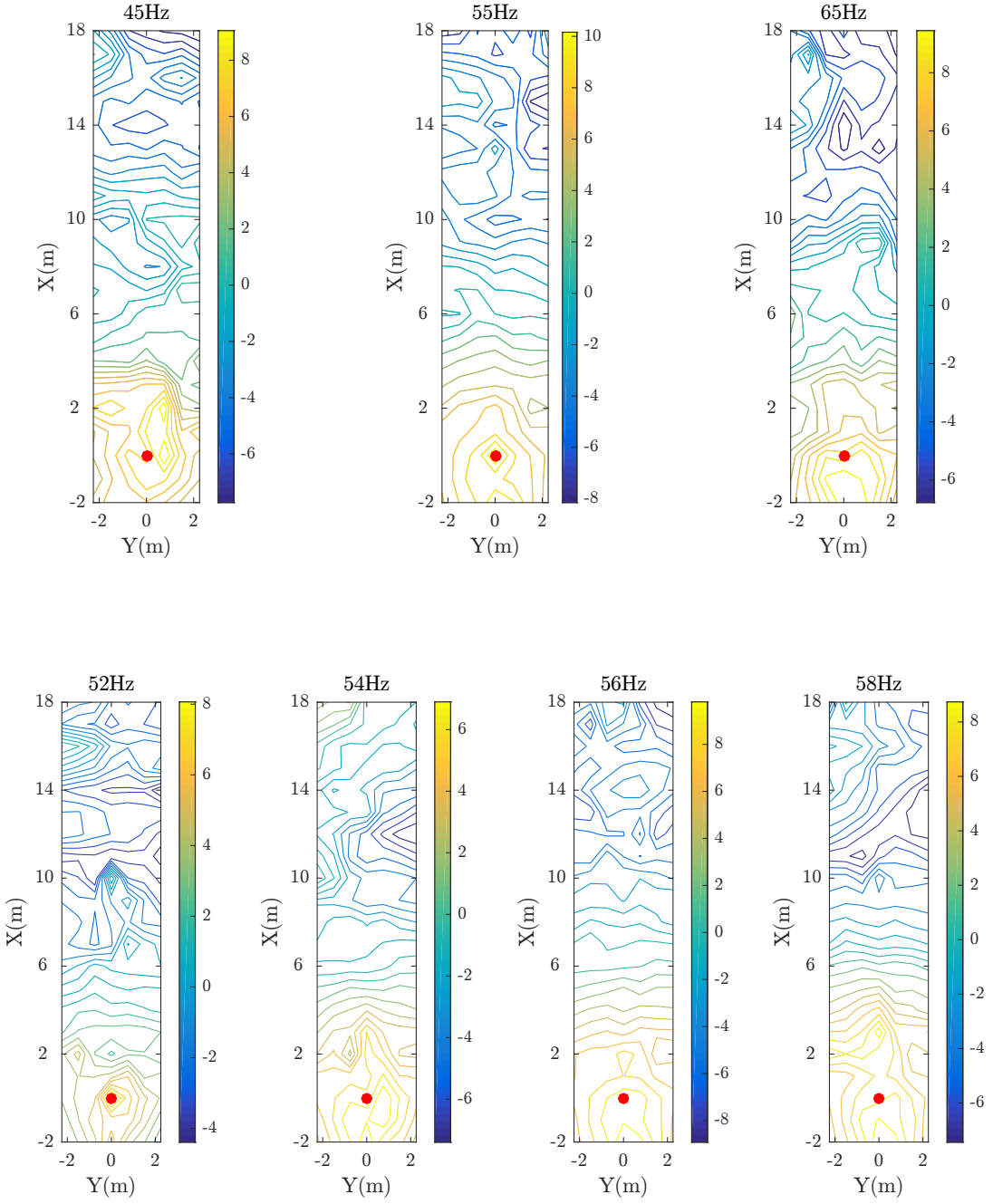

FIGURE 6.9: Contour plots of spatially-unwrapped phase of the normalised CSD between the ground surface vibration and the pressure sensed by the PVDF wire, in radians, using the pipe water gun. The x and y axes correspond to the axes shown in Fig. 6.3 (a)

Using a low frequency of excitation results in the acoustic wave travelling further down the pipe thus minimising the effect of the pipe wall damping. The effectiveness of the cross spectrum density function for tracing the buried pipes is highly affected by environmental noise. A large number of averages were selected for increasing the signal-to-noise ratio leading to manifest the presence of the signals that are masked by noise[98].

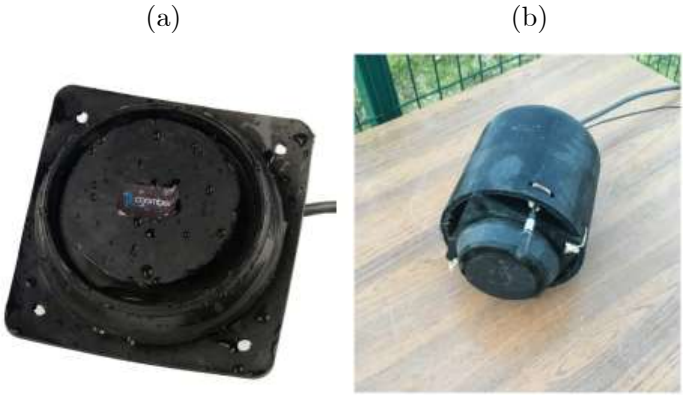

FIGURE 6.10: A photograph of the (a) un-boxed and (b) boxed loudspeaker and the location of hydrophone.

6.5.1 Measurement data from the first grid

The measurement grid points and the excitation source location, used in this section, is shown in Fig. 6.3(a). Phase information was extracted from the experimental data and unwrapped as explained in Sections 6.2 and 5.4.1 respectively. The contour plot of the unwrapped phase for a number of sample frequencies between 52 Hz and 75 Hz is depicted in Fig. 6.11.

Below 50 Hz, the phase data was erratic which is due to (i) the poor performance of the geophone below 50 Hz and (ii) the inability of the speaker to generate low frequency signal below 50 Hz. As seen in Fig. 6.11 at 45 Hz, lower energy was transmitted to the fluid, resulted in detecting signal up to 5 metre distance from the excitation source. The environmental noise seems to cover the rest of the image. From 52 Hz up to 75 Hz, the pipe main axis can be identified, up to 12 m, through looking at the patterns of the conical wave fronts within the image. The reason for the 3 metre offset of the spherical wave fronts from the excitation source location at 75 Hz has not been identified yet. The offset was observed also in the two forthcoming measurements.

The frequencies at which the pipe location is the most obvious are 60 Hz and 75 Hz . As shown in Fig. 6.11 conical shear wave fronts are not limited to a confined area over the pipe axis at the surface. In this case, the signature of the shear conical wave fronts appeared up to 13 m distance from the origin.

Although the frequency phase data is trustworthy from 40 Hz to 200 Hz, the pipe location could not be inferred above 80 Hz. As previously discussed in Chapter 5, at

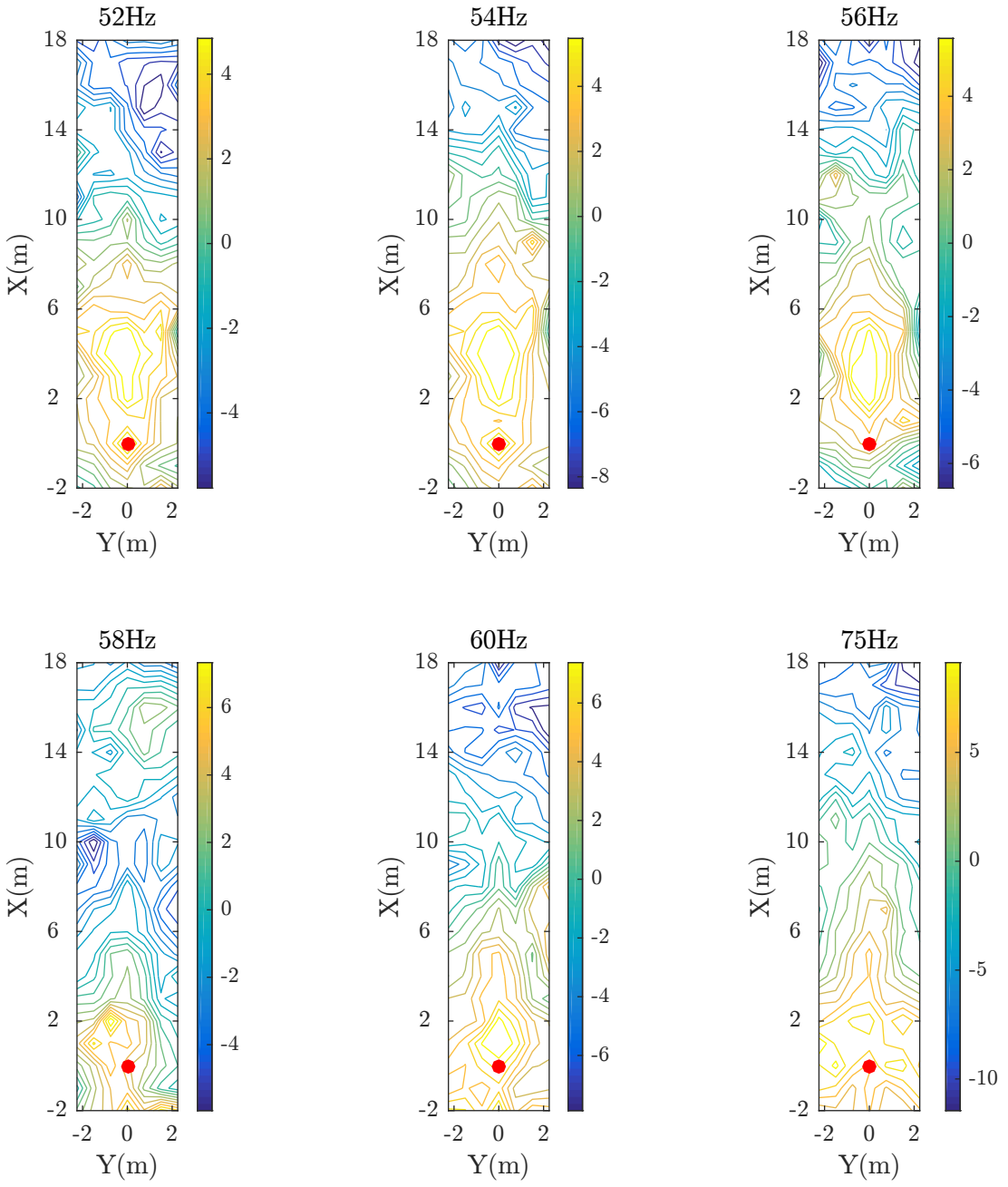

FIGURE 6.11: Contour plots of spatially-unwrapped phase of the normalised CSD between the ground surface vibration and the input voltage to the speaker at six frequencies in radians. The x and y axes correspond to the axes shown in Fig. 6.3(a).

higher frequencies, aliasing will make the wrapped data unreliable unless adopting a better experimental resolution or developing a new unwrapping algorithm. As the speed of dominant wave types near to the excitation source region differs from the rest, the signature of conical wave fronts is yet noticeable at higher frequencies, above 80 Hz up to 200 Hz, starting from approximately 4 metre distance (in this measurement) from the origin. Above 200 Hz, the variation of the phase data rises and spatial aliasing take

over the whole image. In the aforementioned frequency range, it is very likely that the measured signal becomes less coherent to the input signal and the environmental noise become dominant.

6.5.2 Measurement data from the second grid

The measurement grid points and the speaker location, used in this section, is illustrated in Fig. 6.3(b). The illustrative results for a number of sample frequencies between 45 Hz and 79 Hz is depicted in Fig. 6.12. The images below 55 Hz do not show any convincing results to infer the pipe location. As explained in the foregoing measurement, this is due to the poor performance of the source and the sensors at low frequencies. In the 65 Hz - 80 Hz frequency bands, the signature of the shear conical wave fronts becomes apparent up to approximately 6 m distance from the source position. At some frequencies, e.g. 65 Hz, the sign of spherical wave fronts appeared at multiple locations along the image. Analysis of the magnitude data may provide a better understanding on the existence of multiple spherical wave spreading into the external medium.

The frequency bandwidth over which the shear conical wave fronts become more obvious in the image is limited to 70- 80 Hz and some illustrative results is shown in Fig. 6.12. In this frequency range the expected origin of the spherical wave shifted about 3 m from the source location. The shifting might be resulted from the discontinuity along the pipe, where high value of wave reflection occurs along the pipe. Illustrating the PSD of the surface vibrational velocity might lend support to the aforementioned claim that the appearance of spherical wave fronts is due to high amount of energy reflection at the discontinuity along the pipe.

6.5.3 Measurement data from the third grid

The measurement grid points and the speaker location, used in this section, is illustrated in Fig. 6.3(c). The contour plot of the unwrapped phase for a number of sample frequencies between 40 Hz and 80 Hz is depicted in Fig. 6.13. Although the excitation source was relatively close to the pipe end, similar to the illustrative results in the two foregoing sections, the obtained data below 55 Hz still is not convincing to address the pipe location. Beyond 60 Hz, the emitted shear conical wave fronts become more

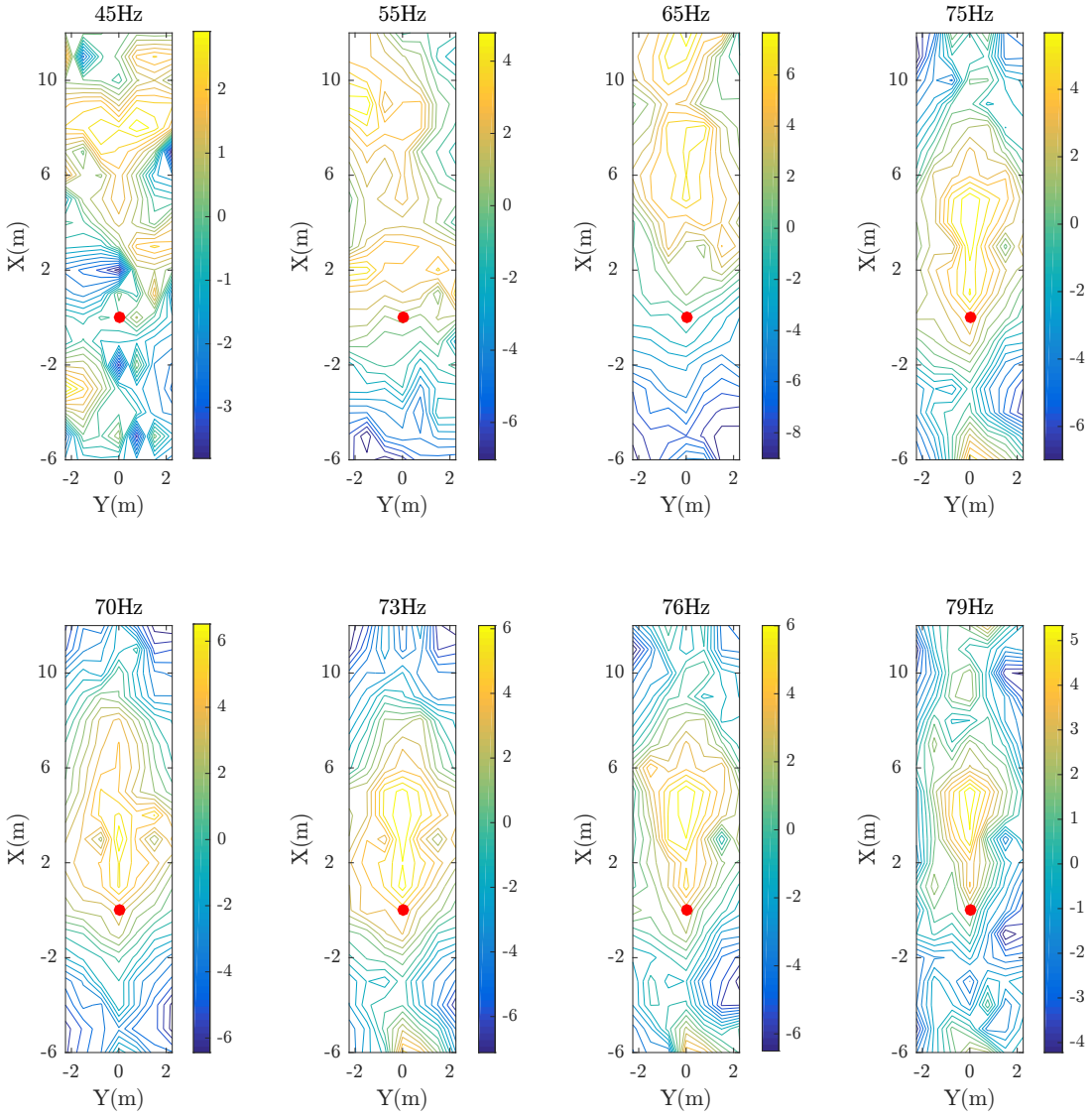

FIGURE 6.12: Contour plots of spatially-unwrapped phase of the normalised CSD between the ground surface vibration and the input voltage to the loudspeaker at six frequencies in radians. The x and y axes correspond to the axes shown in Fig. 6.3(b).

evident. As the excitation source was close to the pipe end, the surface vibration was due to several sources namely spherical wave spreading from the loudspeaker and the pipe end and radiation from the pipe wall.

The frequency band at which the pipe location become the most obvious is 60-70 Hz and some of the illustrative results is shown in Fig. 6.13. As mentioned in the foregoing, the reflection from pipe the end as well as the direct wave radiation from the source misshape the pattern of conical wave fronts.

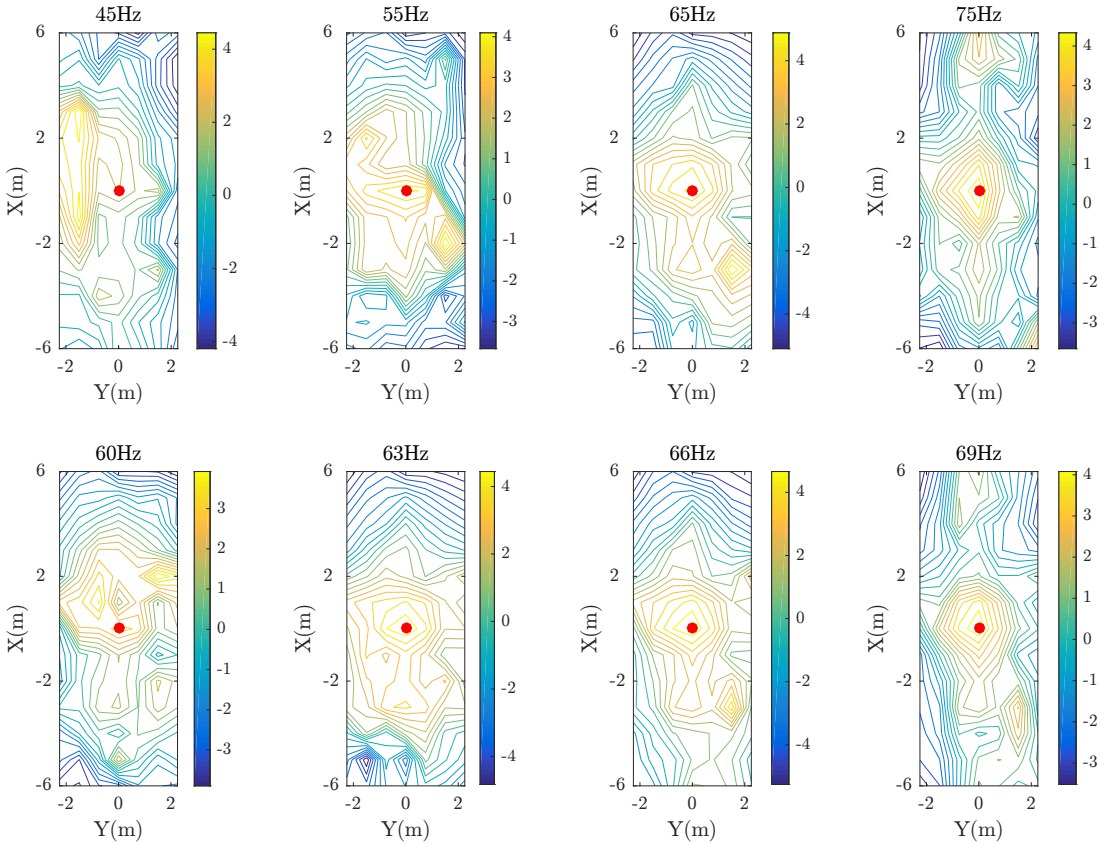

FIGURE 6.13: Contour plots of spatially-unwrapped phase of the normalised CSD between the ground surface vibration and the input voltage to the loudspeaker at eight frequencies, in radians. The x and y axes correspond to the axes shown in Fig. 6.3(c).

6.6 Mapping the buried pipe using structural excitation

The vibro-acoustic technique used in this chapter was initially developed by Muggleton *et al.* [25], as part of Mapping The Underworld project to locate buried plastic water pipes. A shortcoming of their method was applying one dimensional phase unwrapping on their results. The measurements in this section are performed using structural excitation, similar to that performed by Muggleton *et al.* [25]. The aim of repeating the measurement is to benchmark the performance of acoustical exciters with respect to the structural exciter. To shed some light on the data obtained from the previous vibro-acoustic technique, the pipe was loaded with a structural excitation when it was: (i) filled with the water and (ii) empty.

The utilized time extended signal was composed of 64 linear chirps from 10 Hz to 400 Hz, each lasting two seconds. The signal was measured with a sample rate of 1 kHz, and with a low pass filter built into the DAC unit eliminating frequencies above 400 Hz to avoid

aliasing. Cross Spectrum Density (CSD) between the input signal to the speaker and the recorded surface vibration from the sensor was computed by segmenting averaging using a rectangular window of 2000 samples with 50 % overlap. In this measurement it is assumed that the excitation source is 100 % reproducible.

The grid of measurement used for this section is shown in Fig. 6.3(a). The way in which phase information was extracted from the data and the unwrapping process, are explained in Sections 6.2 and 5.4.1 respectively. Pipe instrumentation for applying structural excitation is displayed in Fig. 6.14.

(a) (b) (c)

FIGURE 6.14: Instrumentation of the rig for applying structural excitation to the pipe at the location where the right angle bend bring the pipe to the ground surface. (a) Instrumenting the pipe with two brackets at both side of the pipe circumference. The two brackets have a nut and bolt; one of their side mounted to the pipe wall and the other side allow connecting them to an I beam. (b) Placing the I beam on the brackets and screwing it with bolt ant nuts. (c) Placing the shaker on the bar. The shaker was screwed to the bar.

By applying such an excitation to the pipe, an energy exchange between the axisymmetric fluid and shell dominated wave takes place at the bend location. In this case, the vertical pipe act as a long stinger for the horizontal pipe. By this way of excitation, bending waves are encouraged to propagate along the empty pipe and cause energy radiation to the surrounding medium. For the water filled pipes, nevertheless, high value of the water bulk modulus counteracts the radial displacement of the pipe wall under bending wave displacement.

Two sets of results for the empty and the fluid filled pipe subjected to the structural excitation are shown in Fig. 6.15(a) and (b) respectively. The illustrative results are the two-dimensional unwrapped phase of the normalised frequency response function between the ground surface vibration velocity and applied voltage to the shaker. The utilised phase unwrapping algorithm and the normalised FRF are explained in Sections 5.4.1 and 6.2 respectively.

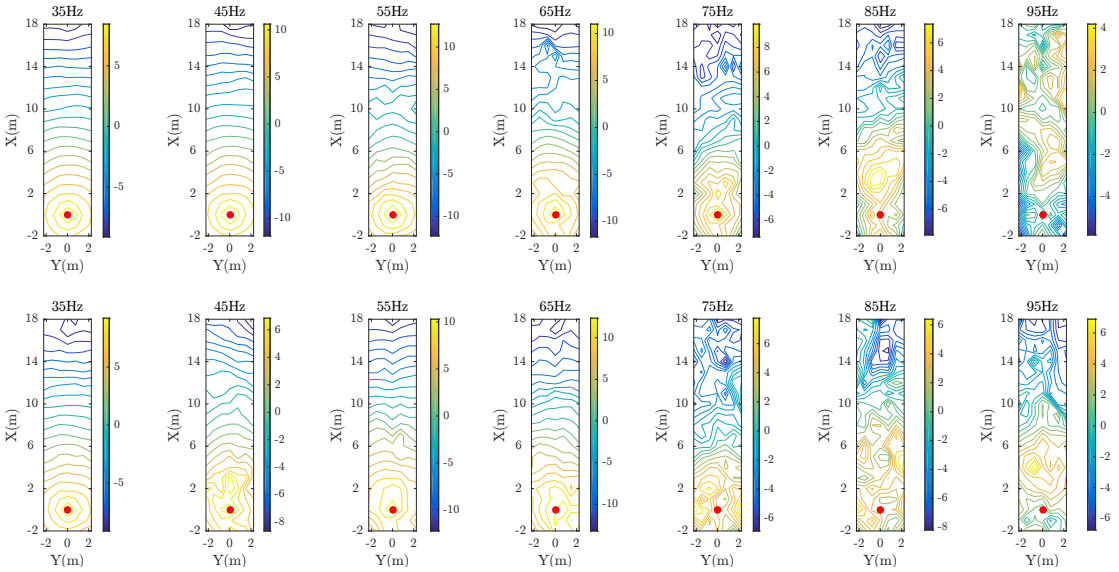

FIGURE 6.15: Contour plots of two dimensional spatially-unwrapped phase of normalised CSD. The x and y axes correspond to the axes shown in Fig. 6.3(a). (a) Empty pipe and (b) fluid filled pipe.

The obtained data from 35 Hz up to 65 Hz shown in Fig. 6.15(a) and (b) reports the circulation of the spherical wave fronts up to 2 meter distance from the excitation point. From approximately 2 metre distance from the excitation point and up to the end of the plot, in phase lines perpendicular to the pipe axis can be seen. Due to the similarity of the phase change value and its shape along the two images, it can be concluded that a spherical wave dominates the entire image in both cases.

As seen in Fig. 6.15(a) at 55 Hz and Fig. 6.15(b) at 45 Hz the curvature of the wave fronts slightly change from 5 m to 10 m distance from the origin. The exact reason of such changes yet have not identified, nevertheless, it might be due to the combination of the spherical wave fronts and re-radiation from the pipe wall to the medium. Having observed the spatial aliasing starting from 10 metre distance up to end of the contour plots, it can be concluded that the spherical wave fronts dominated in those area. The spatial aliasing is a very common practical problems which occurs due to poor resolution of the image. Provided that any conical waves is dominated after a couple of meters from the excitation location, the spatial aliasing should not have been occurred. With the spherical waves controlling the entire image, its no wonder the spatial aliasing region increase when increasing the frequency from 75 Hz to 85 Hz.

The results beyond 95 Hz for the empty pipe is not presented as the image was greatly affected by the spatial aliasing. Nevertheless, a very narrow signature of conical wave

fronts from the fluid filled pipe was observed approximately from 95 Hz to 125 Hz located at 6 m up to 10 meters from the excitation point. Discovering a way to overcome the spatial aliasing of the image, might lead to locate the pipe up to a certain distance from the excitation point.

From the results, it can be concluded that whilst the transmitted energy to the fluid borne wave is critical to ensure that the surface vibration is resulted from the conical wave fronts, the conical wave fronts themselves might be masked by other wave types, particularly in this case by spherical wave fronts.

6.7 Post processing of the magnitude data

This section aims to analyse the obtained data at some specific points and compare the results from different exciters. The reason of this has a two-fold motivation. Firstly, there was a need to support the view that the corrupted region of the image obtained from the shaker excitation above 55 Hz, shown in Fig. 6.15, is due to the spatial phase aliasing. Secondly, provides confirmatory evidence that the frequency phase data of the in-pipe exciters are reliable and its value changes linearly with frequency and is associated to the shear conical wave fronts. It should be noted that each implemented measurement took a day and the data has been collected in different days and the environmental conditions of each test slightly differed from one to another.

6.7.1 Frequency magnitude data of the first grid

The frequency unwrapped phase data obtained from three points corresponding to the x and y coordinates (-2 ,0), (14 ,0), (18 ,0), i.e. directly above the pipe 2 m backside, 14 m and 18 m front side from the excitation source are plotted in this section. These selected locations represent the extreme boundaries of the measurement grid. In view of the fact that first grid point is at 2 m distance before the pipe starting point, it should reflect the phase disturbance of the spherical wave fronts. The second point is selected at 14 m distance from the front-side of the exciter, on account of providing a cross comparison between the obtained data from different exciters and assess the ability of each exciter for driving the fluid borne wave. The phase data from the last grid point might support

the view that only some part of the pipe was detected by the speaker and the pipe water gun. The phase of the surface vibration for this point might be due to noise, only.

A number of similar phenomenon observed on the data are, for sake of brevity, explained only once. The phase jump at 20 Hz might be related to the natural frequency of the I/O SM-geophones. Below 20 Hz the phase data are no longer reliable while after 25 Hz, linear phase changes is observed. Although, extrapolation of the phase data from any graph does not result in a line crossing the origin, mapping the pipe, however, depends upon the relative phase gradient of each point. Several phase jumps also appeared on the plot at higher frequencies. Whilst normalised spectra are used, they still exist in the frequency phase plot. These phase jumps also appeared on the data obtained from unwrapped phase data of CSD between hydrophone and the PVDF sensor. Phase reversal in the horizontal displacement on the minima magnitude of surface vibration is mentioned by Jette and Parker [37]. These jumps, however, are not expected in the vertical plane. The data for the first point; $x = 0, y = -2$, is plotted in Fig. 6.16. In light of the fact that the selected measurement point was located before the starting of the pipe, the recorded surface vibration should be a function of spherical wave fronts. Further analysis, however, is required to justify the dominant wave type around the excitation source, at the surface.

Using different excitation sources, different phase data is obtained. Except the water gun, the rate of phase change from each device, with respect to the frequency is identical. Furthermore, above 50 Hz the slope of phase change increases. Between 25 Hz - 60 Hz, the averaged PSD of the speaker is five times lower than the ambient noise, meaning that SNR= 0.2 or -7 in dB. With 64 signal averaging, the unwrapped phase from the speaker resemble to the shakers and pipe balloon gun unwrapped phase data. The data yielded from phase and coherence plot in Fig. 6.16 provides strong evidence that the phase data where the coherence drops even below 0.1 and with -10 dB SNR is still reliable. The PSDs from the shaker and the pipe balloon gun are much higher than the PSD of the noise level. Therefore, the captured unwrapped phases resemble to the true unwrapped phase signal fore each exciter.

The unwrapped frequency phase data of the second grid points, which is located at 14 m in front of the excitation source, is plotted in Fig. 6.17(a). As seen in Fig. 6.17(a), after approximately 55 Hz the rate of unwrapped phase signal from the speaker is similar to

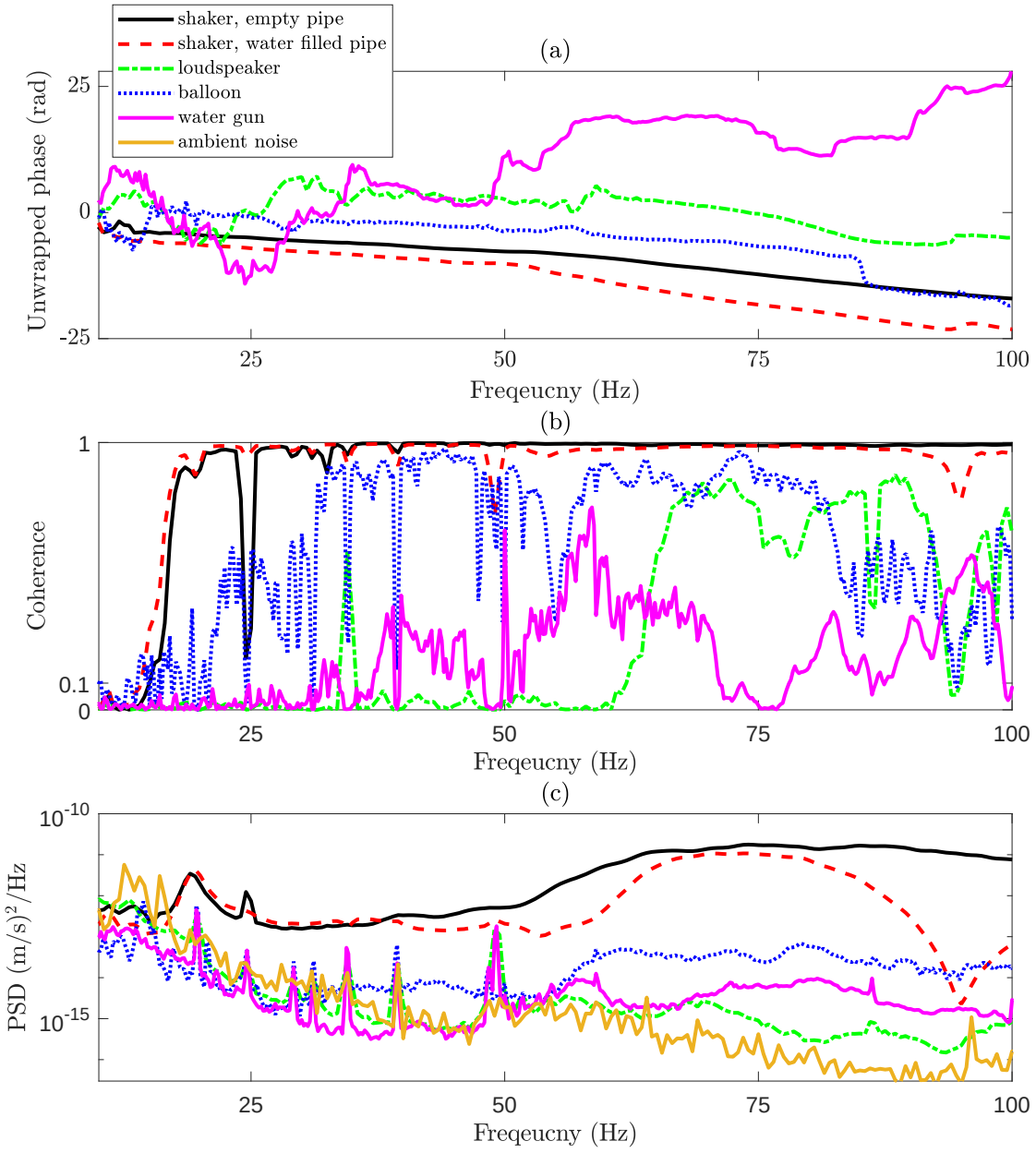

FIGURE 6.16: (a) Frequency-unwrapped phase of the normalised CSD between the ground surface vibration and the input voltage to the loudspeaker or the pressure sensed by the PVDF wire. (b) Ordinary coherence (c) PSD of the surface vibration at the grid location corresponding to $x = 0, y = -2$.

that of the shaker and the pipe balloon data. Before 50 Hz the coherence of the speaker data is below 0.1 and with a PSD amplitude close to the background noise level, meaning than SNR is unity or zero in dB and the unwrapped phase data is not reliable. The phase data from water gun is highly erratic with low coherence and the same vibration level to the background noise level which explain the reason of failure for tracing the pipe. From approximately 60 Hz up to 85 Hz the averaged sloped of unwrapped phase signals from the pipe balloon gun and the shaker on the water filled pipe are very similar to

that of the speaker. Such a consistency confirms the view that ground surface response is due to the same source of excitation, i.e. axisymmetric fluid borne wave. In view of spatial aliasing shown in Fig. 6.14(a) and high unwrapped phase slop from the shaker on the empty pipe, the acquired data at this point from 50 Hz to 100 Hz could be due to a point source originated from the elbow illustrated in Fig. 6.1. The difference between the slope of phase signal. i.e. at approximately 60 Hz for the empty pipe excitation by the shaker means changing to the wave type that dominantly vibrates the surface.

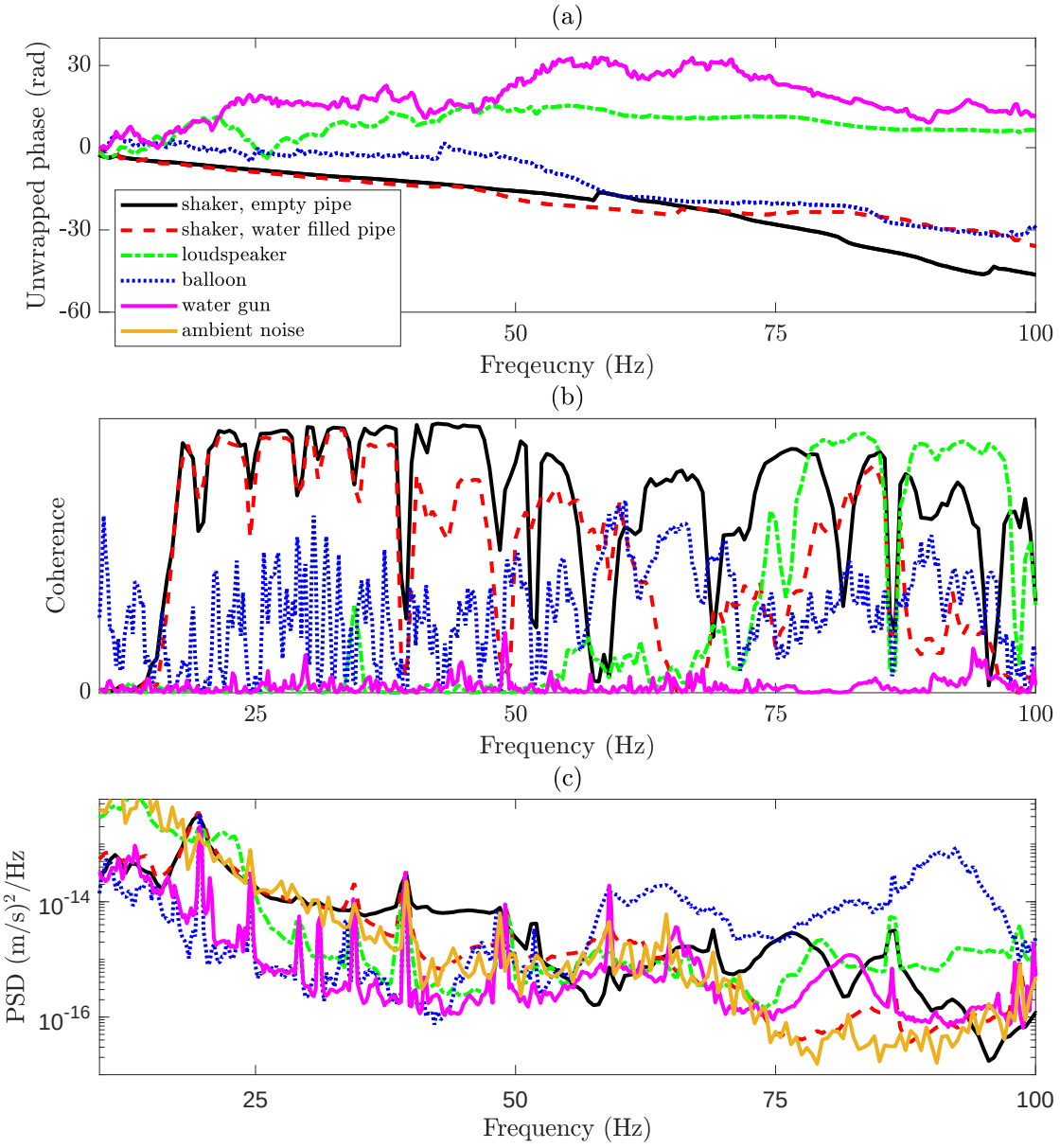

FIGURE 6.17: (a) Frequency-unwrapped phase of the normalised CSD between the ground surface vibration and the input voltage to the loudspeaker or the pressure sensed by the PVDF wire. (b) Ordinary coherence.(c) PSD of the surface vibration at the grid location corresponding to $x = 0, y = 14$.

A considerable reduction in the magnitude of the surface vibration at a distant point from the excitation source, narrows the bandwidth of detection. This reduction, however, should be low at lower frequencies, provided that the surface vibration is due to the re-radiation of conical wave fronts from the pipe wall to the surrounding medium. The area of interest in this study is between 50 Hz - 100 Hz. At the foregoing region the surface vibration from the pipe balloon gun has the highest value, while other exciters were not able to produce high magnitude data at the selected point. Therefore, it can be concluded that the pipe is a better wave transmitter compared to its surrounding medium.

The frequency phase data from the last point is plotted in Fig. 6.18. At this point it is expected that reflection from the pipe end cause spreading of spherical wave fronts or Rayleigh waves into the surrounding medium. As is shown in Fig. 6.18, the rate of phase changes from all devices, except water gun are relatively flat over the bandwidth of measurement. From the magnitude data it can be seen that the surface vibration from the pipe balloon gun is well above the background noise, in PSD amplitude. Beyond 60 Hz, the rate of phase change from the speaker is slightly lower compared to the shaker excitations and the pipe balloon gun.

The phase data from water gun is erratic and the coherence as well as the PSD results suggest that the excitation from this source was not strong enough and no acoustic wave reflection at the pipe end occurred.

6.7.2 Spatial magnitude of the first gird

In many companies that offer pipe location services, use of the magnitude plot is preferable when searching for leakage within the pipe. Moreover, use of the magnitude plot might allow recognition of any discontinuities along the pipe [26]. Therefore, the PSD of the recorded ground surface vibration relative to the vibration velocity measured by the geophone adjacent to the excitation point is plotted in Fig. 6.19. For the sake of comparing the magnitude plot of each source, the contour plots of the magnitude are plotted at 65 Hz, in dB relative to the vibration velocity measured by the geophone adjacent to excitation point.

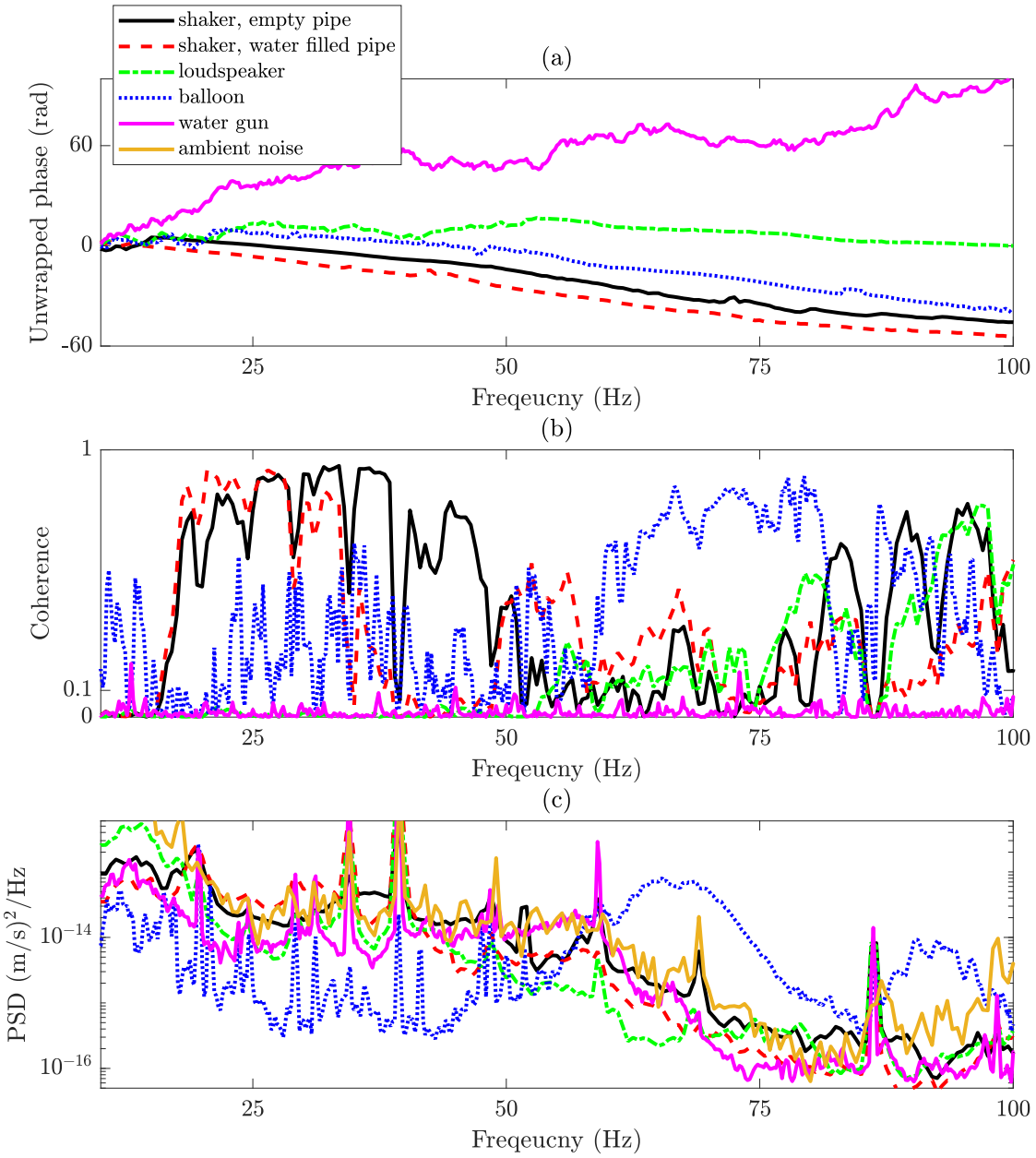

FIGURE 6.18: (a) Frequency-unwrapped phase of the normalised CSD between the ground surface vibration and the input voltage to the loudspeaker or the pressure sensed by the PVDF wire. (b) Ordinary coherence. (c) PSD of the surface vibration at the grid location corresponding to $x = 0, y = 18$.

Large values of the magnitude data near to the excitation point are attributed to a high energy flux into the pipe and particularly to the surrounding medium from exciters. Only in Fig. 6.19(a), the yellow spot at the end of the measurement gird is appeared, implies a strong reflection from the pipe end. In addition, high amplitude of the signal up to a 6 m distance from the excitation point implies high energy radiation from the pipe wall to the surrounding medium over its axis. The other contour plots only illustrate the excitation point location.

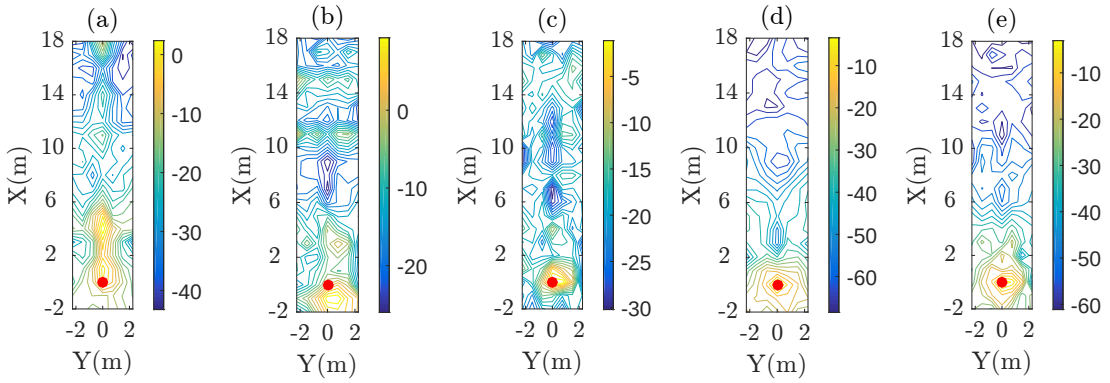

FIGURE 6.19: PSD of the surface vibration at 65 Hz, in dB, relative to the vibration velocity measured by the geophone adjacent to the excitation point. Experimental study performed using the (a) balloon gun (b) water gun (c) underwater speaker (d) shaker excitation on the water filled and (e) empty pipe. The red spot at (0,0) coordinate illustrates the excitation location.

6.7.3 Frequency magnitude data of the second grid

The aim of this section is to shied some light on the obtained by the measurement grid shown in Fig. 6.3(b). To this end, the obtained data from four points corresponding to the x and y coordinates (0 ,2.25),(12 ,0), (-6 ,0), (8 ,0), i.e. 2.25 m offset perpendicular to the pipe axis from the excitation point, directly above the pipe 12 m , -6 and 8 m from the excitation point. These selected locations represent the extreme of the second measurement grid excluding the grid point above the excitation source to exclude the near field effect.

The trend of linear phase change from the pipe balloon gun is observed in a narrower bandwidth compared to the loudspeaker. The trend was observed at places where higher magnitude and coherence was observed.

At (0, 2.25) the unwrapped phase signal from the balloon gun has a linear behaviour, relatively high coherence value and well above the noise level at the demonstrated frequency bandwidth.

Higher value of the surface vibration from the balloon gun at the pipe end compared to the loudspeaker, also confirm higher energy transmission to the fluid. At the pipe end, (12, 0), the PSD values of the balloon gun and the speaker are higher than the noise level above 50 Hz and 70 Hz respectively.

Approximately after 50 Hz, the PSD values from both exciters at (8, 0) and (-6, 0) start become higher from the ambient noise.

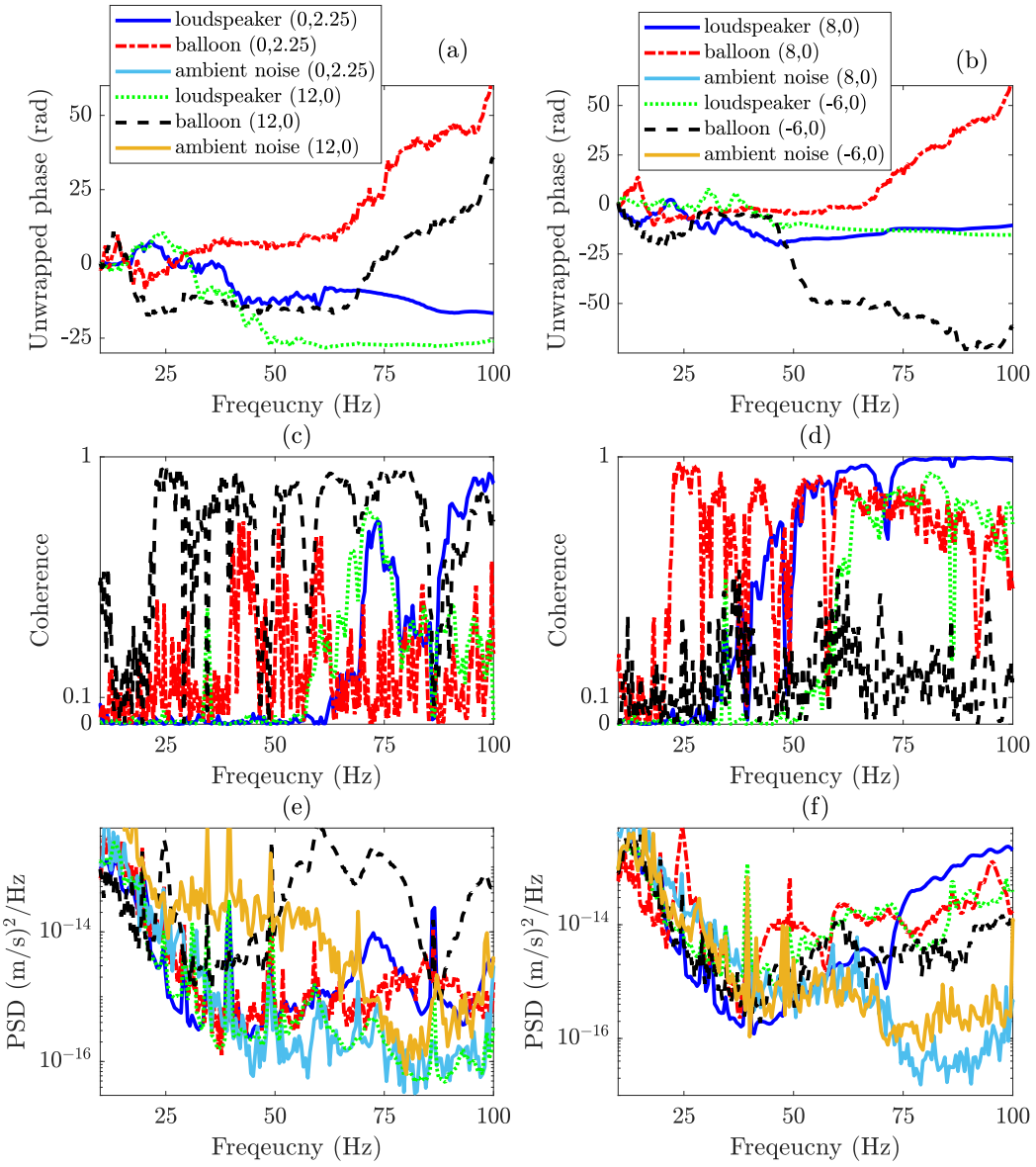

FIGURE 6.20: (a and b) - Frequency-unwrapped phase of the normalised CSD between the ground surface vibration and the input voltage to the loudspeaker or the pressure sensed by the PVDF wire. (c and d) Ordinary coherence and (e and f) PSDs of the ground surface vibration.

The phase from the loudspeaker started with linear trend from where the balloon data starts to have observable phase jump and poses multiple linearity phase change behaviour.

6.7.4 Frequency magnitude data of the third gird

This section aims to provide a further analysis and validate the accuracy of the measurement data acquired by the third grid of measurement point illustrated in Fig. 6.3(c), as

well as making a comparison between the obtained data from the speaker and the pipe balloon gun.

Similar to the two foregoing sections, the linearity of the phase data from the speaker, illustrated in Fig. 6.21(a), is observable for the measurement point (0 ,-2.25), (6,0) approximately from 35 Hz. Their PSDs values are well above the ambient noise with the coherence starting to increase at the aforementioned frequency range. Except the frequency bandwidth of 50 Hz 75 Hz, the coherence data and the PSD value related to the pipe balloon gun for the point (0, -2.25) rather drops and its phase data is no longer reliable. After 75 Hz, however, its PSD value becomes slightly above the surrounding noise level. Except some phase jumps, the recorded data at (6, 0) from the balloon gun changes linearly with the frequency, possesses a relatively high value of coherence and above 50 Hz its PSD value becomes comparable to the ambient noise and higher after 60 Hz.

Given the lower coherence value for the balloon compared to the loudspeaker illustrated in Fig. 6.21(a) and (b), the source location and conical wave patterns are evident in Fig. 6.21.

As expected, there are some ripples on the phase data for the measurement point (-6, 0), which are due to the reflection of the wave from the pipe end. Below 50 Hz, the obtained data from both exciters at (-6,0), is below the noise level. Above 50 Hz, the unwrapped phase from the speaker start to change linearly with less phase jumps. Its PSD values start to become comparable to the background noise and approximately ten times higher above 75 Hz.

6.8 Summary

In this chapter the designed pneumatic devices explained in Chapter 4 are used for mapping the buried pipe through the vibro-acoustic technique. The results from the pneumatic devices illustrated in both, Chapter 5 and this chapter highlight their importance for tracing buried water pipes. Transmission of a high energy at the desired frequency, from the balloon, allow finding the entire length (18 m) of the pipe.

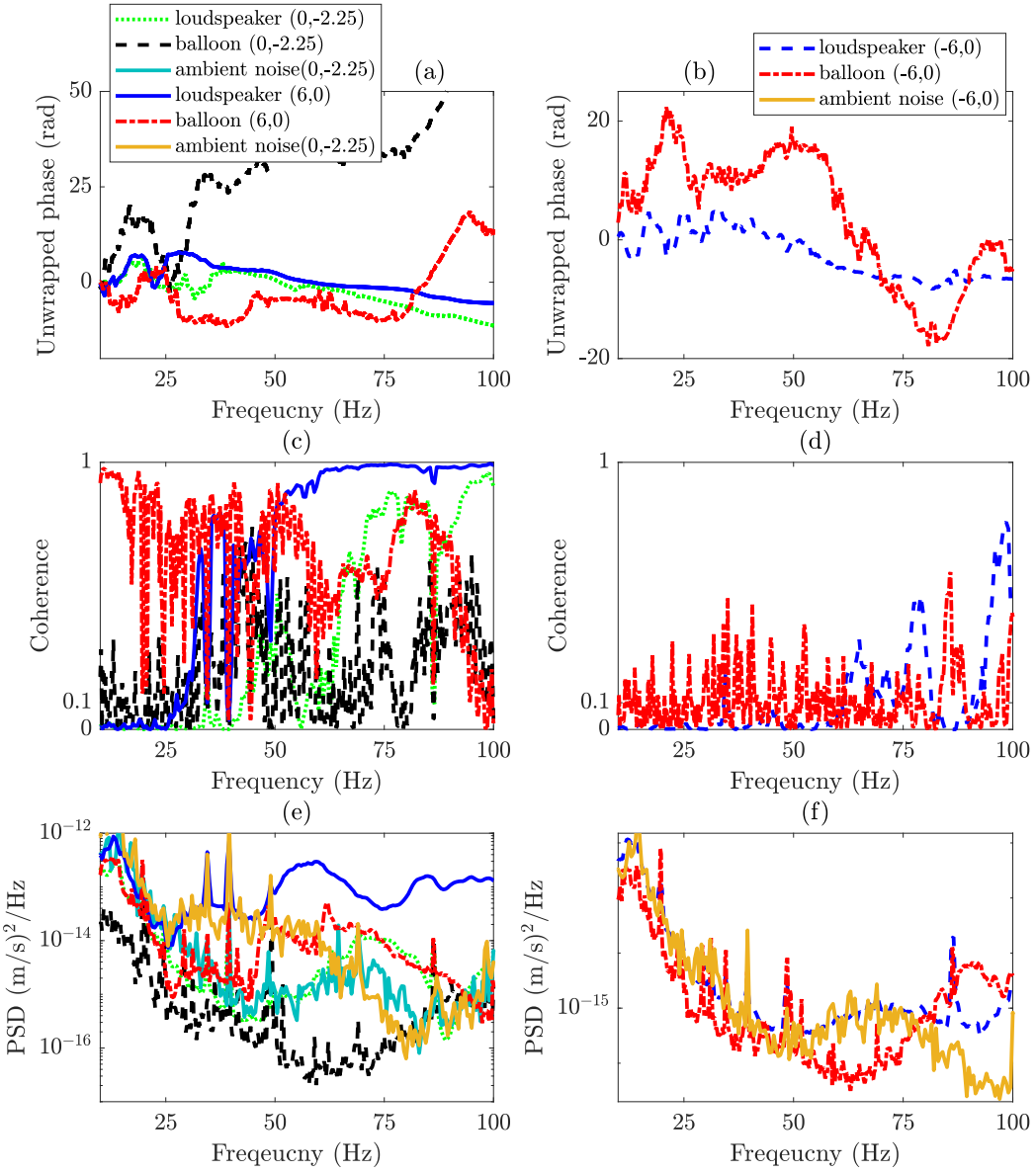

FIGURE 6.21: (a and b) - Frequency-unwrapped phase of the normalised CSD between the ground surface vibration and the input voltage to the loudspeaker or the pressure sensed by the PVDF wire. (c and d) Ordinary coherence and (e and f) PSDs of the ground surface vibration.

The results from water gun was not as good as the balloon excitation. This is because of changes to the test rig condition rather than the excitation source. The obtained data from loudspeaker showed that the pipe can be tracked up to 9 metre distance from the excitation location. This is due to the fact that most of the electroacoustic devices are designed to drive the fluid borne wave at a high frequency, above 100 Hz.

To bench mark the performance of the in-pipe exciters, a similar measurement to the previously used excitation source was repeated. Although a successful detection of buried

pipes through structural excitations was reported in by several researchers and pipe locator companies, the experimental measurement in this chapter showed that, below 95 Hz, the conical wave fronts are likely to be masked via the spherical ones. Therefore, exploiting either phase or magnitude data might end up to a poor detection rate.

Taken as a whole, the illustrative experimental data of this chapter is promising and experimentally validate the in-pipe excitation method for tracing the plastic pipes.

Chapter 7

Conclusions and suggestions for future work

This chapter summarises the findings over the course of my research and demonstrates how they help develop the explored vibro-acoustic technique to detect buried water pipes. Some suggestions for further developing the technique are also made.

7.1 Contribution to knowledge

The focus of this study is centred on enhancing the application of a vibro-acoustic approach following on from an earlier study. The technique was previously developed by other researchers for mapping buried water pipes, essentially plastic ones, through the following procedures: (1) Applying an intentional excitation to drive the pipe contained fluid (2) recoding the ground surface vibration at the vicinity of the suspected pipe location (3) exploiting the phase angle of the frequency response function between the recorded ground surface vibration and the input signal to the exciter whereby the pipe is vibrated. Although an intensive study had been carried on this topic, substantial novelties and helpful information have been gathered in this study. Without the improvements made in this thesis, detection of buried pipes via the explored vibro-acoustic technique would be a difficult task to achieve.

In the utilised vibro-acoustic technique, the distance of the pipe detection is mainly affected by the source ability to drive the axisymmetric fluid borne wave at frequencies

between 10 Hz to 100 Hz. The ambient noise dominants below 10 Hz and, beyond 100 Hz attention due to material damping of the pipe wall as well as the wave radiation from the pipe will not allow to map the remainder of the pipe that is far away from the excitation source. From the previous work on characterization of leak noise it is known that at the desired frequency range, most of the radiation from the pipe is due to the axisymmetric fluid borne wave. Therefore, the thesis began with measuring the wave speed and attenuation of the axisymmetric fluid borne wave, in Chapter 3. Such a measurement was previously conducted by several other researchers, however, yet no convincing description has been made about high variances of the wave attenuation value from the experimental result compared to the theory. Therefore, a simple analytical simulation was developed to explain a potential reason of it. Due to the well coupling of the axisymmetric fluid and structural borne wave, driving either of them can generate the other one to a large extent. As a result, the wave speed and wave attenuation of the axisymmetric structural borne wave were estimated in a similar fashion to measure the axisymmetric fluid borne wave. Owing to the dependency of the axisymmetric fluid and structural borne waves' amplitude to the elastic properties of the pipe, a simple experimental technique was proposed to distinguish between the pipe wall displacement that arises from the two axisymmetric waves. Although several peaks appeared on the ratio of the decomposed waves, the general trend was consistent to the theory. Such a technique might help manifest the deterioration to the condition of pipes through indicating the reduction in their elastic properties due to ageing.

Despite successful mapping of both iron and plastic water pipes was reported from an earlier study, the large attenuation of the signals in both pipe types does not allow mapping the remainder of pipe that is far away from the excitation source. A change in the legislation allowed inside access to the UK water pipe locator companies for determining the location and assessing the condition of buried water pipes. This then allows for the use of moveable acoustic devices to generate acoustic waves within the pipe at any required location, leading to overcome the attenuation problem. Locating buried water distribution systems by means of acoustical exciters is a new area of research and accordingly yet no prototype acoustic source has been manufactured for this matter. Hence, the primary objective of this study was to critically assess and examine acoustic sources, or instead develop or re-engineer one/s, which is/are reproducible, controllable, can fit into a typical water filled pipe and drive the axisymmetric fluid borne wave with

a high amplitude in the frequency range of 10 Hz - 100 Hz.

After intensively reviewing literature on a variety of acoustic exciter, it was learned that current underwater vibratory devices such as underwater speakers are normally designed to generate high frequency signals, above 500 Hz. Using a bigger and weightier underwater speaker, in addition to be big for deploying it within a typical buried pipe, might not effectively drive the contained fluid, at the desired frequency range. Therefore, two novel pneumatic devices are designed and re-engineered receptively, explained in Chapter 4, to drive the pipe contained fluid with a favourable pulsation. The pressure transmitted to the pipe contained fluid from these devices are compared with an electrodynamic shaker and a standard electro-acoustic device. Although the obtained pressure wave from the pipe water gun was slightly lower in amplitude compared to the underwater speaker, it could be a potential source for driving the contained water of smaller pipes.

An analytical simulation is developed in Chapter 5 to throw new light on the concept of the utilised vibro-acoustic technique. Although the model has room for improvement, it was decided to make it very simple and consider only two wave types within the surrounding medium. Owing to the use of an arctangent operator to extract phase information, the results wrapped onto $-\pi$ to π. The wrapped image contains several phase jumps. To illustrate the ground surface response and map the pipe location, a contiguous form of spatial phase data was required. To this end, a simple unwrapping algorithm, called radial unwrapping, was developed and applied to the wrapped phase data. From the analytical simulation it was concluded that close to the excitation source the source waves are dominant and from where the pipe ground borne waves' amplitude become comparable to the source ones, the surface vibration is controlled by the pipe waves. Thus, from the simulation it was outlined that not every pipe exciter/ excitation configuration is suitable for the pipe detection in this technique. An important requirement to manifest the pipe location, is to utilise an excitation source, which can drive the pipe ground borne waves in the surrounding medium with at least a higher amplitude to the source ground borne waves at the vicinity of the measurement. Lower speed of the spherical wave fronts, emitted from the point source, caused spatial aliasing at approximately 50 Hz, which lies at the desired frequency range of pipe searching in the vibro-acoustic technique.

Such aliased or corrupted areas should be isolated from the rest of the image during the

unwrapping process. In practical measurement, several other inconsistencies might exist in the phase image. The radial unwrapping developed in this thesis whilst was a good start to reveal a contiguous form of wave fronts and illustrates the surface response, it does not contain any weighting function to isolate the unreliable phase region, during its processing. Having reviewed, applied and compared the advanced two-dimensional phase unwrapping algorithms, the author suggested an unwrapping algorithm for unwrapping the experimental phase data.

The field experiments performed with the underwater speaker and the balloon gun revealed the desired results. The presence of the conical wave fronts from the pipe ground borne waves, were obvious in the unwrapped phase images. Similar to the analytical simulation, the ground borne waves emitted from the pipe, dominates after a distance where its amplitude became comparable the source wave. In spite of not observing such a trend at every frequency, in 10 Hz to 100 Hz, the obtained results are enthralling for remotely detecting buried plastic pipes. Low amounts of energy transmission from the speaker to the pipe contained fluid, at the desired frequency range, revealed the pipe location up to a 9 m distance from the source of excitation, while the balloon gun successfully mapped the entire length of the pipe. The results from the water gun was not the ones that were expected.

Furthermore, it was experimentally shown that applying axial excitation to a buried pipe with L or inverse T configuration considerably encourage the ground borne waves indirectly-excited from the source applied to the pipe. This method of excitation is widely used in industry and nominated as the most effective way of driving the pipe contained fluid for mapping buried water pipes. Nevertheless, the experimental data in Chapter 6 showed that such a technique drives indirectly a predominant spherical wave fronts and the radiated waves from the pipe were masked.

7.2 Recommendations for future work

This research work has been focused on detection of buried pipes using a vibro-acoustic technique. In view of the research outputs exhibited in this study, the following suggestions are made for the future work.

- From the author point of view, further research requires to identify a ground displacement based sensor which can be well coupled to different surface textures. Using such a sensor might illuminate the pipe ground borne waves more visible compared to the geophone.

- In this thesis, structural excitation was applied from a stand pipe to benchmark the obtained data from the in-pipe excitations against it. It is advantageous to radially vibrate the pipe from the other end where there is no elbow from the pipe in contact to the surrounding medium. Such excitation discourages the ground borne waves generated directly from the elbow.

- In practice locating the buried pipe should be achieved by a circular grid, recording a circular area around the access point to the pipe or the excitation point inside the pipe. The grid should be large enough to cover the area up to where the pipe ground borne waves become dominate.

- Because most buried water pipes are pressurised to some extend, further research can be carried out to illustrate the effect of pressurization level on detecting buried water pipes.

- All the in-situ measurements in this study were conducted on an approximately 18 m long pipe. It is desirable to perform the same measurement on a longer pipe and manifest the maximum distance at which the pipe can be located through the balloon gun.

- In practice, water pipes are buried under the main street where the ambient noise is higher in amplitude compared to the measurements performed in this study. To illustrate the effect of noise on the detection, the vibro-acoustic measurement can be carried out on a buried pipe in the main street.

- The main focus of this thesis was mapping buried water pipes by applying an intentional excitation to their contained fluid. It might be useful to detect the pipe using a water hammer which happens due to the surge effect from the operating pumps or rapid open and close of the valve. The reference signal for estimating the time delay can be achieved from attaching an accelerometer to the pipe from an access point e.g. fire hydrant.

Appendix A

Investigation into the MDPE material properties

In the interest of successful experimental measurements, it is of prime importance to properly calibrate the sensors in advance. Calibration of the accelerometers that are used in this thesis has been undertaken in this chapter. In this chapter, an investigation into the MDPE material properties, out of which most buried water pipes are made, is undertaken. These parameters are required to compare the measured value of the wave number with predictions from Eqs. (2.6) and (2.11).

A.0.1 Calibration of the accelerometers

In Chapter 3, four accelerometers are used to measure the wave speed and attenuation of the axisymmetric fluid and structural borne wave. The aim of this measurement is to check whether the utilised accelerometers are working in phase and their sensitivities are in accordance with the one indicated in the calibration chart. Different methods of accelerometer calibration exist and have been well established in references [99, 100]. In this measurement, however, each accelerometer with the assumed sensitivity of 1 $(\mathrm{mV})/(\mathrm{ms}^{-2})$ is mounted on a calibrated shear accelerometer. The frequency response function (FRF) between the measured acceleration and the applied voltage to the shaker is compared to the FRF of the shear accelerometer with respect to the same parameter. The test rig of this survey is illustrated in Fig. A.1.

FIGURE A.1: Placing a PCB accelerometer on top of the shear accelerometer to calibrate them and check the existence of the phase lag between any two transducer.

The excitation signal was a random noise signal with a frequency range between 10 Hz and 4 kHz. The signals were acquired in a time duration of 30 seconds at the sampling rate of 10 kHz. A low pass filter was built into the acquisition system, filtering signals above 4 kHz so as to avoid aliasing. Fig. A.2 depicts the FRF of the shear accelerometer with respect to the applied voltage to the shaker divided by the FRF of the PCB accelerometer with respect to the same parameter. Deviation of the signal from the reference signal at low frequencies <10 Hz can be attributed to the inability of the shaker to generate signals at low frequencies, while at higher frequencies for instance at 500 Hz and 1 kHz could be due to the machinery work was being undertaken a few meters from the lab. Regression fitting of the data has been carried out for the ratio of the FRF of the shear and the PCB accelerometers which are summarised in Table A.1. As illustrated in Table A.1, the mean value of the obtained magnitude agrees with specification supplied from manufacture. The standard deviation of the measured magnitudes, for all calibrated transducer is less than 1 %. The maximum phase lag deviation between the calibrated transducers and the shear accelerometer is also less 1.5 degree and is acceptable for further using of them.

A.1 Experiment on the cross section of MDPE pipe

Following the calibration of the accelerometers, a preliminary experiment was undertaken to evaluate the material properties of the MDPE pipe, such as Young's modulus,

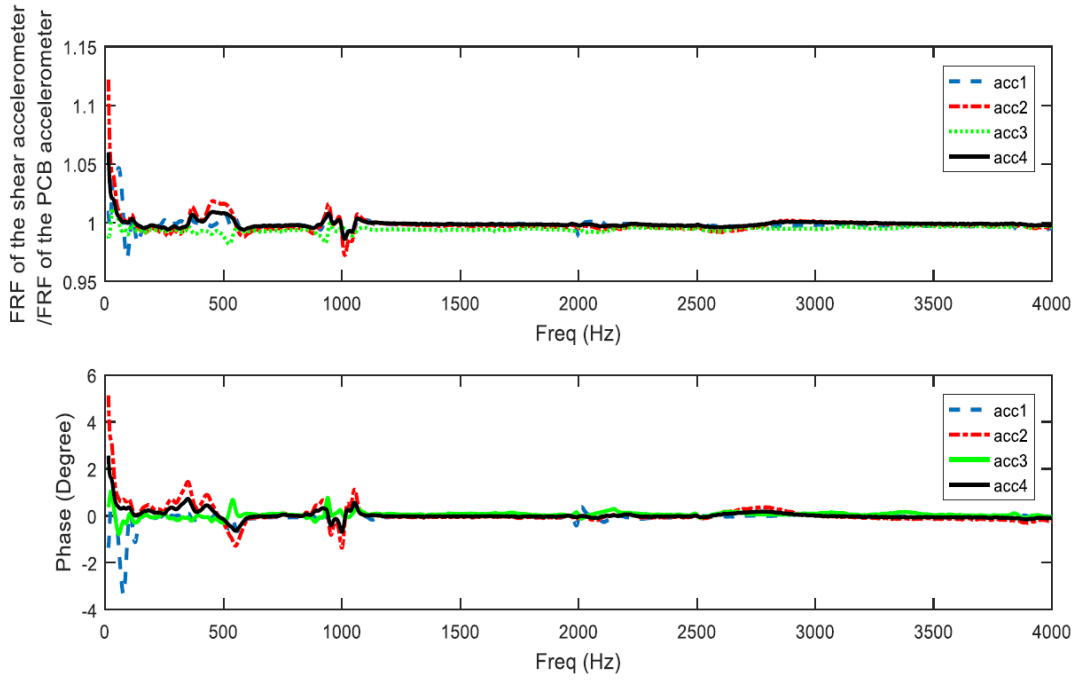

FIGURE A.2: Magnitude and phase of the FRF of the shear accelerometer with respect to the applied voltage to the shaker divided by the FRF of the PCB accelerometers with respect to the same parameter. (a) Obtained sensitivity of the PCB accelerometer. (b) Phase lag between the FRF of the shear accelerometer and the PCB accelerometers.

TABLE A.1: The values associated to the calibration of the PCB accelerometers.

Piezo electric type	Acc1	Acc2	Acc3	Acc4
Serial No.	108187	114879	116606	114872
Mean value of the FRF division	0.99	0.99	1	1
Variance	$2 \times 10^{-}5$	$5 \times 10^{-}5$	$6 \times 10^{-}6$	$6 \times 10^{-}6$
Standard deviation	0.005	0.0.007	0.002	0.002
Sensitivity	0.97 ± 0.005	0.99 ± 0.007	1.00 ± 0.002	0.99 ± 0.002
Manufacture sensitivity specification	0.971	0.986	0.995	0.984
Mean value of the phase lag (degree)	0.07	0.04	0.05	0.05

density, loss factor and Poisson's ratio used in the experimental investigation. This examination was performed in order that the experimentally measured axisymmetric fluid and structural borne wave speed could be compared with theory.

A.1.1 Estimation of the Young's modulus

A section from the MDPE pipe, which has used for the wave speed measurement in Chapter 3 was extracted for further analysis. The geometry of the ring under investigation is depicted in Table A.2.

TABLE A.2: Geometrical properties of the ring.

Material Properties	Wall thickness (m)	Density (kg/m^3)	Mean radius (m)
MDPE	0.011	880	0.18

In this experiment, the ring weight was $m = 0.0514$ kg with the length of 1cm and the density of the ring in Table A.2 was calculated using:

$$\rho_p = \frac{m_r}{\pi L(a_e^2 - a_i^2)}, \tag{A.1}$$

where m_r is total mass of the ring, L_r is its length, a_i and a_e are the inner and outer of the its radius respectively.

The ring was tapped radially via an instrumented hammer in line with the direction of a mounted B&K accelerometer as depicted in Fig. A.3. The data was recorded in a 0-4 kHz frequency range, via a SignalCalc Ace, with a sampling rate of 10 kHz and a low pass filter installed into the acquisition unit, set to filter out frequencies above 4 kHz so as to avoid aliasing. The reliability of the measured data was increased by averaging over five impacts. The accelerometer was mounted at the side of the ring and oriented in a way to measure the radial acceleration of the ring to observe its circumferential mode.

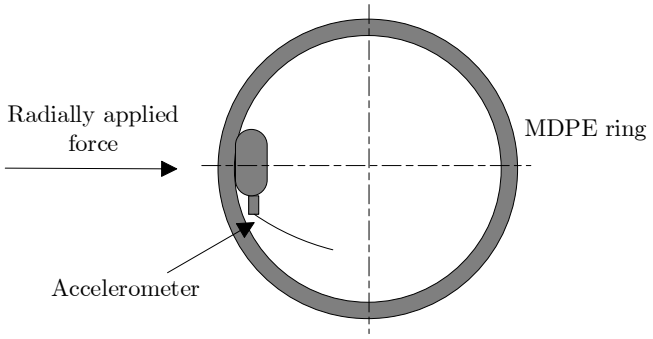

FIGURE A.3: Location of the applied force and measuring acceleration is depicted for calculating the transfer function.

The resonance frequency of the measured data, observed in Fig. A.4, is related to its Young's modules via an analytical solution, given by [101]:

$$f_n = \frac{n(n^2-1))}{2\pi a^2(n^2+1)^{1/2}} \left(\frac{c_p h}{\sqrt{12}}\right), \tag{A.2}$$

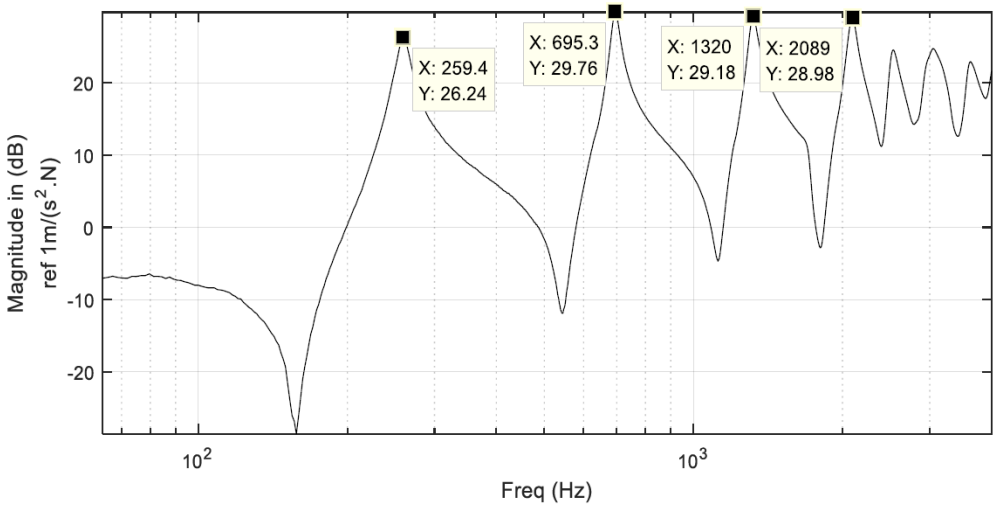

FIGURE A.4: Result for point accelerance of the MDPE ring. The plot is in dB using a ref of 1 m/ (s^2N).

where $c_p = \sqrt{E_p/\rho_p}$, $n = 2, 3, 4, ...$ is the circumferential modal number, π= 3.14 and a is the mean radius of the ring. The termsρ_p and E_p are the density and Young's modulus of the ring respectively. The obtained Young's modulus from each resonance peak observed in Fig. A.4 , using Eq. (A.2) are presented in Table A.3.

TABLE A.3: Young's modulus of the MDPE material corresponded to each resonance peak observed in Fig. A.4.

Circumferential modal number	$n = 2$	$n = 3$	$n = 4$	$n = 5$
Young's modulus (GN/m^2)	1.65	1.56	1.52	1.47

From examining the peaks in Fig. A.4, it was observed that stiffness of the plastic decreases with the frequency, however in practical situation the elastic modulus of viscoelastic materials slightly increases with the frequency. The reasons for the difference between the observed Young's modules from the experimental study might be due to: 1- Random errors from noise. 2- Systematic errors 3- Real effect.

Effect of the random errors from background noise has been mitigated via five times averaging. Possibility of systematic errors is reduced by repeating the test via a recent calibrated hammer. Nevertheless, inserting an inaccurate sensitivity for the hammer only influence on the magnitude of the data, rather than the location of the resonance frequency, along the frequency axis. Thus the only reason for the observed phenomena is might be due to the real effect or the formula presented in Eq. (A.2) becomes no longer valid for the higher frequencies.

The formula presented in Eq. (A.2) is valid for thin rings. It is speculated that at higher frequencies the thickness of the experimented ring becomes comparable to circumferential wavelength. Therefore the obtained Young's modulus was evaluated from the resonance peak attributed to the $n = 2$ mode.

The modal loss factor can be calculated from the half power bandwidth of the resonance peak, using [102]:

$$\eta_p = \frac{f_{n+12} - f_{n-1/2}}{f_n}, \tag{A.3}$$

where $f_{n+\frac{1}{2}}$ and $f_{n-\frac{1}{2}}$ are the two half power frequencies. The half-power point frequency is the point, where the output power was dropped by half, and 3 dB reduces its level. The loss factor is evaluated from the peak related to the $n = 2$ circumferential mode and it is assumed that this obtained loss factor is equal to the structural loss factor at the higher frequencies. The value of the Poisson's ratio illustrated in Table A.4 is based on the measurement in Section A.1.2.

TABLE A.4: Elastic properties of the MDPE pipe.

Material Properties	Loss factor	Young's modulus (GN/m^2)	Density (kg/m^3)
	0.057	1.65	880

The pipe ring frequency, f_{ring}, and the axial shell wave speed, c_{s2}, can be calculated using:

$$f_{\text{ring}} = \frac{c_{s2}}{2\pi a}, \text{ where, } c_{s2} = \sqrt{\frac{E_p}{\rho_p}} = 1370 \text{ m/s}. \tag{A.4}$$

A.1.2 Estimation of Poisson's ratio of MDPE

Another test was undertaken on the MDPE pipe to estimate its Poisson's ratio. Evaluation of this parameter is also required for evaluation of the axisymmetric fluid and shell borne wave speed via the theoretical expression given in Eqs. (2.6) and (2.11) respectively.

The circumferential shell stress of a pipe is given by:

$$\sigma_\theta = \frac{E_p}{1 - v_p^2}\left(\frac{w}{a} + v_p \frac{\partial u}{\partial x}\right), \tag{A.5}$$

where E_p, v_p and a are the Young's modulus, Poisson's ratio and mean radius of the pipe respectively. Referring to Fig. A.5, u and w are the shell displacement in the axial x, and radial r ,directions respectively.

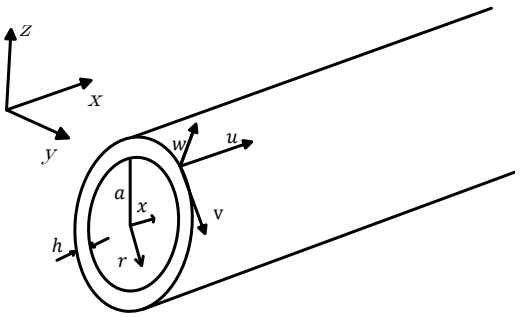

FIGURE A.5: Cylindrical shell: coordinate system and dimensions.

Setting zero circumferential stress for the empty pipe, at well below the ring frequency $\sigma_\theta = 0$ in Eq. (A.5), allows to calculate Poisson's ratio of the MDPE material, as the radial strain of the pipe wall is controlled by its axial strain via Poisson's ratio. Thus:

$$\sigma_\theta = \frac{E_p}{1 - v_p^2}\left(\frac{w}{a} + v_p \frac{\partial u}{\partial x}\right) \tag{A.6}$$

A schematic of the test rig that was used to measure Poisson's ratio of the empty MDPE pipe is illustrated in Fig. A.6. The experimental arrangement consists of 2.14 metre MDPE pipe with an outer diameter of 18 cm and wall thickness of 1.1 cm. The pipe was suspended vertically from a jack and a structural vibration was applied to it from an electrodynamic shaker.

This equation is valid unless the fluid's bulk modulus becomes comparable to the elastic modulus of the pipe wall, which restrict the radial motion of the axisymmetric shell borne waves. The $\varepsilon_\theta = \frac{w}{a}$ term is the circumferential strain and $\varepsilon_x = \frac{\partial u}{\partial x}$ is the axial strain.

Three equidistant positions are selected along the middle section of the pipe for the measurement of the axial and circumferential strain as illustrated in Fig. A.6.. The measurement was carried out by four accelerometers and it was decided to mount all

accelerometers at each measurement point at the interval of $\pi/2$ around the pipe circumference and repeat the measurement three times.

At two positions, (1) and (3), accelerometers were mounted axially to measure the axial acceleration of the pipe wall. At the midpoint, between locations (1) and (3) , the accelerometers were mounted radially onto the pipe wall. The position of the transducers and their distances from each other, and position of the excitation source are also shown in Fig. A.6.

In this approach, a successful measurement is achievable when the axial distance between sensors is smaller than a sixth of the dominant wave's wavelength. It is also required that the sensors are placed at a distance larger than half a dominant near field wave's wavelength away from each end of the pipe, where nearfield influences are significant [63, 103].

Reducing the spacing of the axially mounted accelerometers, along the pipe length, results in identical signals at locations (1) and (3). Therefore, the measured axial stress via subtraction of the axial pipe wall acceleration from the two positions will only evaluate the ambient noise. In contrast, at higher frequencies the wavelength decreases and approaching the sensors' spacing distance and induces errors in the difference between the two signal estimations. Therefore finding the optimal location for the transducer is vital in this study.

The input signal was a sweep sine started from 10 Hz to 1.6 kHz and last for two seconds. The signal then recorded via a ProSig P8020 with sampling frequency of 4 kHz and low pass filter was built into the Prosig, for filtering signals beyond 1.6 kHz to avoid aliasing.

The measured axial strain in the pipe wall illustrated in Fig. A.7, which was obtained by subtracting the axial pipe wall acceleration at the positions (1) and (3), followed by dividing them by ω^2 and δL as illustrated in Eq. (A.7).

$$\varepsilon_x = \frac{\partial u}{\partial x} \approx \frac{(\ddot{x}_3 - \ddot{x}_1)}{\Delta x \omega^2} \tag{A.7}$$

where ω^2 and Δx are the squared angular frequency and the spacing of the point (1) and (3) respectively. The circumferential strain also has plotted in Fig. A.7, which was obtained by the radially mounted accelerometer to the pipe wall, using the expression:

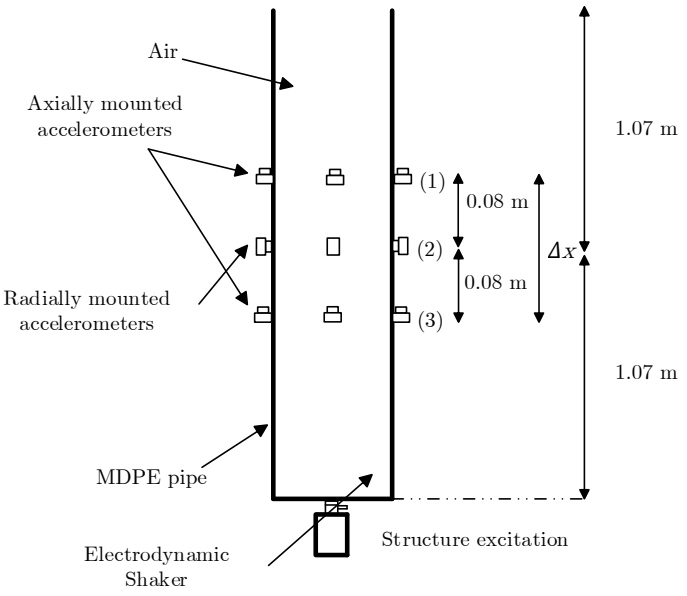

FIGURE A.6: Experimental set up used to estimate the Poisson's ratio of the MDPE pipe.

$$\varepsilon_\theta = \frac{w}{a} = \frac{\ddot{x}_2}{a\omega^2}. \tag{A.8}$$

In the above equation, the $\ddot{x}_2$ term is the measured pipe wall circumferential acceleration with respect to the input force, and its subscript illustrate the location measurement shown in Fig. A.6.

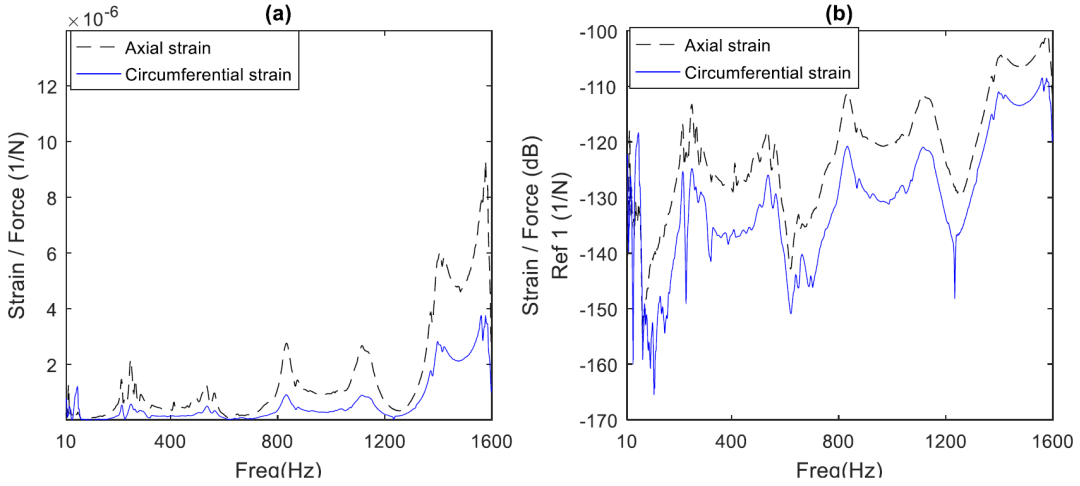

FIGURE A.7: FRF function between the measured strain and the input force, (- - -): axial strain / input force, (——): circumferential strain / input force (solid line). (a) Plotted results in a linear scale (b) Plotting in dB with a reference value of the (1/N).

The main peaks in Fig. A.7 at 251 Hz, 533 Hz 833 Hz, 1116 Hz and 1408 Hz are not consistent to the presented data from the ring experiment, illustrated in Fig. A.4. This

shift in the resonance frequency from the previous experimental study is due to the weight of the cover at the bottom end of the pipe, which was estimated to be about 1.3 kg. This cover was previously assembled to block one end of the pipe with the aim of further experiment on the pipe when it fills with the water. The process of calculation of the weight of the end cover, however, is not presented in here.

By dividing the measured axial strain by the circumferential strain explained in Eqs. (A.7) and (A.8) respectively, the Poisson's ratio of the MDPE pipe is obtained and plotted in Fig. A.8, which indicates a value of 0.42.

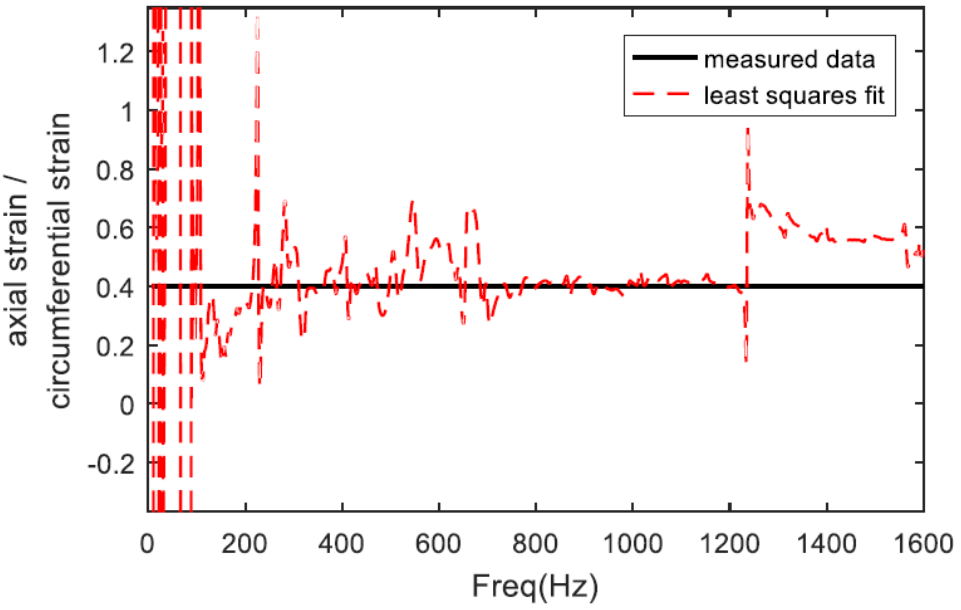

FIGURE A.8: Poisson's ratio of the MDPE pipe calculated by recording the axial and the circumferential strain of the pipe wall.

As illustrated in Fig A.8, at some frequencies the established experimental value, deviates from the expected value, i.e after 1.2 kHz. Above approximately 1.2 kHz, the experimental data is no longer trustable as, one-sixth of the axisymmetric structural borne wave's wavelength can fit into the axial distance between sensors at position (1) and (3). Details of the experimental data is summarised in Table A.5.

TABLE A.5: Details of the survey for the determination of the Poisson's ratio of the MDPE material. The presented data is for the frequencies between 220 Hz to 1.2 kHz, below which the signal are noisy due to similarity of the collected data from the accelerometers.

Mean value	Standard deviation	Estimated Poisson's ratio
0.042	0.09	0.42 ± 0.09

Appendix B

Pressure wave propagation along a pipe section

This appendix explains the pressure fluctuation in a fluid filled pipe of length L when it is excited at one end as illustrated in Fig. B.1.

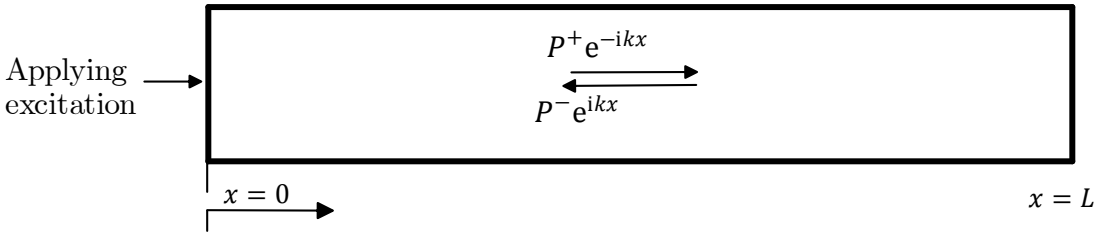

FIGURE B.1: Pressure wave propagation along a pipe section

Due to the termination placed at the other end, a reflection at the boundary is expected, which might be complex and can be explained by:

$$\hat{r} = |\hat{r}|e^{i\phi}, \tag{B.1}$$

where $|\hat{r}|$ and ϕ are the amplitude and phase of the reflection coefficient. The pressure fluctuation as a function of x, $p(x)$, generated by the interference of the two waves along the pipe can be expressed by:

$$p(x,t) = p^+e^{-ikx} + p^-e^{ikx} \tag{B.2}$$

By substituting the boundary conditions at $x = 0$ and $x = L$:

$$\begin{aligned} p^+ + p^- &= p_0, \\ \frac{p^-}{p^+} \mathrm{e}^{2\mathrm{i}kl} &= \hat{r}\mathrm{e}^{\mathrm{i}\varepsilon}, \end{aligned} \tag{B.3}$$

into Eq. (B.2) gives:

$$\begin{aligned} p^+ &= \frac{p_0}{(1 + \hat{r}\mathrm{e}^{-2\mathrm{i}kl})}, \\ p^- &= \frac{p_0 \hat{r}\mathrm{e}^{-2\mathrm{i}kl}}{(1 + \hat{r}\mathrm{e}^{-2\mathrm{i}kl})}. \end{aligned} \tag{B.4}$$

The pressure in the tube as a function of x, can be expressed by:

$$p(x) = p_0 \frac{\mathrm{e}^{-\mathrm{i}kx} \hat{r}\mathrm{e}^{-\mathrm{i}k(2l-x)}}{1 + \hat{r}\mathrm{e}^{-2\mathrm{i}kl}} \tag{B.5}$$

Appendix C

Investigation on the reproducibility of the developed pneumatic sources

Usually in vibro-acoustic techniques, measurements are performed with limited numbers of geophones. Therefore having a reproducible exciter allows to identify the local maxima of the ground surface vibrations which might be due to the discontinuity such as leak or bend along buried pipes. To illustrate the repeatability of the developed pneumatic output signal, a similar experiment as performed in Section 4.5.3 was conducted on the rig shown in Fig. 4.1. The location of excitation source was 0.1 metres away the water surface and the hydrophone was collected data, as shown in Fig. 4.1 (b). For all the tests conducted in this section the pressure regulator was adjusted to a release pressure of 3 bar, and the valve was set to open for 20 ms and close for 4.98 seconds. Each test comprises 16 firings and lasts for 80 seconds.

The PSDs of the output signals of the reference PVDF sensor from the two repeated tests, using the balloon and the water gun are illustrated in Fig. C.1 (a) and Fig. C.2 (a) respectively. The PSDs of the captured signals via the reference PVDF sensor for each test were divided by each other, and the ratio is illustrated in Fig. C.1 (b), and Fig. C.2 (b) respectively. The mean value of the obtained ratio presented in Fig. C.1 (b) and Fig. C.2 (b), is 1.15 and 1.08 with a standard deviation of 0.29 and 0.56 respectively.

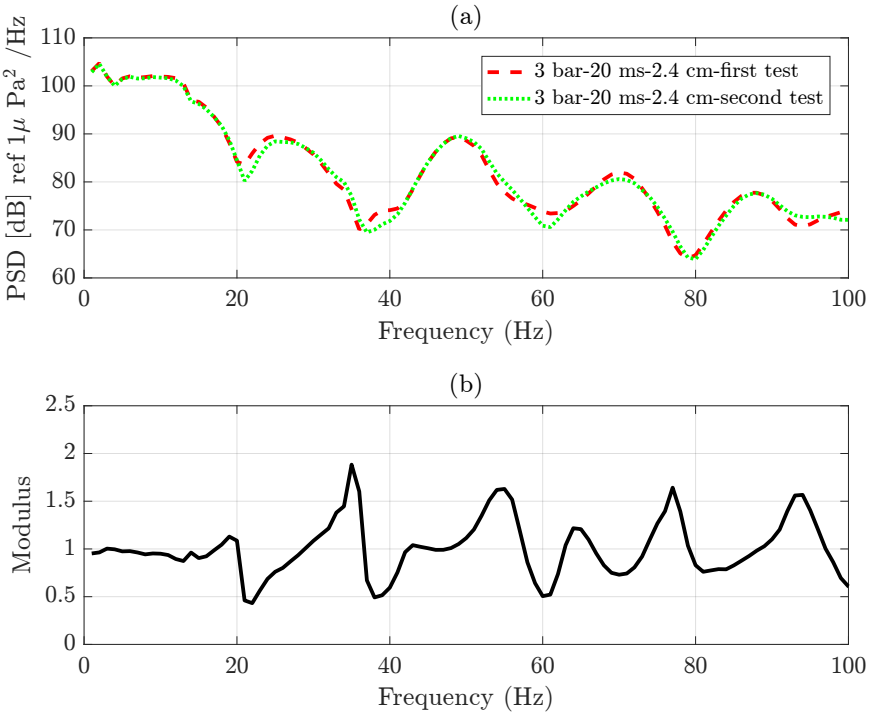

FIGURE C.1: (a) Output signal from the reference PVDF sensor, averaged from eight pulses, resulted from the balloon gun excitation, (- - -) test one and (·····) test two. (b) The ratio of the PSDs measured from the two tests.

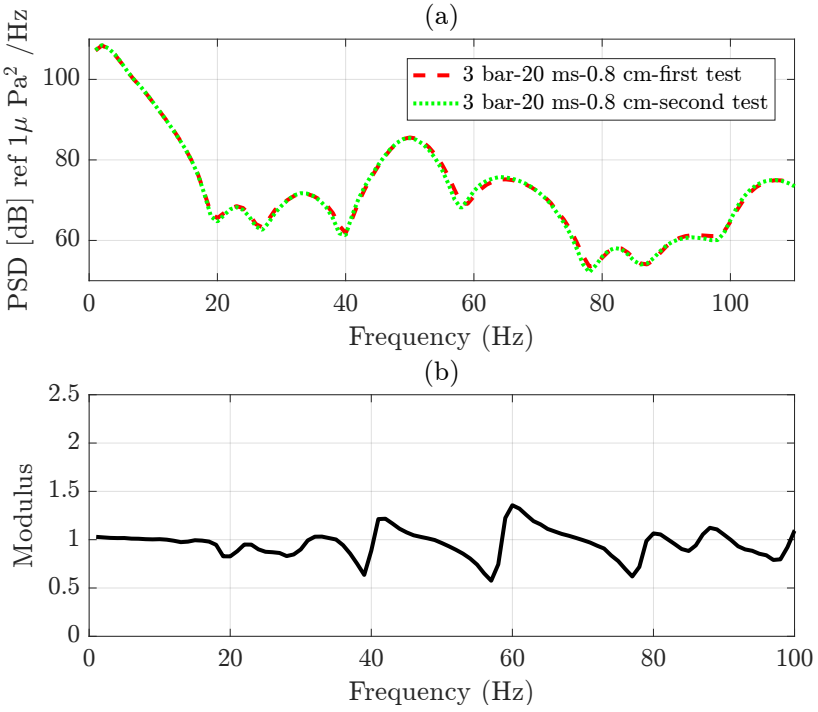

FIGURE C.2: (a) Output signal from the reference PVDF sensor, averaged from eight pulses, resulted from the water gun excitation, (- - -) test one and (·····) test two. (b) The ratio of the PSDs measured from the two tests.

The PSDs of the output signals from the hydrophone for each test, from the balloon and the water gun, is illustrated in Fig. C.3 (a) and Fig. C.4 (a) respectively. The PSDs of the captured signals via the reference PVDF sensor for each test were divided by each other, and the ratio is illustrated in Fig. C.3 (b) and Fig. C.4 (b) respectively. The mean value of the obtained ratio presented in Fig. C.3 (b) and Fig. C.4 (b), is 0.93 and 0.94 with a standard deviation of 0.24 and 0.36 respectively.

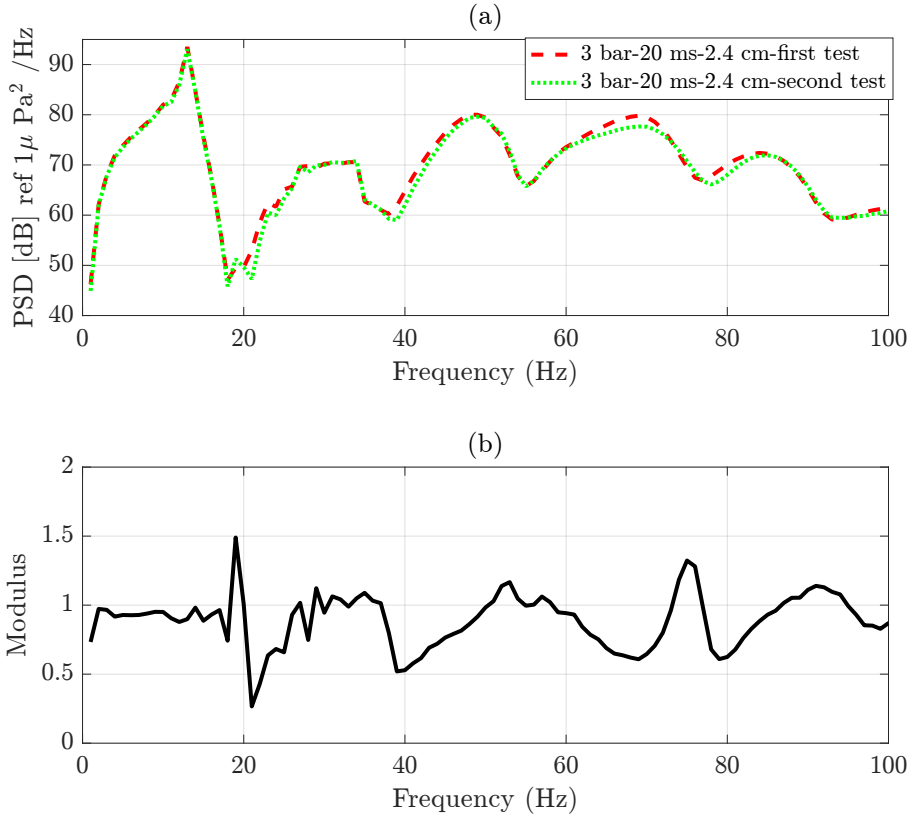

FIGURE C.3: (a) Output signal from the hydrophone, averaged from eight pulses, resulted from the pipe balloon gun excitation, (- - -) test one and (·····) test two. (b) The ratio of the PSDs measured from the two tests.

The frequency response between the fluid pressure recorded by the hydrophone and the output signal from the reference PVDF sensor for each test which were conducted by the balloon and water gun is plotted in Fig. C.5 (a), and Fig. C.6 (a) respectively. The modulus of the frequency responses illustrated in Fig. C.5 (a) and Fig. C.6 (a) are shown in Fig. C.5 (b), and Fig. C.6 (b) respectively.

The mean value of the obtained ratio presented in Fig. C.5 (b) and Fig. C.6 (b), is 1.15, 1.01 and 1.18 with a standard deviation of 0.11 and 0.29 respectively. In vibro-acoustic

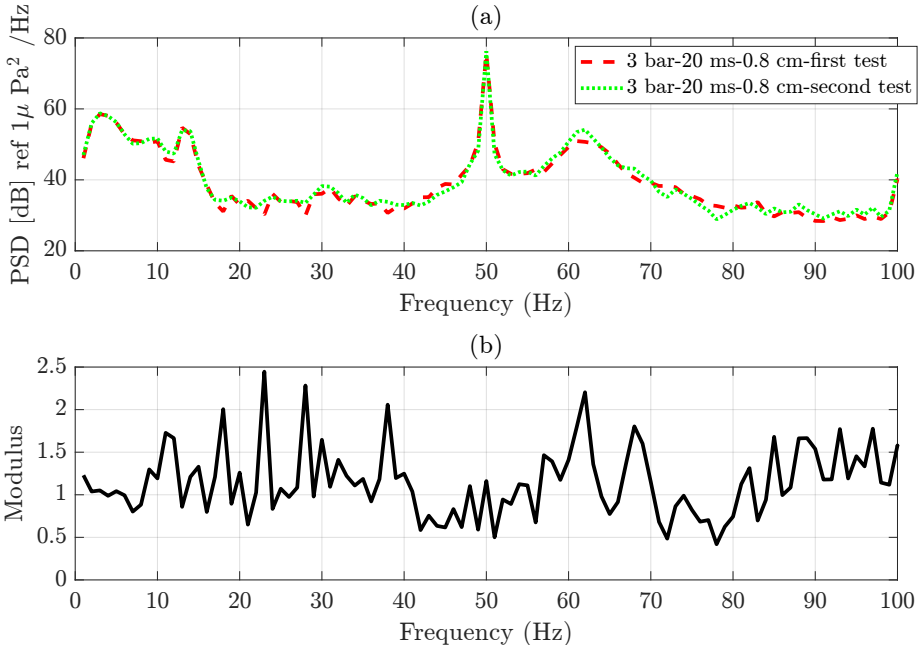

FIGURE C.4: (a) Output signal from the hydrophone, averaged from eight pulses, resulted from the pipe water gun excitation, (- - -) test one and (·····) test two. (b) The ratio of the PSDs measured from the two tests.

technique, the reduction to the surface vibration velocity, after the source location, is of the order of 10 dB [25]. Hence, the device are very much suitable to be used.

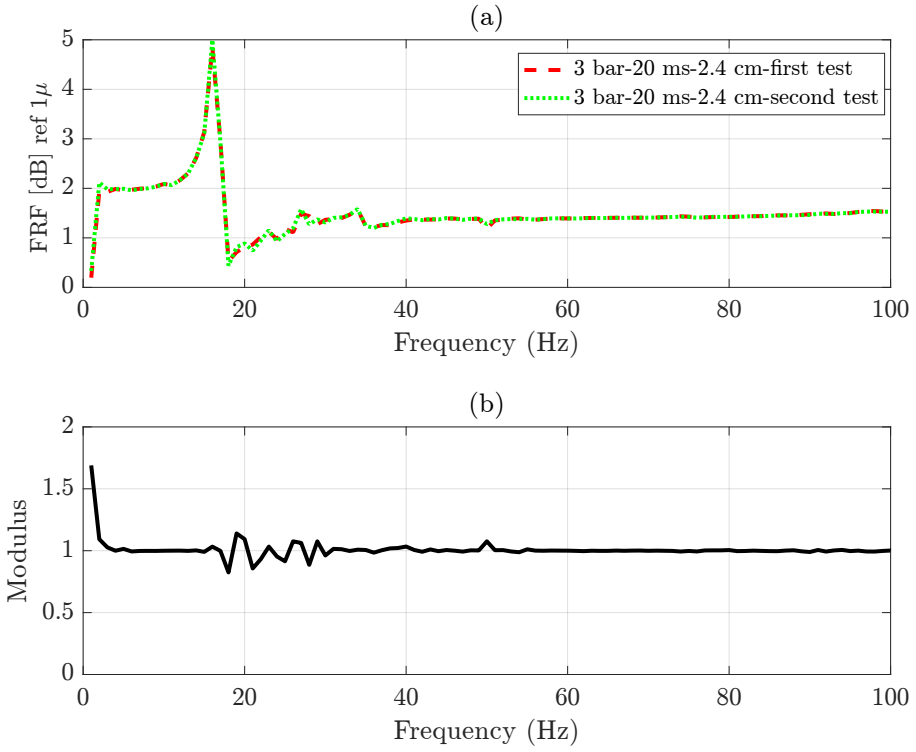

FIGURE C.5: (a) Averaged Frequency Response Function (FRF) from eight pulses, between the pressure recorded from the hydrophone and the reference PVDF from the pipe balloon gun excitation, (- - -) test one and (·····) test two. (b) The ratio of the PSDs measured from the two tests.

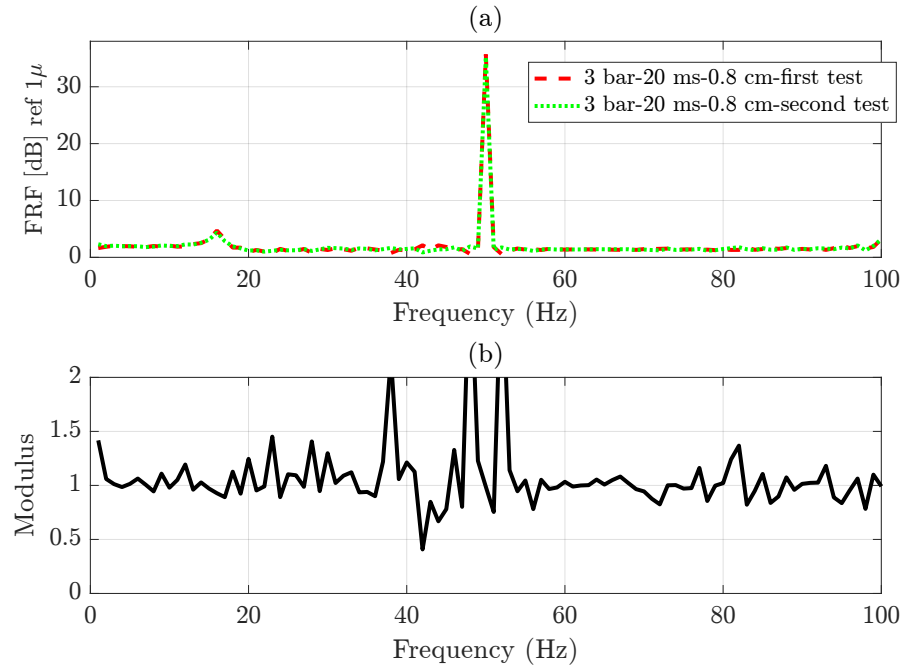

FIGURE C.6: (a) Averaged Frequency Response Function (FRF) from eight pulses, between the pressure recorded from the hydrophone and the reference PVDF from the pipe water gun excitation, (- - -) test one and (·····) test two. (b) The ratio of the PSDs measured from the two tests.

Appendix D

A novel method to measure power transmission to the fluid filled pipe

In-pipe excitation sources are developed in this thesis to generate high amplitude acoustic waves at the desired frequency range. The effectiveness of the each excitation source to deliver energy to the fluid borne wave can be shown by comparing its power transmission to the fluid borne wave. In this section a new power measurement technique is explained.

D.1 Theoretical background

In short, power is defined as the rate at which work is done. The instantaneous input power to a point of a structure can be obtain from multiplying instantaneous values of the input force and vibration velocity of the desired point. Hence instantaneous power, P_I, can be defined as:

$$P_I = F_I V_I, \tag{D.1}$$

where F_I and V_I are instantaneous values of force and in phase velocity at a structure point respectively. In light of investigating the vibration behaviour of structures, it is advantageous to measure the time average power transmission. For a single frequency

excited system, the time average power transmission, $< P >$, at the desired point is defined as:

$$< P >= \frac{\omega}{2\pi} \int_0^{2\pi/\omega} F_I V_I, \tag{D.2}$$

where ω is the angular frequency and $<>$ illustrates time-average.

Substantial literature on power flow into a fluid filled pipe has been presented by Pavic [76, 103–108]. The formulas developed in these papers are based on the surface vibration measurement and can be simplified for lower frequencies. Such formulae are summarised in the following subsections.

D.1.1 Power transmission to a fluid filled pipe

Power transmission to fluid filled cylinders is the sum of the power transmitted to the fluid and the structural borne wave. The time averaged power transmission to the pipe wall and the contained fluid can be obtained by integrating the stress and the particle velocity over a duration of time t. The structural power flow into the pipe wall can be calculated using [109]

$$\left\langle \widehat{W_p} \right\rangle = -\frac{1}{t} \int A_s \left(\sigma_x \dot{\mathrm{u}} + \sigma_\phi \dot{\mathrm{v}}\right) dt = -\frac{1}{2} A_s \,\mathrm{Re}\left(\sigma_x \dot{\mathrm{u}}^* + \sigma_\phi \dot{\mathrm{v}}^*\right), \tag{D.3}$$

where A_s is the pipe wall cross section, $(^*)$ shows the complex conjugate and Re( ) represents the real component within the bracket. The term σ_x and σ_ϕ are the axial and torsional stress into the pipe wall, which can be explained by [34]:

$$\sigma_x = \frac{E_p}{1-v_p^2}\left(\frac{\partial \mathrm{u}}{\partial x} + \frac{v_p}{a}\frac{\partial \mathrm{v}}{\partial \phi} + v_p \frac{\mathrm{w}}{a}\right), \sigma_\phi = \frac{E_p}{2(1+v_p)}\left(\frac{\partial \mathrm{x}}{\partial x} + \frac{1}{a}\frac{\partial \mathrm{u}}{\partial \phi}\right). \tag{D.4}$$

Axial and torsional shell velocity and their spatial derivative can be calculated using [109]:

$$\dot{\mathrm{u}} \approx \frac{\dot{\mathrm{u}}_1 + \dot{\mathrm{u}}_2}{2}, \frac{\partial \dot{\mathrm{u}}^*}{\partial x} = \frac{\dot{\mathrm{u}}_2^* - \dot{\mathrm{u}}_1^*}{\Delta} \text{ and } \dot{\mathrm{v}} \approx \frac{\dot{\mathrm{v}}_1 + \dot{\mathrm{v}}_2}{2}, \frac{\partial \dot{\mathrm{v}}^*}{\partial x} = \frac{\dot{\mathrm{v}}_2^* - \dot{\mathrm{v}}_1^*}{\Delta}, \tag{D.5}$$

where Δ is the distance between transducer along the pipe. The optimal separation distance for measuring power transmitted to a particular wave type is about one-six of its wavelength [109].

D.1.2 Fluid power transmission

The transmitted power to the contained fluid can be evaluated using [109]:

$$\left\langle \widehat{W_f} \right\rangle = -\frac{1}{T}\int A_f p_f \dot{\mathrm{u}}_f \, dt = -\frac{1}{2} A_f \, \mathrm{Re}\{\rho_f \dot{\mathrm{u}}_f^*\}, \tag{D.6}$$

where ω, p_f and A_f are the angular frequency, pressure and the cross section of area of the contained fluid respectively. The value of the pressure and the pressure gradient $\frac{\partial p_f}{\partial x}$ can be calculated using:

$$p_f \approx \frac{p_f(x_1) + p_f(x_2)}{2}, \text{and } \frac{\partial p_f^*}{\partial x} = \frac{p_f^*(x_2) - p_f^*(x_1)}{\Delta}, \tag{D.7}$$

where $p_f(x_1)$ and $p_f(x_2)$ are the fluid pressure at locations x_1 and x_2 along the pipe respectively.

D.1.3 power measurement using spectral density

Verhiji [110] adopted the Pavic method and proposed a cross spectral density method to overcome the problem of phase matching in the time domain. Based on his contribution, the power transmission to a fluid borne wave, illustrated in Eq. (D.6), can be expressed by:

$$\frac{\widehat{W_f}}{\mathrm{Hz}} = \frac{A_f}{\rho_f \omega \Delta} \mathrm{Im}\{S\left(p_{(x_1)} p_{(x_2)}\right)\}, \tag{D.8}$$

where $S(p(x_1)p(x_2))$ is the cross-spectral density between the fluid pressure at locations x_1 and x_2 along the pipe. The represented formula in Eq. (D.8) is related to the intensity measurement, used in the intensity probe which is proportional to the difference of the pressure, at two locations along the pipe followed by multiplication to the cross section

area of the fluid region. The above formula is valid for a semi-infinite structure which possess no disturbance reflection or a structure subjected to high frequencies.

D.2 Proposed power measurement

When the incident and reflected intensity of the propagating disturbance are comparable to one other, the field become highly reactive for the intensity measurement. Therefore, prior to power measurement, a wave decomposition needs to be performed to separate the incident and reflected wave. To this end, the frequency response of the structure at two locations can be used. The decomposition can be performed by using the recorded pressure relative to a reference signal at the two points along a finite length pipe as follows:

$$\begin{bmatrix} P(x_1) \\ P(x_2) \end{bmatrix} = \begin{bmatrix} e^{-\mathrm{i}k_1 x_1} & e^{\mathrm{i}k_1 x_1} \\ e^{-\mathrm{i}k_1 x_2} & e^{\mathrm{i}k_1 x_2} \end{bmatrix} \begin{bmatrix} P^+ \\ P^- \end{bmatrix}. \tag{D.9}$$

By applying matrix inversion into Eq. (D.9), the amplitude of the incident and the reflected wave is given by:

$$\begin{bmatrix} P^+ \\ P^- \end{bmatrix} = \begin{bmatrix} e^{-\mathrm{i}k_1 x_1} & e^{\mathrm{i}k_1 x_1} \\ e^{-\mathrm{i}k_1 x_2} & e^{\mathrm{i}k_1 x_2} \end{bmatrix}^{-1} \begin{bmatrix} P(x_1) \\ P(x_2) \end{bmatrix}. \tag{D.10}$$

Using either of waves propagating in positive and negative x - direction (in this example the positive one is used) and replacing it into Eq. (D.8), followed by rearranging, the transmitted power to the fluid borne wave through the exciter can be evaluated by:

$$\frac{\widehat{W_f}}{\mathrm{Hz}} = \frac{A_f}{\rho_f \omega \Delta} \mathrm{Im}\left\{ S_{(P^+(x_1) P^+(x_2))} \right\} S_{(V_{\mathrm{ref}}\ V_{\mathrm{ref}})}, \tag{D.11}$$

where V_{ref} is the input voltage to the driver.

Appendix E

Spatial aliasing frequency associated to the pipe and source ground-borne waves

In Chapter 5 two sources of excitation were assumed to explain the main features of the vibro-acoustic technique. This appendix gives a brief overview of the required resolution to avoid spatial phase aliasing from the radiation of each source to the ground surface. In this investigation it is assumed that surrounding medium is isotropic and homogeneous. The effects of surface waves, due to the superposition of body waves at the surface of the half space are discarded.

E.1 Direct waves from the source applied to the pipe

Assuming two measurement points located at the surface and distanced Δ_G apart. The first point located at x_1 away from the origin, and d_1 distance from the point of radiation. Point x_2 is located distance d_2 from the same source.

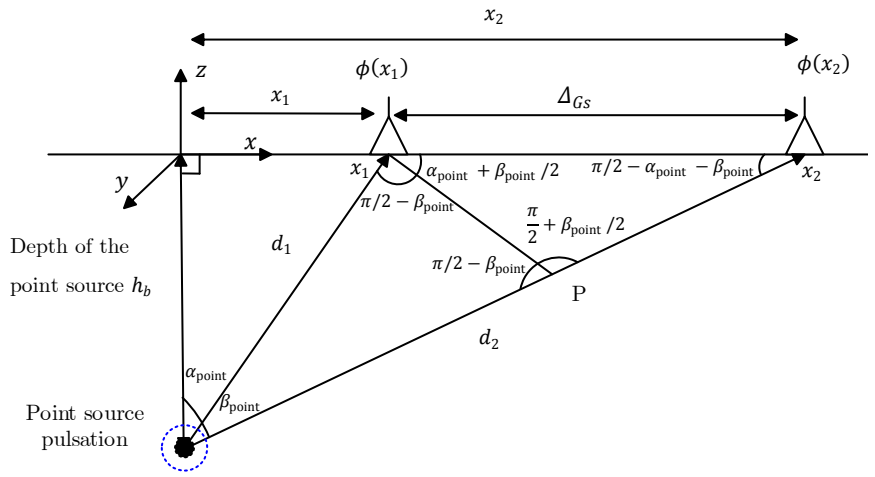

FIGURE E.1: Spherical wave radiation into an elastic medium.

The value of $\phi(x_1), \phi(x_2)$ is given by:

$$\phi(x_1) = kd_1, \phi(x_2) = kd_2, \tag{E.1}$$

As illustrated in Fig. E.1 the distance of points x_1 and x_2 from the source can be described using the parameters such as; depth of the point source h_b and angles; α for x_1 and $\alpha + \beta$ for x_2. The phase difference between the two points is given by:

$$\begin{aligned}\phi(x_2) - \phi(x_2) = k\left(d_2 - d_1\right) = k\left(\Delta_G \frac{\sin(\alpha + \beta/2)}{\cos(\beta/2)}\right) = \\ k\Delta_G\left(\sin(\alpha) + \cos(\alpha)\tan(\beta/2)\right).\end{aligned} \tag{E.2}$$

To avoid spatial phase aliasing:

$$-\pi < k\Delta_G\left(\sin(\alpha) + \cos(\alpha)\tan(\beta/2)\right) \leq \pi. \tag{E.3}$$

Eq. (E.3) can be simplified to:

$$\Delta_G \leq \frac{\lambda_b}{2} \frac{1}{\left(\sin(\alpha) + cos(\alpha)\tan(\beta/2)\right)}. \tag{E.4}$$

To reveal the effect of the second term on the right side of Eq. (E.4), its values by assuming $\alpha + \beta < \pi/2$ is plotted. Such a assumption is required to ensure that the

emitted wave from the point source impinges to the surface. As shown by the colours bar of Fig. E.2, the maximum value of the second term on the right side of Eq. (E.4) is one.

For constant Δ_G, the more measurement are far way from the excitation source, the higher α and lower β will be achieved. Therefore, the phase aliasing takes place first at the closest region to the excitation point and then at further distances.

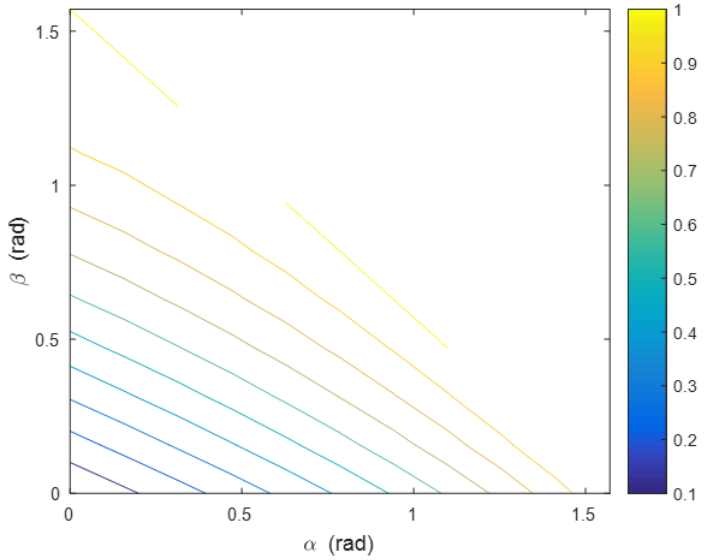

FIGURE E.2: The value of $\dfrac{1}{(\sin(\alpha) + cos(\alpha)\tan(\beta/2))}$ by assuming $\alpha + \beta < \pi/2$.

E.2 Pipe waves

Assuming two measurement points located at the surface, distanced apart and parallel to the buried pipe main axis. The recorded phase from radiation of the conical wave from a buried fluid filled pipe at the two locations, provided that the point source is not existed in the medium can be explained by:

$$\begin{aligned} \phi(x_1) &= k_{(n,s)} x_{(1)\text{pipe}} + k_b D_{\text{pipe}} \\ \phi(x_2) &= k_{(n,s)} x_{(2)\text{pipe}} + k_b D_{\text{pipe}} \end{aligned} \tag{E.5}$$

Phase angle difference between the two points is indicated as:

$$\phi(x_2) - \phi(x_1) = k_{(n,s)} \left(x_{(1)\text{pipe}} - x_{(2)\text{pipe}} \right) \tag{E.6}$$

To avoid spatial phase aliasing along the image:

$$-\pi < \phi(x_2) - \phi(x_1) \leqslant \pi \longrightarrow \Delta_G \leqslant c_{(n,s)}/2f. \tag{E.7}$$

Lets assume that the speed of the axisymmetric fluid borne wave is 300 m/s and the frequency range of interest is 10 - 100 Hz. Therefore, the resolution of 3 m along the pipe axis is enough to ensure that no aliasing takes place when recording the surface vibration form the pipe wave.

Bibliography

[1] W. McMahon, M. Burtwell, and M. Evans, "Minimising Street Works Disruption: The Real Costs of Street Works to the Utility Industry and Society ," WM/12/8. ISBN: 1-84057-408-9, Tech. Rep., 2005.

[2] M. Farrimond and J. Parker, "The importance of seeing through the ground–a utility perspective," in *Proc. 12th International Conference on Ground Penetrating Radar*, 2008.

[3] M. H. Burtwell, M. Evans, and W. McMahon, *Minimising street works disruption: the real costs of street works to the utility industry and society.* UK Water Industry Research Limited, 2006.

[4] "Draindepot Ltd." https://www.draindepot.co.uk/blog/benefits-of-plastic-drainage-pipes, accessed: 2018-05-25.

[5] "Gyroscopic Mapping Services Ltd." https://www.plowmancraven.co.uk/services/gyroscopic-mapping-services, accessed : 2018-12-10.

[6] C. Rogers, T. Hao, S. Costello, M. Burrow, N. Metje, D. Chapman, J. Parker, R. Armitage, J. Anspach, J. Muggleton *et al.*, "Condition assessment of the surface and buried infrastructure–a proposal for integration," *Tunnelling and Underground Space Technology*, vol. 28, pp. 202–211, 2012.

[7] Z. Liu and Y. Kleiner, "State of the art review of inspection technologies for condition assessment of water pipes," *Measurement*, vol. 46, no. 1, pp. 1–15, 2013.

[8] Hulsenbeck, "Verfaren zur elektrishen bodenforshungg," 1926, German Patent 489434. [Online]. Available: https://patents.google.com/patent/DE489434C/en

[9] D. J. Daniels, *Ground Penetrating Radar*. American Cancer Society, 2005. [Online]. Available: https://onlinelibrary.wiley.com/doi/abs/10.1002/0471654507.eme152

[10] A. Annan, "Chapter 1 - electromagnetic principles of ground penetrating radar," in *Ground Penetrating Radar Theory and Applications*, H. M. Jol, Ed. Amsterdam: Elsevier, 2009, pp. 1 – 40. [Online]. Available: http://www.sciencedirect.com/science/article/pii/B9780444533487000016

[11] A. Ristic and D. Petrovacki, "An underground utility detection technology – our experiences," in *Proc. 5th International Conference on Engineering and Environment*, 05 2007.

[12] D. Ayala-Cabrera, M. Herrera, I. Montalvo, and R. Pérez-García, "Towards the visualization of water supply system components with gpr images," *Mathematical and Computer Modelling*, vol. 54, no. 7-8, pp. 1818–1822, 2011.

[13] D. Ayala Cabrera, S. J. Ocana-Levario, J. Izquierdo Sebastián, and R. Pérez García, "Improving water supply system components visualization into gpr images," *Athens journal of technology and engineering*, vol. 1, no. 4, pp. 253–261, 2014.

[14] D. Ayala-Cabrera, J. Izquierdo, R. Pérez-García, and S. Ocaña-Levario, "Probabilistic maps for buried pipes location based on gpr images," *International Journal of Complex Systems in Science*, vol. 4, pp. 27–30, 03 2014.

[15] D. Ayala-Cabrera, J. Izquierdo, I. Montalvo, and R. Perez-Garcia, "Water supply system component evaluation from gpr radargrams using a multi-agent approach," *Mathematical and Computer Modelling*, vol. 57, no. 7-8, pp. 1927–1932, 2013.

[16] D. Ayala-Cabrera, M. Herrera, J. Izquierdo, and R. Perez-Garcia, "Location of buried plastic pipes using multi-agent support based on gpr images," *Journal of Applied Geophysics*, vol. 75, no. 4, pp. 679–686, 2011.

[17] S.-H. Ni, Y.-H. Huang, K.-F. Lo, and D.-C. Lin, "Buried pipe detection by ground penetrating radar using the discrete wavelet transform," *Computers and Geotechnics*, vol. 37, no. 4, pp. 440–448, 2010.

[18] J. Paniagua, M. del Rio, and M. Rufo, "Test site for the analysis of subsoil gpr signal propagation," in *Proceedings of the Tenth International Conference on Grounds Penetrating Radar, 2004. GPR 2004.* IEEE, 2004, pp. 751–754.

[19] M. Beatty. Find That Buried Plastic. https://www.digdifferent.com/online_exclusives/2017/06/find_that_buried_plastic_pipe, accessed: 2018-09-29.

[20] G. R. Olhoeft, "Electrical, magnetic and geometric properties that determine ground penetrating radar performance," in *Proceedings of GPR*, vol. 98, 1998, pp. 27–30.

[21] N. Cassidy, "Introduction to GPR (workshop 1)," in *12th International Conference on Ground Penetrating Radar (GPR08)*, vol. 1619, 2008.

[22] N. J. Cassidy, "Chapter 2 - electrical and magnetic properties of rocks, soils and fluids," in *Ground Penetrating Radar Theory and Applications*, H. M. Jol, Ed. Amsterdam: Elsevier, 2009, pp. 41 – 72. [Online]. Available: http://www.sciencedirect.com/science/article/pii/B9780444533487000028

[23] J. E. Huebler and B. K. Campbell, "Acoustic method for locating concealed pipe," Jul. 7 1992, US Patent 5,127,267. [Online]. Available: https://patents.google.com/patent/US5127267?oq=5127267

[24] A. A. Burns, G. A. Hayter, S. A. Griffin, and J. W. Maresca Jr, "Acoustic system for measuring the location and depth of underground pipe," Dec. 21 1999. [Online]. Available: https://patents.google.com/patent/US6003376A/en?oq=6.003.376

[25] J. Muggleton, M. Brennan, and Y. Gao, "Determining the location of buried plastic water pipes from measurements of ground surface vibration," *Journal of Applied Geophysics*, vol. 75, no. 1, pp. 54–61, 2011.

[26] ST20 Listening Stick Ltd. https://www.hwmglobal.com/st20-listening-stick, accessed: 2018-09-25.

[27] J. Muggleton, M. Brennan, and Y. Gao, "Vibration radiation from buried plastic water pipes: an experimental investigation at the ground surface," *Proc. ISMA, Leuven*, 2012.

[28] "PipeTrack Ltd." http://www.pipetrack.co.uk/faqs.htm, accessed: 2018-12-09.

[29] C. Anderson and S. Offshore, "Pipeline inspection," http://www.ths.org.uk, accessed: 14-11-2013.

[30] J. Wintle, B. Kenzie, G. Amphlett, and S. Smalley, *Best practice for risk based inspection as a part of plant integrity management.* Great Britain, Health and Safety Executive, 2001.

[31] "The Water Supply (Water Fittings) Regulations 1999," http://www.legislation.gov.uk/uksi/1999/1148/contents/made, accessed: 2019-05-17.

[32] L. H. Donnell, "Stability of thin-walled tubes under torsion," US Government Printing Office, 1933. [Online]. Available: https://ntrs.nasa.gov/archive/nasa/casi.ntrs.nasa.gov/19930091553.pdf

[33] W. Flügge, *Stresses in Shells.* Springer Berlin Heidelberg, 1962. [Online]. Available: https://www.springer.com/gp/book/9783662010280

[34] A. W. Leissa, *Vibration of shells*, ser. NASA SP. Scientific and Technical Information Office, National Aeronautics and Space Administration, 1973. [Online]. Available: https://babel.hathitrust.org/cgi/pt?id=uiug.30112002809462&view=1up&seq=3

[35] E. Skelton and J. James, *Theoretical Acoustics of Underwater Structures.* Imperial College Press, 1997. [Online]. Available: https://play.google.com/books/reader?id=y_-3CgAAQBAJ&hl=en_GB&pg=GBS.PR10

[36] C. Fuller, "Monopole excitation of vibrations in an infinite cylindrical elastic shell filled with fluid," *Journal of Sound and vibration*, vol. 96, no. 1, pp. 101–110, 1984.

[37] A. Jette and J. Parker, "Surface displacements accompanying the propagation of acoustic waves within an underground pipe," *Journal of Sound and Vibration*, vol. 69, no. 2, pp. 265–274, 1980.

[38] F. Fahy and P. Gardonio, *Sound and Structural Vibration: Radiation, Transmission and Response*, ser. EngineeringPro collection. Elsevier Science, 2007. [Online]. Available: https://www.elsevier.com/books/sound-and-structural-vibration/fahy/978-0-08-047110-5

[39] C. Fuller and F. J. Fahy, "Characteristics of wave propagation and energy distributions in cylindrical elastic shells filled with fluid," *Journal of sound and vibration*, vol. 81, no. 4, pp. 501–518, 1982.

[40] C. Fuller, "The input mobility of an infinite circular cylindrical elastic shell filled with fluid," *Journal of sound and vibration*, vol. 87, no. 3, pp. 409–427, 1983.

[41] Y. Gu, R. Clark, C. Fuller, and A. Zander, "Experiments on active control of plate vibration using piezoelectric actuators and polyvinylidene fluoride (pvdf) modal sensors," *Journal of vibration and acoustics*, vol. 116, no. 3, pp. 303–308, 1994.

[42] D. Korteweg, "Ueber die fortpflanzungsgeschwindigkeit des schalles in elastischen röhren," *Annalen der Physik*, vol. 241, no. 12, pp. 525–542, 1878.

[43] J. James, "Computation of acoustic power, vibration response and acoustic pressures of fluid-filled pipes." Admiralty marine technology establishment Teddington (England), Tech. Rep., 1982.

[44] S. Oyadiji and G. Tomlinson, "Vibration transmissibility characteristics of reinforced viscoelastic pipes employing complex moduli master curves," *Journal of Sound and Vibration*, vol. 102, no. 3, pp. 347–367, 1985.

[45] P. Esparcieux, "Measurement of vibrational wave characteristics of beams and pipes with and without discontinuity," Ph.D. dissertation, University of Southampton, 1986.

[46] C. H. Sherman and J. L. Butler, *Transducers and arrays for underwater sound*. Springer, 2007, vol. 4. [Online]. Available: http://fumblog.um.ac.ir/gallery/402/Transducers%20and%20Arrays%20for%20Underwater%20Sound.pdf

[47] C. L. Pekeris, "Theory of propagation of explosive sound in shallow water," in *Propagation of Sound in the Ocean*. Geological Society of America, 01 1948. [Online]. Available: https://doi.org/10.1130/MEM27-2-p1

[48] L. Bjorno, "A comparison between measured pressure waves in water arising from electrical discharges and detonation of small amounts of chemical explosives," *Journal of Engineering for Industry*, vol. 92, no. 1, pp. 29–34, 1970.

[49] J. R. Nedwell, "Development of a technique for the experimental determination of the acoustic transmission and reflection characteristics of submerged plates," Ph.D. dissertation, University of Southampton, 1986.

[50] B. F. Giles, "Some notes on air-gun development as a marine seismic source," *The Leading Edge*, vol. 28, no. 11, pp. 1334–1335, 2009. [Online]. Available: https://doi.org/10.1190/1.3259610

[51] B. Dragoset, "Introduction to air guns and air-gun arrays," *The Leading Edge*, vol. 19, no. 8, pp. 892–897. [Online]. Available: https://library.seg.org/doi/epub/10.1190/1.1438741

[52] S. Ronen, S. Denny, R. Telling, S. Chelminski, J. Young, D. Darling, and S. Murphy, *Reducing ocean noise in offshore seismic surveys using low-pressure sources and swarms of motorized unmanned surface vessels*, 2015, pp. 4956–4960. [Online]. Available: https://library.seg.org/doi/abs/10.1190/segam2015-5928795.1

[53] T. Leighton, "From seas to surgeries, from babbling brooks to baby scans: The acoustics of gas bubbles in liquids," *International Journal of Modern Physics B*, vol. 18, no. 25, pp. 3267–3314, 2004.

[54] J. Langhammer, "Experimental studies of energy loss mechanisms in air gun bubble dynamics," *Ph. D. thesis, Norwegian University of Science and Technology*, 1994.

[55] D. Hutchinson and R. S. Detrick, "Water gun vs air gun: A comparison," *Marine geophysical researches*, vol. 6, no. 3, pp. 295–310, 1984.

[56] L. G. Johnson and B. M. D'andrade, "Double tank pinch trigger pump water gun," Sep. 29 1992. [Online]. Available: https://patents.google.com/patent/US5150819?oq=5%2c150%2c819

[57] T. Leighton, "The principles of cavitation," *Ultrasound in food processing*, vol. 12, 1998. [Online]. Available: http://resource.isvr.soton.ac.uk/staff/pubs/PubPDFs/Pub2487.pdf

[58] K. R. Czech and W. Gosk, "Measurement of surface vibration accelerations propagated in the environment," *Procedia engineering*, vol. 189, pp. 45–50, 2017.

[59] R. L. Nigbor, "Six-degree-of-freedom ground-motion measurement," *Bulletin of the Seismological Society of America*, vol. 84, no. 5, pp. 1665–1669, 1994.

[60] Y. Gao, M. Brennan, P. Joseph, J. Muggleton, and O. Hunaidi, "On the selection of acoustic/vibration sensors for leak detection in plastic water pipes," *Journal of Sound and Vibration*, vol. 283, no. 3-5, pp. 927–941, 2005.

[61] J. M. Muggleton, "An Assessment of the Use of a Scanning Laser to Measure Ground Vibration," Institute of sound and vibration research, Southampton , UK., Tech. Rep. 330, 2010.

[62] Y. Gao, Y. Liu, and J. M. Muggleton, "Axisymmetric fluid-dominated wave in fluid-filled plastic pipes: Loading effects of surrounding elastic medium," *Applied Acoustics*, vol. 116, pp. 43–49, 2017.

[63] R. Pinnington and A. Briscoe, "Externally applied sensor for axisymmetric waves in a fluid filled pipe," *Journal of Sound and vibration*, vol. 173, no. 4, pp. 503–516, 1994.

[64] J. M. Muggleton, M. Brennan, and R. Pinnington, "Wavenumber prediction of waves in buried pipes for water leak detection," *Journal of Sound and Vibration*, vol. 249, no. 5, pp. 939–954, 2002.

[65] J. Muggleton and J. Yan, "Wavenumber prediction and measurement of axisymmetric waves in buried fluid-filled pipes: Inclusion of shear coupling at a lubricated pipe/soil interface," *Journal of Sound and Vibration*, vol. 332, no. 5, pp. 1216–1230, 2013.

[66] T. Lin and G. Morgan, "Wave propagation through fluid contained in a cylindrical, elastic shell," *The Journal of the Acoustical Society of America*, vol. 28, no. 6, pp. 1165–1176, 1956.

[67] H. Kolsky, *Stress Waves in Solids*, ser. Dover phoenix editions. Dover Publications, Incorporated, 2003. [Online]. Available: https://books.google.co.uk/books?id=euhRyQEACAAJ

[68] K. Graff, *Wave Motion in Elastic Solids*, ser. Dover Books on Physics Series. Dover Publications, 1991. [Online]. Available: https://books.google.co.uk/books?id=5cZFRwLuhdQC

[69] W. Ewing, W. Jardetzky, and F. Press, *Elastic Waves in Layered Media*, ser. Contribution. McGraw-Hill, 1957, no. no. 189. [Online]. Available: https://books.google.co.uk/books?id=OB5RAAAAMAAJ

[70] A. Verruijt, *An Introduction to Soil Dynamics*, ser. Theory and Applications of Transport in Porous Media. Springer Netherlands, 2009. [Online]. Available: https://books.google.co.uk/books?id=ZXJ4N1zDWl0C

[71] B. Das, *Advanced Soil Mechanics, Second Edition*. Taylor & Francis, 1997. [Online]. Available: https://books.google.co.uk/books?id=IRJ_QgAACAAJ

[72] M. Prek, "Experimental determination of the speed of sound in viscoelastic pipes," *International Journal of Acoustics and Vibration*, vol. 5, no. 3, pp. 146–150, 2000.

[73] J. Muggleton, M. Brennan, and P. Linford, "Axisymmetric wave propagation in fluid-filled pipes: wavenumber measurements in in vacuo and buried pipes," *Journal of Sound and Vibration*, vol. 270, no. 1-2, pp. 171–190, 2004.

[74] H. Boden, "Characterization of fluid machines as sources of fluid-borne noise," Ph.D. dissertation, doctoral Thesis Dept. Techn. Ac., Royal inst. of techn. Sweden. Rep. No. TRITA-TAK-8906 ISSN 0280-2082, 1991.

[75] A. Albert, Ed., *Regression and the Moore-Penrose Pseudoinverse*, ser. ISSN. Elsevier Science, 1972. [Online]. Available: https://books.google.co.uk/books?id=-kOivHeTIWQC

[76] G. Pavić, "Vibroacoustical energy flow through straight pipes," *Journal of Sound and Vibration*, vol. 154, no. 3, pp. 411 – 429, 1992. [Online]. Available: http://www.sciencedirect.com/science/article/pii/0022460X9290776T

[77] M. Möser, M. Heckl, and K.-H. Ginters, "Zur schallausbreitung in flüssigkeitsgefüllten kreiszylindrischen rohren," *Acta Acustica united with Acustica*, vol. 60, no. 1, pp. 34–44, 1986.

[78] E. Kennard, "The new approach to shell theory-circular cylinders," *JOURNAL OF APPLIED MECHANICS-TRANSACTIONS OF THE ASME*, vol. 20, no. 1, pp. 33–40, 1953.

[79] H. Tzou, "A new distributed sensor and actuator theory for "intelligent" shells," *Journal of sound and vibration*, vol. 153, no. 2, pp. 335–349, 1992.

[80] J. Muggleton, M. Brennan, R. Pinnington, and Y. Gao, "A novel sensor for measuring the acoustic pressure in buried plastic water pipes," *Journal of Sound and Vibration*, vol. 295, no. 3-5, pp. 1085–1098, 2006.

[81] *The Growth Or Collapse of a Spherical Bubble in a Viscous Compressible Liquid*, ser. Report: Hydrodynamics Laboratory. Hydrodynamics Laboratory, California Institute of Technology, 1952. [Online]. Available: https://books.google.co.uk/books?id=NJUAkAEACAAJ

[82] C.-S. Chen, "Two interconnected rubber balloons as a demonstration showing the effect of surface tension." [Online]. Available: http://dx.doi.org/10.14288/1.0107206

[83] J. B. Keller and I. I. Kolodner, "Damping of underwater explosion bubble oscillations," *Journal of applied physics*, vol. 27, no. 10, pp. 1152–1161, 1956.

[84] L. E. Kinsler, A. R. Frey, A. B. Coppens, and J. V. Sanders, "Fundamentals of acoustics," *Fundamentals of Acoustics, 4th Edition, by Lawrence E. Kinsler, Austin R. Frey, Alan B. Coppens, James V. Sanders, pp. 560. ISBN 0-471-84789-5. Wiley-VCH, December 1999.*, p. 560, 1999.

[85] M. A. Richards, "Interferometric sar and coherent exploitation," pp. 337–398, 2012. [Online]. Available: https://digital-library.theiet.org/content/books/10.1049/sbra020e_ch8

[86] Y. Lu, W. Zhao, and X. Zhang, "Quality map generation in two-dimensional phase unwrapping process by using edge detection techniques," in *Vision Sensors and Edge Detection*. IntechOpen, 2010.

[87] B. Papandreou, "On the detection of shallow objects using seismic wave reflections," Ph.D. dissertation, University of Southampton, 2011. [Online]. Available: https://eprints.soton.ac.uk/334160/

[88] Y. Gao, J. M. Muggleton, Y. Liu, and E. Rustighi, "An analytical model of ground surface vibration due to axisymmetric wave motion in buried fluid-filled pipes," *Journal of Sound and Vibration*, vol. 395, pp. 142–159, 2017.

[89] M. C. Junger, "The physical interpretation of the expression for an outgoing wave in cylindrical coordinates," *The Journal of the Acoustical Society of America*, vol. 25, no. 1, pp. 40–47, 1953.

[90] D. Ghiglia, D. Ghiglia, M. Pritt, and M. Pritt, *Two-Dimensional Phase Unwrapping: Theory, Algorithms, and Software*, ser. Living Away from Home: Studies. Wiley, 1998. [Online]. Available: https://books.google.co.uk/books?id=pQtTAAAAMAAJ

[91] K. Itoh, "Analysis of the phase unwrapping algorithm," *Appl. Opt.*, vol. 21, no. 14, pp. 2470–2470, Jul 1982. [Online]. Available: http://ao.osa.org/abstract.cfm?URI=ao-21-14-2470

[92] L. Swirski, "CFA Interpolation Detection," *Topics in Security: Forensic Signal Analysis, University of Cambridge*, vol. 30, 2009.

[93] D. Garcia, "Robust smoothing of gridded data in one and higher dimensions with missing values," *Computational statistics & data analysis*, vol. 54, no. 4, pp. 1167–1178, 2010.

[94] M. A. Herráez, D. R. Burton, M. J. Lalor, and M. A. Gdeisat, "Fast two-dimensional phase-unwrapping algorithm based on sorting by reliability following a noncontinuous path," *Applied optics*, vol. 41, no. 35, pp. 7437–7444, 2002.

[95] H. S. Abdul-Rahman, M. A. Gdeisat, D. R. Burton, M. J. Lalor, F. Lilley, and C. J. Moore, "Fast and robust three-dimensional best path phase unwrapping algorithm," *Applied optics*, vol. 46, no. 26, pp. 6623–6635, 2007.

[96] D. C. Ghiglia and L. A. Romero, "Robust two-dimensional weighted and unweighted phase unwrapping that uses fast transforms and iterative methods," *J. Opt. Soc. Am. A*, vol. 11, no. 1, pp. 107–117, Jan 1994. [Online]. Available: http://josaa.osa.org/abstract.cfm?URI=josaa-11-1-107

[97] J. Muggleton and M. Brennan, "The design and instrumentation of an experimental rig to investigate acoustic methods for the detection and location of underground piping systems," *Applied Acoustics*, vol. 69, no. 11, pp. 1101–1107, 2008.

[98] M. Fierro, "Improved performance for leak detection systems through statistical data averaging," Vista Research Technical Memorandum No. 52. [Online].

Available: https://www.vistaprecision.com/images/downloads/TechnicalMemos/52.pdf

[99] M. Serridge and T. R. Licht, "Piezoelectric accelerometers and vibration preamplifiers: theory and application handbook," 1987. [Online]. Available: https://www.bksv.com/media/doc/bb0694.pdf

[100] S. P. Won and F. Golnaraghi, "A triaxial accelerometer calibration method using a mathematical model," *IEEE Transactions on Instrumentation and Measurement*, vol. 59, no. 8, pp. 2144–2153, 2010.

[101] R. Blevins, *Formulas for Natural Frequency and Mode Shape*. R.E. Krieger, 1984. [Online]. Available: https://books.google.co.uk/books?id=ZexnjgEACAAJ

[102] D. Ewins, *Modal Testing: Theory and Practice*, ser. Engineering dynamics series. Research Studies Press, 1984. [Online]. Available: https://kupdf.net/download/d-j-ewins-modal-testing-theory-and-practice_5b07f151e2b6f5414c0149f4_pdf

[103] G. Pavić, "Vibrational energy flow in elastic circular cylindrical shells," *Journal of Sound and Vibration*, vol. 142, no. 2, pp. 293–310, 1990.

[104] G. Pavić, "Techniques for the determination of vibration transmission mechanisms in structures," Ph.D. dissertation, University of Southampton, 1976.

[105] G. Pavić, "Determination of sound power-flow in structures: principles and problems of realization," in *Proceeding of International Congress on Recent Developments in Acoustic Intensity Measuring, CETIM, Senlis, France*, 1981, pp. 209–215.

[106] G. Pavić, "Structural surface intensity-a novel approach in vibration analysis and diagnostics," in *2nd International Congress on Acoustic Intensity Measurement*, 1985, pp. 219–226.

[107] G. Pavić, "Structural surface intensity: An alternative approach in vibration analysis and diagnosis," *Journal of Sound and Vibration*, vol. 115, no. 3, pp. 405 – 422, 1987. [Online]. Available: http://www.sciencedirect.com/science/article/pii/0022460X87902860

[108] G. Pavić, "Acoustical power flow in structures: a survey," in *Proc. Inter-Noise*, vol. 88, 1988, pp. 559–564.

[109] G. Pavić, "Measurement of structure borne wave intensity, part i: Formulation of the methods," *Journal of Sound and Vibration*, vol. 49, no. 2, pp. 221 – 230, 1976. [Online]. Available: http://www.sciencedirect.com/science/article/pii/0022460X76904983

[110] J. Verheij, "Cross spectral density methods for measuring structure borne power flow on beams and pipes," *Journal of Sound and Vibration*, vol. 70, pp. 133–139, 1980.